



The Science and Technology of Carbon Nanotubes

K. Tanaka
T. Yamabe
K. Fukui[†]
Editors

Elsevier

The Science and Technology of Carbon Nanotubes

The Science and Technology of Carbon Nanotubes

Edited by

Kazuyoshi Tanaka

Kyoto University, Japan

Tokio Yamabe

Kyoto University, Japan

Kenichi Fukui[†]

Institute for Fundamental Chemistry, Japan



1999

Elsevier

Amsterdam - Lausanne - New York - Oxford - Shannon - Singapore - Tokyo

ELSEVIER SCIENCE Ltd
The Boulevard, Langford Lane
Kidlington, Oxford OX5 1GB, UK

© 1999 Elsevier Science Ltd. All rights reserved.

This work is protected under copyright by Elsevier Science, and the following terms and conditions apply to its use:

Photocopying

Single photocopies of single chapters may be made for personal use as allowed by national copyright laws. Permission of the Publisher and payment of a fee is required for all other photocopying, including multiple or systematic copying, copying for advertising or promotional purposes, resale, and all forms of document delivery. Special rates are available for educational institutions that wish to make photocopies for non-profit educational classroom use.

Permissions may be sought directly from Elsevier Science Rights & Permissions Department, PO Box 800, Oxford OX5 1DX, UK; phone: (+44) 1865 843830, fax: (+44) 1865 853333, e-mail: permissions@elsevier.co.uk. You may also contact Rights & Permissions directly through Elsevier's home page (<http://www.elsevier.nl>), selecting first 'Customer Support', then 'General Information', then 'Permissions Query Form'.

In the USA, users may clear permissions and make payments through the Copyright Clearance Center, Inc., 222 Rosewood Drive, Danvers, MA 01923, USA; phone: (978) 7508400, fax: (978) 7504744, and in the UK through the Copyright Licensing Agency Rapid Clearance Service (CLARCS), 90 Tottenham Court Road, London W1P 0LP, UK; phone: (+44) 171 631 5555; fax: (+44) 171 631 5500. Other countries may have a local reprographic rights agency for payments.

Derivative Works

Tables of contents may be reproduced for internal circulation, but permission of Elsevier Science is required for external resale or distribution of such material.

Permission of the Publisher is required for all other derivative works, including compilations and translations.

Electronic Storage or Usage

Permission of the Publisher is required to store or use electronically any material contained in this work, including any chapter or part of a chapter.

Except as outlined above, no part of this work may be reproduced, stored in a retrieval system or transmitted in any form or by any means, electronic, mechanical, photocopying, recording or otherwise, without prior written permission of the Publisher.

Address permissions requests to: Elsevier Science Rights & Permissions Department, at the mail, fax and e-mail addresses noted above.

Notice

No responsibility is assumed by the Publisher for any injury and/or damage to persons or property as a matter of products liability, negligence or otherwise, or from any use or operation of any methods, products, instructions or ideas contained in the material herein. Because of rapid advances in the medical sciences, in particular, independent verification of diagnoses and drug dosages should be made.

First edition 1999

Library of Congress Cataloging in Publication Data

A catalog record from the Library of Congress has been applied for.

British Library Cataloguing in Publication Data

A catalogue record from the British Library has been applied for.

ISBN: 0 08 042696 4

Ⓢ The paper used in this publication meets the requirements of ANSI/NISO Z39.48-1992 (Permanence of Paper).

Printed in The Netherlands.

EDITORIAL

Carbon nanotube (CNT) is the name of ultrathin carbon fibre with nanometer-size diameter and micrometer-size length and was accidentally discovered by a Japanese scientist, Sumio Iijima, in the carbon cathode used for the arc-discharging process preparing small carbon clusters named by fullerenes. The structure of CNT consists of enroled graphitic sheet, in a word, and can be classified into either multi-walled or single-walled CNT (MWCNT or SWCNT) depending on its preparation method. It is understood that CNT is the material lying in-between fullerenes and graphite as a quite new member of carbon allotropes.

It should be recognised that while fullerene has established its own field with a big group of investigators, the *raison d'être* of the CNT should become, and actually has become, more and more independent from that of fullerenes. As a novel and potential carbon material, CNTs would be far more useful and important compared with fullerenes from practical points of view in that they will directly be related to an ample field of "nanotechnology". It seems that a considerable number of researchers have been participating into the science of CNTs and there has been remarkable progress in the both experimental and theoretical investigations on MWCNT and SWCNT particularly during the last couple of years. Moreover, almost at the same time, an obvious turning point has been marked for the research of CNT toward explicit application targeting, e.g., electronic and/or energy-storing devices.

These circumstances have assured us that it is high time to prepare an authentic second-generation monograph scoping as far as practical application of CNT in succession of the book earlier published [1] covering the results of rather first-stage studies on CNT. Under this planning the present monograph is entitled "The Science and Technology of Carbon Nanotubes" as the successive version of ref. 1 for the benefit of actual and potential researchers of these materials by collecting and arranging the chapters with emphasis on the technology for application of CNTs as well as the newest science of these materials written by top-leading researchers including our own manuscripts.

In Chaps. 2-4 most updated summaries for preparation, purification and structural characterisation of SWCNT and MWCNT are given. Similarly, the most recent scopes of the theoretical treatments on electronic structures and vibrational structures can be seen in Chaps. 5-7. The newest magnetic, optical and electrical solid-state properties providing vital base to actual application technologies are described in Chaps. 8-10. Explosive research trends toward application of CNTs including the prospect for large-scale synthesis are introduced in Chaps. 11-14. It is the most remarkable feature of this monograph that it devotes more than a half of the whole volume (Chaps. 8-14) to such practical aspects. The editors truly appreciate that all of the authors should like to offer the readers the newest developments of the science and technological aspects of CNTs.

It is our biggest sorrow that in the course of preparation of this monograph one of the Editors, Professor Kenichi Fukui, Nobel Laureate of 1981 in Chemistry, passed away on January 9, 1998. As one of the editors he was eager to see actual utilisation of CNT in nanotechnological devices as he described in Chap. 1 from the profound scientific viewpoint.

Finally we would like to express our sincere gratitude to Dr. Vijala Kiruvanayagam of Elsevier Science for her kind cooperation as well as encouragement toward publication of this monograph.

KAZUYOSHI TANAKA

Chief Editor

Reference

1. Carbon Nanotubes, ed. M. Endo, S. Iijima and M. S. Dresselhaus, Pergamon, Oxford, 1996.

CONTENTS

Editorial	
K. Tanaka (Chief Editor).....	iii
Chapter 1 Prospect	
late K. Fukui	1
Chapter 2 Synthesis and Purification of Multi-Walled and Single-Walled Carbon Nanotubes	
M. Yumura.....	2
Chapter 3 Electron Diffraction and Microscopy of Carbon Nanotubes	
S. Amelinckx, A. Lucas and P. Lambin.....	14
Chapter 4 Structures of Multi-Walled and Single-Walled Carbon Nanotubes. EELS Study	
T. Hanada, Y. Okada and K. Yase.....	29
Chapter 5 Electronic Structure of Single-Walled Carbon Nanotubes	
K. Tanaka, M. Okada and Y. Huang.....	40
Chapter 6 Phonon Structure and Raman Effect of Single-Walled Carbon Nanotubes	
R. Saito, G. Dresselhaus and M. S. Dresselhaus.....	51
Chapter 7 Behaviour of Single-Walled Carbon Nanotubes in Magnetic Fields	
H. Ajiki and T. Ando.....	63
Chapter 8 Electronic Properties of Carbon Nanotubes Probed by Magnetic Measurements	
M. Kosaka and K. Tanigaki.....	76

Chapter 9 Optical Response of Carbon Nanotubes F. Bommeli, L. Degiorgi, L. Forro and W. A. de Heer.....	89
Chapter 10 Electrical Transport Properties in Carbon Nanotubes J. -P. Issi and J. -C. Charlier.....	107
Chapter 11 Capillarity in Carbon Nanotubes D. Ugarte, T. Stöckli, J.-M. Bonard, A. Châtelain and W. A. de Heer.....	128
Chapter 12 Large-Scale Synthesis of Carbon Nanotubes by Pyrolysis K. Tanaka, M. Endo, K. Takeuchi, W. -K. Hsu, H. W. Kroto, M. Terrones and D. R. M. Walton.....	143
Chapter 13 Carbon Nanotubes as a Novel π-Electron Material and Their Promise for Technological Applications S. Yoshimura	153
Chapter 14 Frontiers of Carbon Nanotubes and Beyond H. Ago and T. Yamabe.....	164
Subject Index	184
Author Index	190

CHAPTER 1

Prospect

late KENICHI FUKUI

*Institute for Fundamental Chemistry
34-4 Nishihiraki-cho, Takano, Sakyo-ku
Kyoto 606-8103, Japan*

Various mesoscopic systems have their own unique characteristics, some of which are of importance due to bridging function over classical and quantum mechanics. It is quite natural that human beings living in macroscopic world could hardly grasp the phenomena occurring in the microscopic world in an intuitive manner. This situation offers a vital sense in the "observation" problem necessarily accompanied with the classical means. The fundamental core of the argument between Einstein-Podolsky-Rosen and Bohr starting in 1935 actually lies in this point. However, recent development of experimental techniques finally comes to suggest the possibility to realise the "Schrödinger-cat states" in a mesoscopic system [1,2].

Carbon nanotubes (CNTs) as well as fullerenes are splendid gift brought to the Earth from the red giant carbon stars in the long-distant universe through the spectroscopy. Moreover, those belong to new carbon allotropes of the mesoscopic scale with well-defined structures. In particular, CNTs are considered to be the materials appropriate to realise intriguing characteristics related to the mesoscopic system based on their size and physicochemical properties.

In a mesoscopic system in which both classical- and quantum-mechanical pictures become compatible even for a short time is realised, its pragmatic significance would be very large considering technical level of today. This book is expected to offer the starting point of such new developments. In this sense, I like to express my wholehearted admiration to the eminent work of Dr. Sumio Iijima who first discovered CNT. The timely contents of this book are readily conceivable by the excellent authors and I also appreciate the wisdom of my colleague editors.

References

1. Zurek, W. H., *Physics Today*, 1991, Oct., 36.
2. Monroe, C., Meekhof, D. M., King, B. E. and Wineland, D. J., *Science*, 1996, **272**, 1131.

CHAPTER 2

Synthesis and Purification of Multi-Walled and Single-Walled Carbon Nanotubes

MOTOO YUMURA

*National Institute of Materials and Chemical Research,
1-1 Higashi, Tsukuba, Ibaraki 305-8565, Japan*

1 Introduction

Since the discovery of carbon nanotube (CNT) by Iijima [1], many researchers have been attracted to this material and a large number of studies have been piled up. CNT was first synthesized as a by-product in arc-discharge method in synthesis of fullerenes and are currently being prepared by many kinds of methods including arc-discharge [2-14], laser ablation [15-20] and catalytic decomposition of hydrocarbon [21-27]. In addition, electrolysis [28] and solar-energy [29] methods have also been proposed. As for the application of CNT, there has been a remarkable progress in recent days such as that to the field-electron emitter [30-34], for instance. Considering such rapid growth in many directions, we can expect that CNT could become one of the most important materials in the 21st century. In this chapter, keeping the application of CNT in mind, an outline of the present situation and the future of the synthesis of this material is described. Aspects toward large-scale synthesis is given in Chap. 12. CNT can be classified into two types: One is multi-walled CNT (MWCNT) [1,2] and the other single-walled CNT (SWCNT) [3]. The former had been discovered earlier than the latter. The MWCNT is comprised of 2 to 30 concentric graphitic layers, diameters of which range from 10 to 50 nm and length of more than 10 μm . On the other hand, SWCNT is much thinner with the diameters from 1.0 to 1.4 nm.

There have been a considerable efforts at synthesis and purification of MWCNT for the measurements of its physical properties. The time is, however, gradually maturing toward its industrial application. As to SWCNT, it could not be efficiently obtained at first and, furthermore, both of its purification and physical-properties measurement were difficult. In 1996, it became that SWCNT could be efficiently synthesized [14,16] and, since then, it has become widely studied mainly from the scientific viewpoints. In what follows, the synthesis and purification of MWCNT and SWCNT are to be summarised itemisingly.

2 MWCNT

MWCNT was originally discovered as a by-product of synthesis of C₆₀ as described above. The yield of MWCNT is 30 ~ 50 % in the electric arc-discharge method using pure carbon. However, from academic point of view, many researchers currently seem to be working at SWCNT, probably tired with tedious purification process of MWCNT particularly synthesized in arc-discharge method. Nonetheless, MWCNT is still attractive due to their ample ability for industrial application utilising its high chemical stability and high mechanical strength [35]. For instance, MWCNT has intrinsic properties suitable for field emitters in the form of a sharp tip with nanometer-scale radius of curvature, high mechanical stiffness, chemical inertness and high electrical conductivity. In addition to these eminent characteristics it also has the unique coaxial shape, which will afford good possibilities to be applied to various fields of industry (see Chaps. 13 and 14).

2.1 Synthesis

2.1.1 Electric arc discharge

When the arc-discharge is carried on keeping the gap between the carbon electrodes about 1 mm, cylindrical deposit forms on the surface of the cathode. Diameter of this cathode deposit is the same as that of the anode stick. Under the conditions that diameter of the anode carbon is 8 mm with the arc-electric current of 80 A (voltage is about 23.5 V) and He pressure of 300 Torr, the cathode deposit grows at the rate of ca. 2~3 mm per min. This cylindrical cathode deposit consists of two portions; the inside is black fragile core and the outside hard shell. The inner core has the fabric structure growing along the length of the cathode-deposit cylinder, the inside of which includes nanotubes and polyhedral graphitic nanoparticles. The outer-shell part consists of the crystal of graphite. Figure 1 shows a rotating-cathode arc-discharge method [6a] which enables long-term operation.

MWCNT grows only inside the cathode deposit and does not exist in other places in the reactor. Quantity of MWCNT obtained depends on the pressure of He atmosphere in the reactor, which is the most important parameter. The highest quantity of MWCNT is obtained when the pressure of He is ca. 500 Torr. When this value becomes below 100 Torr, almost no MWCNT grow. This contrasts to that the highest quantity of fullerene is obtained when the pressure becomes 100 Torr or less.

Another important parameter is the electric current for discharge. If the current density is too high, the quantity of the hard shell increases and that of the MWCNT decreases. To keep the arc discharge stable and the electrode cool are effective to increase in the product quantity of MWCNT. A considerable quantity of graphite is produced in the cathode deposit even under the most suitable condition to the synthesis of MWCNT.

The bundle of MWCNT can be released in ultrasonic cleaner using ethanol as the solvent. The scanning tunnelling microscope (STM) image of thus released MWCNT is shown in Fig. 2.

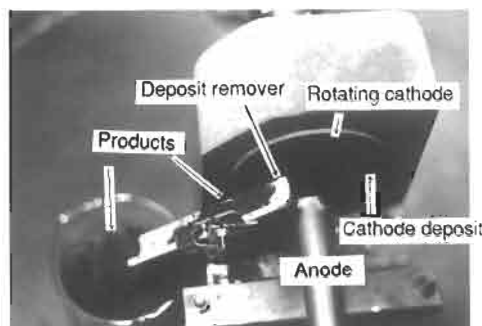


Fig. 1. The rotating-cathode DC arc method [6a]. The cathode deposit is immediately taken out of the discharge by rotation and cropped within one turn. This method offers high stability and reliability of the handling and makes the continuous mass production possible.

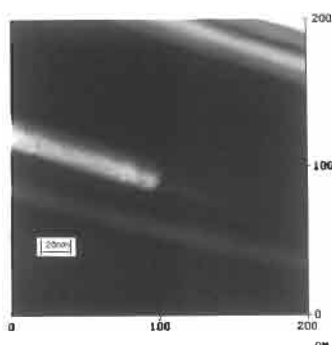


Fig. 2. STM image of MWCNT [6b].

2.1.2 Laser ablation

Laser-ablation method shown in Fig. 3 was used when C_{60} was first discovered in 1985 [15]. This method has also been applied for the synthesis of CNT, but length of MWCNT is much shorter than that by arc-discharge method [17]. Therefore, this method does not seem adequate to the synthesis of MWCNT. However, in the synthesis of SWCNT described later (Sec. 3.1.2), marvelously high yield has been obtained by this method. Hence, laser-ablation method has become another important technology in this respect.

2.1.3 Catalytic decomposition of hydrocarbon

For extension of the application of MWCNT, the key technology is obviously to develop the method for mass production by which high quality MWCNT can be produced with lower cost. It has been well known for a long time that carbon

fibre is synthesized by catalytic decomposition of hydrocarbon [36] in the reactor shown in Fig. 4. Endo et al. reported that MWCNT is contained in carbon fibre synthesized from benzene with Fe particle as the catalyst [21]. Furthermore, MWCNT can be synthesized from acetylene with catalyst [22-25]. Catalyst metals used for MWCNT are listed in Table 1 [24].

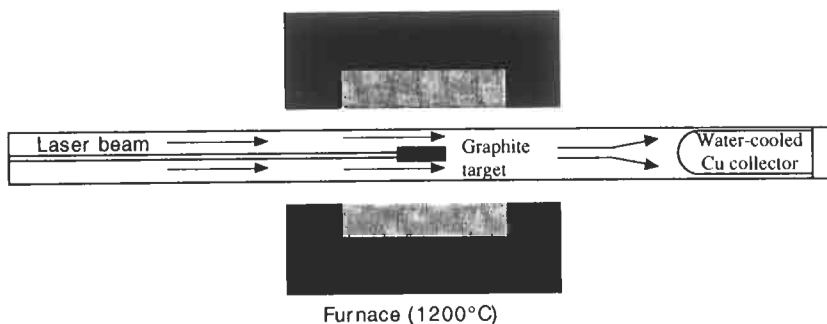


Fig. 3. Schematic drawing of the laser-ablation method.

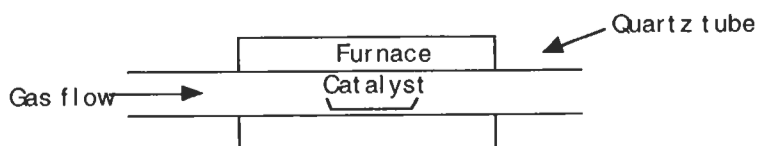


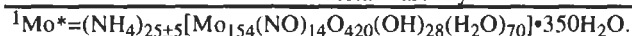
Fig. 4. Schematic drawing of the apparatus used for the catalytic decomposition of hydrocarbon.

MWCNT synthesized by catalytic decomposition of hydrocarbon does not contain nanoparticle nor amorphous carbon and hence this method is suitable for mass production. The shape of MWCNT thus produced, however, is not straight more often than that synthesized by arc-discharge method. This difference could be ascribed to the structure without pentagons nor heptagons in graphene sheet of the MWCNT synthesized by the catalytic decomposition of hydrocarbon, which would affect its electric conductivity and electron emission.

Crucial point in this method lies in controlled production of MWCNT with regard to length, diameter and alignment. To overcome these problems, novel catalyst methods have been developed. Li et al [25] have reported a method for producing aligned CNT (nanotubes brushes) grown on silicates by using Fe particle on meso-porous silica. Terrones et al. [26] have developed a controlled production method of aligned-MWCNT bundles (see Fig. 5) by using thin film of Co catalyst patterned on the silica substrate.

Table 1. Catalyst metals for MWCNT synthesis.

Metal	Catalyst		Temp. (°C)	Carbon source	Ref.
	Catalyst type	Preparation method			
Fe	Ultra fine particle	Decomposition of metallocene	1060	Benzene	21
	Silica support	Pore impregnation	700	Acetylene	22,23
	Zeolite or Clay support	Ion exchange	700	Acetylene	22
	Graphite support	Impregnation	700	Acetylene	23
	Ultra fine particle	Decomposition of metal carbonyl	800	Acetylene	24
	Silica support	Sol-gel process	700	Acetylene	25
Co	Ultra fine particle	Laser etching of Co thin film	1000	Triazine	26
	Ultra fine particle	Decomposition of metal carbonyl	800	Acetylene	24
	Silica support	Pore impregnation	700	Acetylene	22,23
	Zeolite or Clay support	Ion exchange	700	Acetylene	22
Ni	Graphite support	Impregnation	700	Acetylene	23
	Graphite support	Impregnation	700	Acetylene	23
	Ultra fine particle	Decomposition of Ni(C ₈ H ₁₂) ₂	800	Acetylene	24
Mo	Ultra fine particle	Decomposition of Mo* ¹	800	Acetylene	24
Mn	Ultra fine particle	Decomposition of metal carbonyl	800	Acetylene	24
Pd	Ultra fine particle	Decomposition of metal carbonyl	800	Acetylene	24



2.2 Purification

2.2.1 Isolation of MWCNT

In the isolation process of MWCNT, nanoparticles and graphite pieces should be first removed. It is considerably difficult, indeed, to execute the isolation of MWCNT. The main reason for this comes from that the usual separation methods, such as filtration and centrifuge, are effective to remove the big pieces of graphite but not so effective to remove nanoparticles. Therefore, a method to leave only MWCNT by burning nanotubes under oxidising atmosphere after removal of big pieces of graphite has been proposed [37]. This method utilises the property of nanoparticles burnt out faster than MWCNT. The reaction with oxygen starts from the edge of nanoparticles and then proceeds to their centres. Compared with nanoparticle, it takes more time for MWCNT to be completely burnt out, since MWCNT is much longer than nanoparticle. Therefore, cease of burning after appropriate period leaves only MWCNT, but the crop quantity of which is very small.

In order to accelerate the oxidation rate of graphite at lower temperature and to

increase the crop quantity after burning, the raw cathode sediment is treated with CuCl_2 to give the graphite-Cu compound prior to the burning process [38]. This compound can be burnt at lower temperature and hence undesirable consumption of MWCNT is avoided.

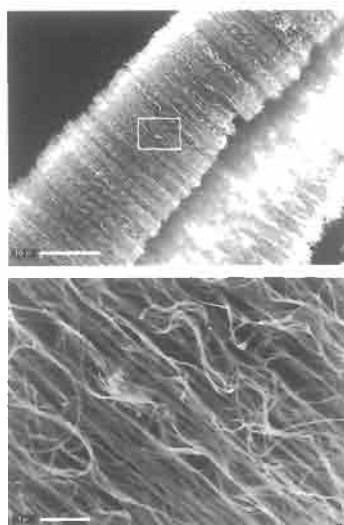


Fig. 5. Scanning electron microscope (SEM) images of aligned MWCNT of uniform length ($40\ \mu\text{m}$) and diameters ($30\text{-}50\ \text{nm}$). Scales bars are $10\ \mu\text{m}$ (top) and $1\ \mu\text{m}$ (bottom) (Courtesy of Drs. M. Terrones and D. R. M. Walton).

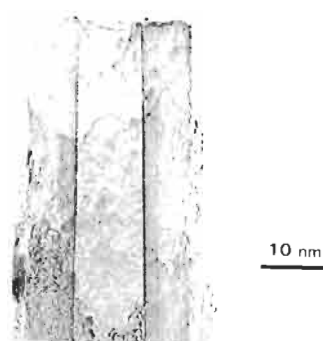


Fig. 6. Transmission electron microscope (TEM) image of MWCNT with the open end. The cap of the tube was removed using the purification process.

2.2.2 Preparation of MWCNTs for field emission

As mentioned above, employment of MWCNT for field emitter will be one of the most important applications of MWCNT. For this purpose, MWCNT is prepared by the chemical purification process [30,38], in which graphite debris and nanoparticles are removed by oxidation with the aid of CuCl_2 intercalation [38]. Purified MWCNT is obtained in the form of black and thin "mat" (a flake with thickness of ca. a few hundreds of μm). Figure 7 shows a typical transmission electron microscope (TEM) picture of MWCNT with an open end, which reveals that a cap is etched off and the central cavity is exposed.



Fig. 7. TEM image of SWCNT growing radially from a La-carbide particles [10b].

3 SWCNT

Preparation research of SWCNT was also put forth by Iijima and his co-worker [3]. The structure of SWCNT consists of an enrolled graphene to form a tube without seam. The length and diameter depend on the kinds of the metal catalyst used in the synthesis. The maximum length is several μm and the diameter varies from 1 to 3 nm. The thinnest diameter is about the same as that of C_{60} (i.e., ca. 0.7 nm). The structure and characteristics of SWCNT are apparently different from those of MWCNT and rather near to fullerenes. Hence novel physical properties of SWCNT as the one-dimensional material between molecule and bulk are expected. On the other hand, the physical property of MWCNT is almost similar to that of graphite used as bulk [6c].

3.1 Synthesis

SWCNT is synthesized by almost the same method as that for the synthesis of MWCNT. Remarkable difference lies in the fact that metallic catalyst is indispensable to the synthesis of fullerenes. The metal compounds used as the catalyst are listed in Table 2 [8].

Table 2. Metals and metal compounds catalysts for SWCNT synthesis (modified from ref. 8).

Metals /compounds	Experimental conditions ¹	Locations of SWCNT ²	Density of SWCNT ³
Fe	Fullerene	Soot	High
		Extended deposit	High
Ni	Tube	Soot	Low
	Fullerene	Soot	High
Co	Fullerene	Extended deposit	High
		Soot	Low
		Soot	Low
Fe/Ni	Fullerene	Soot	High
		Weblike	High
		Soot	Very high
Fe/Co	Fullerene	Soot	Very high
		Soot	Very high
		Weblike	Very high
Ni/Co	Fullerene	Soot	Low
		Soot	High
		Weblike	Very high
Ni/Cu	Fullerene	Soot	Very high
		Soot	Very high
		Weblike	Very high
Ni/Cu	Tube	Soot	Low
Ni/Ti	Tube	Soot	Very low
Cu/Co	Tube	Soot	Low
Mg/Ni	Tube	Soot	Low
Y ₂ O ₃ /Co	Tube	Soot	Low, radial
YC ₂	Tube	Soot	High, radial

¹"Fullerene" for arc discharge at 100-Torr He and "Tube" at 550 Torr.

²"Soot" and "Extended deposit" protruding from the usual cathodic deposit, and "Weblike deposit."

³Categorised as very high, high, low and very low.

3.1.1 Electric arc discharge

SWCNT is synthesized by co-evaporation of carbon and catalyst (mostly metals) in arc discharge. In early time, Fe [3], Co [4], Ni [8, 10] or rare-earth element [10] was employed as the catalyst (see Fig. 7). In these syntheses, however, the yield of SWCNT was quite low. In the improved method, the catalyst consisting of more than one element such as Co-Pt [12,13] or Ni-Y [14] is used to increase the yield of SWCNT (e.g., more than 75 % with Ni-Y [14]).

3.1.2 Laser ablation

Although laser-ablation method with pure carbon as the target only gives fullerenes, SWCNT can be obtained at high yield by mixing Co-Ni into the target carbon [16]. Isolation of thus synthesized SWCNT is rather of ease since the crude product is almost free of nanoparticle and amorphous carbon [39]. Such

SWCNT sample has widely been used for the physical-property measurements [40].

3.1.3 Catalytic synthesis

Very recently, it has been reported that SWCNT can be synthesized by decomposition of benzene with Fe catalyst [27]. It would be of most importance to establish the controllability of the diameter and the helical pitch in this kind of synthesis of SWCNT toward the development of novel kinds of electronic devices such as single molecule transistor [41]. It can be said that this field is full of dream.

3.2 Purification

Since SWCNT is easily oxidised compared with MWCNT [42], the purification process such as the burning method cannot be applied to that purpose. Tohji et al., however, have succeeded in this by employing the water-heating treatment [43] and, furthermore, the centrifuge [44] and micro-filtration [39, 44] methods can also be employed. It has recently been reported that SWCNT could be purified by size-exclusion chromatography method [45], which made separation according to its length possible. This method looks effective to obtain SWCNT of a high degree of purity. Development of the differentiation method of SWCNT with its diameter is still an open problem.

4 Conclusion

MWCNT was first discovered by arc-discharge method of pure carbon and successive discovery of SWCNT was also based on the same method in which carbon is co-evaporated with metallic element. Optimisation of such metallic catalyst has recently been performed. Although these electric arc methods can produce gram quantity of MWCNT and SWCNT, the raw product requires rather tedious purification process.

The laser-ablation method can produce SWCNT under co-evaporation of metals like in the electric arc-discharge method. As metallic catalyst Fe, Co or Ni plays the important role and their combination or addition of the third element such as Y produces SWCNT in an efficient manner. But it is still difficult in the laser-ablation method to produce gram quantity of SWCNT. Nonetheless, remarkable progress in the research of physical properties has been achieved in thus synthesized SWCNT.

Fe, Co or Ni is also crucial in the catalytic decomposition of hydrocarbon. In order to efficiently obtain CNT and to control its shape, it is necessary and indispensable to have enough information on chemical interaction between carbon and these metals. It is quite easy for the catalytic synthesis method to scale up the CNT production (see Chap. 12). In this sense, this method is considered to have the best possibility for mass production. It is important to further improve the process of catalytic synthesis and, in order to do so, clarification of the mechanism of CNT growth is necessary to control the synthesis. CNT can be synthesized by the chemical reaction at relatively low

temperature fortunately. There could be, in general, a lot of possibilities in the control of chemical reaction at 1000-1500°C. It is of much interest to watch the development of study along this line.

The study on CNT commenced in Japan and, nowadays, a large number of investigators from all over the world participate in the research. It is considered that it is now high time for the turning point in the study on CNT in the sense that the phase of research should shift from basic to applied science including more improvement in efficiency of the synthesis, separation and purification. It is expected that CNT will be one of the most important materials in the 21st century and, hence, it is the most exciting thing for us to participate in science and technology of CNT.

References

1. Iijima, S., *Nature*, 1991, **354**, 56.
2. Zhao, X., Ohkohchi, M., Wang, M., Iijima, S., Ichihashi, T. and Ando, Y., *Carbon*, 1997, **35**, 775.
3. Iijima, S. and Ichihashi, T., *Nature*, 1993, **363**, 603.
4. Bethune, D. S., Kiang, C. H., de Vries, M. S., Gorman, G., Savoy, R., Vazquez, J. and Beyers, R., *Nature*, 1993, **363**, 605.
5. Kiang, C. H., Goddard, III., W. A., Beyers, R., Bethune, D. S., *Carbon*, 1995, **33**, 903.
6. (a) Ohshima, S., Yumura, M., Uchida, K., Tasaka, Y., Yoda, S., Kuriki, Y. and Ikazaki, F., High production of multi-wall carbon nanotubes by using rotating cathode arc methods. In *Proceedings the 4th IUMRS International Conference in Asia Symposium I Super Carbon*, ed. S. Fujiwara, M. Kamo, R. Ruoff, R. Heimann, D. Marton and H. Hiraoka. MYU, Tokyo, 1998, 69; (b) Yumura, M., Uchida, K., Niino, H., Ohshima, S., Kuriki, Y., Yase, K. and Ikazaki, F., *Materials Research Society Symposium Proceedings*, Vol. 349, ed. C. L. Renschler, D. M. Cox, J. J. Pouch and Y. Achiba, Materials Research Society, Pittsburgh, 1994, pp. 231; (c) Imamura, M., Shimada, H., Matsubayashi, N., Yumura, M., Uchida, K., Ohshima, S., Kuriki, Y., Yoshimura, Y., Sato, T., Nishijima, A., *Jpn. J. Appl. Phys.*, 1994, **33**, L1016.
7. Lin, X., Wang, K., Dravid, V. P., Chang, R. P. H. and Ketterson, J. B., *Appl. Phys. Lett.*, 1994, **64**, 181.
8. Seraphin, S., *J. Electrochem. Soc.*, 1995, **142**, 290.
9. Seraphin, S. and Zhou, D., *Appl. Phys. Lett.*, 1994, **64**, 2087.
10. (a) Saito, Y., Kawabata, K., Okuda, M., *J. Phys. Chem.*, 1995, **99**, 16076; (b) Saito, Y., Okuda, M., Tomita, M. and Hayashi, T., *Chem. Phys. Lett.*, 1995, **236**, 419.
11. Ajayan, P. M., Lambert, J. M., Bernier, P., Barbedette, L. and Colliex, C., *Chem. Phys. Lett.*, 1993, **215**, 509.
12. Lambert, J. M., Ajayan, P. M., Bernier, P., Planeix, J. M., Brotons, V., Coq, B. and Castaing, J., *Chem. Phys. Lett.*, 1994, **226**, 364.
13. Maser, W. K., Bernier, P., Lambert, J. M., Stephan, O., Ajayan, P. M., Colliex, C., Brotons, V., Planeix, J. M., Coq, B., Molinie, P. and Lefrant, S., *Synth. Met.*, 1996, **81**, 243.
14. Journet, C., Maser, W. K., Bernier, P., Loiseau, A., de la Chapelle, M., Lamy, Lefrant, S., Deniard, P., Lee, R. and Fischer, J. E., *Nature*, 1997,

- 388**, 756.
15. Kroto, H. W., Heath, J. R., O'Brien, S. C., Curl, R. F. and Smalley, R. E., *Nature*, 1985, **318**, 162.
 16. Thess, A., Lee, R., Nikolaev, P., Dai, H., Petit, P., Robert, J., Xu, C., Lee, Y. H., Kim, S. G., Rinzler, A. G., Colbert, D. T., Scuseria, G. E., Tománek, D., Fischer, J. E. and Smalley, R. E., *Science*, 1996, **273**, 483.
 17. Guo, T., Nikolaev, P., Rinzler, A. G., Tománek, D., Colbert, D. T. and Smalley, R. E., *J. Phys. Chem.*, 1995, **99**, 10694.
 18. Guo, T., Nikolaev, P., Thess, A., Colbert, D. T. and Smalley, R. E., *Chem. Phys. Lett.*, 1995, **243**, 49.
 19. Yudasaka, M., Komatsu, T., Ichihashi, T. and Iijima, S., *Chem. Phys. Lett.*, 1997, **278**, 102.
 20. Yudasaka, M., Komatsu, T., Ichihashi, T., Achiba, Y. and Iijima, S., *J. Phys. Chem. B*, 1998, **102**, 4892.
 21. Endo, M., Takeuchi, K., Kobori, K., Takahashi, K., Kroto, H. W. and Sakar, A., *Carbon*, 1995, **33**, 873.
 22. Fonseca, A., Hernadi, K., Piedigrosso, P. and Colomer, J. -F., *Appl. Phys. A*, 1998, **67**, 11.
 23. Ivanov, V., Fonseca, A., Nagy, J. B., Lucas, A., Lambin, P., Bernaerts, D. and Zhang, X. B., *Carbon*, 1995, **33**, 1727.
 24. Muller, T. E., Reid, D. G., Hsu, W. K., Hare, J. P., Kroto, H. W. and Walton, D. R. M., *Carbon*, 1997, **35**, 951.
 25. Li, W. Z., Xie, S. S., Qian, L. X., Chang, B. H., Zou, B. S., Zhou, W. Y., Zhao, R. A. and Wang, G., *Science*, 1996, **274**, 1701.
 26. Terrones, M., Grobert, N., Olivares, J., Zhang, J. P., Terrones, H., Kordatos, K., Hsu, W. K., Hare, J. P., Townsend, P. D., Prassides, K., Cheetham, A. K., Kroto, H. W. and Walton, D. R. M., *Nature*, 1997, **388**, 52.
 27. Cheng, H. M., Li, F., Su, G., Pan, H. Y., He, L. L., Sun, X. and Dresselhaus, M. S., *Appl. Phys. Lett.*, 1998, **72**, 3282.
 28. Hsu, W. K., Hare, J. P., Terrones, M., Kroto, H. W. and Walton, D. R. M., *Nature*, 1995, **377**, 687.
 29. Laplaze, D., Bernier, P., Maser, W. K., Flamant, G., Guillard, T. and Loiseau, A., *Carbon*, 1998, **36**, 685.
 30. Saito, Y., Hamaguchi, K., Hata, K., Uchida, K., Tasaka, Y., Ikazaki, F., Yumura, M., Kasuya, A. and Nishina, Y., *Nature* 1997, **389**, 554.
 31. Saito, Y., Hamaguchi, K. and Uemura, S., *Jpn. J. Appl. Phys.*, 1998, **37**, L346.
 32. Saito, Y., Hamaguchi, K., Uemura, S., Uchida, K., Tasaka, Y., Ikazaki, F., Yumura, M., Kasuya, A. and Nishina, Y., *Appl. Phys. A*, 1998, **67**, 95.
 33. Wang, Q. H., Setlur, A. A., Lauerhaas, J. M. and Dai, J. Y., *Appl. Phys. Lett.*, 1998, **72**, 2912.
 34. Service, R. F., *Science*, 1998, **281**, 940.
 35. Ebbesen, T. W., Lezec, H. J., Hiura, H., Bennett, J. W., Ghaemi, H. F. and Thio, T., *Nature*, 1996, **382**, 678.
 36. Baker, R. T. K. and Harris, P. S., *Chemistry and Physics of Carbon*, 1978, **14**, 83.
 37. Ebbesen, T. W., Ajayan, P. M., Hiura, H. and Tanigaki, K., *Nature*, 1994, **367**, 519.
 38. Ikazaki, F., Ohshima, S., Uchida, K., Kuriki, Y., Hayakawa, H. Yumura,

- M., Takahashi, K. and Tojima, K., *Carbon*, 1994, **32**, 1539.
39. Rinzler, A. G. Liu, J., Dai, H., Nikolaev, P., Huffman, G. B., Rodriguez-Macias, F. J., Boul, P. J., Lu, A. H., Heyman, D., Colbert, D. T., Lee, R. S., Fischer, J. E., Rao, A. M., Eklund, P.C. and Smalley, R. E., *Appl. Phys. A*, 1998, **67**, 29
40. Rao, A. M., Richter, E., Bandow, S., Chase, B., Eklund, P. C., Williams, K. A., Fng, S., Subbaswamy, K. R., Menon, M., Thess, A., Smalley, R. E., Dresselhaus, G. and Dresselhaus, M. S., *Science*, 1997, **275**, 187.
41. Dresselhaus, M. S., *Physics World*, 1996, 18.
42. Tohji, K. Private communication.
43. Tohji, K., Takahashi, H., Shinoka, Y., Shimizu, N., Jeyadevan, B., Matsuoka, I., Saito, Y., Kasuya, A., Ohsuna, T., Hiraga, K. and Nishina, Y., *Nature*, 1996, **383**, 679.
44. Bandow, S., Asaka, S., Zhao, X. and Ando, Y., *Appl. Phys. A*, 1998, **67**, 23
45. Duesberg, G. S., Muster, J., Krstic, V., Burghard, M. and Roth, S., *Appl. Phys. A*, 1998, **67**, 117.

CHAPTER 3

Electron Diffraction and Microscopy of Carbon Nanotubes

SEVERIN AMELINCKX,¹ AMAND LUCAS²
and PHILIPPE LAMBIN²

¹*EMAT-Laboratory, Department of Physics, University of Antwerp (RUCA),
Groenenborgerlaan 171, B-2020 Antwerpen, Belgium*

²*Department of Physics, Facultés Universitaires Notre-Dame de la Paix, rue de
Bruxelles 61, B-5000 Namur, Belgium*

1 Introduction

Among the several known types of carbon fibres the discussion in this chapter is limited to the electric arc grown multi-walled carbon nanotubes (MWCNTs) as well as single-walled ones (SWCNTs). For MWCNT we restrict the discussion to the idealised coaxial cylinder model. For other models and other shapes we refer to the literature [1-6].

2 Observations

2.1 Electron diffraction (ED) patterns [7,8]

A diffraction pattern of a single MWCNT (Fig. 1) contains in general two types of reflexions (i) a row of sharp $00.l$ ($l = \text{even}$) reflexions perpendicular to the direction of the tube axis, (ii) graphite-like reflexions of the type $h0.o$ (and $hh.o$) which are situated in most cases on somewhat deformed hexagons inscribed in circles with radii $g_{h0.o}$ (or $g_{hh.o}$).

Towards the central line these reflexions are sharply terminated at the positions of graphite reflexions, but they are severely streaked along the normal to the tube axis in the sense away from the axis. Mostly the pattern contains several such deformed hexagons of streaked spots, which differ in orientation giving rise to "split" graphite reflexions. The extent of the deformation of the hexagon depends on the direction of incidence of the electron beam with respect to the tube axis. With increasing tilt angle of the specimen pairs of reflexions related by a mirror operation with respect to the projection of the tube axis, approach one another along the corresponding circle and finally for a critical tilt angle they coalesce

into a single symmetrically streaked reflexion situated on the projection of the tube axis (Fig. 2). For certain tubes spots, situated on the projection of the tube axis, are sharp and unsplit under normal incidence [9].

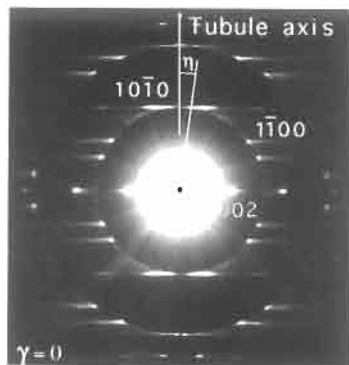


Fig. 1. Typical ED pattern of polychiral MWCNT. The pattern is the superposition of the diffraction patterns produced by several isochiral clusters of tubes with different chiral angles. Note the row of sharp $00.l$ reflexions and the streaked appearance of 10.0 and 11.0 type reflexions. The direction of beam incidence is approximately normal to the tube axis. The pattern exhibits $2mm$ planar symmetry [9].

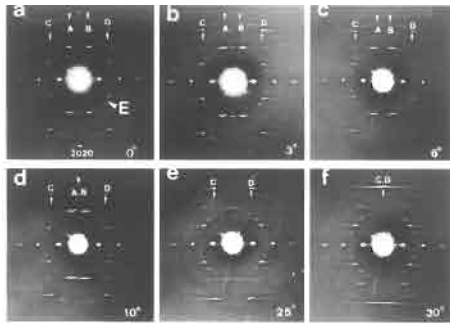


Fig. 2. Evolution of an ED pattern on tilting the specimen about an axis perpendicular to the tube axis. (a,b,c) The spots A and B as well as C and D approach one another. In (d) the spots A and B coalesce. In (f) the spots C and D form a single symmetrical streak. The positions of the spots $00.l$ remain unchanged. On moving the spots A and B as well as C and D describe arcs of the same circles centred on the origin [9].

Diffraction patterns of well isolated SWCNT are difficult to obtain due to the small quantity of diffracting material present, and also due to the fact that such tubes almost exclusively occur as bundles (or ropes) of parallel tubes, kept together by van der Waals forces.

Simulated SWCNT ED patterns will be presented below. The most striking difference with the MWCNT ED patterns is the absence of the row of sharp $00.l$ reflexions. In the diffraction pattern of ropes there is still a row of sharp reflexions perpendicular to the rope axis but which now corresponds to the much larger interplanar distance caused by the lattice of the tubes in the rope. The $h0.0$ type reflexions are moreover not only asymmetrically streaked but also considerably broadened as a consequence of the presence of tubes with different Hamada indices (Fig. 3).

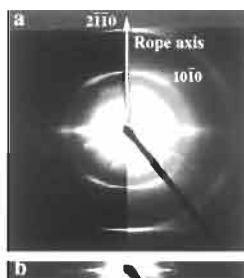


Fig. 3. (a) Diffraction pattern of a well formed rope (superlattice) of armchair-like tubes. Note the presence of superlattice spots in the inset (b). The broadening of the streaks of $10\bar{1}0$ type reflexions is consistent with a model in which the SWCNTs have slightly different chiral angles.

2.2 High resolution images [8-13]

An image of an MWCNT obtained by using all available reflexions usually exhibits only prominently the $00.l$ lattice fringes (Fig. 4) with a 0.34 nm spacing, representing the "walls" where they are parallel to the electron beam. The two walls almost invariably exhibit the same number of fringes which is consistent with the coaxial cylinder model.

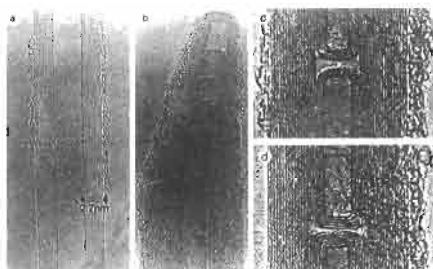


Fig. 4. Singularities in MWCNT imaged by means of basal plane lattice fringes. (a) Straight ideal MWCNT. (b) Capped MWCNT. The tube closes progressively by clusters of 2-5 graphene layers. (c)(d) Bamboo-like compartments in straight tubes.

SWCNTs are imaged as two parallel lines with a separation equal to the tube diameter (Fig. 5). By image simulation it can be shown that under usual observation conditions the black lines correspond to graphene sheets seen edge on in MWCNT as well as in SWCNT tubes [7].

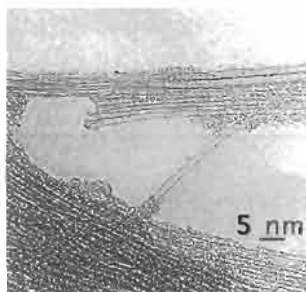


Fig. 5. Isolated SWCNT split off from a rope. The diffraction pattern produced by such a single tube is usually too weak to be recorded by present methods. The single graphene sheet in the walls is imaged as a dark line.

In the central parts of certain images of MWCNT (Fig. 6) also the 0.21 nm spacing ($d_{10.0}$) is resolved, providing structure detail. The set of 0.21 nm fringes roughly normal to the tube axis are often curved revealing the polychiral nature of the tubes. The hexagonal bright dot pattern observed in certain areas of the central part is consistent with a graphitic lattice. Other areas exhibit orientation difference moiré patterns due to the superposition of the graphene sheets either in the "front" and "rear" walls of the tube or of different isochiral clusters of graphene sheets. The orientation difference is a consequence of the chiral character of the tube.

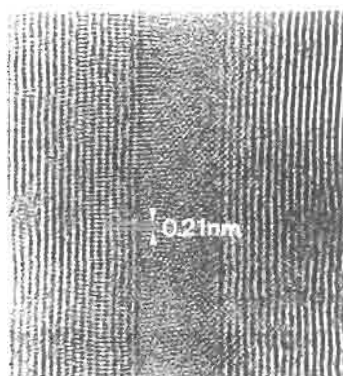


Fig. 6. High resolution image of straight part of an MWCNT; the 0.21 nm spacing is resolved next to the basal 0.34 nm spacing. The 0.21 nm fringes are curved [9].

Under normal incidence high resolution images of ropes reveal usually sets of parallel lines corresponding to the parallel tubes. Occasionally a small segment of a rope is strongly bent making it possible to observe locally a rope along its length axis (Fig. 7). Such images show that the SWCNT are arranged on a hexagonal lattice. Due to the deformation resulting from van der Waals attraction the tubes in the lattice acquire an hexagonal cross section [14,15].

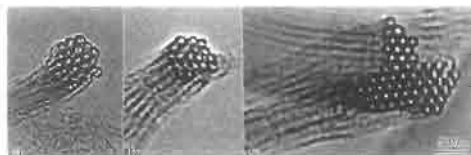


Fig. 7. High resolution images of ropes seen along their length axis. Note the hexagonal lattice of SWCNT's (Courtesy of A. Loiseau).

3 Interpretation of the ED Patterns

3.1 Intuitive interpretation

Several levels of interpretation have been proposed in the literature [9,16-19]. The $00.l$ reflexions are attributed to diffraction by the sets of parallel c -planes tangent to the cylinders in the walls as seen edge on along the beam direction; their positions are independent of the direction of incidence of the electron beam.

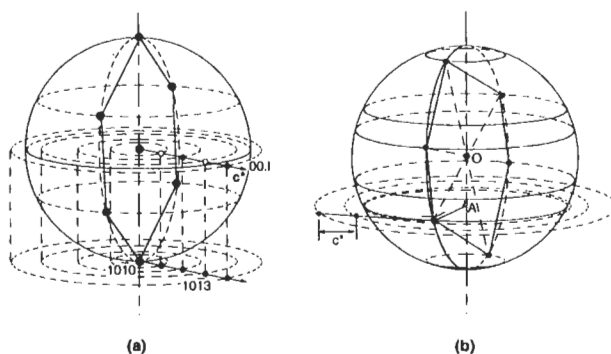


Fig. 8. Diffraction space according to the "disordered stacking model" (a) achiral (zigzag) tube (b) chiral tube. The parallel circles represent the inner rims of diffuse coronae, generated by streaked reflexions. The $00.l$ nodes generate sharp circles. In (a) two symmetry related 10.0 type nodes generate one circle. In the chiral case (b) each node generates a separate corona [9].

The "split" reflexions of the type $h0.0$ (and $hh.0$) can be associated with the graphene sheets in the tangent planes perpendicular to the beam direction along

"top" and "bottom" part of the tube; the splitting results from the orientation difference between the structures in these planes. The magnitude of the splitting is a measure for (but is not identical to) the chiral angle η of the corresponding tube or cluster of isochiral tubes [20]. The overall symmetry of the ED pattern should obey $2mm$ planar symmetry.

3.2 The disordered stacking model [4,6,9]

In a somewhat more sophisticated geometrical model it is assumed that the stacking in the walls is strongly disordered. As a consequence of the circumference increase by πc of successive coaxial cylinders the relative stacking of successive graphene sheets has to change with azimuth. Moreover assuming that nucleation of successive sheets takes place in random positions on the instantaneous surface the stacking is likely to be fully disordered in each volume element. The diffraction space of a disordered volume element of parallel graphene sheets consists of streaks along the local $[00.l]^*$ direction, through the hexagonal array of nodes in the local $(00.l)^*$ plane and of a row of sharp nodes, spaced by $2c^*$ along the local $[00.l]^*$ direction.

The diffraction space of the MWCNT is thus formed by the loci generated by rotation about the tube axis, of the "features" of the local diffraction space of a volume element (Fig. 8). The resulting diffraction space consists of sharp circles in the plane through the origin perpendicular to the tube axis, described by the sharp $00.l$ nodes. The streaked nodes hereby generate "coronae" which are limited inwards by sharp circles with radii $gh_{0,0}$ (or $gh_{h,0}$) in planes perpendicular to the tube axis and which fade gradually outwards (Fig. 8). In chiral tubes each streaked node generates a separate corona whereas in a chiral tube two mirror symmetrically related nodes generate a single corona. According to this model the diffraction pattern, which in ED is a planar section through the origin of diffraction space, has $2mm$ planar symmetry. This model accounts correctly for the geometrical behaviour on tilting, however taking intensities into account the $2mm$ symmetry is sometimes broken in experimental images. The following model explains why this is so.

3.3 The homogeneous shear model [16,17]

We now consider a cluster of isochiral coaxial tubes. Along the generator chosen as the origin of the azimuth the stacking is assumed to be well ordered and of the graphite type: ABAB ..., ABCABC ... or AAA We inquire how this stacking changes with azimuth due to the systematic circumference increase and how this is reflected in diffraction space. We look in particular for the locus of the reciprocal lattice node corresponding to a family of lattice planes of the un bent structure, parallel to the tube axis (Fig. 9).

In direct space successive layers are sheared homogeneously along cylindrical surfaces, one relative to the adjacent one, as a consequence of the circumference increase for successive layers. In diffraction space the locus of the corresponding reciprocal lattice node is generated by a point on a straight line which is rolling without sliding on a circle in a plane perpendicular to the tube axis. Such a locus

is an evolute of the circle. For equatorial reflexions (i.e. with a diffraction vector \mathbf{g} perpendicular to the tube axis) the radius of the circle is $|\mathbf{g}|$ and the full pattern is generated by a set of equispaced points ($2c^*$) on a tangent line to the circle. For a diffraction vector enclosing an angle γ with the equator the radius of the circle, on which the linear set of points with spacing $2c^*$ is rolling without sliding, is $g \cos \gamma$ [17].

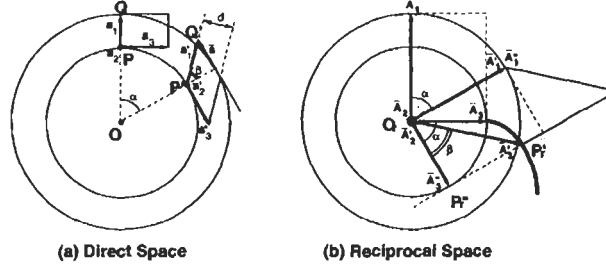


Fig. 9. Illustrating the "homogeneous shear model". In (a) the unit cell built on $(\mathbf{a}_1, \mathbf{a}_2, \mathbf{a}_3)$ is sheared and becomes $(\mathbf{a}_1', \mathbf{a}_2', \mathbf{a}_3')$ at azimuth α . In (b) the corresponding reciprocal unit cells $(\mathbf{A}_1, \mathbf{A}_2, \mathbf{A}_3)$ and $(\mathbf{A}_1', \mathbf{A}_2', \mathbf{A}_3')$ are represented. Two successive tubes in an MWCNT are represented in (a). The locus described by the point P_r' is an evolute of the circle with radius (\mathbf{A}_3) [16].

The full pattern consists of an integer number of pairs of circle evolutes starting at equispaced cusps, separated by $2c^*$ along the generating circle. If the initial stacking is disordered the cusps where pairs of evolutes start are distributed at random along the generating circle. They give rise to a fine structure of the coronae described above; this may cause the reinforcements sometimes observed in the streaks. For a more detailed discussion we refer to refs. 16 and 17.

3.4 Kinematical theory [18,19,21]

3.4.1 SWCNT [18]

Assuming kinematical diffraction theory to be applicable to the weakly scattering CNTs, the diffraction space of SWCNT can be obtained in closed analytical form by the direct stepwise summation of the complex amplitudes of the scattered waves extended to all scattering centres, taking the phase differences due to position into account.

The planar representation of a graphene SWCNT is shown in Fig. 10. The "wrapping" vector of the SWCNT with Hamada indices (L, M) , $\mathbf{X}\mathbf{X}' = L\mathbf{a}_1 + M\mathbf{a}_2$ (L, M ; integer) is referred to the base vectors \mathbf{a}_1 and \mathbf{a}_2 (with $|\mathbf{a}_1| = |\mathbf{a}_2| = a$) which enclose an angle of 60° . The tube is obtained by rolling up the graphene strip limited by the parallel segments AB in such a way that X and X' coincide. On rolling up the outer parts of the strip are assumed to emerge from the plane of the drawing. The solid straight line in Fig. 10 is hereby transformed into a

right-handed "primitive" helix along which the scattering centres have cylindrical coordinates

$$\rho_j = R_0; \quad z_j = z_0 + jp; \quad \phi_j = \phi_0 + \frac{2\pi}{P}(z_j - z_0) = \phi_0 + \frac{2\pi pj}{P} \quad (j; \text{integer}) \quad (1)$$

where z_0 and ϕ_0 refer to the origin, p is the z -level difference between two successive scattering centres; P is the pitch of the helix. The chiral angle is η and $C^2 = L^2 + M^2 + LM = 4\pi^2 R_0^2$; R_0 is the radius of the cylinder on which the helix is wound.

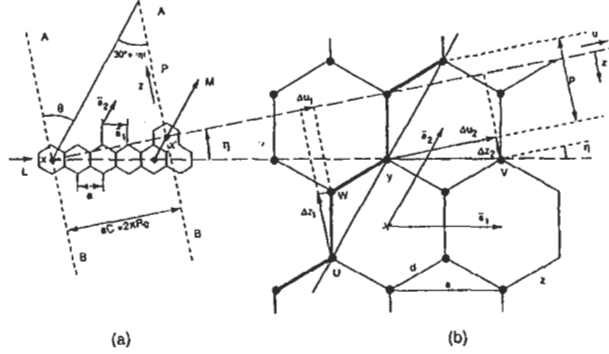


Fig. 10. Kinematical theory (a) Planar development of chiral CNTs illustrating the positions of the scattering centres. The SWCNT is formed by making the limiting lines AB of the strip of graphene structure to coincide on rolling up the strip. (b) Magnified view of part of (a). The solid straight line becomes a right-handed primitive helix on rolling up. The heavy zigzag line becomes a zigzag helix on rolling up. The figure also illustrates the meaning of the symbols $L, M, p, P, \theta, \eta, C, \Delta z_1, \Delta \phi_1, \Delta z_2$ and $\Delta \phi_2$ ($L > 0, M > 0$).

We first construct right handed zigzag helices, represented by thick solid zigzag lines in Fig. 10 and consisting of two "parallel" primitive helices related by the shift $(\Delta u_1, \Delta z_1)$ corresponding to a screw displacement $(\Delta \phi_1, \Delta z_1)$ along the cylindrical surface with radius R_0 . We subsequently note that the complete SWCNT consists of L such parallel zigzag helices which are related in the planar representation by displacements $j\Delta u_2, j\Delta z_2$ ($j = 1, L-1$) corresponding in space to screw displacements $j\Delta \phi_2, j\Delta z_2$. The relation between ϕ and u is given by $\Delta \phi = 2\pi(\Delta u/C)$. A similar decomposition of the same SWCNT in $L-|M|$ left handed primitive helices is equally possible.

From the preceding decomposition in primitive helices follows that the amplitude diffracted by an SWCNT can be expressed in terms of the "structure" amplitude $A_1(\mathbf{k})$ of a primitive helix which was shown in ref. 18 to be

$$A_1(\mathbf{k}) = \frac{2\pi}{p} f_C(\mathbf{k}) \exp(ik_z z_0) \sum_{m,n}^{+\infty} J_n(k_\perp R_0) \exp\left[in(\phi_k - \phi_0) + \frac{\pi}{2}\right] \times \delta\left[k_z - 2\pi\left(\frac{n}{p} + \frac{m}{p}\right)\right] \quad (2)$$

with $f_C(\mathbf{k})$: atomic scattering factor of carbon
 \mathbf{k} : position vector in diffraction space (\mathbf{k} -space) with components (k_x, k_y, k_z) $\mathbf{k} = \mathbf{K} - \mathbf{K}_0$ (\mathbf{K}_0 incident wave vector; \mathbf{K} scattered wave vector)
 k_\perp : component of \mathbf{k} normal to the tube axis (z -axis) $k_\perp^2 = k_x^2 + k_y^2$
 k_z : component of \mathbf{k} parallel to the z -axis
 $\phi_k = \arctan(k_y/k_x)$; azimuth of \mathbf{k}
 J_n : Bessel function of order n ; (m, n) integers

The δ functions limit the non-vanishing regions of k -space to discrete layer planes perpendicular to k_z . These layer planes are infinitely sharp, because the helix was assumed to be infinitely long. Limiting the summation to a finite length of the helix would lead to broadening of these layer planes. For a zigzag helix the complex diffracted amplitude becomes

$$A_2(\mathbf{k}) = A_1(\mathbf{k}) [1 + \exp\{i(k_z \Delta z_1 - n \Delta \phi_1)\}] \quad (3)$$

hereby the origin of the second primitive helix was displaced with respect to that of the first one and the corresponding phase shift was taken into account. The exponent can be expressed in terms of the basic parameters L and M ,

$$A_2(\mathbf{k}) = A_1(\mathbf{k}) \left[\exp \frac{2\pi i}{3L} \{n + m(2L + m)\} + 1 \right] \quad (4)$$

Finally the scattered amplitude for the complete SWCNT is obtained by summing the complex amplitudes of the L zigzag helices taking the phase differences properly into account by choosing a different origin for each zigzag helix. This leads to the summation of a finite geometrical progression:

$$A_{ss} \equiv A_L(\mathbf{k}) = A_2(\mathbf{k}) \sum_{j=0}^{L-1} \exp\{i(k_z \Delta z_2 - n \Delta \phi_2)j\} \quad (5)$$

in which the basic parameters L and M can be introduced. One obtains finally, after some simple but lengthy algebra

$$A_L(\mathbf{k}) = \frac{4\pi C}{3d} \sum_{l=-\infty}^{+\infty} F_l(\mathbf{k}) \delta\left(k_z - \frac{2\pi l}{T}\right) \quad (6)$$

where

$$\begin{aligned}
F_l(\mathbf{k}) = & \exp\left(\frac{2\pi i z_0 l}{T}\right) \sum_{m,s=-\infty}^{+\infty} J_{sL-mM}(k_{\perp} R_0) \\
& \times \exp\left\{i\left(sL - mM\right)\left(\phi_k - \phi_0 + \frac{\pi}{2}\right)\right\} f_C(\mathbf{k}) \\
& \times \left[1 + \exp\left\{\frac{2\pi i(s+2m)}{3}\right\}\right] \delta\left(l, \frac{s(L+2M)}{N} + \frac{m(2L+M)}{N}\right)
\end{aligned} \tag{7}$$

with $T = C\sqrt{3}/N$; N is the largest common divisor of $2L+M$ and $L+2M$; $d = a\sqrt{3}$, $n+mM = sL$ ($s = \text{integer}$). The origin of the different factors is clear from the stepwise summation procedure. The δ -functions express selection rules limiting the non-vanishing values of $A_L(\mathbf{k})$ to discrete layer planes.

This last expression allows us to compute the scattering density $A_L(\mathbf{k})A_L^*(\mathbf{k})$ in each point \mathbf{k} of the diffraction space. Ewald's construction, generalised to a continuous distribution of scattering density, allows then to obtain the diffraction pattern for an arbitrary direction of incidence of the electron beam, as a quasi-planar section of diffraction space with a plane normal to the incident beam direction. Only sections containing the origin of diffraction space can experimentally be realised. The fine structure present in sections $k_z = \text{constant} \neq 0$ of diffraction space can nevertheless be explored by tilting the specimen revealing in this way line profiles through the layer planes.

3.4.2 MWCNT [18]

The diffraction space of MWCNTs can be computed by summing the complex amplitudes due to each of the constituent coaxial tubes. Taking into account possible differences in Hamada indices (L_j, M_j) as well as the relative stacking (described by $z_{0,j}, \phi_{0,j}$) one can formally write

$$A_{\text{MW}}(\mathbf{k}) = \sum_j A_{ss,j}(\mathbf{k}, L_j, M_j, z_{0,j}, \phi_{0,j}) \tag{8}$$

The diffraction patterns due to different isochiral clusters are superimposed and well separated in a polychiral MWCNT diffraction pattern, suggesting that interference between waves scattered by tubes with different chiral angles can be neglected. It is therefore meaningful to discuss only isochiral clusters of tubes. Such clusters are only compatible with a constant intercylinder spacing $c/2$ for pairs of Hamada indices satisfying the condition $C^2 \equiv L^2 + M^2 + LM = (\pi c/a)^2$. Approximate solutions are for instance (8, 1) and (5, 5) [16,17].

3.4.3 Ropes of SWCNT [22,23]

The diffraction space of ropes of parallel SWCNT can similarly be computed by summing the complex amplitudes of the individual SWCNTs taking into account the relative phase shifts resulting from the lattice arrangement at

positions $\mathbf{R}_{l_1, l_2} = l_1 \mathbf{A}_1 + l_2 \mathbf{A}_2$ (l_1, l_2 ; integers) ($\mathbf{A}_1, \mathbf{A}_2$; base vectors of the two-dimensional (2D) hexagonal lattice of tube axes) $|\mathbf{A}_1| = |\mathbf{A}_2| = 2R_0$. Formally one can write

$$A_{\text{bundle}}(\mathbf{k}) = \sum_{l_1, l_2=0}^{N_1, N_2} A_{ss, l_1, l_2}(\mathbf{k}, L_{l_1, l_2}, M_{l_1, l_2}, z_{0, l_1, l_2}, \phi_{0, l_1, l_2}) \exp(i\mathbf{k} \cdot \mathbf{R}_{l_1, l_2}) \quad (9)$$

A hexagonal lattice of identical SWCNT's leads in diffraction space to a 2D lattice of nodes at positions $h_1 \mathbf{B}_1 + h_2 \mathbf{B}_2$ with $\mathbf{A}_i \cdot \mathbf{B}_j = 2\pi \delta_{ij}$. Spots corresponding to such nodes are visible in Fig. 3.

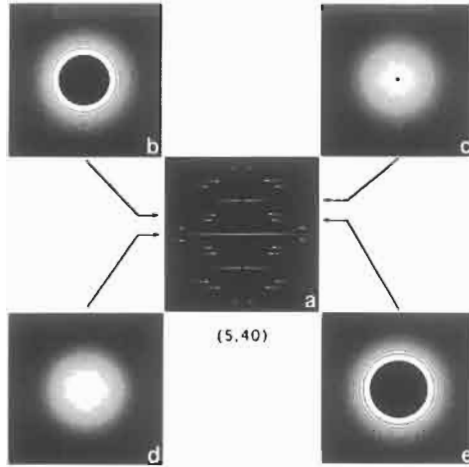


Fig. 11. Simulated diffraction space of a chiral (40, 5) SWCNT. (a) Normal incidence diffraction pattern with $2mm$ symmetry; (b), (c), (d) and (e) four sections of diffraction space at the levels indicated by arrows. Note the absence of azimuthal dependence of the intensity. The radii of the dark circles are given by the zeros of the sums of Bessel functions [17].

3.4.4 Simulation of diffraction patterns [17,19]

Several sections of the diffraction space of a chiral SWCNT (40, 5) are reproduced in Fig. 11. In Fig. 11(a) the normal incidence pattern is shown: note the $2mm$ symmetry. The sections $k_z = \text{constant}$ exhibit bright circles having radii corresponding to the maxima of the Bessel functions in Eq.(7). The absence of azimuthal dependence of the intensity is consistent with the point group symmetry of diffraction space, which reflects the symmetry of direct space i.e. the infinite chiral tube as well as the corresponding diffraction space exhibit a rotation axis of infinite multiplicity parallel to the tube axis.

Azimuth dependence is clearly present for achiral tubes such as for instance the (10, 10) tube of Fig. 12, where it reflects the 20-fold rotation symmetry of this tube in direct space.

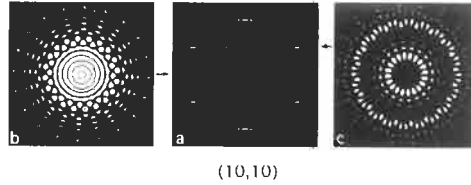


Fig. 12. Simulated diffraction space for a (10, 10) armchair tube. (a) Normal incidence pattern, note the absence of $oo.l$ spots. (b) Equatorial section. The pattern has 20-fold symmetry. (c) The section $k_z = g_{10\bar{1}0}(\sqrt{3}/2)$. The pattern contains 20 radial "black" lines, i.e. extinction occurs for the corresponding azimuthal orientations of Ewald's plane [17].

Figure 13 shows several sections of the diffraction space for a 10-layer MWCNT with Hamada indices $(8k, k)$ with $k = 5, 6, 7, \dots, 14$. For the sections (a)(a₁)(a₂) the initial stacking is assumed to be the ABAB ... stacking. Figure 13(a) is the normal incidence pattern; it lacks $2mm$ symmetry (a₁) and (a₂) are sections at the level of the indicated layer lines $k_z = \text{constant}$. Note the presence of well defined circle evolutes with two types of turning points spaced by c^* along the generating circle. For the sections (b)(b₁)(b₂) the initial stacking is randomly disordered. The normal incidence pattern (b) now exhibits approximately $2mm$ symmetry. In the layer planes (b₁) and (b₂) diffuse coronae are present.

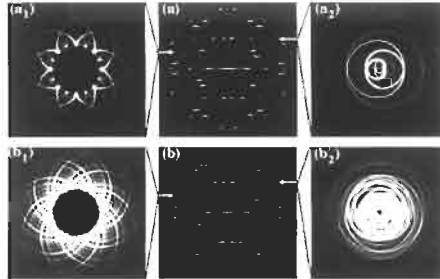


Fig. 13. Simulated diffraction space of a 10-layer monochiral MWCNT with Hamada indices $(40+8k, 5+k)$ with $k=0, \dots, 9$. In (a), (a₁) and (a₂) the initial stacking at ϕ_0 was ABAB... whereas in (b), (b₁) and (b₂) the initial stacking was random. (a) The normal incidence pattern has a centre of symmetry only. (a₁)(a₂) The cusps are of two different types. The arc length separating the cusps is c^* (b) The normal incidence pattern now exhibits $2mm$ symmetry. (b₁)(b₂) The cusps are distributed at random along the generating circles of the evolutes. These sections represent the diffuse coronae referred to in the "disordered stacking model" [17].

4 Microstructural Characterisation of CNTs

The length and the diameter of MWCNT can be measured directly by TEM. From high-resolution transmission electron microscopy (HRTEM) images exhibiting *oo.l* fringes follows the number of coaxial tubes and possibly the microstructure of the caps in MWCNT, as viewed along the incident electron beam [24]. Also anomalous intercylinder spacings and defects are revealed in this way [1,11].

The average intercylinder spacing, which depends somewhat on the diameter, can be derived from the *oo.l* reflexions in the diffraction pattern, using the *ho.o* (or *hh.o*) spacing of graphite for internal calibrations since the latter seems to be independent of curvature.

The angular splitting of the *ho.o* (or *hh.o*) reflexions is a measure for the chiral angle η . However the observed splitting depends as the direction of incidence of the electron beam and must thus be corrected for tilt [20,25].

Using HRTEM the chiral angle can also be deduced from the moiré or coincidence pattern formed in the central area of the tube image between "front" and "back" surfaces of the tube.

The diffraction patterns of isochiral clusters of tubes with different chiral angles in MWCNTs are superimposed in the composite pattern, the different chiral angles can be measured separately by diffraction contrast imaging [26].

The conventional hand of a particular isochiral cluster of tubes can be deduced from dark field diffraction contrast tilting experiments [26].

Acknowledgements

The illustrations in this contribution were mostly taken from papers published by the authors in collaboration with various colleagues. The references to the original publications are mentioned in the figure captions. In this respect thanks are due to Prof. Dr. G. Van Tendeloo, Prof. Dr. J. Van Landuyt, Dr. D. Bernaerts and Dr. X. B. Zhang. Figures 3, 5, 11 and 12 are taken from as yet unpublished work in collaboration with Dr. D. Bernaerts. Thanks are due to the staff of the EMAT photographic laboratory for meticulous work and to Miss H. Evans for skillful typing and editing of the camera-ready manuscript. Thanks are due to A. Loiseau for the use of Figure 7. This text presents results of the Belgian programme on InterUniversity Poles of Attraction initiated by the Belgian Prime Minister's Office of Science Policy Programming (IUAP4/10). The scientific responsibility is assumed by the authors.

References

1. Amelinckx, S., Bernaerts, D., Zhang, X. B., van Tendeloo, J. and van Landuyt, J., *Science*, 1995, **267**, 1334.
2. Bernaerts, D., Zhang, X. B., Zhang, X. F., Amelinckx, S., van Tendeloo, G., van Landuyt, J., Ivanov, V. and Nagy, J. B., *Phil. Mag. A*, 1995, **71**, 605.
3. Zhang, X. B., Zhang, X. F., Bernaerts, D., van Tendeloo, G., Amelinckx,

- S., van Landuyt, J., Ivanov, V., Nagy, J. B., Lambin, Ph. and Lucas, A., *Europhys. Lett.*, 1994, **27**, 141.
4. Amelinckx, S., Bernaerts, D., van Tendeloo, G., van Landuyt, J., Lucas, A. A., Mahot, M. and Lambin, Ph. In *Physics and Chemistry of Fullerenes and Derivatives (Proceedings of the International Winter School on Electronic Properties of Novel Materials)*, ed. H. Kuzmany, J. Fink, M. Mehring and S. Roth, World Scientific, Singapore, 1995, pp 515.
5. Amelinckx, S., Luyten, W., Krekels, T., van Tendeloo, G. and van Landuyt, J., *J. Cryst. Growth*, 1992, **121**, 543; Luyten, W., Krekels, T., Amelinckx, S., van Tendeloo, G., van Dyck, D. and van Landuyt, J., *Ultramicroscopy*, 1993, **49**, 123.
6. Amelinckx, S. and Bernaerts, D., The geometry of multishell nanotubes. In *Supercarbons, Synthesis, Properties and Applications*, Springer Series in Materials Science, Vol. 33, ed. S. Yoshimura and R. P. H. Chang, Springer Verlag, Berlin, 1998.
7. Zhang, X. F., Zhang, X. B., van Tendeloo, G., Amelinckx, S., Op de Beeck, M. and van Landuyt, J., *J. Cryst. Growth*, 1993, **130**, 368.
8. Iijima, S., *Nature*, 1991, **354**, 56.
9. Zhang, X. B., Zhang, X. F., Amelinckx, S., van Tendeloo, G. and van Landuyt, J., *Ultramicroscopy*, 1994, **54**, 237.
10. Iijima, S., Ichihashi, T. and Ando, Y., *Nature*, 1992, **356**, 776.
11. Liu, M. and Cowley, J., *Carbon*, 1994, **32**, 393; Liu, M. and Cowley, J., *Mater. Sci. Eng.*, 1994, **A185**, 131; Liu, M. and Cowley, J., *Ultramicroscopy*, 1994, **53**, 333.
12. Iijima, S. and Ichihashi, T., *Nature*, 1993, **363**, 603.
13. Ajayan, P. M. and Iijima, S., *Nature*, 1992, **358**, 23.
14. Loiseau, A., Journet, C., Henrard, L., Bernier, P., Larny de la Chapelle, M. and Lefrant, S., Bundles of single wall nanotubes produced by the electric arc technique. In *Electron Microscopy ICEM-14*, Vol. 3, ed. H. A. Calderón Benarides and M. J. Yacamán, Cancun, Mexico, 1998, pp. 115.
15. Iijima, S., Electron microscopy of nanotubes. In *Electron Microscopy ICEM-14*, Vol. 3, ed. H. A. Calderón Benarides and M. J. Yacamán, Cancun, Mexico, 1998, pp. 17.
16. Bernaerts, D. and Amelinckx, S., Electron microscopy study of coiled carbon tubules. In *Handbook of Microscopy*, Vol. 3, ed. S. Amelinckx, J. van Landuyt, G. van Tendeloo, and D. van Dyck, Wiley-VCH, Weinheim, 1996, pp. 437.
17. Bernaerts, D., Amelinckx, S., Lambin, Ph. and Lucas, A. A., *Appl. Phys. A*, 1998, **67**, 53.
18. Lambin, Ph. and Lucas, A. A., *Phys. Rev. B*, 1997, **56**, 3571.
19. Qin, L. C., *J. Mater. Res.*, 1994, **9**, 2450.
20. Zhang, X. B., and Amelinckx, S., *Carbon*, 1994, **32**, 1537.
21. Lucas, A. A., Lambin, P., Mairesse, R. and Mathot, M., *Bull. de l'Acad. Roy. de Belgique, Classe des Sci.*, 1996, **7-12**, 423-452.
22. Guo, T., Nikolaev, P., Rinzler, A. G., Tománek, D., Colbert, D. T. and Smalley, R. E., *J. Phys. Chem.*, 1995, **99**, 10694; Guo, T., Nikolaev, P., Thess, A., Colbert, D. T. and Smalley, R. E., *Chem. Phys. Lett.*, 1995, **243**, 49.
23. Thess, A., Le, R., Nikolaev, P., Dai, H., Petit, P., Robert, J., Xu, C., Lee, Y. H., Kim, S. G., Colbert, D. T., Scuseria, G., Tománek, D., Fisher, R.

- E. and Smalley, R. E., *Science*, 1996, **273**, 483.
24. Ajayan, P. M., Ichihashi, T. and Iijima, S., *Chem. Phys. Lett.*, 1993, **202**, 384.
25. Qin, L. C., Ichihashi, T., and Iijima, S., *Ultramicroscopy*, 1997, **67**, 181
26. Bernaerts, D., Op de Beeck, M., Amelinckx, S., van Landuyt, J. and van Tendeloo, G., *Phil. Mag. A*, 1996, **74**, 723.

CHAPTER 4

Structure of Multi-Walled and Single-Walled Carbon Nanotubes. EELS Study

TAKESHI HANADA, YUJI OKADA and KIYOSHI YASE

*National Institute of Materials and Chemical Research,
1-1 Higashi, Tsukuba, 305-8565, Japan*

Several structural characterisations of carbon nanotubes (CNTs) with the cylindrical graphite are reviewed from the viewpoint of transmission electron microscopy (TEM). Especially, electron energy loss spectroscopy (EELS) by using an energy-filtered TEM is applied to reveal the dependence of fine structure of EELS on the diameter and the anisotropic features of CNTs.

1 Introduction – Morphological Features of CNTs

Since the discovery of carbon nanotubes (CNTs) [1], most of the observational works have been performed by using transmission electron microscope (TEM) [2,3]. There are three types of investigations: (i) longitudinal-direction observation of CNTs in addition to their cross-sectional one [1-10], (ii) structural analysis by transmission electron diffraction (TED) [1,4,5,11,12] and (iii) electron energy loss spectroscopy (EELS) to evaluate the electronic structures of CNTs [5,13-16]. Topological observation has also been carried out by using scanning tunnelling microscope (STM) [17] and atomic force microscope (AFM) [18].

TEM image obtained from a multi-walled CNT (MWCNT) lying in the plane of the specimen-support grid, is a longitudinal slice of tubes to represent pairs of dark lines as shown in Fig. 1(c). The number of pairs of lines corresponds to the number of graphitic sheets constructing the tubes. The distance between adjacent straight lines corresponds to the (002) spacing of graphitic sheets (0.34 nm). When the CNT has no inclusions in the hollow, the image would be vacant in the centre. This confirms that CNTs consist of coaxial graphitic sheets. When the CNTs are embedded in an epoxy resin and then ultra-microtomed to be thin section, the images reveal coaxial circles as shown in Fig. 1(d). The number of circles also corresponds to that of graphitic sheets.

It is known that the electrical properties of CNTs; insulator, semiconductor or metal, are caused by the structure in graphitic sheet [2,3]. It is difficult to observe the individual graphitic structure in a sheet of CNT by TEM, because

those images are the projection along the incident electron beam and are superimposed by both the top and bottom layers as shown in Fig. 1(a). Although it is scarcely able to obtain a lattice image of the graphitic structure from a single-walled CNT (SWCNT), whole the CNT should be aligned normal to the incident electrons without any inclination and bending. Therefore, it is difficult to detect the helicity in a CNT from the images. Some investigations have been devoted to the structures at the end and around the bends of CNTs. There would be the presence of pentagons or heptagons, but it is also not easy to distinguish the individual polygons by TEM.

On the other hand, TED patterns can assign the fine structure. In general, the pattern includes two kinds of information. One is a series of strong reflexion spots with the indexes of $\{00l\}$, 002, 004 and 006, and 101 from the side portions of MWCNTs as shown in Fig. 1(b). The indexes follow those of graphite. The TED pattern also includes the information from the top and bottom sheets in tube. The helicity would appear as a pair of arcs of 110 reflexions. In the case of nano-probed TED, several analyses in fine structures have been done for SWCNT to prove the dependence on the locations [11,12].

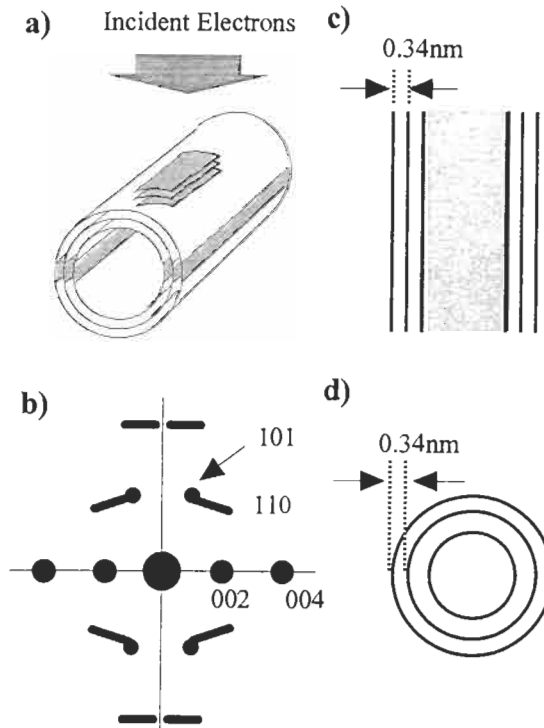
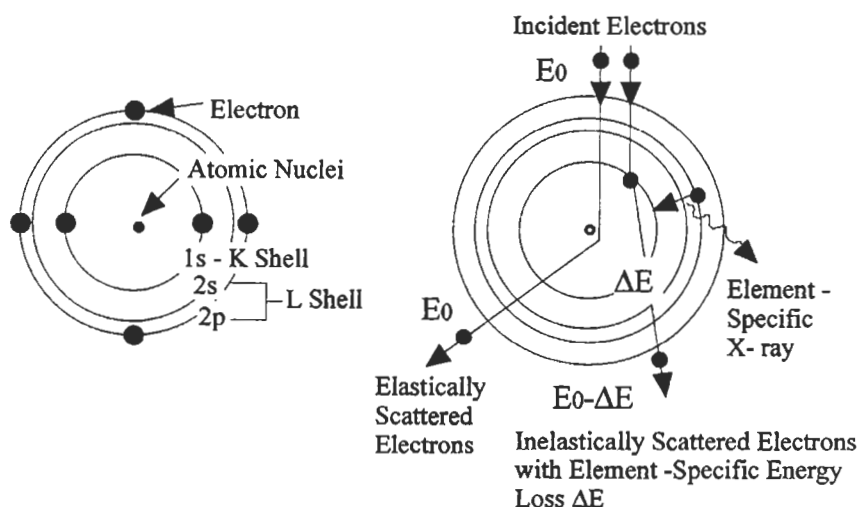


Fig. 1. (a) Geometrical relationship between incident electron beams in TEM and CNT, (b) typical TED pattern, (c) schematic illustration of image of CNT and (d) cross-sectional view of CNT. In the TED pattern, the indexes follow those of graphite.

The precise description of geometrical structures of CNTs has been reported by Iijima [1], who was the first discoverer of carbon microtubules. Electron diffraction (ED) results are presented in Chap. 3. In this chapter, the authors will focus on the electronic structures of CNTs from the viewpoint of EELS by using TEM equipped with an energy-filter in the column or under the column.

2 EELS of Carbon Materials

Carbon has six electrons around the atomic core as shown in Fig. 2. Among them two electrons are in the K-shell being the closest position from the centre of atom, and the residual four electrons in the L-shell. The former is the 1s state and the latter are divided into two states, 2s and 2p. The chemical bonding between neighbouring carbon atoms is undertaken by the L-shell electrons. Three types of chemical bonds in carbon are; single bond contributed from one 2s electron and three 2p electrons to be cited as sp^3 bonding, double bond as sp^2 and triple bond as sp from the hybridised atomic-orbital model.



Left: **Fig. 2.** Atomic structure of carbon.

Right: **Fig. 3.** Elastic and inelastic interactions between incident electrons and atom.

When high-energy electrons are injected into thin specimen, most of them tend to pass through without any perturbation occurring from the substances, because the cross section of atomic nuclei is small enough to such electrons. Some of the incident electrons are elastically scattered to be diffracted, and the others

interact with electrons around atom to lose the energy as shown in Fig. 3. The value of energy loss in the incident electrons ΔE corresponds to the transferred excitation energy for the inner-shell, valence or conduction electrons in substances. More than 285 eV is necessary for the K-shell electrons in carbon atom to be excited to vacuum level as the ionisation energy. Since the ionisation energy is strongly dependent on each element, it is available to analyse the species from the energy loss known as characteristic X-ray measurement.

Furthermore, the chemical bondings can be distinguished as the difference in the core-loss region of EELS patterns. The fine structures in EELS beyond the ionisation edge, an energy-loss near-edge structure (ELNES), give the information on the binding states. As shown in Fig. 4, EEL spectra of graphite (a) as well as C₆₀ represent a sharp π^* excitation peak at 285 eV being lower than the main peak around 285 - 320 eV, while of diamond (b) have not. The sharp peak at 285 eV is assigned as $1s \rightarrow \pi^*$ excitation and indicates the presence of energy level for the excited states in carbon atoms. The height and width of peaks depend on the density of excited states and the width of them, respectively. The oscillation terms in σ^* excitation, an extended energy-loss fine-structure (EXELFS) up to several hundreds eV from the ionisation edge, result from the interference between the electrons scattered by neighbouring atoms and the incident electrons, which represents the coordination of atoms and the distance between atoms.

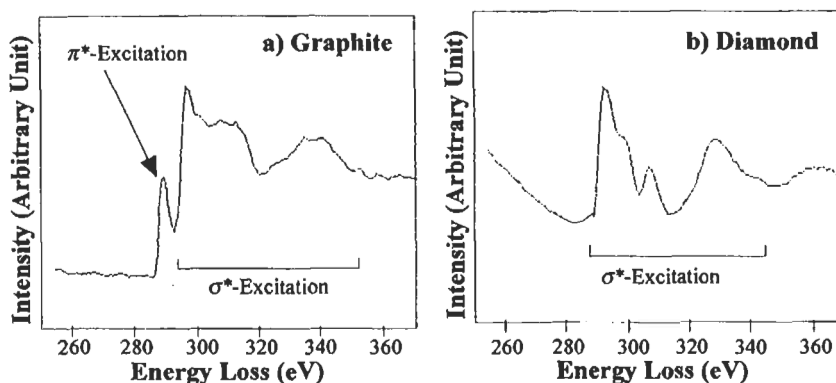


Fig. 4. EEL spectra of (a) graphite and (b) diamond. These carbon allotropes represent different spectra: sp^2 bonding especially exhibits π^* -excitation peak lower than the σ^* -excitation peaks (modified from ref. 16).

3 Instruments and Characterisation Procedure

Figure 5 shows a ray path in TEM equipped with a Castaing-Henry imaging filter lens (Zeiss CEM-902). The imaging filter lens consists of a double magnetic prism and an electrostatic mirror. There is a limitation to accelerating

voltage of 80 - 100 keV due to the risk of electrical breakdown at higher voltage. Nowadays, a purely magnetic filter lens, Ω (omega) filter, has been developed to be in routine use instead of the prism in Fig. 5. Other type of energy filter, post-column imaging spectrometer supplied from GATAN as Gatan Imaging Filter (GIF) is set under the fluorescent screen.

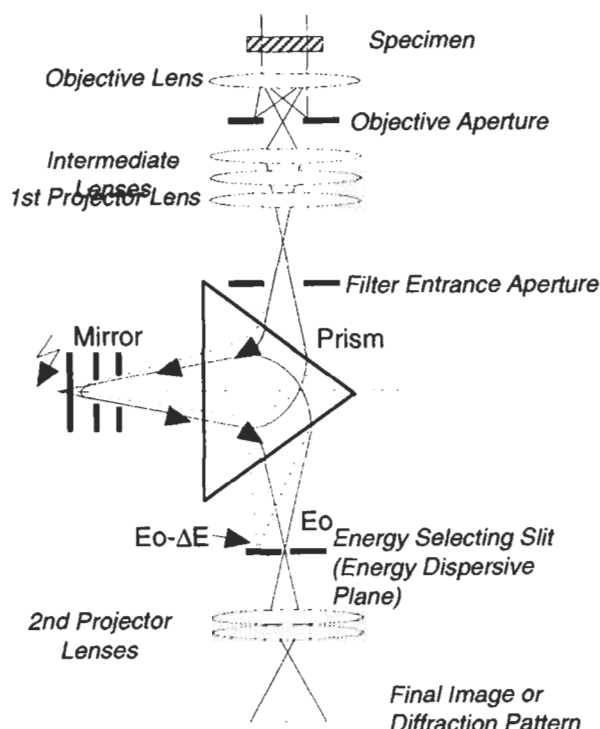


Fig. 5. Electron ray path of Castaing-Henry energy filter.

Although a TEM gives a two-dimensional (2D) intensity distribution of the specimen, the energy losses in an EEL spectrum offer us a new dimension of electron microscopy. When the electrons with the information as image or diffraction are introduced into the prism spectrometer, energy-lost electrons with an energy of $E_0 - \Delta E$ should be bent more than the elastically scattered electrons with E_0 . The intensity distribution, EELS pattern, can be obtained on an energy dispersive plane. If the energy selecting slit was removed from the ray path, the spectrum can be recorded on 2D detector such as fluorescent screen, photographic film or CCD camera. Energy-filtering TEM can also be used to obtain an electron spectroscopic images (ESI) with an energy selecting slit in the energy dispersive plane. The filtered image or diffraction pattern appears on a fluorescent screen. It offers (1) zero-loss images protected from image blurring due to chromatic aberration and zero-loss diffraction patterns eliminating the inelastic

background, (2) better contrast images by taking a different energy losses and (3) elemental distribution (elemental mapping) using energy-lost electrons at the ionisation edges.

According to the qualitative analysis of CNTs by using high resolution and high voltage (1 MeV) TEM equipped with a GIF [15], only 20 carbon atoms in 6 layers tube were detected in carbon distribution image. In addition, the carbon mapping from a conical-tip region with progressive closure of graphitic sheets could distinguish the difference of 6 graphitic sheets in the intensity profile. One can get further information concerning EELS and electron spectroscopic imaging (ESI) by using an energy-filtered TEM in the textbooks [19-21].

3 Dependence of EEL Spectra on the Diameter of CNTs

Although EELS patterns of CNTs are essentially the same as those of graphite, there are subtle but significant deviations in the spectra. Figure 6(a) shows the EEL spectra of CNTs and graphite in the energy ranges of 0 - 45 eV (plasmon loss) and (b) 280 - 300 eV (core-loss), obtained by a high resolution EEL spectrometer [13,14]. The energy resolution was 0.27 - 0.40 eV at the full width at half maximum (FWHM) of the zero-loss peak. There are two prominent peaks

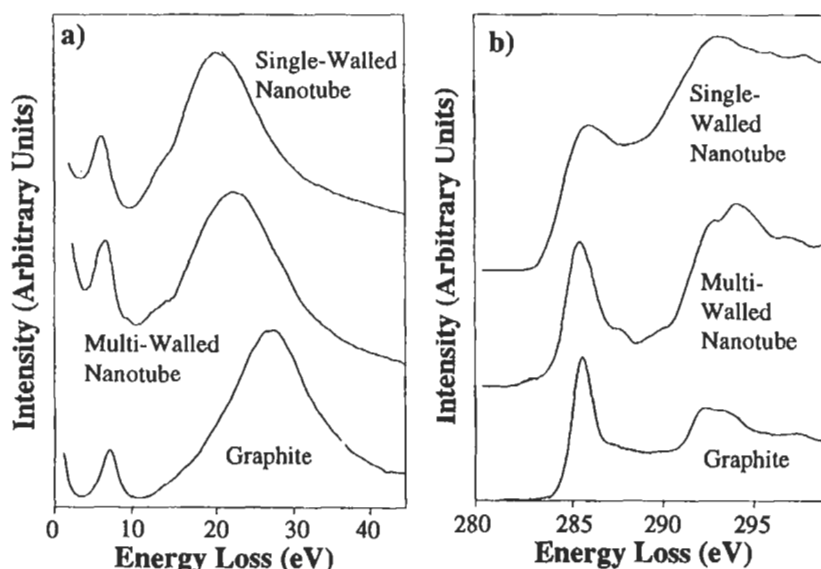


Fig. 6. EEL spectra of bundle of four SWCNTs, MWCNT and graphite in the energy ranges (a) from 0 to 45 eV (plasmon region) and (b) from 280 to 300 eV (carbon K-edge) (modified from ref. 14).

in the low-loss region, 5 - 8 eV and 20 - 28 eV assigned to the π plasmon caused by the transition between π and π^* electron energy states and the

collective excitation of all the valence electrons ($\pi+\sigma$ plasmon), respectively. Both the energies of the π plasmon and the $\pi+\sigma$ plasmon peaks of SWCNT are lower than those of MWCNT and graphite. Note that, in this case, the EELS was not obtained from an SWCNT but from a bundle consisting of four SWCNTs. Although the EEL spectra obtained from this SWCNT bundle showed the same plasmon energy, the $\pi+\sigma$ plasmon peak for MWCNT was shifted depending on the diameters. This can be interpreted by the fact that every graphitic sheet of the SWCNTs in the bundle has the same curvature, while the mean curvatures of the graphitic sheets in MWCNTs are different for tubes with different diameters.

On the other hand, in the core-loss region, there are also two peaks. One is the transition from 1s states to the unoccupied π^* levels at 286 eV and the other is that to the unoccupied σ^* levels at 292 eV. Both peaks of the bundle of SWCNTs are broader than those of MWCNT and graphite. The π^* excitation peak of the MWCNT is slightly broader than that of graphite. The peak width relates to the energy states of excitation. The broadening of the π^* energy states was caused by the curvature of the graphitic sheets and the effect of bundle formation. When the MWCNTs with different diameters, 5, 10 and 20 nm, were measured, the π^* transition peaks of thinner CNTs tended to be narrower [16]. In such a case, the broadening of the 1s $\rightarrow \pi^*$ transition peak could be due to the strong curvature of the graphitic sheet.

4 Angular Dependence of EEL Spectra of CNTs

Dravid et al. examined anisotropy in the electronic structures of CNTs from the viewpoint of momentum-transfer resolved EELS, in addition to the conventional TEM observation of CNTs, cross-sectional TEM and precise analysis by TED [5]. Comparison of the EEL spectra of CNTs with those of graphite shows lower π peak than that of graphite in the low-loss region (plasmon loss), as shown in Fig. 7(a). It indicates a loss of valence electrons and a change in band gap due to the curved nature of the graphitic sheets.

The core-loss spectra of CNTs were compared with those of graphite under similar geometrical conditions. One is that the incident electrons are parallel to the tube axis (Fig. 7(b)), and the other normal (Fig. 7(c)). In the former case, the c -axis of all the sheets in CNTs is radially perpendicular to the electron beam. The core-loss EEL spectrum is identical to that of graphite, in which π^* excitation peak is smaller than that of σ^* . However, in the latter case, the tube axis is normal to the electron beam and the c -axis changes its direction according to the tubular structure with respect to the electron beam. The result in EEL spectrum of CNT shows that σ^* excitation peak is stronger than that of π^* , unless in graphite the prominent π^* excitation peak appears. Such strong anisotropy of the electronic structure of CNTs concluded from the EELS should be concomitant with the strongly anisotropic electronic and magnetic properties. As mentioned above, EEL spectrum is sensitive to the structure. If a narrow slit was used instead of an objective aperture to be selected, a series of $\{00l\}$ reflexion spots (000, 002, etc.) accompanied by the spectra from an MWCNT

appear on the fluorescent screen as shown in Fig. 8. It is called an angular-resolved EELS to probe the dependence of energy loss (ΔE) on the scattering angle (Θ) or momentum transfer. Leapman et al. examined the angular distributions of peaks in the EEL spectra from graphite in detail [22]. They concluded that the experimental results well agreed with the theoretical distributions for transitions to the final π^* and σ^* states in a hybridised atomic-orbital model.

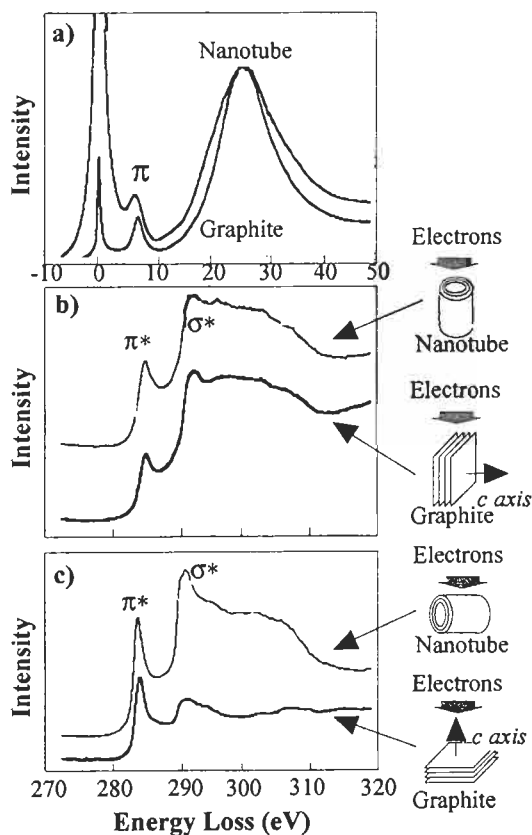
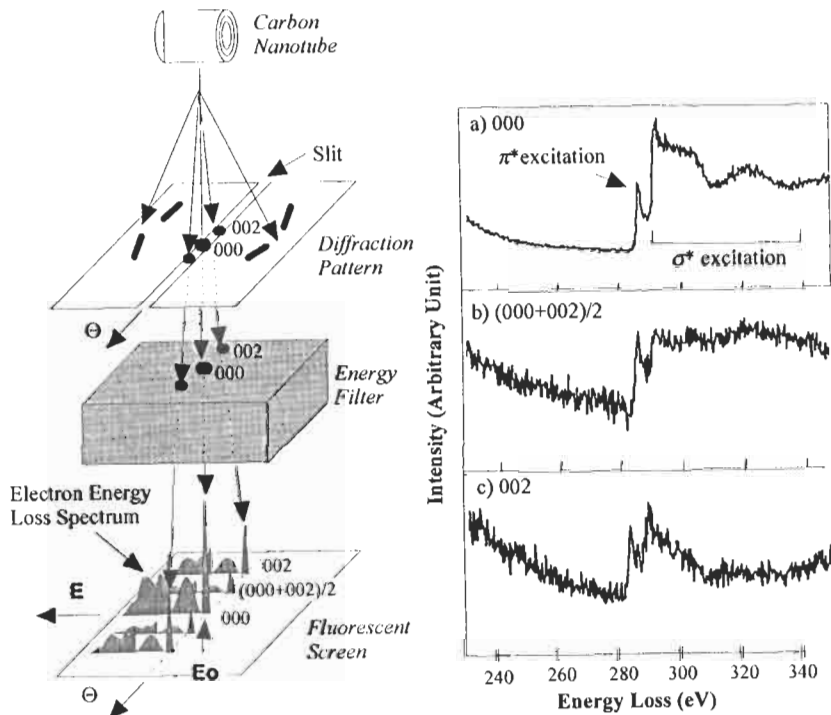


Fig. 7. (a) Low-loss EEL spectra of CNT and graphite and carbon core-loss EEL spectra of graphite and tubes in (b) normal geometry (the electron beam normal to the c -axis) and in (c) parallel geometry (the electron beam parallel to the c -axis of graphite and perpendicular to the tube axis) (modified from ref. 5).

Figure 9 shows angular distribution of EELS of an MWCNT with a diameter of 100 nm [16]. The core-loss spectra obtained from the 000 and 002 reflexions much resemble those of an MWCNT and graphite (Figs. 6(b) and 7(c)). The π^* excitation peak is smaller than that of σ^* excitation peak. In contrast, the

intermediate position, $(000+002)/2$, represents different feature in EEL spectrum as shown in Fig. 9(b). As mentioned above, when the tube is laid normal to the incident electrons, c -axis changes its direction according to the tubular structure. The 000 spot includes the whole information from the top and bottom, and both sides of tube, but the 002 spot has the information of the piling graphitic sheets oriented normal to the incident electrons. The situation might resemble that of graphite in Fig. 7(b). The reflected electrons along the direction of Θ are free from the top and bottom planes of tube. The scattered electrons at intermediate position would include the strong interaction with lots of π electrons, which are arranged normal to the side planes and have large cross sections with respect to the incident electrons. So that the π^* excitation peak should be larger than that of σ^* excitation peak as in Fig. 9(b).



Left: **Fig. 8.** Schematic illustration of angular-resolved EEL spectra for CNT with anisotropic structure.

Right: **Fig. 9.** EEL spectra of an MWCNT obtained from the locations at 000, intermediate and 002 reflexions in the reciprocal space (modified from ref. 16).

5 Summary

Although CNTs showed similar EELS pattern in plasmon-loss and core-loss regions to graphite, SWCNT and fine MWCNT with a diameter less than 5 nm had different features. Furthermore, it has been found out that the angular-dependent EELS along the direction normal to the longitudinal axis of CNT shows stronger contribution from π electrons than σ electrons. It has been confirmed that the anisotropy of CNT exists in the structure and electronic property.

References

1. Iijima, S., *Nature*, 1991, **354**, 56.
2. Ebbesen, T.W., *Physics Today*, 1996, (6), 26.
3. Cook, J., Sloan, J. and Green, M. H., *Chemistry and Industry*, 1996, (8) 600.
4. Iijima, S. and Ichihashi, T., *Nature*, 1993, **363**, 603.
5. Dravid, V. P., Lin, X., Wang, Y., Wang, X. K., Yee, A., Ketterson, J. B. and Chang, R. P. H., *Science*, 1993, **259**, 1601.
6. Wang, X. K., Lin, X. W., Dravid, V. P., Ketterson, J. B. and Chang, R. P. H., *Appl. Phys. Lett.*, 1993, **62**, 1881.
7. Ajayan, P. M., Stephan, O., Colliex, C. and Trauth, D., *Science*, 1994, **265**, 1212.
8. Yase, K., Tanigaki, N., Kyotani, M., Yumura, M., Uchida, K., Ohshima, S., Kuriki, Y. and Ikazaki, F. In *Materials Research Society Symposium Proceedings*, Vol. 359, ed. P. Bernier, D. S. Bethune, L. Y. Chiang, T. W. Ebbesen, R. M. Metzger and J. W. Mintmere, Materials Research Society, Pittsburgh, 1995, pp. 81.
9. Bursill, L. A., Peng, J. -L. and Fan, X. -D., *Phil. Mag.*, A, 1995, **71**, 1161.
10. Fan, X. -D. and Bursill, L. A., *Phil. Mag.*, A, 1995, **72**, 139.
11. Cowley, J. M., Nikolaev, P., Thess, A. and Smalley, R. E., *Chem. Phys. Lett.*, 1997, **265**, 379.
12. Cowley, J. M. and Sundell, F. A., *Ultramicroscopy*, 1997, **68**, 1.
13. Kuzuo, R., Terauchi, M. and Tanaka, M., *Jpn. J. Appl. Phys.*, 1992, **31**, L1484.
14. Kuzuo, R., Terauchi, M., Tanaka, M. and Saito, Y., *Jpn. J. Appl. Phys.*, 1994, **33**, L1316.
15. Kurata, H., Isoda, S. and Kobayashi, T., *Microscopy, Microanalysis and Microstructure*, 1995, **6**, 405.
16. Yase, K., Horiuchi, S., Kyotani, M., Yumura, M., Uchida, K., Ohshima, S., Kuriki, Y., Ikazaki, F. and Yamahira, N., *Thin Solid Films*, 1996, **273**, 222.
17. Lin, N., Ding, J., Yang, S. and Cue, N., *Carbon*, 1996, **34**, 1295.
18. Tsang, S. C., de Oliveira, P., Davis, J. J., Green, M. L. H. and Hill, H. A. O., *Chem. Phys. Lett.*, 1996, **249**, 413.
19. Reimer, L., *Energy-Filtering Transmission Electron Microscopy*, Springer-Verlag, Berlin, Heidelberg, 1995, pp. 1-42 and pp. 347-400.
20. Egerton, R. F., *Electron Energy-Loss Spectroscopy in the Electron Microscope*, 2nd edn., Plenum Press, New York-London, 1996.
21. *Transmission Electron Energy Loss Spectrometry in Materials Science*, ed. M. M. Disko, C. C. Ahn and B. Fultz, The Minerals, Metals &

- Materials Society (TMS), Warrendale, Pennsylvania, 1992.
22. Leapman, R. D., Fejes, P. L. and Silcox, J., *Phys. Rev. B*, 1983, **28**, 2361.

CHAPTER 5

Electronic Structures of Single-Walled Carbon Nanotubes

KAZUYOSHI TANAKA,¹ MAYUMI OKADA² and YUANHE HUANG³¹*Department of Molecular Engineering, Graduate School of Engineering, Kyoto University, Sakyo-ku, Kyoto 606-8501, Japan*²*Institute for Fundamental Chemistry, 34-4 Nishihiraki-cho, Takano, Sakyo-ku, Kyoto 606-8103, Japan*³*Department of Chemistry, Beijing Normal University, Beijing 100875, China***1 Introduction**

Studies on the electronic structure of carbon nanotube (CNT) is of much importance toward its efficient utilisation in electronic devices. It is well known that the early prediction of its peculiar electronic structure [1-3] right after the Iijima's observation of multi-walled CNT (MWCNT) [4] seems to have actually triggered the subsequent and explosive series of experimental researches of CNT. In that prediction, alternative appearance of metallic and semiconductive nature in CNT depending on the combination of diameter and pitch or, more specifically, chiral vector of CNT expressed by two kinds of non-negative integers (a , b) as described later (see Fig. 1).

In this chapter the results of detailed research on the realistic electronic structure of single-walled CNT (SWCNT) are summarised with explicit consideration of carbon-carbon bond-alternation patterns accompanied by the metal-insulator transition inherent in low-dimensional materials including CNT. Moreover, recent selective topics of electronic structures of CNT are also described. Throughout this chapter the terminology "CNT" stands for SWCNT unless specially noted.

2 Electronic Structure of CNT*2.1 Definition of the configuration of tube (a , b)*

In order to examine the electronic structures of CNT it is necessary to first define the classification of structural configurations of CNT. The configuration of a CNT is constructed by enrolling a graphite sheet as illustrated in Fig. 1. That is,

any tube configuration can be generated by superimposing the hexagon at the original point (denoted by O) to a hexagon indicated by (a, b) defined by a chiral vector $\mathbf{R} = a\mathbf{x} + b\mathbf{y}$, where \mathbf{x} and \mathbf{y} are the primitive vectors whose lengths are both equal to $\sqrt{3} d_{C-C}$ with d_{C-C} indicating the C-C bond length. The tube generated by such a chiral vector (a, b) is called tube (a, b) in most of the literatures and, hence, we also use this notation in this chapter. The sector-range expressed by $0 \leq \theta \leq \pi/6$ is enough for the generation of any tubes except the enantiomeric tube (b, a) . Note that, however, definition of θ often depends on each researcher.

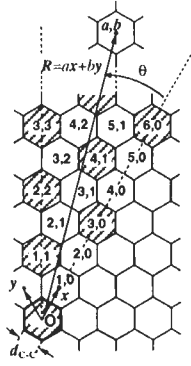


Fig. 1. Schematic representation of generation of tube (a, b) . Note $a \geq b$. Hexagons with chiral vectors satisfying $2a + b = 3N$ in condition I are shadowed.

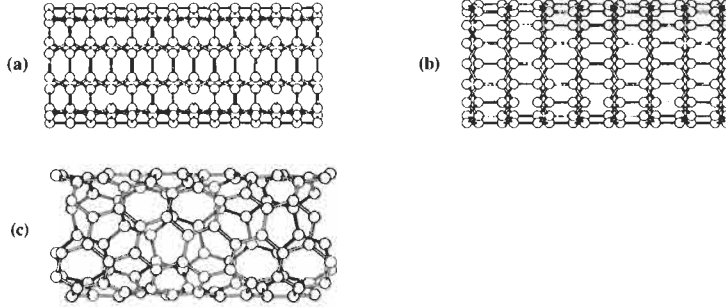


Fig. 2. Outlook of CNT with (a) armchair (tube (a, a)), (b) zigzag (tube $(a, 0)$) and (c) helical (tube (a, b) with $0 < \theta < \pi/6$) structures.

The diameter D of tube (a, b) and the conformation angle θ with equal d_{C-C} are given by,

$$D = \frac{\sqrt{3} d_{C-C}}{\pi} \sqrt{a^2 + ab + b^2},$$

$$\theta = \arccos\left(\frac{2a+b}{2\sqrt{a^2+ab+b^2}}\right) \quad \left(0 \leq \theta \leq \frac{\pi}{6}\right). \quad (1)$$

The tubes (a, a) and $(a, 0)$ are generated from hexagons with $\theta = \pi/6$ and 0 , respectively. These tubes become non-helical and are called, respectively, armchair and zigzag structures. Other condition $(0 < \theta < \pi/6)$ generates the tube (a, b) of helical structures (see Fig. 2).

2.2 Electronic properties of CNT - Simple analysis -

Right after the discovery of MWCNT [4] several reports on the electronic structures of CNT were almost immediately reported based on rather simple tight-binding method or its equivalent [1-3,5,6]. The most interesting and important features therein [1-3] were that CNT will become either metallic or semiconductive depending on the configuration of CNT, that is,

Condition I

CNT is metallic if $2a + b = 3N$ (N ; positive integer)

CNT is semiconductive if $2a + b \neq 3N$

assuming that there is no bond alternation of carbon-carbon bond distances. The terminology "metallic" signifies zero bandgap here. This condition is easily understood from the analytical expression of band structure for any tube (a, b) ,

$$E(k)_N^\pm = \alpha \pm \beta \left[1 + 4\cos\left(\frac{2\pi N}{a} - \frac{a+2b}{2a}kl\right) \cdot \cos\left(\frac{kl}{2}\right) + 4\cos^2\left(\frac{kl}{2}\right) \right]^{1/2} \quad (N = 1, 2, 3, \dots, a) \quad (2)$$

where α and β represent the Coulomb and transfer integrals, respectively, as usual and $l (\equiv (3/2)d_{C-C})$ the translation length of the unit cell. A typical metallic band structure is shown in Fig. 3.

Although it is required to refine the above condition I in actuality, this rather simple but impressive prediction seems to have much stimulated the experiments on the electrical-conductivity measurement and the related solid-state properties in spite of technological difficulties in purification of the CNT sample and in direct measurement of its electrical conductivity (see Chap. 10). For instance, for MWCNT, a direct conductivity measurement has proved the existence of metallic sample [7]. The electron spin resonance (ESR) (see Chap. 8) [8] and the ^{13}C nuclear magnetic resonance (NMR) [9] measurements have also proved that MWCNT can show metallic property based on the Pauli susceptibility and Korringa-like relation, respectively. On the other hand, existence of semiconductive MWCNT sample has also been shown by the ESR measurement [10]. For SWCNT, a combination of direct electrical conductivity and the ESR measurements has confirmed the metallic property of the sample employed therein [11]. More recently, bandgap values of several SWCNT

samples with different combination of chiral vectors a and b have been estimated by the scanning tunnelling microscope/scanning tunnelling spectroscopy (STM/STS) methods [12,13].

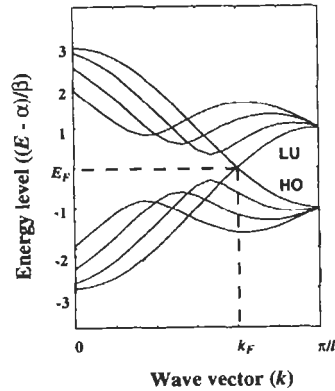


Fig. 3. Hückel-type band structure of tube (10, 10).

2.3 Consideration of bond alternation - Realistic analysis -

As mentioned above, the condition I is rather naive for consideration of the electronic structure of actual CNT due to the following two reasons:

(1) It is well known that metallic electronic structure is not generally realised in low-dimensional materials on account of metal-insulator transition (or Peierls transition [14]). This transition is formally required by energetical stabilisation and often accompanied with the bond alternation, an example of which is illustrated in Fig. 4 for metallic polyacetylene [15]. This kind of metal-insulator transition should also be checked for CNT satisfying $2a + b = 3N$, since CNT is considered to belong to also low-dimensional materials. Representative bond-alternation patterns are shown in Fig. 5. Expression of band structures of any isodistant tubes (a, b) is equal to those in Eq.(2). Those for bond-alternation patterned tube (a, b) are given by,

$$E(k)_N^\pm = \alpha \pm \beta \left[m^2 + 4m \cos \left(\frac{\pi N}{a} + \frac{(a-b)kl}{2a} \right) \times \cos \left(\frac{\pi N}{a} - \frac{(a+b)kl}{2a} \right) + 4 \cos^2 \left(\frac{\pi N}{a} - \frac{(a+b)kl}{2a} \right) \right]^{\frac{1}{2}} \quad (3)$$

(for Alt 1; $N = 1, 2, 3, \dots, a$)

where m is defined by the ratio $\beta_{C=C}/\beta_{C-C}$ and

$$E(k)_N^{\pm} = \alpha \pm \beta \left[m^2 + 4m \cos \left\{ \frac{\pi N}{a} - \frac{(2a+b)kl}{2a} \right\} \right. \\ \left. \times \cos \left(\frac{\pi N}{a} - \frac{bkl}{2a} \right) + 4 \cos^2 \left(\frac{\pi N}{a} - \frac{bkl}{2a} \right) \right]^{\frac{1}{2}} \\ \text{(for Alt 2; } N = 1, 2, 3, \dots, a) \quad (4)$$

The analytical expression for the Kekulé type has also been derived [16] but omitted here for simplicity.

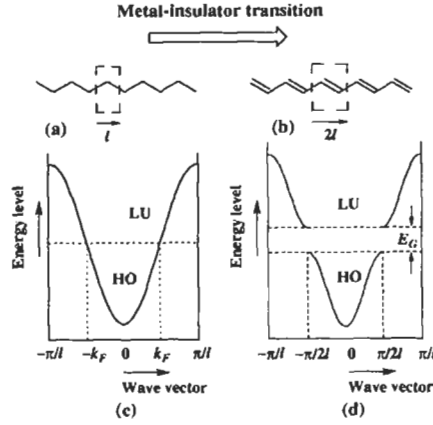


Fig. 4. Peierls transition in metallic polyacetylene and accompanied generation of bond alternation. Note that the semiconductive (or insulating) structure accompanied with the bond alternation is the more energetically stable.

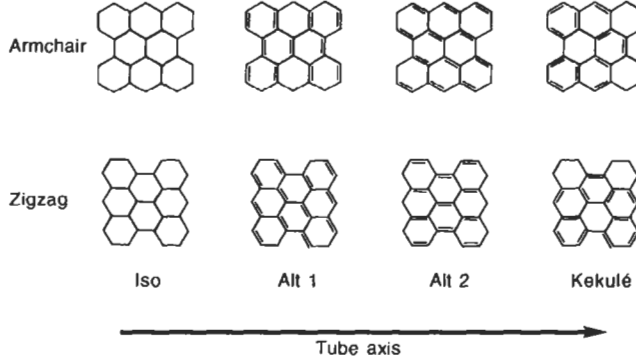


Fig. 5. Possible bond-alternation patterns of CNTs: (a) Isodistant (Iso), (b) bond-alternant 1 (Alt 1), (c) bond-alternant 2 (Alt 2) and (d) Kekulé patterns.

Changes in the bandgap values depending on these patterns are summarised in Table 1 [16], where it is shown that only armchair-type CNT can have zero bandgap at a certain bond-alternation pattern even if they have not isodistant bond patterns. It should be emphasised that actual bond pattern is decided only by the viewpoints of energetical stabilisation, which cannot be predicted by the Hückel-type tight-binding calculation.

Table 1. The bandgap values of CNTs satisfying $2a + b = 3N$ with various bond-alternation patterns.

	Armchair tube (a, a)	Zigzag tube $(a, 0)$	Helical tube (a, b)
Iso	0	0	0
Alt 1	0	$2 \beta \cdot (\sqrt{1+m+m^2} - 1)$	Non-zero ^a
Alt 2	$2 \beta \cdot \left\{ m^2 - \frac{(1-3m)^2}{4m} \right\}$	$2 \beta \cdot (m - 1)$	Non-zero ^a
Kekulé	$2 \beta \cdot (m - 1)$	$2 \beta \cdot (m - 1)$	$2 \beta \cdot (m - 1)$

^aThese values lie between those of the corresponding armchair and zigzag structures. The explicit expressions have been given in ref. 16.

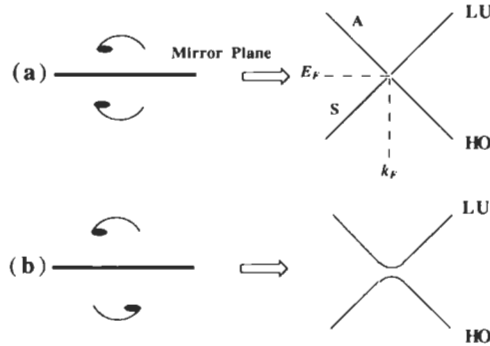


Fig. 6. Examples of (a) mirror symmetry and (b) non-symmetry with respect to the tube axis. The HO-LU band crossing in (a) changes into 'avoid crossing' in (b). Notations S and A signify symmetric and antisymmetric with respect to the mirror symmetry, respectively, for instance.

(2) Appearance of the metallic structure of CNT is based on the crossing of the highest occupied (HO) and the lowest unoccupied (LU) bands (see, e.g., Fig. 3), each accompanying pseudo π -type crystal orbital. Note that pseudo π -type orbital, particularly when all the valence atomic orbitals (AO) are taken into consideration, implies that its main AO component is normal to the cylindrical CNT surface. The band crossing mentioned above is possible when these two

pseudo π bands belong to different subsymmetry groups [17], which can be satisfied with only in the tube having a mirror symmetry with respect to a plane including the tube axis on it (see Fig. 6). For instance, helical-type tubes (a, b) cannot become metallic even if they satisfy the relationship $2a + b = 3N$ due to lack in such mirror symmetry, the fact of which is neglected in the Hückel-type tight-binding calculations dealing with only the topological network of CNT. Considering the implication shown in Table 1, the metallic property can thus appear only in Iso or Alt 1 type of tube (a, a) and Iso type of tube $(a, 0)$ as far as such bond patterns are favoured from energetical point of view. The energetical optimisation including σ -electrons has only been performed with respect to tubes $(5, 5)$ and $(9, 0)$ (both with diameters of ~ 7 Å) hitherto [18], where it was found Alt 1 type is the most stable in tube $(5, 5)$ and Alt 2 in tube $(9, 0)$. Therefore, it has been turned out that tube $(5, 5)$ can be metallic but tube $(9, 0)$ not in actuality as shown in Fig. 7. Hence the improved version of the condition I can be summarised as,

Condition II

Armchair structure:	Tube (a, a) will have the bond pattern of Alt 1 and be metallic.
Zigzag structure:	Tube $(3a, 0)$ will have the bond pattern of Alt 2 and be narrow-gap semiconductive.
Helical structure:	Tube (a, b) with $2a + b = 3N$ will be narrow-gap semiconductive.
All other tubes:	Wide-gap semiconductive.

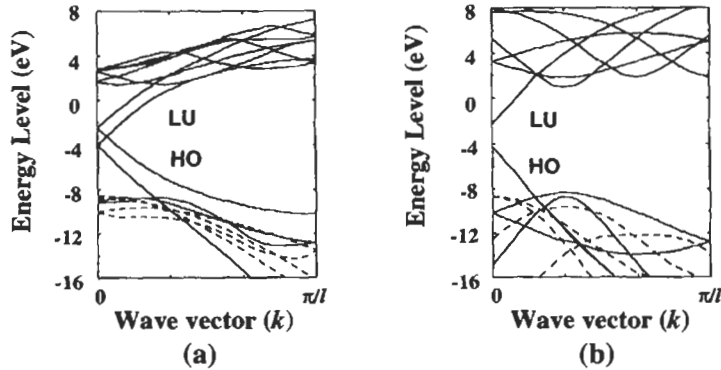


Fig. 7. Band structures of energetically optimised (a) tube $(5, 5)$ and (b) tube $(9, 0)$ [18].

A couple of theoretical studies [5,19] have hitherto attempted to estimate the Peierls transition temperature (T_p) for metallic CNT. A detailed theoretical check with respect to the stability of metallic wavefunction in tube $(5, 5)$ has also

assured that the wavefunction is stable against the Peierls transition causing the band opening or, in other words, metal-insulator transition [20]. Lack in the Peierls transition of tube (5, 5) can be understood from small values of special interelectron repulsion integrals called as Fermi integrals [21]. This tendency will possibly be able to extend to the tubes with larger diameters such as tube (10, 10), to which observed metallic properties of SWCNT has been ascribed [11,22].

3 Related Topics of Electronic Structure of CNT

3.1 Interlayer and intertube interactions

An MWCNT has inner concentric tube(s) with smaller diameter(s) inside its hollow, and it is normally prepared in the carbon electrode of the arc-discharging method or by chemical vapour deposition method (see Chaps. 2 and 12). Influence of such inner tubes on the most outer layer in MWCNT is of interest with respect to electronic similarity of MWCNT and SWCNT.

The optimised interlayer distance of a concentric bilayered CNT by density-functional theory treatment was calculated to be 3.39 Å [23] compared with the experimental value of 3.4 Å [24]. Modification of the electronic structure (especially metallic state) due to the inner tube has been examined for two kinds of models of concentric bilayered CNT, (5, 5)-(10, 10) and (9, 0)-(18, 0), in the framework of the Hückel-type treatment [25]. The stacked layer patterns considered are illustrated in Fig. 8. It has been predicted that metallic property would not change within this stacking mode due to symmetry reason, which is almost similar to the case in the interlayer interaction of two graphene sheets [26]. Moreover, in the three-dimensional graphite, the interlayer distance of which is 3.35 Å [27], there is only a slight overlapping (0.03-0.04 eV) of the HO and the LU bands at the Fermi level of a sheet of graphite plane [28,29].

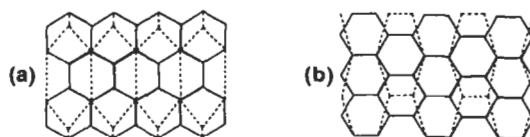


Fig. 8. Stacking patterns of bilayered CNTs: (a) (5, 5)-(10, 10) and (b) (9, 0)-(18, 0). The inner tube lattice (dotted line) is projected onto the outer one (solid line) (simplified from ref. 25).

Thus it seems that the electronic structure of the inner tube does not seriously affect that of the most outside tube in MWCNT. More detailed theoretical and experimental examination on MWCNT is obviously desirable for complete understanding of miscellaneous interlayer interaction.

It has been referred to that SWCNT forms a bundle or rope by aggregating several hundreds of SWCNTs in parallel [22]. Intertube interaction in such

bundle of tube (10, 10) has been examined by a perturbation technique and it has been clarified that the interaction causes the broken symmetry leading to the pseudogap of ca. 0.1 eV [30]. Such pseudogap would result in semimetal-like temperature dependence of electrical conductivity of the SWCNT rope with both electron and hole charge carriers.

3.2 Superconductivity

It will be intriguing to theoretically examine the possibility of superconductivity in CNT prior to the actual experimental assessment. A preliminary estimation of superconducting transition temperature (T_c) for metallic CNT has been performed considering the electron-phonon coupling within the framework of the BCS theory [31]. It is important to note that there can generally exist the competition between Peierls- and superconductivity (BCS-type) transitions in low-dimensional materials. However, as has been described in Sec. 2.3, the Peierls transition can probably be suppressed in the metallic tube (a, a) due to small Fermi integrals as a whole [20].

In metallic tube (a, a) two bands cross at the Fermi level (see, Figs. 3 and 7(a)), the electron-phonon coupling between the two different bands should be also considered in general. The superconducting transition temperature (T_c) for tube (5, 5) has been estimated, in the course of which it was found that the intraband backward scattering by the longitudinal modes plays an important role for the occurrence of superconducting state. Specifically for tube (5, 5) with a diameter of $\sim 7 \text{ \AA}$, the T_c was obtained to be $1.5 \times 10^{-4} \text{ K}$. This extremely low T_c seems to eventually come from the small density of states at the Fermi level in metallic tube (5, 5), which seems to common to tube (a, a) since the expression forms of the HO and the LU bands in sinusoidal functions do not essentially change for any a as is clear from Eq.(2) [16].

This restriction, however, could be circumvented by the doped CNT with either Lewis acid or base [32-36], since such doping, even to semiconductive CNT could enhance the density of states at the Fermi level as well as bring about the metallic property. Appearance of metallic conductivity in helical CNT by such doping process would be of interest in that it could make molecular solenoid of nanometer size [37].

4 Summary

Electronic structures of SWCNT have been reviewed. It has been shown that armchair-structural tubes (a, a) could probably remain metallic after energetical stabilisation in connection with the metal-insulator transition but that zigzag ($3a, 0$) and helical-structural tubes (a, b) would change into semiconductive even if the condition $2a + b = 3N$ is satisfied. There would not be so much difference in the electronic structures between MWCNT and SWCNT and these can be regarded electronically similar at least in the zeroth order approximation. Doping to CNT with either Lewis acid or base would newly cause intriguing electronic properties including superconductivity.

Acknowledgement

We are grateful to financial support from the project of Institute for Fundamental Chemistry, supported by the Japanese Society for the Promotion of Science - Research for the Future Program (JSPS-RFTF98P00206).

References

1. Tanaka, K., Okahara, K., Okada, M. and Yamabe, T., *Chem. Phys. Lett.*, 1992, **191**, 469.
2. Saito, R., Fujita, M., Dresselhaus, G. D. and Dresselhaus, M., *Phys. Rev. B*, 1992, **46**, 1804.
3. Hamada, N., Sawada, S. and Oshiyama, A., *Phys. Rev. Lett.*, 1992, **68**, 1579.
4. Iijima, S., *Nature*, 1991, **56**, 354.
5. Mintmire, J. W., Dunlap, B. I. and White, C. T., *Phys. Rev. Lett.*, 1992, **68**, 631.
6. Harigaya, K., *Phys. Rev. B*, 1992, **45**, 12071.
7. Ebbesen, T. W., Lezec, H. J., Hiura, H., Bennett, J. W., Ghaemi, H. F. and Thio, T., *Nature*, 1996, **382**, 54.
8. Kosaka, M., Ebbesen, T. W., Hiura, H. and Tanigaki, K., *Chem. Phys. Lett.*, 1994, **225**, 161.
9. Maniwa, Y., Hayashi, M., Kumazawa, Y., Tou, H., Kataura, H., Ago, H., Ono, Y., Yamabe, T. and Tanaka, K. In *AIP Conference Proceedings (Proceedings of XIIth International Winterschool of Electronic Properties of Novel Materials - Progress in Molecular Nanostructures)*, Vol. 42, Ed. H. Kuzmany, J. Fink, M. Mehring and S. Roth, American Institute of Physics, Woodbury, NY, 1998, pp. 87.
10. Tanaka, K., Sato, T., Yamabe, T., Okahara, K., Uchida, K., Yumura, M., Niino, H., Ohshima, S., Kuriki, Y., Yase, K. and Ikazaki, F., *Chem. Phys. Lett.*, 1994, **223**, 65.
11. Thess, A., Lee, R., Nikolaev, P., Dai, H., Petit, P., Robert, J., Xu, C., Lee, Y. H., Kim, S. G., Rinzler, A. G., Colbert, D. T., Scuseria, G. E., Tománek, D., Fisher, J. E. and Smalley, R. E., *Science*, 1996, **273**, 483.
12. Wildöer, J. W. G., Venema, L. C., Rinzler, A. G., Smalley, R. E. and Dekker, C., *Nature*, 1998, **391**, 59.
13. Odom, T. W., Huang, J. -L., Kim, P. and Lieber, C. M., *Nature*, 1998, **391**, 62.
14. Peierls, R. *Quantum Theory of Solids*, Oxford Univ. Press, London, 1955, Chap. 5.
15. Tanaka, K. and Yamabe, T., *Electronic Structure of Conductive Conjugated Systems and Their Physicochemical Properties*, in *Advances in Quantum Chemistry*, Vol. 17, ed. P. -O. Löwdin, Academic Press, New York, 1985, pp. 251 and references therein.
16. Okahara, K., Tanaka, K., Aoki, H., Sato, T. and Yamabe, T., *Chem. Phys. Lett.*, 1994, **219**, 462.
17. Heine, V., *Group Theory in Quantum Mechanics*, Pergamon, London, 1960, Chap. 6.

18. Tanaka, K., Ago, H., Yamabe, T., Okahara, K. and Okada, M., *Intern. J. Quantum Chem.*, 1997, **63**, 637.
19. Huang, Y., Okada, M., Tanaka, K. and Yamabe, T., *Solid State Commun.*, 1996, **97**, 303.
20. Tanaka, K., Okada, M., Huang, Y., Yoshii, T. and Ito, A., submitted.
21. Tanaka, K., Kobayashi, H., Okada, M., Kobashi, M. and Yamabe, T., *Intern. J. Quantum Chem.*, 1992, **42**, 45.
22. Cowley, J. M., Nikolaev, P., Thess, A., and Smalley, R. E., *Chem. Phys. Lett.*, 1997, **265**, 379.
23. Charlier, J. -C. and Michenaud, J. -P., *Phys. Rev. Lett.*, 1993, **70**, 1858.
24. Ebbesen, T. W. and Ajayan, P. M., *Nature*, 1992, **358**, 220.
25. Saito, R., Dresselhaus, D. and Dresselhaus, M. S., *J. Appl. Phys.*, 1993, **73**, 494.
26. Tanaka, K., Aoki, H., Ago, H., Yamabe, T. and Okahara, K., *Carbon*, 1997, **35**, 121.
27. See, e. g., Hérol, A. In *Physics of Intercalation Compounds*, ed. L. Pietronero and E. Tosatti, Springer, Berlin, 1981, pp. 7.
28. Slonczewski, J. C. and Weiss, P. R., *Phys. Rev.*, 1958, **109**, 272.
29. McClure, J. W., *Phys. Rev.*, 1957, **108**, 612; 1960, **119**, 606.
30. Delaney, P., Choi, H. G., Ihm, J., Louie, S. G. and Cohen, M. L., *Nature*, 1998, **391**, 466.
31. Huang, Y., Okada, M., Tanaka, K. and Yamabe, T., *Phys. Rev. B*, 1996, **53**, 5129.
32. Zhou, O., Fleming, R. M., Murphy, D. W., Chen, C. H., Haddon, R. C., Ramirez, A. P. and Glarum, S. H., *Science*, 1994, **263**, 1744.
33. Mordkovich, V. Z., Baxendale, M., Yoshimura, S. and Chang, R. P. H., *Carbon*, 1996, **34**, 1301.
34. Baxendale, M., Mordkovich, V. Z., Yoshimura, S. and Chang, R. P. H., *Phys. Rev. B*, 1997, **56**, 2161; 1998, **57**, 9349.
35. Baxendale, M., Mordkovich, V. Z., Yoshimura, S., Chang, R. P. H. and Jansen, A. G. M., *Phys. Rev. B*, 1998, **57**, 15629.
36. Lee, R. S., Kim, H. J., Fischer, J. E., Thess, A. and Smalley, R. E., *Nature*, 1997, **388**, 255.
37. Tanaka, K., Okahara, K., Okada, M. and Yamabe, T., *Fullerene Sci. & Tech.*, 1993, **1**, 137.

CHAPTER 6

Phonon Structure and Raman Effect of Single-Walled Carbon Nanotubes

RIICHIRO SAITO,¹ GENE DRESSELHAUS² and MILDRED S. DRESSELHAUS³

¹*Department of Electronic Engineering, University of Electro-Communications, Chofu, 182-8585 Tokyo, Japan*

²*Francis Bitter Magnet Laboratory, Massachusetts Institute of Technology, Cambridge, Massachusetts 02139 USA*

³*Department of Electrical Engineering and Computer Science and Department of Physics, Massachusetts Institute of Technology, Cambridge, Massachusetts 02139, USA*

The phonon dispersion relations of the carbon nanotubes (CNTs) are obtained by the force constant model scaled from those two-dimensional graphite. Using non-resonant bond polarisation theory, the Raman intensity of a single-walled CNT (SWCNT) is calculated as a function of the diameter and chirality of the CNT. The calculated Raman frequencies clearly depend on the CNT diameter. The polarisation and sample orientation dependence of the Raman intensity shows that the symmetry of the Raman modes can be obtained by varying the direction of the CNT axis, keeping the polarisation vectors of the light fixed. The effect of the finite length of the CNT on the Raman intensity is important for obtaining the middle frequency range of the Raman modes. The resonant Raman effect of CNT distinguishes metallic and semiconducting CNTs.

1 Raman Spectra of Nanotube

An important advance in carbon nanotube (CNT) science [1,2] is the synthesis of single-walled CNTs (SWCNTs) in high yield using transition metal catalysts, resulting in a bundle of SWCNTs containing a triangular lattice of CNTs, known as a *rope* [3,4]. Using such CNT ropes, several solid state properties pertaining to a single CNT have been observed. In particular, many groups [5-9] have reported Raman spectra for SWCNTs in which they assigned observed Raman modes with specific (n, m) CNTs. They showed that the Raman signal from the rope consists of not only the graphite-related E_{2g} (or E_g) modes, which occur in the high frequency region around $1550\text{-}1600\text{ cm}^{-1}$, but also contains a

low frequency ($50\text{-}300\text{ cm}^{-1}$) A_{1g} -active mode that is not observed in graphite, and is known as the CNT radial breathing mode. In the intermediate frequency region ($400\text{-}1350\text{ cm}^{-1}$), weak signals are also observed, but the assignment of each Raman feature to a specific (n, m) SWCNT is still not understood. Thus it is important to investigate the Raman spectra theoretically in order to assign the spectra to (n, m) CNTs reliably.

The group theory for CNTs predicts that, depending on the CNT symmetry, there are 15 or 16 Raman-active modes at $k=0$ for all armchair (n, n) , zigzag $(n, 0)$ and chiral (n, m) , ($n \neq m$) CNTs [1,10]. The number of Raman-active modes does not depend on the number of carbon atoms in the unit cell, which is given by $2N = 4(n^2 + m^2 + nm)/d_R$ for (n, m) CNTs [1]. Here d_R is the highest common divisor of $(2m+n)$ and $(2n+m)$. Raman-active modes corresponding to the (A_{1g}, E_{1g}, E_{2g}) or (A_1, E_1, E_2) irreducible representations of the point group for the unit cell, depending on whether the CNT is achiral or chiral, respectively. The A_{1g} , E_{1g} and E_{2g} Raman modes, which behave like a second-rank tensor, have 0 (x^2+y^2, z^2), 2 (xz, yz) and 4 (x^2-y^2, xy) nodes of vibration around the tube axis in the z direction. Furthermore, since there are two equivalent carbon atoms, A and B, in the unit cell, the Raman modes consist of in-phase and out-of-phase motions for the A and B atoms, which appear in the low and high frequency regions, respectively.

An interesting point concerns polarisation effects in the Raman spectra, which are commonly observed in low-dimensional materials. Since CNTs are one-dimensional (1D) materials, the use of light polarised parallel or perpendicular to the tube axis will give information about the low dimensionality of the CNTs. The availability of purified samples of aligned CNTs would allow us to obtain the symmetry of a mode directly from the measured Raman intensity by changing the experimental geometry, such as the polarisation of the light and the sample orientation, as discussed in this chapter.

In the following sections, we first show the phonon dispersion relation of CNTs, and then the calculated results for the Raman intensity of a CNT are shown as a function of the polarisation direction. We also show the Raman calculation for a finite length of CNT, which is relevant to the intermediate frequency region. The enhancement of the Raman intensity is observed as a function of laser frequency when the laser excitation frequency is close to a frequency of high optical absorption, and this effect is called the resonant Raman effect. The observed Raman spectra of SWCNTs show resonant-Raman effects [5, 8], which will be given in the last section.

2 Phonon Dispersion Relations

A general approach for obtaining the phonon dispersion relations of CNTs is given by tight binding molecular dynamics (TBMD) adopted for the CNT geometry, in which the atomic force potential for general carbon materials is used [5,10]. Here we use the scaled force constants from those of two-dimensional (2D) graphite [2,11], and we construct a force constant tensor for a

constituent atom of the SWCNT so as to satisfy the rotational sum rule for force constants [12,13]. Since we have $2N$ carbon atoms in the unit cell, the dynamical matrix to be solved becomes a $6N \times 6N$ matrix. The equations of motion for the displacement of the i th coordinate, $\vec{u}_i = (x_i, y_i, z_i)$ for $2N$ atoms in the unit cell are given by $M_i \ddot{\vec{u}}_i = \sum_j K^{(ij)}(\vec{u}_j - \vec{u}_i)$, ($i=1, \dots, 2N$), where M_i is the mass of the i th atom and $K^{(ij)}$ represents the 3×3 force constant tensor that couples the i th and j th atoms. In a 1D material, the force constant tensor for a given \vec{k} vector is given by multiplying the force constant parameters with the phase factor $\exp(ik\Delta z_{ij})$, where Δz_{ij} is the distance between i th and j th atoms along the tube axis. The sum over j is normally taken over only a few neighbour distances relative to the i th site, which for a 2D graphene sheet has been carried out up to 4th nearest-neighbour interactions [14]. Using the Fourier transform of the displacements \vec{u}_i , we get a $6N \times 6N$ dynamical matrix $D(\vec{k})$ for a given \vec{k} which satisfies $D(\vec{k})\vec{u}_{\vec{k}} = 0$. To obtain the eigenvalues $\omega^2(\vec{k})$ for $D(\vec{k})$ and the non-trivial eigenvectors $\vec{u}_{\vec{k}} \neq \vec{0}$, we solve the secular equation $\det D(\vec{k}) = 0$ for a given \vec{k} vector.

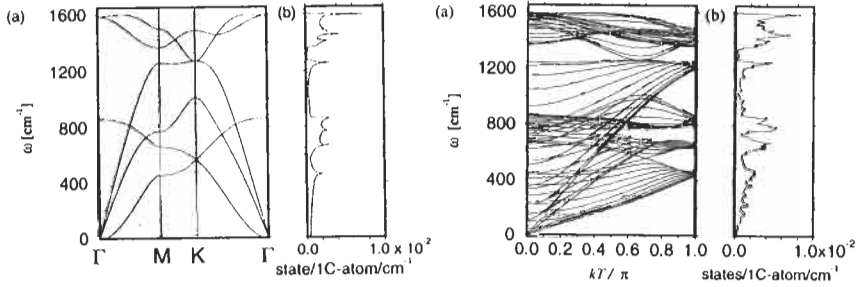


Fig. 1. (a)Phonon dispersion relations and (b)phonon density of states for 2D graphite (left) and a (10, 10) CNT (right) [12].

In Fig. 1 we show the results thus obtained for (a) the phonon dispersion relations $\omega(k)$ and (b) the phonon density of states (DOS) for 2D graphite (left) and a (10, 10) armchair CNT (right). Here T denotes the unit vector along the CNT axis [1]. For the $2N = 40$ carbon atoms per circumferential strip for the (10, 10) CNT, we have 120 vibrational degrees of freedom, but because of mode degeneracies there are only 66 distinct phonon branches, for which 12 modes are non-degenerate and 54 are doubly degenerate. The phonon DOS for the (10, 10) CNT is close to that for 2D graphite, reflecting the zone-folded CNT phonon dispersion.

There are four acoustic modes in CNT. The lowest acoustic modes are the transverse acoustic (TA) modes, which are doubly degenerate, and have x and y

displacements perpendicular to the CNT z axis. The next acoustic mode is the "twisting" acoustic mode (TW), which has θ -dependent displacements in the CNT surface. The highest energy mode is the longitudinal acoustic (LA) mode whose displacements occur in the z direction. The sound velocities of the TA, TW and LA phonons for a (10, 10) CNT, $v_{TA}^{(10,10)}$, $v_{TW}^{(10,10)}$ and $v_{LA}^{(10,10)}$, are estimated as $v_{TA}^{(10,10)} = 9.42$ km/s, $v_{TW}^{(10,10)} = 15.00$ km/s and $v_{LA}^{(10,10)} = 20.35$ km/s, respectively. The calculated phase velocity of the in-plane TA and LA modes of 2D graphite are $v_{TA}^G = 15.00$ km/s and $v_{LA}^G = 21.11$ km/s, respectively. Since the TA mode of the CNT has both an 'in-plane' and an 'out-of-plane' component, the CNT TA modes are softer than the in-plane TA modes of 2D-graphite. The calculated phase velocity of the out-of-plane TA mode for 2D-graphite is almost 0 km/s because of its k^2 dependence. On the other hand, the TW and LA modes of the CNT have only an in-plane component which is comparable in slope to the in-plane TA and LA modes of 2D graphite, respectively. It is noted that the sound velocities that we have calculated for 2D graphite are similar to those observed in three-dimensional (3D) graphite [15], for which $v_{TA}^{3D} = 12.3$ km/s and $v_{LA}^{3D} = 21.0$ km/s. The discrepancy comes from the interlayer interaction between the adjacent graphene sheets.

From the value for $v_{LA}^{(10,10)}$, the elastic constant, C_{11} , where l denotes zz , can be estimated by $v_{LA} = \sqrt{C_{11}/\rho}$, in which ρ is the mass density of the carbon atoms. When we assume a triangular lattice of CNTs with lattice constants [4] $a = 16.95$ Å and $c = 1.44 \times \sqrt{3}$ Å, the mass density ρ becomes 1.28×10^3 kg/m³ from which we obtain the Young's modulus $C_{11} = 530$ GPa. The Young modulus, is almost the same as for C_{11} since C_{12} is expected to be much smaller than in 2D graphite. This value for the Young's modulus is much smaller than $C_{11} = 1060$ GPa for graphite [15] and the range discussed by several other groups [16,17]. The difference in the estimate for the Young's modulus, given here, is due to the smaller values for the mass density.

It is interesting to note that the lowest phonon mode with non-zero frequency at $k = 0$ is not a nodeless A_{1g} mode, but rather an E_{2g} mode with four nodes in which the cross section of the CNT is vibrating with the symmetry described by the basis functions of $x^2 - y^2$ and xy . The calculated frequency of the E_{2g} mode for the (10, 10) CNT is 17 cm⁻¹. Though this predicted mode is expected to be Raman-active, there is at present no experimental observation of this mode. Possible reasons why this mode has not yet been observed experimentally are that the frequency may be too small to be observed readily because of the strong Rayleigh scattering very close to $\omega = 0$, or that the frequency of the E_{2g} mode may be modified by the effect of tube curvature and inter-CNT interactions.

The strongest low frequency Raman mode is the radial breathing A_{1g} mode whose frequency is calculated to be 165 cm⁻¹ for the (10, 10) CNT. Since this frequency is in the silent region for graphite and other carbon materials, this A_{1g} mode provides a good marker for specifying the CNT geometry. When we plot the A_{1g} frequency as a function of CNT diameter for (n, m) in the range

$8 \leq n \leq 10$, $0 \leq m \leq n$, the frequencies are inversely proportional to r within only a small deviation due to CNT curvature [12]. The fitted power law for the A_{1g} radial breathing mode that is valid in the region $3 \text{ \AA} \leq r \leq 7 \text{ \AA}$:

$$\omega(r) = \omega_{(10,10)} \left(\frac{r_{(10,10)}}{r} \right)^{1.0017 \pm 0.0007} \quad (1)$$

should be useful to experimentalists. Here $\omega_{(10,10)}$ and $r_{(10,10)}$ are, respectively, the frequency and radius of the (10, 10) armchair CNT, with values of $\omega_{(10,10)} = 165 \text{ cm}^{-1}$ and $r_{(10,10)} = 6.785 \text{ \AA}$, respectively. As for the higher frequency Raman modes, we see some dependence on r , since the frequencies of the higher optical modes can be obtained from the folded k values in the phonon dispersion relation of 2D graphite [7].

3 Raman Intensity

Using the calculated phonon modes of a SWCNT, the Raman intensities of the modes are calculated within the non-resonant bond polarisation theory, in which empirical bond polarisation parameters are used [18]. The bond parameters that we used in this chapter are $\alpha_{||} - \alpha_{\perp} = 0.04 \text{ \AA}^3$, $\alpha_{||} + 2\alpha'_{\perp} = 4.7 \text{ \AA}^2$ and $\alpha'_{||} - \alpha'_{\perp} = 4.0 \text{ \AA}^2$, where α and α' are the polarisability parameters and their derivatives with respect to bond length, respectively [12]. The Raman intensities for the various Raman-active modes in CNTs are calculated at a phonon temperature of 300K which appears in the formula for the Bose distribution function for phonons. The eigenfunctions for the various vibrational modes are calculated numerically at the Γ point ($k=0$).

3.1 The polarisation dependence of the Raman intensity

In Fig. 2, we show the calculated Raman intensities for the (10, 10) armchair, (17, 0) zigzag and (11, 8) chiral CNTs, whose radii are, respectively, 6.78 \AA , 6.66 \AA and 6.47 \AA and are close to one another. The Raman intensity is normalised in each figure to a maximum intensity of unity. Further the Raman intensity is averaged over the sample orientation of the CNT axis relative to the Poynting vector, in which the average is calculated by summing over the many possible directions, weighted by the solid angle for that direction. Here we consider two possible geometries for the polarisation of the light: the VV and VH configurations. In the VV configuration, the incident and the scattered polarisations are parallel to each other, while they are perpendicular to each other in the VH direction.

When we compare the VV with the VH configurations for the polarised light, the Raman intensity shows anisotropic behaviour. Most importantly, the A_{1g} mode at 165 cm^{-1} is suppressed in the VH configuration, while the lower frequency E_{1g} and E_{2g} modes are not suppressed. This anisotropy is due to the

degenerate vibrations of the E modes, whose eigenfunctions are partners that are orthogonal to each other, thus giving rise to large VH signals.

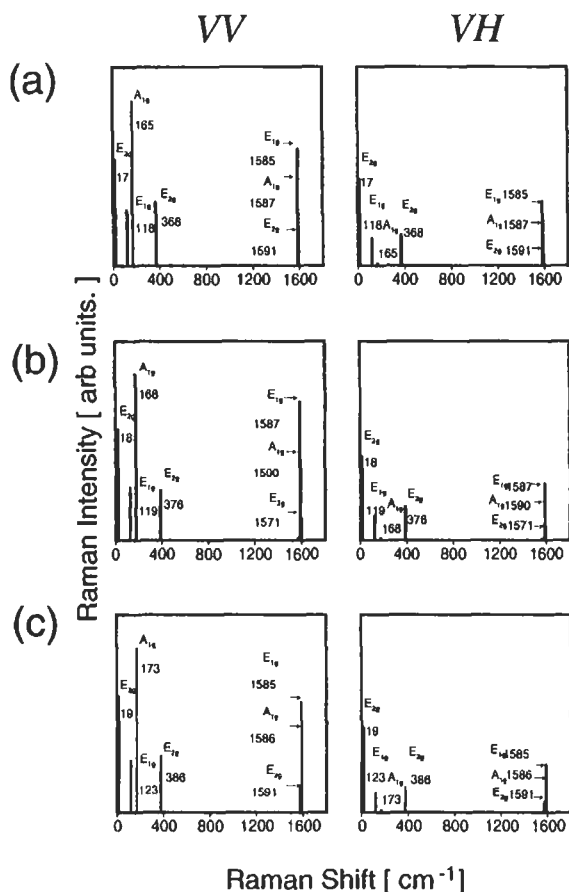


Fig. 2. Polarisation dependence of the Raman scattering intensity for (a) (10, 10) armchair ($r=6.78$ Å), (b) (17, 0) zigzag ($r=6.66$ Å) and (c) (11, 8) chiral ($r=6.47$ Å) CNTs. The left column is for the VV configuration and the right column is for the VH configuration [12].

It is interesting that the higher frequency A_{1g} mode does not show much suppression between the VV and VH geometries, which is related to the direction of the vibrations. In the high frequency region, the Raman active A_{1g} modes come from folding the E_{2g} mode of 2D graphite at 1582 cm^{-1} which corresponds to $\text{C}=\text{C}$ bond stretching motions for one of the three nearest neighbour bonds in the unit cell. When we see the directions of the out-of-phase motions of the A_{1g} modes, the $\text{C}=\text{C}$ bond-stretching motions can be seen in the horizontally and the vertically vibrating $\text{C}=\text{C}$ bonds for armchair and zigzag

CNTs, respectively. Thus, in the cylindrical geometry, we may get a result that is not so polarisation sensitive. On the other hand in C_{60} , since all 60 atoms are equivalent, no carbon atom can move in an out-of-phase direction around the C_5 axes for either of the two A_{1g} modes, so that both modes show similar polarisation behaviours to each other [1].

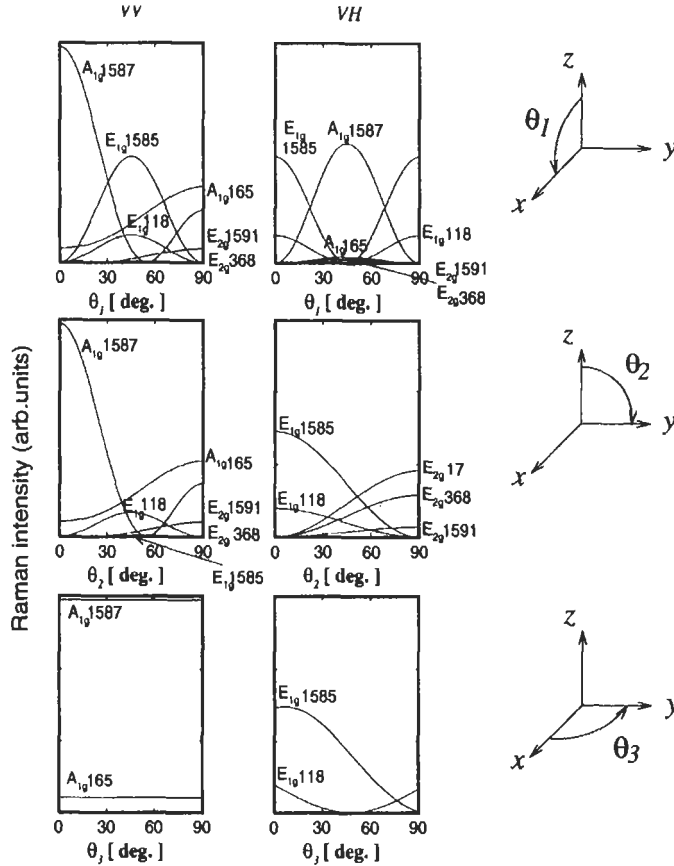


Fig. 3. Raman intensities as a function of the sample orientation for the (10, 10) armchair CNT. As shown on the right, θ_1 and θ_2 are angles of the CNT axis from the z axis to the x axis and the y axis, respectively. θ_3 is the angle of the CNT axis around the z axis from the x axis to the y axis. The left and right hand figures correspond to the VV and VH polarisations [12].

When we compare the calculated Raman intensities for armchair, zigzag and chiral CNTs of similar diameters, we do not see large differences in the lower frequency Raman modes. This is because the lower frequency modes have a long

wavelength, in-phase motion, so that these modes cannot see the chirality of the CNT in detail, but rather the modes see a homogeneous elastic cylinder.

It is noted that we do not obtain any intensity in the calculation for the intermediate frequency region. However the Raman experiments on SWCNTs show weak peaks in the intermediate region which have been assigned to armchair modes [5]. In the experiment broad peaks around 1350 cm^{-1} are known to be associated with symmetry-lowering effects in disordered graphite [19] and in carbon fibres [15]. The relative intensity of the broad peak around 1350 cm^{-1} to the strong E_{2g} mode at 1582 cm^{-1} is sensitive to the lowering of the crystal symmetry of 3D graphite [19,20], and the amount of disorder in carbon fibres [15] and in graphite nano-clusters [21] can be controlled by the heat treatment temperature T_{HT} or by ion implantation [22]. The non-zero-centre phonon mode at 1365 cm^{-1} has a flat energy dispersion around the M point in the Brillouin zone of graphite, which implies a high phonon DOS [23]. Moreover, in small aromatic molecules, though the frequency and the normal mode displacements are modified by the finite size effect, these M point phonon modes become Raman active [24] and have a large intensity [21,25]. Thus some symmetry-lowering effects such as the effect of the end caps, the bending of the CNT, and other possible defects are relevant to the Raman intensity for this M-point mode, though the presence of disordered carbon phases could also contribute to this mode.

When we calculate the Raman intensity of a (10, 10) CNT for a finite length $20\hat{T}$ where \hat{T} is the unit vector along the tube axis, we get weak peaks with A_{1g} symmetry in the intermediate frequency region for in-phase vibrations that are parallel to the tube axis. In the infinite straight tube, this vibration is silent because of the absence of polarisation along the z axis. However, in the finite CNT, polarisation effects appear at the ends of the CNT, which is why we get scattering intensity from the A_{1g} modes in the intermediate frequency region in the case of tubes with finite length with different numbers of nodes. The reason why we get Raman scattering intensity at several frequencies is relevant to the standing waves arising in tubes of finite length. Because of the lack of periodic symmetry, all overtone modes become Raman active. It is noted that there is a special edge mode at 1217 cm^{-1} for which the A_{1g} breathing mode is localised at an open end of the CNT. These modes are possible origins for Raman peaks in the intermediate frequency region.

3.2 Sample orientation dependence

Next we show the Raman intensity of the (10, 10) armchair CNT as a function of sample orientation (see Fig. 3). Here we rotate the CNT axis from the z axis by fixing the polarisation vectors to lie along the z and x axes, respectively for the V and H polarisations. In this geometry, three rotations of the CNT axis are possible for the VV and the VH configurations, and these three rotations are denoted by θ_i ($i = 1, 2, 3$). Here θ_1 and θ_2 are the angles of the CNT axis from the z axis to the x and y axes, respectively, while θ_3 is the angle of the CNT axis around the z axis from the x to the y axis. Since we put the horizontal

polarisation vector along the x axis, θ_1 and θ_2 are different from each other for the VH configuration. Even for the VV configuration, the rotations by θ_1 and θ_2 are not equivalent to each other in the case of the (10, 10) armchair, since the (10, 10) armchair CNT has a ten-fold symmetry axis (C_{10}) which is not compatible with the Cartesian axes. Here we define the x, y, z axes so that we put a carbon atom along the x axis when $\theta_3 = 0^\circ$. In Fig. 3, we show the relative Raman intensities for the (10, 10) armchair CNT for the VV and VH configurations as a function of θ_i ($i=1, 2, 3$).

When we look at the Raman intensity as a function of θ_1 , the A_{1g} mode at 1587 cm^{-1} has a maximum at $\theta_1 = 0$ for the VV configuration, while the E_{1g} mode at 1585 cm^{-1} has a maximum at $\theta_1 = 45^\circ$. Thus, we should be able to distinguish these two close-lying modes in the higher frequency region from each other experimentally if we have an axially aligned CNT sample. As for the other Raman-active modes, we can also distinguish them by their frequencies and polarisations. Even the modes belonging to the same irreducible representation do not always have the same basis functions, since we have two inequivalent atoms A and B in the hexagonal lattice. For example, the displacements for the A_{1g} mode at 165 cm^{-1} has a different functional form from those for the A_{1g} mode at 1587 cm^{-1} .

From Fig. 3 it is seen that the angular dependences of almost all the Raman intensities on θ_1 and θ_2 are similar to each other for the VV configuration, except for the E_{1g} mode at 1585 cm^{-1} . The difference of the E_{1g} modes between θ_1 and θ_2 at 1585 cm^{-1} is due to the form of the basis function. There is also a symmetry reason why we can see only A modes and E modes in the VV (θ_3) and the VH (θ_2 and θ_3) configurations, respectively. On the other hand, we can see that there are some very weak intensities in the figure, since the x, y, z coordinate is incompatible with the ten-fold symmetry axis of each CNT. Even if we get an aligned sample along the z axis, the xy direction of the constituent CNTs should be random, since the 10-fold symmetry of the (10, 10) CNT does not satisfy the symmetry of the triangular CNT lattice. Thus an averaged angular dependence for θ_1 and θ_2 is expected for a general aligned sample.

4 Resonant Raman Spectra of CNTs

Quantum effects are observed in the Raman spectra of SWCNTs through the resonant Raman enhancement process, which is seen experimentally by measuring the Raman spectra at a number of laser excitation energies. Resonant enhancement in the Raman scattering intensity from CNTs occurs when the laser excitation energy corresponds to an electronic transition between the sharp features (i.e., $(E - E_i)^{-1/2}$ type singularities at energy E_i) in the 1D electronic DOS of the valence and conduction bands of the carbon CNT.

Since the separation energies between these sharp features in the 1D DOS are strongly dependent on the CNT diameter, a change in the laser excitation energy may bring into optical resonance a CNT with a different diameter. However,

CNTs with different diameters have different vibrational frequencies for their A_{1g} radial breathing mode in accordance with Eq.(1). By comparing the experimental Raman spectra taken for different laser excitation energies, we see large differences in the vibrational frequencies of the strong A_{1g} radial breathing mode, consistent with a resonant Raman effect involving CNTs of different diameters. In the range of laser excitations energies between 1.7 - 2.2 eV, a dramatic change is observed in the characteristic features of the Raman spectra near 1580 cm^{-1} , and this effect is identified with the resonant Raman enhancement of metallic CNTs. Since metallic CNTs have a peak at the energy three times as far from E_F as semiconducting CNT in the 1D electronic DOS, the resonant Raman effect is much more selective for metallic tubes relative to their semiconducting counterparts [8]. These quantum effects in the resonant Raman spectra thus lend strong credibility to the 1D aspects of the electronic and phonon structure of SWCNTs, and provide clear confirmation for the theoretical predictions about the singularities in the 1D electronic DOS. Good agreement is found between the resonant Raman studies and experimental determinations of the 1D DOS as studied by scanning tunnelling microscope/scanning tunnelling spectroscopy (STM/STS) [26-28].

By using different catalysts and growth temperatures for the synthesis of ropes of SWCNTs, it is possible to obtain a different diameter distribution for SWCNT samples. At present, it is possible to vary the peak in the diameter distribution between 0.9 and 2.0 nm [7,27,29]. By carrying out Raman experiments on CNT samples with different diameter distributions, changes in the characteristics of the Raman spectra can be investigated.

Raman spectra have also been reported on ropes of SWCNTs doped with the alkali metals K and Rb and with the halogen Br_2 [30]. It is found that the doping of CNTs with alkali metals and halogens yield Raman spectra that show spectral shifts of the modes near 1580 cm^{-1} associated with charge transfer. Upshifts in the mode frequencies are observed and are associated with the donation of electrons from the CNTs to the halogens in the case of acceptors, and downshifts are observed for electron charge transfer to the CNT from the alkali metal donors. These frequency shifts of the CNT Raman-active modes can in principle be used to characterise the CNT-based intercalation compound for the amount of intercalate uptake that has occurred on the CNT wall.

5 Summary

In summary, we have investigated the Raman intensity of armchair, zigzag and chiral CNTs, as a function of their polarisation geometry and sample orientation. We found that there is no significant dependence on chiral angle of the intensity but diameter dependence for the lower frequency Raman modes below 500 cm^{-1} for CNTs. The sample orientation dependence of the Raman intensity shows that not only the symmetry but also the direction of the displacements give rise to their own angular dependence, which can be used for distinguishing between the symmetry assignments for the higher frequency

Raman modes. Such a symmetry analysis will also be useful for identifying the chirality of CNTs. The spectral features in the intermediate frequency range may come from the finite length of CNTs. The resonant Raman intensity may reflect differences in the DOS between metallic and semiconducting CNTs.

Acknowledgements

The authors (RS, GD and MSD) thank the International Joint Research Program of the New Energy and Industrial Technology Organization (NEDO), Japan for their support. Part of the work by RS is supported by a Grant-in-Aid for Scientific Research (No. 09243211) from the Ministry of Education and Science of Japan. The MIT work was partly supported by the NSF (DMR 95-10093).

References

1. Dresselhaus, M. S., Dresselhaus, G. and Eklund, P. C., *Science of Fullerenes and Carbon Nanotubes*, Academic Press, New York, NY, 1996.
2. Saito, R., Dresselhaus, M. S. and Dresselhaus, G., *Physical Properties of Carbon Nanotubes*, Imperial College Press, London, 1998.
3. Guo, T., Jin, C.-M. and Smalley, R. E., *Chem. Phys. Lett.*, 1995, **243**, 49.
4. Thess, A., Lee, R., Nikolaev, P., Dai, H., Petit, P., Robert, J., Xu, C., Lee, Y. H., Kim, S. G., Rinzler, A. G., Colbert, D. T., Scuseria, G. E., Tománek, D., Fischer, J. E. and Smalley, R. E., *Science*, 1996, **273**, 483.
5. Rao, A. M., Richter, E., Bandow, S., Chase, B., Eklund, P. C., Williams, K. W., Menon, M., Subbaswamy, K. R., Thess, A., Smalley, R. E., Dresselhaus, G. and Dresselhaus, M. S., *Science*, 1997, **275**, 187.
6. Kataura, H., Kimura, A., Maniwa, Y., Suzuki, S., Shiromaru, H., Wakabayashi, T., Iijima, S. and Achiba, Y., *Jpn. J. Appl. Phys.*, 1998, **37**, L616.
7. Kasuya, A., Sasaki, Y., Saito, Y., Tohji, K. and Nishina, Y., *Phys. Rev. Lett.*, 1997, **78**, 4434.
8. Pimenta, M. A., Marucci, A., Brown, S. D. M., Matthews, M. J., Rao, A. M., Eklund, P. C., Smalley, R. E., Dresselhaus, G. and Dresselhaus, M. S., *J. Mater. Res.*, 1998, **13**, 2396.
9. Journet, C., Maser, W. K., Bernier, P., Loiseau, A., Lamy de la Chapelle, M., Lefrant, S., Deniard, P., Lee, R. and Fischer, J. E., *Nature*, 1997, **388**, 756.
10. Yu, J., Kalia, K. and Vashishta, P., *Europhys. Lett.*, 1995, **32**, 43.
11. Jishi, R. A., Inomata, D., Nakao, K., Dresselhaus, M. S., and Dresselhaus, G., *J. Phys. Soc. Jpn.*, 1994, **63**, 2252.
12. Saito, R., Takeya, T., Kimura, T., Dresselhaus, G. and Dresselhaus, M. S., *Phys. Rev. B*, 1998, **57**, 4145.
13. Madelung, O., *Solid State Theory*, Springer-Verlag, Berlin, 1978.
14. Jishi, R. A., Venkataraman, L., Dresselhaus, M. S. and Dresselhaus, G., *Chem. Phys. Lett.*, 1993, **209**, 77.
15. Dresselhaus, M. S., Dresselhaus, G., Sugihara, K., Spain, I. L. and

- Goldberg, H. A., *Graphite Fibers and Filaments*, Springer Series in Materials Science, Vol. 5, Springer-Verlag, Berlin, 1988.
16. Treacy, M. M. J., Ebbesen, T. W. and Gibson, J. M., *Nature*, 1996, **381**, 678.
 17. Yakobson, B. I. and Smalley, R. E., *American Scientist*, 1997, **85**, 324.
 18. Guha, S., Menéndez, J., Page, J. B. and Adams, G. B., *Phys. Rev. B*, 1996, **53**, 13106.
 19. Tuinstra, F. and Koenig, J. L., *J. Chem. Phys.*, 1970, **53**, 1126.
 20. Lespade, P., Al-Jishi, R. and Dresselhaus, M. S., *Carbon*, 1982, **20**, 427.
 21. Matthews, M. J., Bi, X. X., Dresselhaus, M. S., Endo, M. and Takahashi, T., *Appl. Phys. Lett.*, 1996, **68**, 1078.
 22. Dresselhaus, M. S. and Kalish, R., *Ion Implantation in Diamond, Graphite and Related Materials*, Springer Series in Materials Science, Vol. 22, Springer-Verlag, Berlin, 1992.
 23. Al-Jishi, R. and Dresselhaus, G., *Phys. Rev. B*, 1982, **26**, 4514.
 24. Yoshizawa, K., Okahara, K., Sato, T., Tanaka, K. and Yamabe, T., *Carbon*, 1994, **32**, 1517.
 25. Krichene, S., Buisson, J. P. and Lefrant, S., *Synth. Met.*, 1986, **17**, 589.
 26. Wildöer, J. W. G., Venema, L. C., Rinzler, A. G., Smalley, R. E. and Dekker, C., *Nature*, 1998, **391**, 59.
 27. Odom, T. W., Huang, J. L., Kim, P. and Lieber, C. M., *Nature*, 1998, **391**, 62.
 28. Dresselhaus, M. S., *Nature*, 1998, **391**, 19.
 29. Bandow, S., Asaka, S., Saito, Y., Rao, A. M., Grigorian, L., Richter, E. and Eklund, P. C., *Phys. Rev. Lett.*, 1998, **80**, 3779.
 30. Rao, A. M., Eklund, P. C., Bandow, S., Thess, A. and Smalley, R. E., *Nature*, 1997, **388**, 257.

CHAPTER 7

Behaviour of Single-Walled Carbon Nanotubes in Magnetic Fields

HIROSHI AJIKI¹ and TSUNEYA ANDO²¹*Department of Physical Science, Graduate School of Engineering Science, Osaka University 1-3 Machikaneyama Toyonaka 560-8531, Japan*²*Institute for Solid State Physics, University of Tokyo 7-22-1 Roppongi, Minato-ku, Tokyo 106-8666, Japan*

A brief review is given on electronic properties of carbon nanotubes, in particular those in magnetic fields, mainly from a theoretical point of view. The topics include a giant Aharonov-Bohm effect on the band gap and optical absorption spectra, a magnetic-field induced lattice distortion and a magnetisation and susceptibility of ensembles, calculated based on a $\mathbf{k}\cdot\mathbf{p}$ scheme.

1 Introduction

A carbon nanotube (CNT) can be either a metal or semiconductor depending on their diameters and helical arrangement when we ignore effect of curvature, which causes hybridisation of π - and σ -orbital for a CNT with extremely small diameter [1]. This result was first predicted by means of a tight-binding model [2] and can be well reproduced in a $\mathbf{k}\cdot\mathbf{p}$ method [3]. In this chapter we give electronic properties of a single-walled CNT (SWCNT) in magnetic fields with use of the $\mathbf{k}\cdot\mathbf{p}$ method.

The $\mathbf{k}\cdot\mathbf{p}$ method provides analytic descriptions on electronic states of CNT. It shows, for example, that the band gap of a semiconducting CNT is inversely proportional to the diameter because of a linear dispersion of the bands. It is suitable also for descriptions of the electronic motion in external perturbations such as electric and magnetic fields.

In Sec. 2 the effective mass equation is introduced and the band structure is discussed with a special emphasis on an Aharonov-Bohm effect. Optical absorption spectra are discussed in Sec. 3. A lattice instability, in particular induced by a magnetic field perpendicular to the tube axis, is discussed in Sec. 4 and magnetic properties of ensembles of CNTs are discussed in Sec. 5.

2 Aharonov-Bohm Effect

A CNT is specified by a chiral vector $\mathbf{L} = n_a \mathbf{a} + n_b \mathbf{b}$ with integer n_a and n_b and basis vectors \mathbf{a} and \mathbf{b} ($|\mathbf{a}| = |\mathbf{b}| = a = 2.46 \text{ \AA}$) as is shown in Fig. 1. In the (x', y') system of coordinates fixed onto a graphite sheet, we have $\mathbf{a} = (a, 0)$ and $\mathbf{b} = (-a/2, \sqrt{3}a/2)$. We introduce another coordinate system on CNTs, where the x and y directions are along the circumference and the axis, respectively.

A graphite sheet is a zero-gap semiconductor in the sense that the conduction and valence bands consisting of π -states touch at K and K' points of the Brillouin zone, whose wave vectors are given by $\mathbf{K} = (2\pi/a)(1/3, 1/\sqrt{3})$ and $\mathbf{K}' = (2\pi/a)(2/3, 0)$. The unit cell has an area $\sqrt{3}a^2/2$ and contains two carbon atoms (denoted as A and B) as shown in Fig. 1.

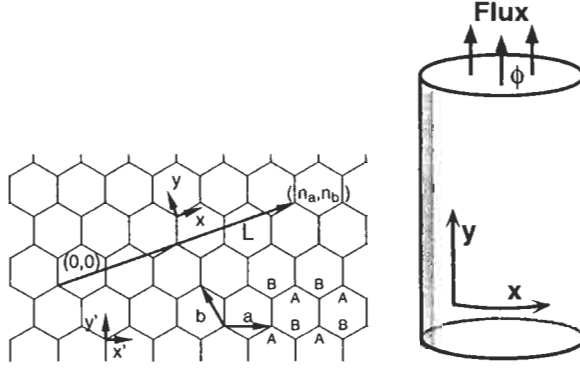


Fig. 1. A single layer of graphite and a CNT in a magnetic flux passing through its cross section.

Electronic states (with an appropriate choice of phases of the Bloch functions) near K and K' points of two-dimensional (2D) graphite are described by the $\mathbf{k} \cdot \mathbf{p}$ equation:

$$\begin{aligned} \gamma(\sigma_x k_x + \sigma_y k_y) F_K(\mathbf{r}) &= \varepsilon(\mathbf{k}) F_K(\mathbf{r}), \\ \gamma(\sigma_x k_x - \sigma_y k_y) F_{K'}(\mathbf{r}) &= \varepsilon(\mathbf{k}) F_{K'}(\mathbf{r}), \end{aligned} \quad (1)$$

where γ is the band parameter, $\mathbf{k} = (k_x, k_y)$ is a wave-vector operator, and σ_x , σ_y and σ_z are the Pauli spin matrices. In the above equations, the envelope functions are written as

$$F_K(\mathbf{r}) = \begin{pmatrix} F_K^A(\mathbf{r}) \\ F_K^B(\mathbf{r}) \end{pmatrix}, \quad F_{K'}(\mathbf{r}) = \begin{pmatrix} F_{K'}^A(\mathbf{r}) \\ F_{K'}^B(\mathbf{r}) \end{pmatrix}. \quad (2)$$

Eq.(1) has the form of Weyl's equation for massless neutrinos.

Electronic states of CNTs with sufficiently large diameter can be obtained by imposing the generalised periodic boundary condition in the circumference direction, $\Psi(\mathbf{r} + \mathbf{L}) = \Psi(\mathbf{r})\exp(2\pi i\varphi)$, with $\varphi = \phi/\phi_0$, where ϕ is an Aharonov-Bohm (AB) magnetic flux passing through the cross section of CNT and $\phi_0 = hc/e$ is the magnetic flux quantum. The Bloch functions at the K and K' points change their phase by $\exp(2\pi i\nu/3)$ and $\exp(-2\pi i\nu/3)$, respectively, where ν is an integer defined by $n_a + n_b = 3M + \nu$ with integer M and can take 0 and ± 1 . This phase change should be cancelled by that of the envelope functions and the boundary condition for the envelope function associated with the K point is given by

$$F_K(\mathbf{r} + \mathbf{L}) = F_K(\mathbf{r}) \exp\left[2\pi i\left(\varphi - \frac{\nu}{3}\right)\right], \quad (3)$$

At the K' point, ν should be replaced by $-\nu$ in this equation.

Energy levels in CNT are obtained by putting $k_x = \kappa_{\nu\varphi}(n)$ and $k_y = k$ in the above $\mathbf{k}\cdot\mathbf{p}$ equation as [3]

$$\varepsilon_{\nu\varphi}^{(\pm)}(n, k) = \pm\gamma\sqrt{\kappa_{\nu\varphi}(n)^2 + k^2}, \quad \kappa_{\nu\varphi}(n) = \frac{2\pi}{L}\left(n + \varphi - \frac{\nu}{3}\right), \quad (4)$$

where n is an integer and the upper (+) and lower (−) signs represent the conduction and valence bands, respectively. In the absence of a magnetic flux, $\varphi = 0$, CNT becomes metallic for $\nu = 0$ and semiconducting with gap $E_g = 4\pi\gamma/3L$ for $\nu = \pm 1$. Figure 2 compares this gap to that obtained in a tight-binding model [4].

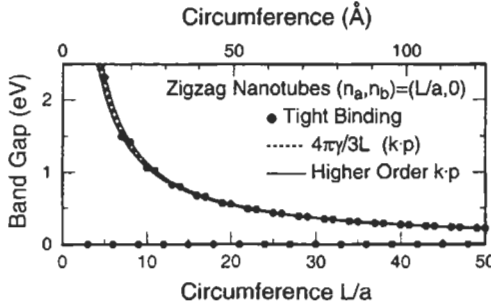


Fig. 2. Energy gap of monolayer CNTs specified by $(n_a, n_b) = (m, 0)$. The dots are calculated in a tight-binding model and the dotted line represents $4\pi\gamma/3L$ given in the $\mathbf{k}\cdot\mathbf{p}$ scheme. The solid lines are the results of a higher order $\mathbf{k}\cdot\mathbf{p}$ scheme. Use has been made of $\gamma = 6.46$ eV Å.

In the presence of a magnetic flux, the boundary condition is changed by the Aharonov-Bohm effect and the band gap exhibits an oscillation between 0 and $2\pi\gamma/L$ with period ϕ_0 as is shown in Fig. 3.

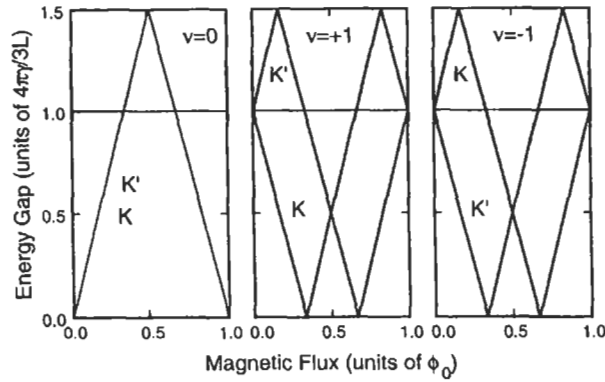


Fig. 3. Energy gap versus magnetic flux passing through the tube cross section for metallic ($v=0$) and semiconducting ($v=\pm 1$) CNT.

In the presence of a magnetic field H perpendicular to the tube axis, the effective field for electrons in a CNT is given by $H(x) = H\cos(2\pi x/L)$ which is periodic in the circumference direction. The parameter characterising its magnitude is given by $(L/2\pi l)^2$, where $l = \sqrt{\hbar/eH}$ is the magnetic length or the radius of the smallest cyclotron orbit. In the case $(L/2\pi l)^2 \ll 1$, the field can be regarded as a small perturbation, while in the case $(L/2\pi l)^2 \gg 1$, Landau levels are formed on the cylinder surface.

Table 1. Typical magnetic fields (T) for CNTs with different circumferences. At the field corresponding to $\phi = \phi_0$ the total magnetic flux passing through the cross section is equal to the flux quantum and at $(L/2\pi l)^2 = 1$ the magnetic length is equal to the diameter of CNT.

Circumference (Å)		50	100	200	400	800
Diameter (Å)		16	32	64	127	255
Gap (meV)		541	270	135	68	34
Magnetic field (T)	$\phi = \phi_0$	2080	520	130	32	8
	$(L/2\pi l)^2 = 1$	1040	260	65	16	4

An interesting feature of Weyl's equation lies in the fact that Landau levels are formed at energy $\epsilon = 0$. This has long been known as the origin of a large diamagnetism of graphite. Figure 4 gives some examples of energy bands of a metallic and semiconducting CNT in perpendicular magnetic fields, which clearly shows the formation of flat Landau levels at the Fermi level in high fields. Note that there is no difference in the spectra between metallic ($v = 0$) and semiconducting ($v = \pm 1$) CNTs for $(L/2\pi l)^2 \gg 1$. This comes from the fact that the wave function is localised in the circumference direction and the boundary condition becomes irrelevant. Thus in high field the energy bands become

independent of an AB flux also. Table 1 gives typical magnetic fields as a function of the circumference and diameter of CNT.

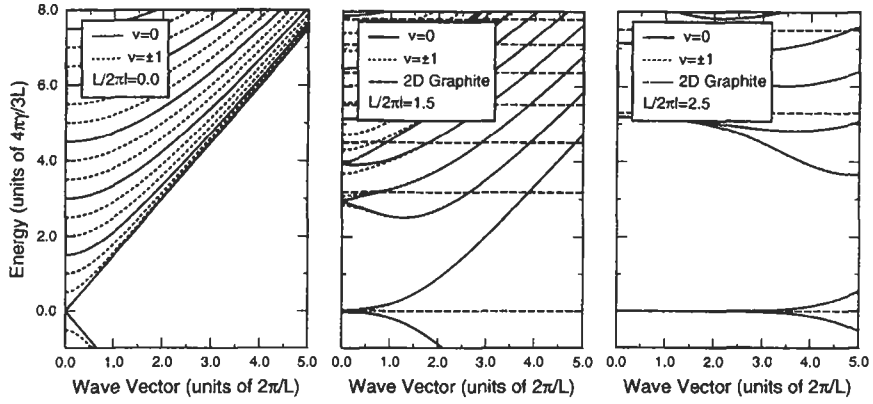


Fig. 4. Some examples of calculated energy bands of a metallic CNT in magnetic fields perpendicular to the axis.

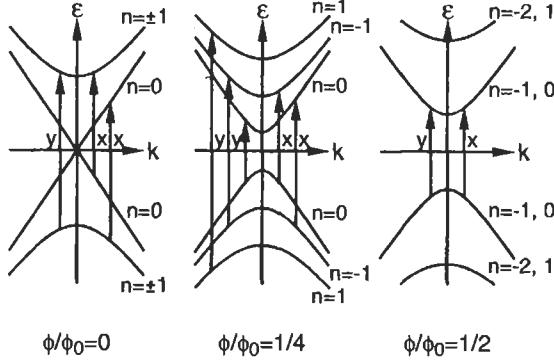


Fig. 5. Energy bands of a metallic CNT in the presence of a magnetic flux and allowed optical transitions for the x and y polarisations.

3 Optical Absorption

In the optical absorption, two different polarisations of light should be considered: the electric field is along (parallel or y polarisation) and perpendicular (perpendicular or x) to the axis. Figure 5 shows the energy band of a metallic CNT for flux $\phi/\phi_0 = 0, 1/4$ and $1/2$ and the process of optical transitions for the parallel and perpendicular polarisations. Some examples of calculated absorption

spectra of semiconducting CNTs in a magnetic flux are given in Fig. 6 [5]. For parallel polarisation, the spectrum changes dramatically as a function of the magnetic flux due to the AB effect. In the case of the perpendicular polarisation, on the other hand, the incident electric field induces a large polarisation of CNT, which suppresses the absorption almost completely.

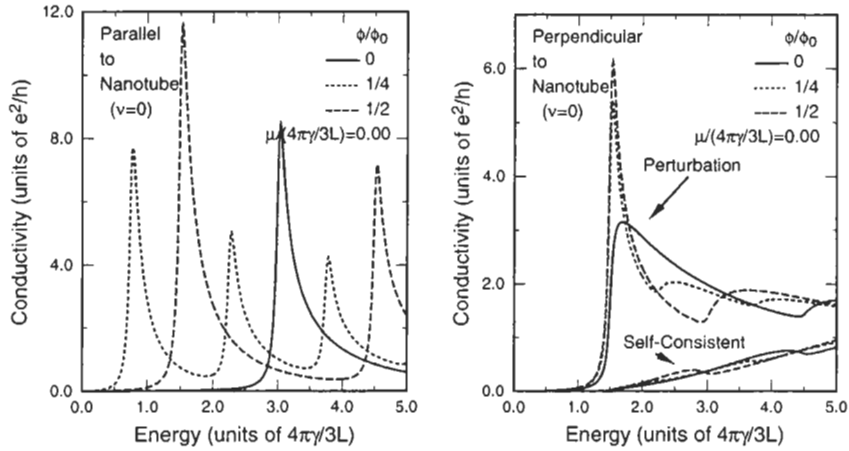


Fig. 6. Calculated optical absorption spectra of a metallic CNT in a magnetic flux. In the case that the electric field is parallel to the axis (left), the absorption exhibits a distinct AB effect. In the case of the perpendicular polarisation (right) the depolarisation effect suppresses the absorption almost completely.

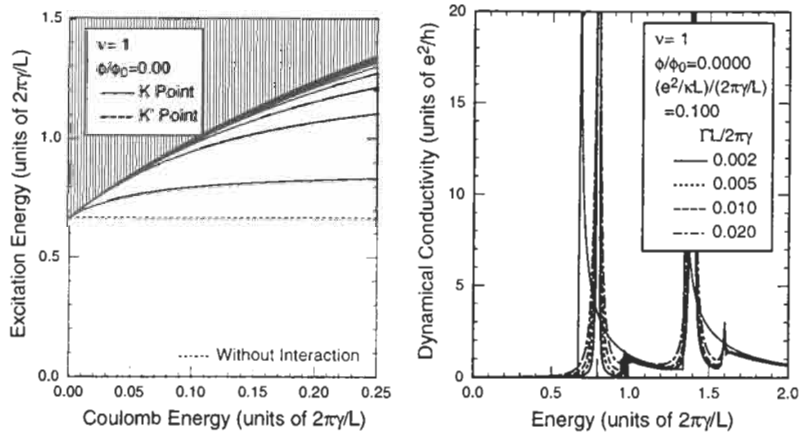


Fig. 7. Calculated optical excitation spectra (left) and exciton absorption spectra (right) of a semiconducting CNT for a parallel polarisation.

It is well known that the exciton binding energy becomes infinite in the limit of an ideal one-dimensional (1D) electron-hole system [6,7]. This is the origin of the large enhancement of the oscillator strength of the 1D exciton. Figure 7 gives some examples of optical excitation and absorption calculated in a conventional screened Hartree-Fock approximation used in bulk systems. It shows that the band gap is strongly enhanced by the Coulomb interaction and the exciton bound states lie at energies slightly higher than the band gap in the absence of the Coulomb interaction and that considerable optical intensity is transferred to the lowest exciton bound states.

4 Lattice Distortion

It is known that a metallic 1D system is unstable against lattice distortion and turns into an insulator. In CNTs instabilities associated two kinds of distortions are possible, in-plane and out-of-plane distortions as shown in Fig. 8. The in-plane or Kekulé distortion has the form that the hexagon network has alternating short and long bonds ($-u_1$ and $2u_1$, respectively) like in the classical benzene molecule [8,9,10]. Due to the distortion the first Brillouin zone reduces to one-third of the original one and both K and K' points are folded onto the Γ point in a new Brillouin zone. For an out-of-plane distortion the sites A and B are displaced up and down ($\pm u_2$) with respect to the cylindrical surface [11]. Because of a finite curvature of a CNT the mirror symmetry about its surface are broken and thus the energy of sites A and B shift in the opposite direction.

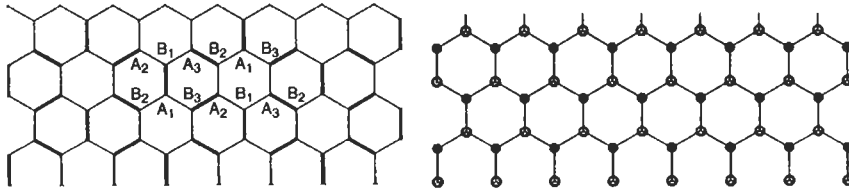


Fig. 8. Lattice distortions in a graphite sheet. For an in-plane distortion (left), the bond denoted by a thin line becomes shorter and that denoted by a thick line becomes longer, leading to a unit cell three times as large as the original. For an out-of-plane distortion (right), an atom denoted by a black dot is shifted down and that denoted by a white circle moves up.

In the presence of lattice distortions, the $\mathbf{k} \cdot \mathbf{p}$ equation is given by the 4×4 matrix equation given by

$$\begin{pmatrix} \gamma (\sigma_x k_x + \sigma_y k_y) + \sigma_z \Delta_2 & -i\sigma_y \Delta_1 \\ i\sigma_y \Delta_1 & \gamma (\sigma_x k_x - \sigma_y k_y) + \sigma_z \Delta_2 \end{pmatrix} \begin{pmatrix} F_K(\mathbf{r}) \\ F_{K'}(\mathbf{r}) \end{pmatrix}$$

$$= \varepsilon \begin{pmatrix} FK(\mathbf{r}) \\ FK'(\mathbf{r}) \end{pmatrix}, \quad (5)$$

which is equivalent to the relativistic Dirac equation [12]. The energy bands are given by

$$\varepsilon_{\phi}^{(\pm)}(n, k, \Delta_1, \Delta_2) = \pm \sqrt{\gamma^2 \kappa_{\phi}(n)^2 + \gamma^2 k^2 + \Delta_1^2 + \Delta_2^2}. \quad (6)$$

This shows that the gap given by $E_g = 2\sqrt{\Delta_1^2 + \Delta_2^2}$ opens up in the absence of a magnetic flux.

The gap parameters Δ_1 and Δ_2 are determined by the minimisation of the total energy given by

$$E = 4 \sum_{n=-\infty}^{\infty} \sum_k \varepsilon_{\phi}^{(-)} g_0(|\varepsilon_{\phi}^{(-)}|) + N \frac{K_1 \Delta_1^2}{2f_1^2} + N \frac{K_2 \Delta_2^2}{2f_2^2}, \quad (7)$$

where $\varepsilon_{\phi}^{(-)}$ is the valence-band energy, K_1 and K_2 are the force constants for the in- and out-of-plane distortions, respectively, and N is the total number of carbon atoms. Further, f_1 and f_2 are defined by $\Delta_1 = f_1 u_1$ and $\Delta_2 = f_2 u_2$. We have introduced a cutoff function $g_0(\varepsilon)$ in order to extract the contribution from the states in the vicinity of the top of the valence band. The results are independent of the choice of cutoff functions as long as the function decays smoothly with energy and the cutoff energy is sufficiently large.

The gap parameters are determined under the condition that the total energy becomes minimum, and it is found that two kinds of distortions cannot coexist and that a distortion having a larger effective coupling constant $\lambda = \sqrt{3} a f^2 / \pi K \gamma$ occurs, where $(K, f) = (K_i, f_i)$ with $i = 1$ or 2 . The gap parameter is obtained as

$$E_g(\phi) = E_g \sqrt{1 - \left(\frac{\phi}{\phi_0}\right)^2}, \quad \phi_c = \frac{\phi_c}{\phi_0} = \frac{L E_g}{4 \pi \gamma},$$

$$E_g = \frac{2 \pi \gamma}{L} \exp\left(-\frac{L}{a \lambda} - 1 - C\right), \quad C \approx 0.1445972. \quad (8)$$

The gap parameter or lattice distortion vanishes in the critical AB flux ϕ_c which opens the gap as large as that due to the distortion. For $\phi = 0$, the gap decreases exponentially as a function of the circumference L/a . Table 2 gives some examples for an in-plane Kekulé distortion.

For out-of-plane distortion the coefficient $f_2 = \Delta_2/u_2$ is expected to be proportional to a/L , since f_2 becomes nonzero for the finite curvature. Thus, the coupling constant is proportional to $(a/L)^2$ and the gap decreases very rapidly with the diameter as $\exp[-(L/a)^3]$. It is concluded that metallic CNTs are quite

stable against lattice distortions and hold metallic properties even at low temperatures except in extremely narrow CNTs.

The situation changes drastically in the presence of a high magnetic field perpendicular to the axis. As has been discussed in Sec. 2, Landau levels without dispersion appear at the Fermi level considerably, leading to a magnetic-field induced distortion [13,14].

Table 2. Calculated energy gap due to an in-plane Kekulé distortion for CNTs having chiral vector $L/a = (m, 2m)$. The critical magnetic flux ϕ_c and the corresponding magnetic field are also shown. The coupling constant is $\lambda \approx 1.62$.

m		5	10	20
Diameter	(Å)	6.78×10^0	1.36×10^1	2.71×10^1
Circumference	(Å)	2.13×10^1	4.26×10^1	8.52×10^1
E_g	(meV)	2.38×10^0	5.68×10^{-3}	6.46×10^{-8}
u	(Å)	6.29×10^{-5}	1.50×10^{-7}	1.71×10^{-12}
ϕ_c		7.58×10^{-4}	3.62×10^{-6}	8.23×10^{-11}
H_c	(T)	8.67×10^0	1.04×10^{-2}	5.89×10^{-8}

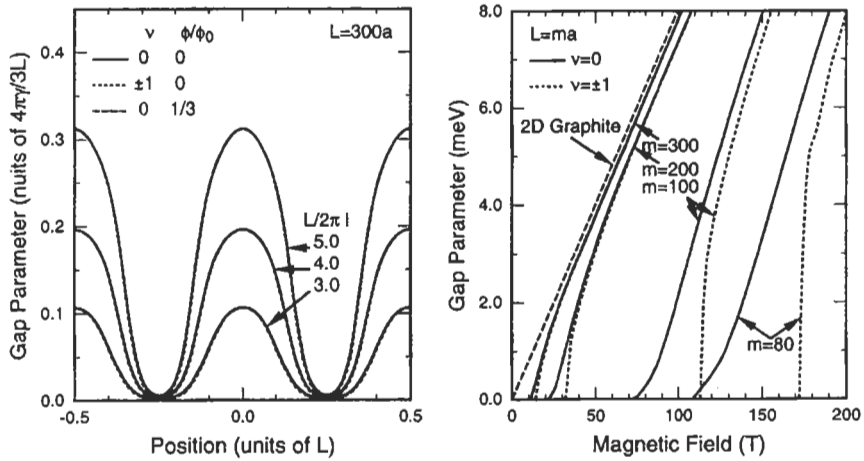


Fig. 9. An example of calculated in-plane lattice distortions induced by a high magnetic field (left) and the dependence of the maximum gap due to in-plane lattice distortions on a magnetic field (right).

The electron wave function becomes localised in the top and bottom part of the cylindrical surface where the effective magnetic field perpendicular to the tube surface is the largest. Thus the boundary condition along the circumference direction becomes less important in high magnetic fields as has been discussed in Sec. 2. Consequently the distinction between metallic and semiconducting

CNTs also. Further, the spatial variation of the distortion should also be considered.

The generalised $\mathbf{k} \cdot \mathbf{p}$ equation is the same as Eq.(5) except that the gap parameters are dependent on the position and should satisfy the boundary conditions:

$$\Delta_1(\mathbf{r} + \mathbf{L}) = \Delta_1(\mathbf{r}) \exp\left(i \frac{2\pi v}{3}\right), \quad \Delta_2(\mathbf{r} + \mathbf{L}) = \Delta_2(\mathbf{r}). \quad (9)$$

The extra phase factor appearing in the boundary condition for $\Delta_1(\mathbf{r})$ guarantees the fact that the equations remain the same under translation $\mathbf{r} \rightarrow \mathbf{r} + \mathbf{L}$ even for $v = \pm 1$. Some examples of explicit numerical results for the in-plane distortion are given in Fig. 9. The figures clearly show that the lattice distortion is induced by a magnetic field in particular for CNTs with large diameter for both metallic and semiconducting CNTs and that the maximum gap approaches that of a graphite sheet.

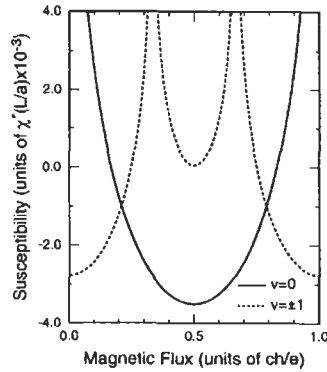
5 Magnetic Properties

For a magnetic field perpendicular to the tube axis, CNTs usually exhibit diamagnetism similar to that of graphite [16,17]. For a magnetic field parallel to the axis, on the other hand, the magnetic response of CNTs becomes completely different. Figure 10 shows an example of calculated differential susceptibility as a function of a magnetic flux passing through the cross section. The most prominent feature appears for a metallic CNT as the large paramagnetic susceptibility which diverges logarithmically. This is caused by a sudden opening up of a gap due to the AB effect.

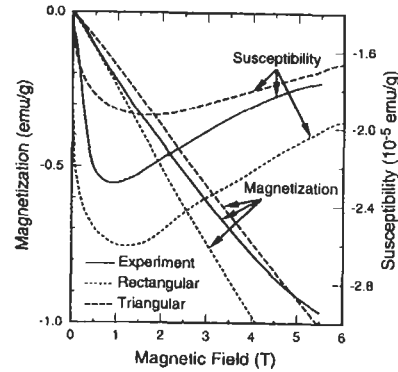
Realistic samples contain CNTs with different layer numbers, circumferences, and orientations. If effects of small interlayer interactions are neglected, the magnetic properties of a multi-walled CNT (MWCNT) are given by those of an ensemble of single-walled CNTs (SWCNTs). The distribution function for the circumference, $\rho(L)$, is not known and therefore we shall consider following two different kinds. The first is the rectangular distribution, $\rho(L) = 1/(L_{mx} - L_{mn})$ for $L_{mn} < L < L_{mx}$, which roughly corresponds to the situation that CNTs with different circumferences are distributed equally and the average layer number of MWCNTs is independent of the circumference. In realistic samples, however, the layer number increases with the outer circumference length and the distribution becomes asymmetric. The most extreme case can be realised if we assume that the inner-most shell of a CNT is L_{mn} . In this case the distribution is given by a triangular form, $\rho(L) = 2(L_{mx} - L)/(L_{mx} - L_{mn})^2$ for $L_{mn} < L < L_{mx}$.

Figure 11 shows magnetisation and differential susceptibility calculated for the rectangular and triangular distribution with $L_{mn} = 22 \text{ \AA}$ corresponding to the finest CNT so far observed and $L_{mx} = 942.5 \text{ \AA}$ corresponding to the thickest CNT. The experimental result of ref. 15 is also included. The calculation can

explain the experiments qualitatively, but more detailed information on the distribution of CNTs is required for more quantitative comparison.



Left: **Fig. 10.** Differential susceptibilities of a CNT in the presence of a magnetic flux.



Right: **Fig. 11.** Calculated ensemble average of magnetic moment and differential susceptibility for CNTs with rectangular (dotted lines) and triangular (dashed lines) circumference distributions having $L_{mn}=22 \text{ \AA}$ and $L_{mx}=942.5 \text{ \AA}$. The solid lines denote experimental results [15].

The magnetic moment is negative (diamagnetic) and its absolute value increases as a function of the magnetic field. This overall dependence is governed by that of the magnetic moment for perpendicular magnetic field and the parallel contribution or the AB effect appears as a slight deviation. This deviation becomes clearer in the differential susceptibility. In fact, the differential susceptibility increases with the decrease of the magnetic field sharply in weak magnetic fields $(L/2\pi l)^2 \lesssim 0.2$. This is a result of the divergent paramagnetic susceptibility of metallic CNTs in the parallel field, i. e., the AB effect.

6 Summary and Recent Developments

Electronic properties of CNTs, in particular, electronic states, optical spectra, lattice instabilities, and magnetic properties, have been discussed theoretically based on a $\mathbf{k}\cdot\mathbf{p}$ scheme. The motion of electrons in CNTs is described by Weyl's equation for a massless neutrino, which turns into the Dirac equation for a massive electron in the presence of lattice distortions. This leads to interesting properties of CNTs in the presence of a magnetic field including various kinds of Aharonov-Bohm effects and field-induced lattice distortions.

The same $\mathbf{k}\cdot\mathbf{p}$ scheme has been extended to the study of transport properties of CNTs. The conductivity calculated in the Boltzmann transport theory has shown a large positive magnetoresistance [18]. This positive magnetoresistance has been confirmed by full quantum mechanical calculations in the case that the mean free path is much larger than the circumference length [19]. When the mean free path is short, the transport is reduced to that in a 2D graphite, which has also interesting characteristic features [20].

Effects of impurity scattering in CNTs have been studied in detail and a possibility of complete absence of back scattering has been pointed out and proved rigorously except for scatterers having a potential range smaller than the lattice constant [21, 22]. This absence of back scattering disappears in magnetic fields, leading to a huge positive magnetoresistance. The conductance of an SWCNT was observed quite recently [23, 24], but experiments show large charging effects presumably due to nonideal contacts. It is highly desirable to become able to measure transport of an SWCNT with ideal Ohmic contacts.

The $\mathbf{k}\cdot\mathbf{p}$ scheme has been used also for the study of transport across junctions connecting tubes with different diameters through a region sandwiched by a pentagon-heptagon pair [25]. In junctions systems, the conductance was predicted to exhibit a universal power-law dependence on the ratio of the circumference of two CNTs [26]. An intriguing dependence on the magnetic-field direction was predicted also [27]. These newer topics will be discussed elsewhere.

Acknowledgements

The authors would like to thank T. Seri, T. Nakanishi, H. Matsumura and H. Suzuura for discussion. The work is supported in part by Grant-in-Aid for Scientific Research from Ministry of Education, Science and Culture, Japan.

References

1. Blase, X., Benedict, L. X., Shirley, E. L. and Louie, S. G., *Phys. Rev. Lett.*, 1994, **72**, 1878.
2. Hamada, N., Sawada, S. and Oshiyama, A., *Phys. Rev. Lett.*, 1992, **68**, 1579.
3. Ajiki, H. and Ando, T., *J. Phys. Soc. Jpn.*, 1993, **62**, 1255.
4. Ajiki, H. and Ando, T., *J. Phys. Soc. Jpn.*, 1996, **65**, 505.
5. Ajiki, H. and Ando, T., *Physica B*, 1994, **201**, 349; *Jpn. J. Appl. Phys. Suppl.*, 1995, **34**, 107.
6. Loudon, R., *Am. J. Phys.*, 1959, **27**, 649.
7. Elliot, R. J. and Loudon, R., *J. Phys. Chem. Solids*, 1959, **8**, 382; 1960, **15**, 196.
8. Mintmire, J. W., Dunlap, B. I. and White, C. T., *Phys. Rev. Lett.*, 1992, **68**, 631.
9. Harigaya, K., *Phys. Rev. B*, 1992, **45**, 12071.
10. Harigaya, K. and Fujita, M., *Phys. Rev. B*, 1993, **68**, 16563.
11. Saito, R., Fujita, M., Dresselhaus, G. and Dresselhaus, M. S., *Phys. Rev. B*, 1992, **46**, 1804.
12. Viet, N. A., Ajiki, H. and Ando, T., *J. Phys. Soc. Jpn.*, 1994, **63**, 3036.

13. Ajiki, H. and Ando, T., *J. Phys. Soc. Jpn.*, 1995, **64**, 260.
14. Ajiki, H. and Ando, T., *J. Phys. Soc. Jpn.*, 1996, **65**, 2976.
15. Heremans, J., Olk, C. H. and Morelli, D. T., *Phys. Rev. B*, 1994, **49**, 15112.
16. Ajiki, H. and Ando, T., *J. Phys. Soc. Jpn.*, 1998, **62**, 2470 [Errata, *J. Phys. Soc. Jpn.*, 1994, **63**, 4267].
17. Lu, J. P., *Phys. Rev. Lett.*, 1995, **74**, 1123.
18. Seri, T. and Ando, T., *J. Phys. Soc. Jpn.*, 1997, **66**, 169.
19. Ando, T. and Seri, T., *J. Phys. Soc. Jpn.*, 1997, **66**, 3558.
20. Shon, N. H. and Ando, T., *J. Phys. Soc. Jpn.*, 1998, **67**, 2421.
22. Ando, T., Nakanishi, T. and Saito, R., *J. Phys. Soc. Jpn.*, 1998, **67**, 2857.
23. Tans, S. J., Devoret, M. H., Dai, H. -J., Thess, A., Smalley, R. E., Geerligs, L. J. and Dekker, C., *Nature*, 1997, **386**, 474.
24. Bockrath, M., Cobden, D. H., McEuen, P. L., Chopra, N. G., Zettl, A., Thess, A. and Smalley, R. E., *Science*, 1997, **275**, 1922.
25. Matsumura, H. and Ando, T., *J. Phys. Soc. Jpn.*, 1998, **67**, 3542.
26. Tamura, R. and Tsukada, M., *Solid State Commun.*, 1997, **101**, 601; *Phys. Rev. B*, 1997, **55**, 4991; *Z. Phys. D*, 1997, **40**, 432.
27. Nakanishi, T. and Ando, T., *J. Phys. Soc. Jpn.*, 1997, **66**, 2973; *Physica B*, 1998, **249-251**, 136.

CHAPTER 8

Electronic Properties of Carbon Nanotubes
Probed by Magnetic MeasurementsMAYUMI KOSAKA¹ and KATSUMI TANIGAKI²

¹*Fundamental Research Laboratories, NEC Corporation
34 Miyukigaoka, Tsukuba 305-8501, Japan*

²*Department of Material Science, Osaka City University
PREST, Japan Science and Technology Corporation
3-3-138 Sugimoto, Sumiyoshi-ku, Osaka 558-8585, Japan*

1 Introduction

Since the discovery of carbon nanotubes (CNTs) in 1991 [1], the band structures for CNTs have been calculated by a number of authors [2-7]. They have predicted that CNTs can be metallic, narrow- or broad band-gap semiconductors. After macroscopic quantities of CNTs were synthesized [8], it has become possible to explore their practical properties.

Multi-walled CNTs (MWCNTs) are produced by arc discharge between graphite electrodes but other carbonaceous materials are always formed simultaneously. The main by-product, nanoparticles, can be removed utilizing the difference in oxidation reaction rates between CNTs and nanoparticles [9]. Then, it was reported that CNTs can be aligned by dispersion in a polymer resin matrix [10]. However, the parameters of CNTs are uncontrollable, such as the diameter, length, chirality and so on, at present. Furthermore, although the CNTs are observed like cylinders by transmission electron microscopy (TEM), some reports have pointed out the possibility of non-cylindrical structures and the existence of defects [11-14].

Single-walled CNTs (SWCNTs) are produced by arc discharge with either Fe, Co or Ni catalyst [15-17]. Later, it was reported that two different bi-metallic catalysts, Fe-Ni and Co-Ni, showed a striking increase of SWCNTs contents compared to that using a single catalyst [18]. Furthermore, laser ablation of graphite targets doped with Co and Ni produces SWCNTs in yields of more than 70% [19]. In this process, the CNTs are nearly uniform in diameter and self-organised as crystalline ropes, which consist of 100 to 500 SWCNTs in a two-dimensional triangular lattice with a lattice constant of 17 Å. The ferromagnetic catalyst residues in the sample can be eliminated by vacuum-annealing at 1500°C [19], microfiltration with a heat treatment at 450°C or centrifugal separation [20].

Here, we review the electronic properties of MWCNT and SWCNT probed by magnetic measurements. MWCNTs are discussed with a classification of the following four categories: (1) crude CNTs, (2) purified CNTs, (3) aligned CNTs and (4) alkali-doped CNTs.

2 Basis of Magnetic Measurements

Since electron spin resonance (ESR) measurements are mainly focused as a probe of the electronic properties of CNTs in this report, the basis of magnetic measurements is briefly mentioned in this chapter.

ESR can detect unpaired electrons. Therefore, the measurement has been often used for the studies of radicals. It is also useful to study metallic or semiconducting materials since unpaired electrons play an important role in electric conduction. The information from ESR measurements is the spin susceptibility, the spin relaxation time and other electronic states of a sample. It has been well known that the spin susceptibility of the conduction electrons in metallic or semimetallic samples does not depend on temperature (so called Pauli susceptibility), while that of the localised electrons is dependent on temperature as described by Curie law.

The studies of the conduction electron ESR (CESR) sometimes have not been effective, ex. for copper oxide high T_c superconductors, because the spin-orbit coupling is strong in the case of heavy constituent elements. It significantly reduces the relaxation time of CESR and broadens the linewidth until the CESR signal is undetectable. However, CESR studies for carbon molecular crystal are rather useful because the effect of the spin-orbit coupling on the relaxation times is small.

3 Electronic Properties for Multi-Walled Nanotubes

3.1 Crude CNTs

Crude CNTs containing nanoparticles are produced by the arc-discharge method [8]. Although the quantitative value of CNTs cannot be determined because of the unknown amounts of nanoparticles, the whole susceptibility and spin susceptibility of the crude CNTs are reported by a number of researchers.

Figure 1 shows the temperature dependencies of the static magnetic susceptibilities measured by superconducting quantum interference device (SQUID) for the crude CNTs, highly oriented pyrolytic graphite (HOPG), C₆₀ and other forms of carbon under the magnetic field of 0.5 T [21]. The larger magnitude of χ for the CNTs compared to graphite was observed. The diamagnetic χ in graphite is understood to arise from interband transitions, which dominate the magnetic response for this semimetal [22]. The observed large magnitude of χ for CNTs suggests that, in at least one of the two principal directions, either normal or parallel to the symmetry axis, χ is larger than that in graphite if it is compared in a similar direction. One plausible explanation is

that, because the individual CNTs are closed structures, ring currents may flow around the waist of the CNT in response to a field along the tube axis. In graphite, ring currents are confined to the planes and only flow when the field has a component normal to this direction. In this interpretation, the diamagnetism of the CNTs would be greater than that of graphite because of the different current pathways provided by the two materials. At a high field of 5 T, χ is diamagnetic with the same temperature dependence as graphite [23]. In this field range, the magnetic length $(\hbar c/eH)^{1/2}$ is much smaller than the perimeter of the CNTs. Therefore, the susceptibility probes only small local areas of the graphite planes, and is expected to be the geometrical average of that of rolled-up sheets of graphite.

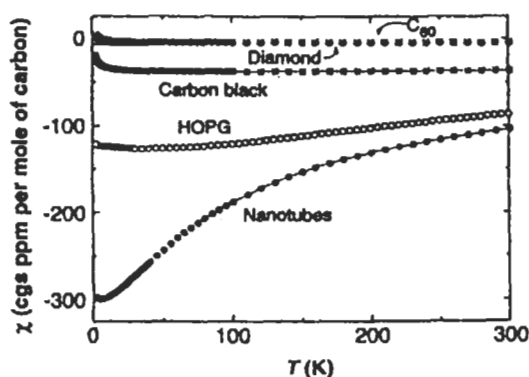


Fig. 1. Orientationally averaged magnetic susceptibility of various forms of carbon [21].

It is reported that a CESR peak is observed for the crude CNTs and the spin susceptibility does not depend on temperature [24]. The spin susceptibility is about three times as small as that in the non-particle CNTs. This ratio indicates that the ratio of CNTs and nanoparticles in the crude CNTs is about 1:2.

3.2 Purified CNTs

CNTs are purified by oxidizing the crude ones as prepared. During the oxidation process, the nanoparticles are removed gradually and eventually only open CNTs remain [9]. An intrinsic CESR was observed from these purified CNTs [12]. The temperature dependencies of susceptibility, linewidth and g -value of the CESR are shown in Fig. 2 (open circle). We find a temperature independent spin susceptibility (Pauli) $\chi_s = 4.3 \times 10^{-8}$ emu/g.

The result indicates the presence of metallic, narrow-gap semiconducting and/or semimetallic CNTs and is in agreement with theoretical predictions [2-7]. The

spin susceptibility of the purified CNTs is similar to that of the graphite powder, the values of which range between $1 \times 10^{-8} - 4 \times 10^{-8}$ emu/g [25,26].

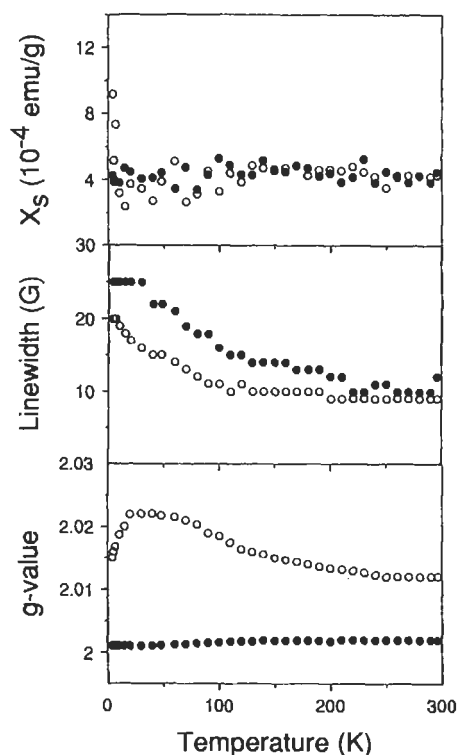


Fig. 2. Temperature dependencies of spin susceptibilities, linewidths and g -values of the CESR for the purified CNTs (open circle) and the annealed purified CNTs (solid circle).

With increasing temperature, the linewidth of the CESR of purified CNTs decreases from 30 G at low temperature to 10 G at room temperature. This temperature dependence of the linewidth can be explained by the motional narrowing as it is observed in the case of graphite powder [26]. The g -value of the CESR depends on temperature from 2.022 at 30 K to 2.012 at room temperature, this also resembling that of graphite. The g -value of graphite is determined by the distribution of the g_{ab} and g_c values (a, b axes are parallel to the planes and c axis is perpendicular to the planes) as shown in Fig. 3 [27]. The g_c of graphite depends on temperature due to the changes in the interlayer interactions of graphitic sheets [28]. If the CNTs have perfect cylindrical structures, the interlayer spacing should remain relatively constant. A plausible interpretation of the strong temperature dependence of the g -value observed for

the CNTs could be that they are highly defective and have a local structure similar to small graphitic sheets.

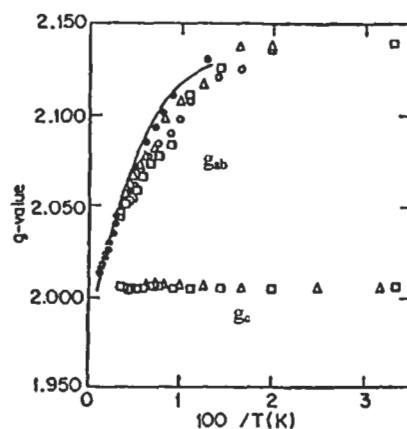


Fig. 3. Temperature dependence of the g -value of graphite for a, b axes and that for c axis (modified from refs. 26 and 27).

For reducing the defects of the CNTs, we annealed the non-particle CNTs at 2850°C [12]. The CESR was still observed as shown in Fig. 2 (top) (closed circle). However, the g -value of the CESR of the annealed CNTs shifts greatly from that of the before-annealed CNTs and the temperature dependence becomes nearly constant (Fig. 2 bottom). The observed g -value and the temperature dependence are similar to those of the in-plane characteristics of graphite (Fig. 3). Although we did not have definite evidence for what was changed during annealing, the observed g -value behaviour for the annealed CNTs can be reasonably explained, supposing that the ideal structure of CNTs is cylindrical. In another method for removing nanoparticles, no CESR was observed for the non-particle CNTs [29]. The ESR-silent result indicates that the non-particle CNTs are neither metallic nor semimetallic, but semiconducting with wide band-gap. The different kinds of CNTs might be obtained by the different methods applied.

3.3 Aligned CNTs

Filtering the tube suspension through a 0.2 μm pore ceramic paper leaves a uniform black deposit on the paper and can produce aligned CNT films [30]. The deposited material was transferred on a thin Teflon sheet by pressing the tube-coated side of the filter on the plastic and then the filter was lifted off to expose the surface. Scanning electron microscopic study reveals that the tubes are highly aligned perpendicular to the Teflon surface [30].

The static magnetic susceptibilities of the aligned CNTs with keeping tube's cylindrical direction parallel χ_{\parallel} and perpendicular χ_{\perp} to the magnetic field were measured by SQUID as shown in Fig. 4 [31]. The CNTs are diamagnetic with

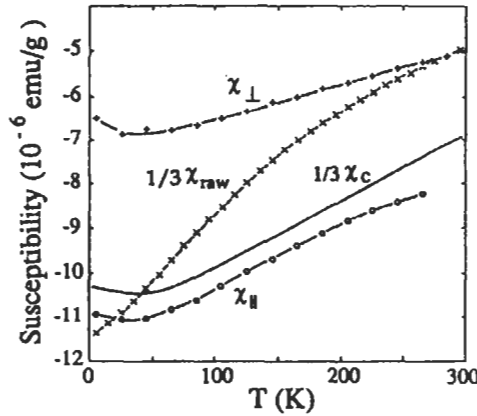


Fig. 4. Static magnetic susceptibility vs temperature. Nanotubes with the magnetic field perpendicular to the tubes (+), parallel to the tubes (o), unprocessed CNT-containing material (x) and planar graphite (solid line) [31].

an anisotropic character. The magnitude of the susceptibilities increases with decreasing temperature. The measurements of non-aligned sample give the susceptibility value as the same as the orientational average $(2\chi_{\perp} + \chi_{\parallel})/3$ of the aligned sample. The average susceptibility is close to the graphite orientational average, $(2\chi_{ab} + \chi_c)/3$ [21]. For graphite, the susceptibility χ_c is much larger than χ_{ab} [32]. Assuming a simple CNT model consisting of planar graphene sheets rolled up in a tube, the relationships of $\chi_{\perp\text{model}} = (\chi_c + \chi_{ab})/2$ and $\chi_{\parallel\text{model}} = \chi_{ab}$ can be used. It leads to $|\chi_{\perp\text{model}}| \gg |\chi_{\parallel\text{model}}|$, however, experimental observations is in contrast to the model. The observed large $|\chi_{\parallel}|$ may be caused by the ring currents around the tube axis, and the reduced values of $|\chi_{\perp}|$ are likely due to both the curvature effects and the shorter intercalation distance than that of graphite intercalation [33,34].

Pauli spin susceptibility for the aligned CNTs has been measured and it is reported that the aligned CNTs are also metallic or semimetallic [30]. The temperature dependence of g_{\parallel} and g_{\perp} is plotted in Fig. 5(a). Both values increase with decreasing temperature down to 40 K. A similar increase is observed for graphite. The g -value dependence on the angle θ at 300 K is shown in Fig. 5(b) (inset). The g -value varies between $g_{\parallel} = 2.0137$ and $g_{\perp} = 2.0103$ while the direction of magnetic fields changes from parallel to perpendicular to the tubes. These observed data fit well as

$$\begin{aligned}
 g &= \{(g_{\parallel} \cos \theta)^2 + (g_{\perp} \sin \theta)^2\}^{1/2} \approx g_{\parallel} + (g_{\perp} - g_{\parallel}) \sin^2 \theta \\
 &= 2.0137 - 0.0034 \sin^2 \theta.
 \end{aligned}
 \tag{1}$$

In the simple model of CNTs described earlier, its g -value can be estimated using the g -values of graphite at 300 K,

$$g = g_{ab} + \frac{1}{2}(g_c - g_{ab})\sin^2\theta = 2.0026 + 0.0230\sin^2\theta, \quad (2)$$

where $g_c=2.050$ and $g_{ab}=2.0026$, the factor $1/2$ arises from the cylindrical geometry. Comparing the model with the tubes, whereas in graphite $g_{ab} < g_c$, $g_{\parallel} > g_{\perp}$ is obtained in the tubes. This inversion is similar to the one observed in the static susceptibilities and, as for graphite, probably has the same origin.

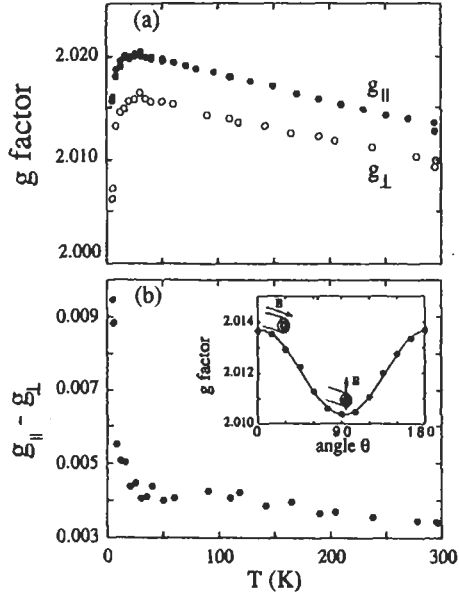


Fig. 5. g -values of the CNTs vs temperature, (a) for parallel, $\theta=0^\circ$ (\bullet) and perpendicular, $\theta=90^\circ$ (\circ) orientations. (b) The anisotropy $g_{\parallel} - g_{\perp}$ vs temperature. (inset) Angular dependence of the g -value of the CNTs at $T=300$ K. The fit shown by the solid line corresponds to $g=2.0137-0.0034\sin^2\theta$ [31].

3.4 Alkali-metal doped CNTs

Doping of alkali-metals into CNTs has been examined [11]. The X-ray powder diffraction (XRD) patterns of the K- or Rb-doped CNTs show that alkali-metals are intercalated between the CNT layers. The hexagonal unit cell is essentially the same as that of the stage-1 alkali-metal intercalated graphite AC₈ (A=K, Rb). For a sample doped with Rb, the observed lattice parameter of the perpendicular

direction of CNTs, 5.68 \AA , corresponds to an expansion by 2.3 \AA in the interlayer spacing. An overall composition is determined to be AC_8 by the weight gain. TEM observations reveal that some of the CNTs are intercalated by K between the CNT layers as shown in Fig. 6 [14]. Both sides of CNTs are intercalated from the surface to about 8 nm deep. Although nobody has observed the defects in the CNTs or nested structures directly, closed cylindrical CNTs cannot be intercalated with alkali-metals between the cylinders.

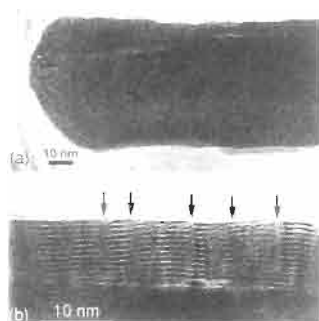


Fig. 6. (a) Medium and (b) high magnification TEM images of a partially intercalated CNTs [14].

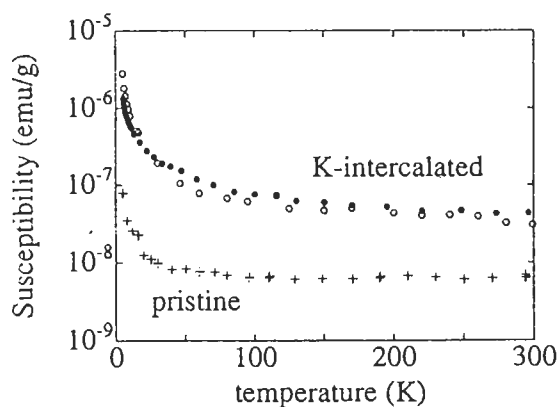


Fig. 7. Susceptibility of the pristine sample (+) and of the K-doped sample (closed circle). The open circle points correspond to the susceptibility of the K-intercalated powder before the film deposition procedure [35].

An ESR study for the K-doped CNTs with a doping level of 1-2% has been reported [35]. The comparison of spin susceptibilities χ_s between pristine and K-intercalated CNTs is shown in Fig. 7. A significant increase of the susceptibility

is associated with the doping process. The Pauli susceptibilities are 0.6×10^{-8} emu/g for pristine and 2.3×10^{-8} emu/g for K-doped sample. This indicates that K-doped CNTs are still good conductors. The g -value of the ESR is very sensitive to the orientation of the tube axis with respect to the angle θ . Before doping, the g -value varies between $g=2.014$ to $g=2.010$ as described in paragraph 3.3, while it is almost isotropic with $g=2.0028$ after K-doping. The temperature dependence of the g -value is also changed from temperature dependent for pristine to temperature independent for K-doped sample. The increasing spin susceptibility and the decreasing ESR g -value with decreasing temperature are similar to the effects observed for graphite intercalation compounds.

3.5 Electronic properties by other measurements

Lastly, we discuss electronic properties by other measurements in comparison with that by magnetic measurements.

Scanning tunnelling microscopy (STM) has been used to investigate the structure and electronic properties of CNTs [36]. The bias-voltage dependent images indicate that the CNT bundles are small band-gap semiconductors. The first direct electrical transport measurements performed on a CNT bundle also exhibited a semimetallic behaviour like rolled graphene sheets with a similar band structure above 2 K [37]. Using the simple two-band model for graphite, the band overlap is estimated to be 3.7 meV and it is about 10 times smaller than for crystalline graphite. Four-probe contact resistivity measurements on a large bundle of CNTs (60 μm diameter and 350 μm in length between the two potential contacts) was reported that the bundle is semimetallic [38]. Subsequently, electrical resistance measurement on individual CNTs (total diameter around 50 nm) has been succeeded [39]. Above 1 K, a typical semimetallic behaviour is observed, being consistent with the simple two-band model for semimetallic graphite.

These results are consistent with the electronic properties of CNTs probed by magnetic measurements. In sum, most of MWCNTs show semimetallic behaviour experimentally.

4 Electronic Properties for SWCNTs

SWCNTs have been produced by carbon arc discharge and laser ablation of graphite rods. In each case, a small amount of transition metals is added to the carbon target as a catalyst. Therefore the ferromagnetic catalysts resided in the sample. The residual catalyst particles are responsible for a very broad ESR line near $g=2$ with a linewidth about 400 G, which obscures the expected conduction electron response from SWCNTs.

In the case that SWCNTs were produced by laser ablation with Co and Ni, a very weak and narrow signal was superposed on the main broad line. To confirm that this narrow line is associated with SWCNTs, the sample was vacuum-annealed at 1500°C to remove the remaining Co and Ni.

The XRD peaks characteristic of Co and Ni disappeared after the treatment, as did the broad ESR line, successfully leaving only the narrow asymmetric line with 26 G linewidth as shown in Fig. 8 [40]. The g -value of the narrow line is $g=2.002 \pm 0.001$. The narrow ESR line shows Dysonian at all temperatures in the range of 4-300 K. Furthermore, the ESR intensity is quite independent of T and thus the density of conduction electrons is invariant as a function of temperature as shown in Fig. 9. These show that the material is highly metallic, even at low T .

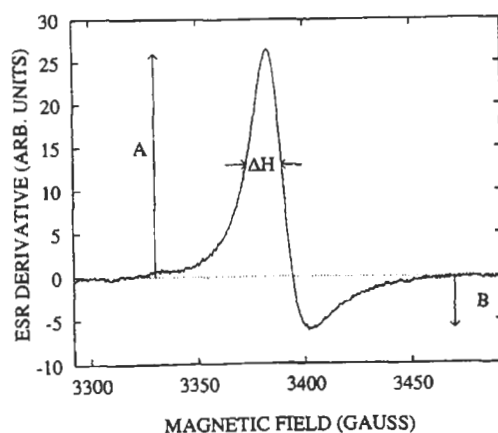


Fig. 8. ESR spectrum of as-grown bulk SWCNTs recorded at 100 K [40].

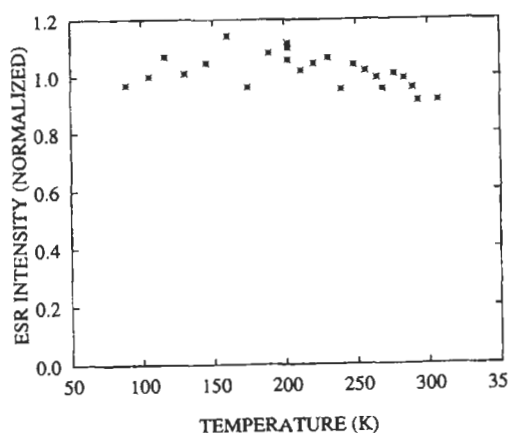


Fig. 9. Normalised temperature dependence of the ESR intensity for an SWCNT sample [40].

However in the case that SWCNTs were purified by the centrifugal separation using an aqueous solution of cationic surfactants or by the microfiltration

technique followed by heat treatment at 450°C, there was no ESR signal originating from the conduction electrons of CNTs [41].

Some explanations could be possible for these contradictory results. One is that a various types of CNTs may be obtained by different methods, since SWCNTs as much as 50 % are chiral and nonmetallic [42]. The other is that the result may be attributable to the contact condition of SWCNT bundles. When the bundles closely contact each other, the SWCNT system will likely become a three-dimensional one just as in the case of contacted MWCNTs.

5 Concluding Remarks

We have reviewed the electronic properties of CNTs probed by magnetic measurements. MW- and SWCNTs can individually be produced, however, the parameters of CNTs are uncontrollable, such as diameter, length, chirality and so on, at the present stage. Since the features of CNTs may depend on the synthesis and purification methods, some different experimental observation on CNT properties has been reported. It is important, however, that most of papers have clarified metallic CNTs are actually present in both MW- and SWCNTs. The characteristic of CESR of SWCNTs is different from that on non-annealed MWCNTs, but rather similar to that on annealed multi-walled ones. The relationship of the electronic properties between SW- and MWCNTs has not yet been fully understood. The accurate control in parameter of CNTs is necessary in order to discuss more details of CNTs in future.

References

1. Iijima, S., *Nature*, 1991, **354**, 56.
2. Saito, R., Fujita, M., Dresselhaus, G. and Dresselhaus, M. S., *Phys. Rev. B*, 1992, **46**, 1804.
3. Saito, R., Fujita, M., Dresselhaus, G. and Dresselhaus, M. S., *Appl. Phys. Lett.*, 1992, **60**, 2204.
4. Hamada, N., Sawada, S. and Oshiyama, A., *Phys. Rev. Lett.*, 1992, **68**, 1579.
5. Tanaka, K., Okahara, K., Okada, M. and Yamabe, T., *Chem. Phys. Lett.*, 1992, **191**, 469.
6. Mintmire, J. M., Dunlap, B. I. and White, C. T., *Phys. Rev. Lett.*, 1992, **68**, 631.
7. Blasé, X., Benedict, L. X., Shirley, E. L. and Louie, S. G., *Phys. Rev. Lett.*, 1994, **72**, 1878.
8. Ebbesen, T. W. and Ajayan, P. M., *Nature*, 1992, **358**, 220.
9. Ebbesen, T. W., Ajayan, P. A., Hiura, H. and Tanigaki, K., *Nature*, 1994, **367**, 519.
10. Ajayan, P. M., Stephan, O., Colliex, C. and Trauth, D., *Science*, 1994, **265**, 1212.
11. Zhou, O., Fleming, R. M., Murphy, D. W., Chen, C. H., Haddon, R. C., Ramirez, A. P. and Glarum, S. H., *Science*, 1994, **263**, 1744.
12. Kosaka, M., Ebbesen, T. W., Hiura, H. and Tanigaki, K., *Chem. Phys.*

- Lett.*, 1995, **233**, 47.
13. Ebbesen, T. W. and Takada, T., *Carbon*, 1995, **33**, 973.
 14. Suzuki, S. and Tomita, M., *J. Appl. Phys.*, 1996, **79**, 3739.
 15. Thess, A., Lee, R., Nikolaev, P., Dai, H., Petit, P., Robert, J., Xu, C., Lee, Y. H., Kim, S. G., Rinzler, A. G., Colbert, D. T., Scuseria, G. E., Tománek, D., Fischer, J. E. and Smalley, R. E., *Science*, 1996, **273**, 483.
 16. Iijima, S. and Ichihashi, T., *Nature*, 1993, **363**, 603.
 17. Bethune, D. S., Kiang, C. H., de Vries, M. S., Gorman, G., Savoy, R. Vazquez, J. and Beyers, R., *Nature*, 1993, **363**, 605.
 18. Saito, Y., Yoshikawa, T., Okuda, M., Fujimoto, N., Sumiyama, K., Suzuki, K., Kasuya, A. and Nishina, Y., *J. Phys. Chem. Solids*, 1993, **54**, 1849.
 19. Seraphin, S. and Zhou, D., *Appl. Phys. Lett.*, 1994, **64**, 2087.
 20. Bandow, S., Rao, A. M., Williams, K. A., Thess, A., Smalley, R. E. and Eklund, P. C., *J. Phys. Chem. B*, 1997, **101**, 8839.
 21. Ramirez, A. P., Haddon, R. C., Zhou, O., Fleming, R. M., Zhang, J., McClure, S. M. and Smalley, R. E., *Science*, 1994, **265**, 84.
 22. McClure, J. W., *Phys. Rev.*, 1959, **104**, 666.
 23. Heremans, J., Olk, C. H. and Morelli, D. T., *Phys. Rev. B*, 1994, **49**, 15122.
 24. Kosaka, M., Ebbesen, T. W., Hiura, H. and Tanigaki, K., *Chem. Phys. Lett.*, 1994, **25**, 161.
 25. Singer, L. S. and Wagoner, G., *J. Chem. Phys.*, 1962, **37**, 1812.
 26. Wagoner, G., *Phys. Rev.*, 1960, **118**, 647.
 27. Murata, M., Master thesis, Institute of Materials Science, University of Tsukuba, Tsukuba, 1993.
 28. Morgan, W. C., *Carbon*, 1972, **10**, 73.
 29. Tanaka, K., Sato, T., Yamabe, T., Okahara, K., Uchida, K., Yumura, M., Niino, H., Ohshima, S., Kuriki, Y., Yase, K. and Ikazaki, F., *Chem. Phys. Lett.*, 1994, **223**, 65.
 30. de Heer, W. A., Bacsá, W. S., Châtelain, A., Gerfin, T., Humphrey-Baker, R., Forro, L. and Ugarte, D., *Science*, 1995, **268**, 845.
 31. Chauvet, O., Forro, L., Bacsá, W. S., Ugarte, D., Doudin, B. and de Heer, W. A., *Phys. Rev. B*, 1995, **52**, R6963.
 32. McClure, J. W., *Phys. Rev.* 1960, **119**, 606.
 33. McClure, J. W., *Phys. Rev.*, 1957, **108**, 612.
 34. Tatar, R. C. and Rabii, S., *Phys. Rev. B*, 1982, **25**, 4126.
 35. Chauvet, O., Baumgartner, G., Carrard, M., Bacsá, W. S., Ugarte, D., de Heer, W. A. and Forro, L., *Phys. Rev. B*, 1996, **53**, 13996.
 36. Zhang, Z. and Lieber, C. M., *Appl. Phys. Lett.*, 1993, **62**, 2792.
 37. Langer, L., Stockman, L., Heremans, J. P., Bayot, V., Olk, C. H., Haesendonck, C. V., Bruynseraede, Y. and Issi, J. -P., *J. Mater. Res.*, 1994, **9**, 927.
 38. Song, S. N., Wang, X. K., Chang, R. P. H. and Ketterson, J. B., *Phys. Rev. Lett.*, 1994, **72**, 697.
 39. Langer, L., Bayot, V., Grivei, E., Issi, J. -P., Heremans, J. P., Olk, C. H., Stockman, L., van Haesendonck, C. and Bruynseraede, Y., *Phys. Rev. Lett.*, 1996, **76**, 479.
 40. Petit, P., Jouguelet, E., Fischer, J. E., Thess, A. and Smalley, R. E., *Phys. Rev. B*, 1997, **56**, 9275.
 41. Bandow, S., Asaka, S. and Ando, Y., *Appl. Phys. A*, 1998, **66**, 1.

42. Cowley, J. M., Nikolaev, P., Thess, A. and Smalley, R. E., *Chem. Phys. Lett.*, 1997, **265**, 379.

CHAPTER 9

Optical Response of Carbon Nanotubes

FRANK BOMMELI,¹ LEONARDO DEGIORGI,¹
 LASZLO FORRO² and WALT A. DE HEER²

¹*Laboratorium für Festkörperphysik, ETH-Zurich, CH-8093 Zurich, Switzerland*

²*Departement de Physique, EPF-Lausanne, CH-1015 Lausanne, Switzerland*

1 Introduction

The synthesis of molecular carbon structures in the form of C₆₀ and other fullerenes stimulated an intense interest in mesoscopic carbon structures. In this respect, the discovery of carbon nanotubes (CNTs) [1] in the deposit of an arc discharge was a major break through. In the early days, many theoretical efforts have focused on the electronic properties of these novel quasi-one-dimensional structures [2-5]. Like graphite, these mesoscopic systems are essentially sp² bonded. However, the curvature and the cylindrical symmetry cause important modifications compared with planar graphite.

The classification of the tubes as metals or semiconductors is based on the way the underlying graphite band structure is folded when one applies azimuthal periodic boundary conditions of the tube. The boundary conditions depend strongly on how the CNTs are rolled [2-5]. Particularly and just to quote one example, Mintmire et al. calculated the electronic structure using a so-called all-electron Gaussian-orbital based local-density-functional approach and also taking into account the electron-lattice interaction with a Fröhlich Hamiltonian. They established that fullerenes tubules would appear to have the advantages of a carrier density similar to metals (as opposed to graphite) and a simple metallic phase (i.e., zero band gap) at 300 K (as opposed to polyacetylene), with a concomitant relatively high conductivity as result of the small diameter [2].

The availability of well aligned CNT films started also an intensive experimental work, with particular emphasis on the transport and magnetic properties as well as on the optical response (see Chaps. 8 and 10). Transport properties [6], conduction electron spin resonance (ESR) and static magnetic susceptibility measurements [7] show anisotropic behaviours, when measuring along or perpendicular to the tubes. In Fig. 1 the resistivity of the tubes measured along and perpendicular to the axis as well as the inverse resistive scattering time, obtained from ESR measurements, are displayed. The resistivity of the tubes, measured using the conventional four points method [8], increases with decreasing temperature in both orientations (solid and dotted lines). The

anisotropy between the two orientation varies with temperature. The anisotropy is defined as the ratio $A = \rho_{\alpha\perp} / \rho_{\alpha\parallel}$, where $\rho_{\alpha\perp}$ is the resistivity perpendicular and $\rho_{\alpha\parallel}$ parallel to the tubes axis. A ranges from 8 to 10, as it can be estimated from Fig. 1. Furthermore, the Pauli susceptibility above 40 K was found to be consistent with a semimetal. The typical insulating behaviour contrasts with the inverse resistive scattering time obtained from ESR measurement which displays metallic behaviour i.e., it decreases with decreasing temperature at least down to about 10 K (full dots in Fig. 1). Moreover, it was also found that the intrinsic resistivity of the tubes, estimated from the ESR linewidth, is about two orders of magnitude lower than the dc resistivity (ρ_{dc}) [7]. This is consistent with the interpretation of ρ_{dc} being dominated by the intertube contact resistances [9].

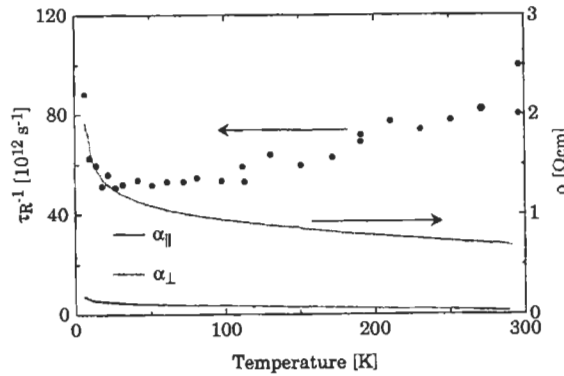


Fig. 1. The resistivity ρ_{dc} (solid and dotted line)[6] and the inverse scattering time (plain dots) τ_R^{-1} [7] which is proportional to the product $T_1 \cdot \Delta g^2$ (T_1^{-1} is the linewidth and Δg the g -shift of the ESR signal). For a metal, the resistivity and τ_R^{-1} are expected to decrease when lowering the temperature [7].

In view of this apparent contradictory outcome from the transport and magnetic properties, we were motivated to investigate the dynamics of the charge excitation spectrum by optical methods. In fact, the optical measurement is a powerful contactless experimental tool which should in principle allow to unfold the disagreement between $\tau_R^{-1}(T)$ and $\rho(T)$ since the optical response of a metal and of an insulator are in principle dramatically different.

2 Nanotube Preparation and Experiment

The CNTs were prepared by the group at EPF in Lausanne [10] following the method of Ebbesen et al. [11]. A 100 A, 20 V dc arc between a 6.5 mm diameter graphite anode and a 20 mm graphite cathode is sustained in a 6.7×10^4 Pa helium atmosphere for about twenty min. Nanotubes were found on the cathode, where they were encapsulated in a cylindrical 1 cm long shell. The shell was cracked and the powdery soot-like deposit extracted. The powder was then

ultrasonically dispersed in spectroscopic grade ethanol and centrifuged to remove larger particles. Transmission electron microscopy revealed that the suspension contained CNTs, nominally 1 to 5 μm long and 10 ± 5 nm in diameter. However, besides the tubes, it was also observed that a substantial fraction (20-40 %) of the material was present in the form of small polyhedral carbon particles. By drawing the tube suspension through a 0.2 μm pore ceramic filter, a uniform black deposit remains on the filter. The tubes are then deposited on a Delrin or Teflon surface, by pressing the tubes' coated side of the filter onto the polymer. They are preferentially oriented perpendicular to the surface and are called β -aligned. Figure 2(a) shows a β -aligned CNT film. When the surface is lightly rubbed with a thin Teflon sheet or aluminium foil, the surface becomes silvery in appearance and scanning electron microscopy shows that it is densely covered with CNTs, oriented in the direction in which the film had been rubbed [6]. We call the surfaces, where the tubes are oriented in the plane of the surface, α_{\parallel} and α_{\perp} aligned, for the parallel and perpendicular direction, respectively. Figure 2(b) shows an α -aligned CNT film. Our CNT films had a typical thickness ranging between 1 and 5 μm .

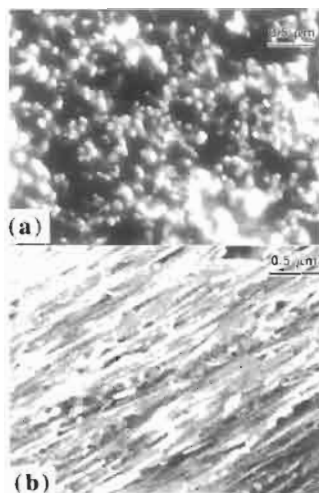


Fig. 2. (a) The surface of a film of CNTs deposited on a ceramic filter. The tubes are β -aligned, with their axes perpendicular to the surface such that only tube tips are seen. (b) After mechanical treatment, the morphology dramatically changes and the surface is densely covered with CNTs that lie flat on the surface and are aligned in the direction in which the surface was rubbed (α -aligned), indicating that the tubes were pushed over by the treatment. The tube tips in (a) appear to be larger than the true tube diameters in (b) partially because the tubes are often bundled together and partially because of an artifact caused by focusing and local charging effects. As a matter of fact, when we observe inclined tubes, the tip images appear brighter and have larger diameters than the tube images [6].

We have determined the optical properties as a function of temperature by measuring the reflectivity $R(\omega)$ of the oriented CNT films from the far infrared (FIR) up to the ultra-violet (UV) (i.e., from 20 cm^{-1} up to $3 \times 10^4 \text{ cm}^{-1}$), using three spectrometers with overlapping frequency ranges [12, 13].

The investigated specimens had nice and flat reflecting surfaces, and equivalent samples (i.e., with the same film thickness) gave similar results. The roughness of the surface and the finite CNT size effects were taken into account by coating the investigated specimens with a thin gold layer. Such gold coated samples were used as references. The average thickness of the film is generally smaller than the expected penetration depth of light in the far-infrared. Therefore, we looked at the influence of the substrate on the measured total reflectivity of the substrate-CNT film composite. Even though for film thicknesses above $3 \mu\text{m}$ we did not find any qualitative and quantitative change in the reflectivity spectra due to the substrate, we appropriately took into account the effects due to multiple reflections and interferences at the film and substrate interface. Further details of the experimental procedure and data analysis can be found in refs. 12 and 13. The corrected and intrinsic reflectivity of the CNT films differ only by a few percent in intensity (particularly in FIR) but not in the overall shape from the measured one. The real part $\sigma_1(\omega)$ of the optical conductivity is then obtained through a Kramers-Kronig transformation of the corrected $R(\omega)$. The frequency range of the measured reflectivity spectrum has been extrapolated towards zero by a constant value as for an insulator (see below) [12,13]. For energies larger than 4 eV, the reflectivity of the α orientations has been extrapolated up to 40 eV using the reflectivity of highly oriented pyrolytic graphite (HOPG) [14] normalised at the experimental values of the reflectivity of the CNTs at 4 eV. Over 40 eV, $R(\omega)$ was assumed to drop off as ω^{-2} .

3 The Optical Spectra

Figure 3(a) presents the reflectivity while Fig. 3(b) the corresponding optical conductivity spectra at 300 K for light polarized parallel (α_{\parallel}) and perpendicular (α_{\perp}) to the tubes. There is a weak anisotropy, mainly manifested by an overall decrease of the $R(\omega)$ intensity along α_{\perp} . Moreover, we have not found any temperature dependence in our optical spectra, in agreement with the rather weak temperature dependence of the ESR and *dc* transport properties (Fig. 1) [6,7]. Although the reflectivity increases from the visible down to the FIR in a metallic-like fashion (i.e., as in the case of an overdamped plasma edge), it tends to saturate towards zero-frequency and displays a broad bump at about 6 meV. This behaviour of $R(\omega)$ does not allow a straightforward metallic extrapolation to 100 % for frequency tending towards zero, and, therefore, the measured $R(\omega)$ is apparently consistent with the one of an insulator. Figure 4 shows our measurements of the β configuration which are qualitatively similar to the findings in the α directions. The optical conductivities, displayed in Figs. 3(b) and 4(b) for the α and β directions, respectively, are characterised by a vanishing conductivity for $\omega \rightarrow 0$, by a broad absorption peaked at about 6-9 meV and

finally by high frequency excitations due to HOPG electronic interband transitions [14].

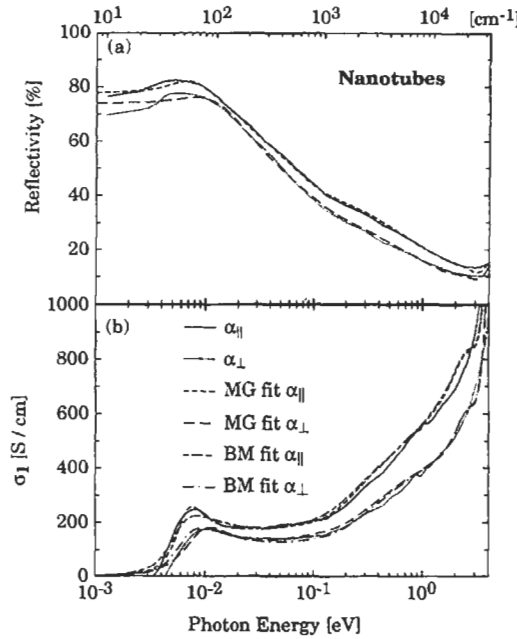


Fig. 3. Reflectivity (a) and optical conductivity spectra (b) of oriented CNTs films along the $\alpha_{||}$ and α_{\perp} directions. Bruggeman (BM) and Maxwell-Garnett (MG) fits (see text and Table 2) are also presented.

The mid- and far-infrared spectral range can be described within two possible scenarios: In the first one, we can ascribe the broad absorption at 9 meV to a phonon mode. However, there are several arguments against this possibility. First of all, graphite has a transverse optical (TO) phonon mode at about 6 meV which, however, is not IR active [15] (see also Chap. 6). Of course, one might argue that this mode can be activated by symmetry breaking, but our feature at 9 meV is very broad and temperature independent. These features are rather unusual for phonon modes, which tend to appear as sharp absorptions with width decreasing with temperature. Secondly, the FIR absorption shifts in frequency when measuring different specimens and consequently cannot be strictly considered as an intrinsic feature of the CNTs. Another problem is the vanishing small conductivity for $\omega \rightarrow 0$, which contrasts with the intrinsic *dc* conductivity evaluated from ESR investigation (Fig. 1). Therefore, we want to suggest an alternative interpretation, which will relate the FIR absorption at 9 meV to the particular morphology of our specimens. This second scenario, to be developed here will lead to the identification of the intrinsic metallic nature of the CNTs

[12,13]. To start, we shall first flash on the phenomenological approach used to interpret the data.

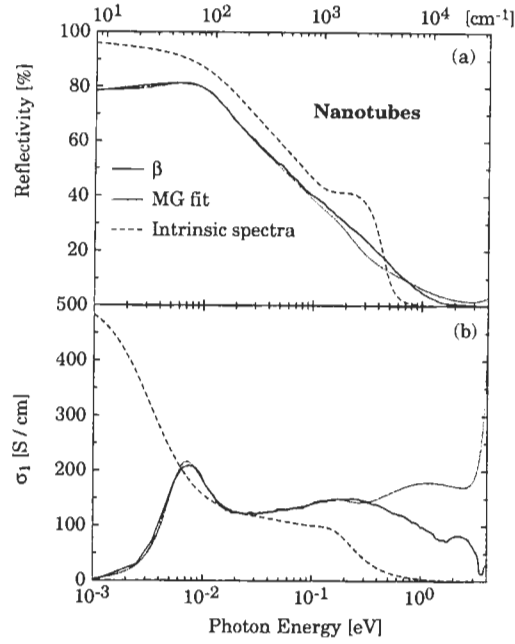


Fig. 4. The reflectivity (a) and the optical conductivity (b) in the β direction are similar to the ones along the α directions (Fig. 3). However, the absence of data above 4 eV changes the high energy spectrum of the optical conductivity. These changes are not relevant for the low frequency spectral range. The Maxwell-Garnett (MG) fit is also displayed as well as the intrinsic reflectivity and conductivity calculated from the fit (see Table 2 for the parameters).

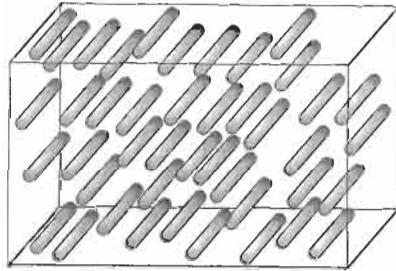


Fig. 5. Schematic representation of the measured CNT films. The effective medium is the result of tubes dispersed in an insulating host (glassy graphite).

4 Effective Medium Theories

Our oriented films cannot be really considered as bulk materials. It is more appropriate to compare our specimens to an effective medium composed of small particles (i.e., CNTs) dispersed in a dielectric host (i.e., glassy graphite) as is schematically shown in Fig. 5. Different theories describe the electrodynamic response of such a composite medium. Here, we will concentrate our attention to the Maxwell-Garnett model (MG) and the Bruggeman model (BM) [18]. Both, the Maxwell-Garnett model and the more sophisticated Bruggeman model, which is a generalisation of the MG theory, can correctly account for the features seen in our experimental optical data. In order to simplify the discussion, in the following we will assume that we have metallic particles dispersed in an insulator.

4.1 The Maxwell-Garnett model

The case when the metallic particles are surrounded by an insulator is sketched in Fig. 6, which corresponds to the morphology of our samples (Fig. 5). The electrodynamic response of a composite medium with such a morphology can be computed in the Maxwell-Garnett theory [16,17], which is an application of the Clausius-Mossotti model for polarisable particles embedded in a dielectric host. To apply the Maxwell-Garnett theory, the particles must be sufficiently large so that the macroscopic Maxwell equations can be applied to them but not so large that they approach the wavelength of light in the medium. At a photon energy of 1 meV, the wave length is about 0.2 mm and the size of the tubes 5 μm . Therefore, we are in the limit of applicability of the MG model.

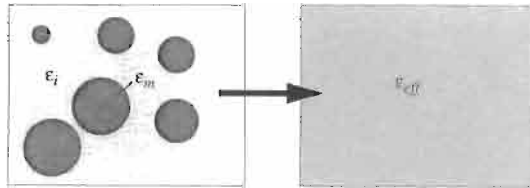


Fig. 6. MG model: the metal with dielectric function ($\epsilon_m(\omega)$) particles are surrounded by an insulator ($\epsilon_i(\omega)$) (left). The mixture results in an effective medium ϵ_{eff} (right).

Let us consider small metallic particles with complex dielectric function $\epsilon_m(\omega)$ embedded in an insulating host with complex dielectric function $\epsilon_i(\omega)$ as shown in Fig. 6. The ensemble, particles and host, have an effective dielectric function $\epsilon_{eff}(\omega) = \epsilon_{eff,1}(\omega) + i\epsilon_{eff,2}(\omega)$. We can express the electric field \mathbf{E} at any point inside the metallic component as

$$\mathbf{E} = \mathbf{E}_0 - \tilde{\mathbf{N}} \frac{\mathbf{P}}{\epsilon_0} \quad (1)$$

with \mathbf{E}_0 the external applied field, \mathbf{P} the polarisation, $\tilde{\mathbf{N}} = \begin{pmatrix} N_1 & 0 & 0 \\ 0 & N_2 & 0 \\ 0 & 0 & N_3 \end{pmatrix}$

the demagnetisation tensor and ϵ_0 is the dielectric constant. The polarisation in vacuum is then given by

$$\mathbf{P} = \epsilon_0(\epsilon(\omega) - 1) \mathbf{E} = n\alpha(\omega)\mathbf{E}_0 \quad (2)$$

where n is the density of dipoles, α the complex polarisability and ϵ the complex dielectric function. Using Eqs.(1) and (2), we obtain the Clausius-Mossotti equation which expresses the relationship between ϵ , the density n and the polarisability α :

$$n\alpha(\omega) = \frac{(\epsilon(\omega) - 1) \epsilon_0}{1 + (\epsilon(\omega) - 1) N} \quad (3)$$

where N is one component of the $\tilde{\mathbf{N}}$ tensor for one specific spatial direction. Actually, Eq.(3) must be modified to take into account the fact that the metallic particles are dispersed in a polarisable insulator rather than in vacuum (i.e., $\epsilon_i(\omega) \neq 1$). Thus in the local electric field approximation, it is necessary to construct a cavity filled with an insulating medium ($\epsilon_i(\omega)$) instead of a completely evacuated cavity, as in Eq.(3). This leads to a generalised Clausius-Mossotti equation:

$$n\alpha(\omega) = \frac{(\epsilon_{eff} - \epsilon_i) \epsilon_0}{N\epsilon_{eff} + (1 - N) \epsilon_i} \quad (4)$$

As the metallic particles are assumed to be sufficiently large for macroscopic dielectric theory to be applicable, we can substitute for α the expression for the polarisability of metallic particle immersed in an insulator. The dipole moment is given by the integration of the polarisation over the volume V . Thus, if the polarisation is uniform:

$$\mathbf{p} = \alpha(\omega)\mathbf{E} = \frac{(\epsilon_m - \epsilon_i) \epsilon_0}{N\epsilon_m + (1 - N) \epsilon_i} V \mathbf{E} \quad (5)$$

Inserting Eq.(5) in Eq.(4) leads directly to the Maxwell-Garnett result:

$$\epsilon_{eff} = \epsilon_i \frac{\{N + f(1 - N)\}\epsilon_m + (1 - N)(1 - f)\epsilon_i}{N(1 - f)\epsilon_m + (fN + 1 - N)\epsilon_i} \quad (6)$$

with the volume or filling fraction of particles $f = nV$. To calculate the geometrical factor N , we approximate our tubes by ellipsoids [19]:

$$N = \int \frac{abc}{2(s+a^2)^{3/2}(s+b^2)^{1/2}(s+c^2)^{1/2}} ds \quad (7)$$

a , b and c represent the main axis of an ellipsoid. N is tabulated in Table 1 for some special cases.

Table 1. The geometrical factor for some extreme case of ellipsoids.

Type of sample	Axis	N
Sphere	equivalent	1/3
Thin plate	perpendicular	1
Thin plate	in the plane	0
Long cylinder	longitudinal	0
Long cylinder	transverse	1/2

We now want to study the consequences of such a model with respect to the optical properties of a composite medium. For such a purpose, we will consider the phenomenological Lorentz-Drude model, based on the classical dispersion theory, in order to describe qualitatively the various components [20]. Therefore, a Drude term defined by the plasma frequency and scattering rate, will describe the optical response of the bulk metal or will define the intrinsic metallic properties (i.e., $\epsilon_m(\omega)$ in Eq.(6)) of the small particles, while a harmonic Lorentz oscillator, defined by the resonance frequency, the damping and the mode strength parameters, will describe the insulating host (i.e., $\epsilon_i(\omega)$ in Eq.(6)).

For small metallic particles dispersed in a dielectric (insulating) host medium, Eq.(6) predicts an insulating-like behaviour of the effectively measured $R(\omega)$ and a shift of the Drude peak in $\sigma_1(\omega)$ from zero frequency (i.e., as for bulk metal) to a finite resonance frequency ω_{rs} , as for an insulator. In the simple case of spherical metallic particles dispersed in a non-absorbing host (i.e., $\epsilon_{i,2}(\omega) = 0$) and a small filling factor we obtain $\omega_{rs} \approx \omega_p / (\sqrt{1 + 2\epsilon_i})$. Figure 7(a) shows the reflectivity of a metal (plain line) and of an effective medium (dotted line) composed of particles from the same metal immersed in an insulating host. Figure 7(b) displays the optical conductivity obtained with the same parameters as for the reflectivity curves. ω_{rs} depends on the filling factor f , the geometrical factor N and the intrinsic plasma frequency ω_p of the metallic particles [12,13,17]. Furthermore, the width of the absorption at ω_{rs} is twice the scattering relaxation rate Γ of the free charge carriers. Such an approach has been used successfully on various occasions and quite recently also for the high- T_c cuprates [21].

We now consider the influence of the various parameters in the Maxwell-Garnett approach. Figure 8 displays the behaviour of $\sigma_1(\omega)$ if we only change the filling

factor f in Eq.(6). f changes the position of the resonance peak at ω_{rs} . With a filling factor of 1, only metal is present and we do not see, as expected, any deviation from the normal Drude behaviour. For $f = 0$, no metal is present and the optical response is the one of the insulating host. Between these two limits, the resonance peak ω_{rs} shifts to higher frequencies with decreasing filling factor. In other words, by increasing the metallic content of the medium, the conductivity tends to the usual Drude-like behaviour. The $\sigma_1(\omega)$ curve with $f = 0$ is not shown in the graph as its value is zero in the displayed spectral range.

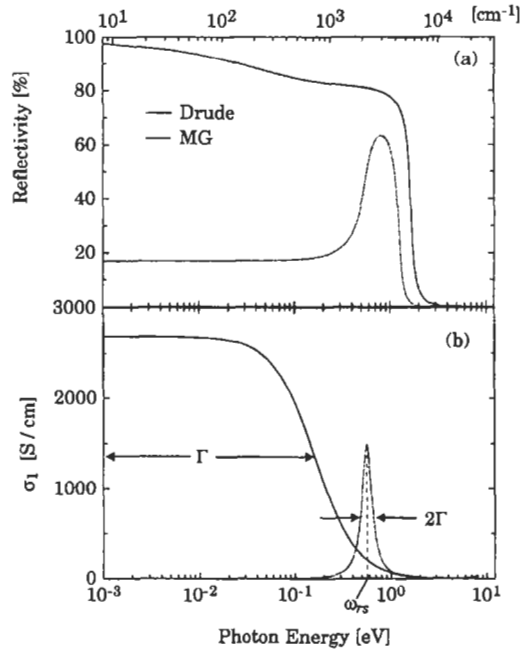


Fig. 7. Model calculations for the reflectivity (a) and the optical conductivity (b) for a simple (bulk) Drude metal and an effective medium of small metallic spherical particles in a dielectric host within the MG approach. The (bulk) Drude and the metallic particles are defined by the same parameters set: the plasma frequency $\hbar\omega_p = 2$ eV, the scattering rate $\hbar\Gamma = 0.2$ eV. A filling factor $f = 0.5$ and a dielectric host-medium represented by a Lorentz harmonic oscillator with mode strength $\hbar\omega_{p,1} = 10$ eV, damping $\hbar\Gamma_1 = 1$ eV and resonance frequency $\hbar\omega_1 = 15$ eV were considered for the calculations.

The geometrical factor, like the filling factor, shifts the position of the resonance peak. When $N = 0$ we have the case of an infinite cylinder (see Table 1). An infinite cylinder connects one side of the crystal to the other. Therefore, the electrons travel freely through the crystal. Actually, this is not the situation of metallic particles dispersed in an insulator any more. The situation corresponds

to the so-called percolation limit and we have a Drude-like behaviour. Figure 9 shows the model calculations for metallic particles dispersed in an insulator with $f = 0.5$. By varying the geometrical factor from zero to one, we change the shape of the particles from an elongated cylinder ($N = 0$) to a sphere ($N = 1/3$), then to a cylinder perpendicular to the main axis ($N = 1/2$) and finally to a perpendicular thin plate ($N = 1$). Therefore, by changing N from 0 to 1, the peak shifts from zero frequency towards higher frequency.

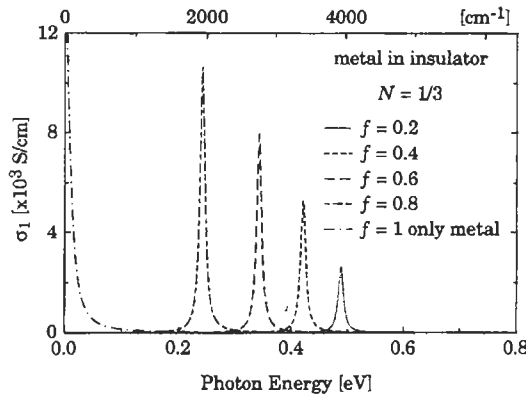


Fig. 8. Calculations performed considering metallic spherical particles (i.e., $N = 1/3$) with intrinsic Drude parameters $\hbar\omega_p = 1$ eV, $\hbar\Gamma = 0.01$ eV, dispersed in an insulating matrix with parameters $\hbar\omega_{p,1} = 2$ eV, $\hbar\Gamma_1 = 1$ eV and $\hbar\omega_1 = 5$ eV, and filling factor f between 0.2 and 1.

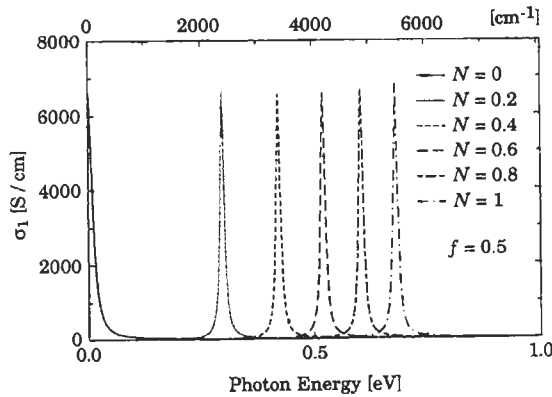


Fig. 9. Case of metallic particles with Drude parameters $\hbar\omega_p = 1$ eV, $\hbar\Gamma = 0.01$ eV, dispersed in an insulating matrix with parameters $\hbar\omega_{p,1} = 2$ eV, $\hbar\Gamma_1 = 1$ eV and $\hbar\omega_1 = 5$ eV, filling factor $f = 0.5$ and geometrical factor N between 0 and 1.

The limit of validity of the MG model is defined by the so-called percolation limit which is reached when the metallic grains are too numerous to be considered as separated. For spheres, the limit is reached with $f_p \approx 0.7$ and for aligned cylinders $f_p \approx 0.9$. For $f_p > 0.9$, we have to invert the point of view: We no longer have metal grains in an insulating matrix but insulating grains in a metallic host [17]. Due to the nature of our CNT films, we will make the assumption that the shape and size of the tubes are constant. Our grains remain unchanged in shape even close to the percolation limit. Such a percolation limit is reached only when rigid spheres or cylinders are effectively in contact.

There is another limitation of the MG approach, consisting in the assumption that the medium was not modified by the insertion of metallic particles. This is of course too crude, and the Bruggeman model, treated next, removes this limitation.

4.2 The Bruggeman model

The Bruggeman model is an extension of the Maxwell-Garnett theory. Bruggeman considered the modification of the medium due to the insertion of metallic particles in the insulating host [18]. By an incremental process, each infinitesimal inclusion of particles modifies the medium, i.e., each grain feels the presence not only of the insulating host but also of the other metallic whits. Figure 10 schematically shows the process. In order to clarify this point let us describe step by step the build up of the effective medium. In order to simplify the discussion, we will again assume that we dip small metallic particles in an insulating host.

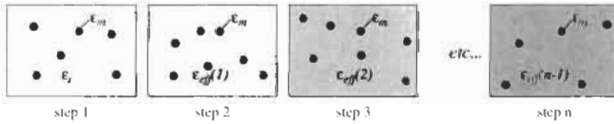


Fig. 10. In the first step few small metallic particles are dispersed in an insulating host. This modifies the medium which now has a dielectric function $\epsilon_{eff}(\omega)$ instead of $\epsilon_i(\omega)$. We repeat iteratively this process (in n consecutive steps) of adding metallic particles until we reach a filling factor f .

The first act consists of removing a small part of the insulator (ϵ_i) and replacing it by a small amount df_1 of metal (ϵ_m). Thereafter with Eq.(6), we calculate $\epsilon_{eff}(1)$. For the first step, there is no difference with MG. If we now add another amount df_2 of metallic particles (ϵ_m) in the brand new system ($\epsilon_{eff}(1)$), we can again calculate the new effective dielectric function with Eq.(6). Instead of using ϵ_i for the dielectric function of the host, we now use $\epsilon_{eff}(1)$ obtained by the previous step. Since we removed some insulating material and replaced it with metal, we have to replace the filling factor f by $df_i / (1 - f_{i-1})$. f_{i-1} is the amount of metal already in the material and df_i the metal we add at step i . The

incremental process stops when $f = \sum df_i$. After the last step, $\epsilon_{eff}(n)$ corresponds to the dielectric function of the mixed medium.

The main phenomenological difference in BM compared to MG is a broadening of the resonance peak at ω_{rs} which, however, does not shift. The model calculations in Fig. 11 have been performed for spheres ($N = 1/3$) with filling factors of 0.5 and 0.9. The parameters, chosen to be equal for both models, are given in the figure caption. It immediately appears that we will not find any drastic difference in the interpretation of the data for the MG or the BM model.

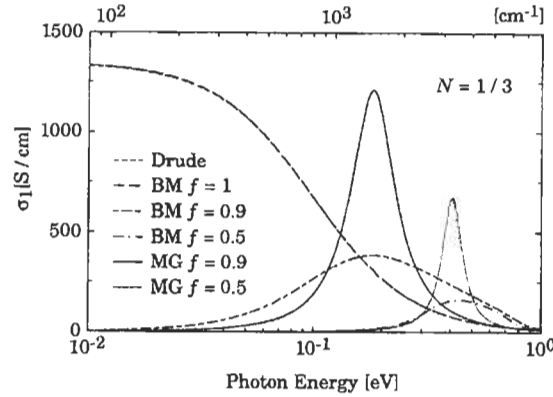


Fig. 11. The Bruggeman model (BM) takes into account the modification of the effective medium by the adjunction of metal in the medium. The net effect is a broadening of the resonance peak. The parameters of the metallic spheres in these calculations are: $\hbar\omega_p = 1$ eV and $\hbar\Gamma = 0.1$ eV. The insulating host is defined by: $\hbar\omega_{p,1} = 1$ eV and $\hbar\Gamma_1 = 1$ eV and $\hbar\omega_1 = 20$ eV. Note that the normal Drude curve is superimposed with the Bruggeman curve with $f = 1$.

5 Discussion

For the discussion of our data, we use the above models assuming small metallic CNT particles dispersed in an insulating glassy graphite (i.e., polycrystalline clusters of graphite) dielectric host-medium. We extracted the graphite's dielectric function (i.e., our host medium $\epsilon_i(\omega)$) by modelling the measured optical properties of HOPG [14] within the classical dispersion theory of Lorentz [12,13,20]. The best fits of MG and BM are shown in Fig. 3, while Table 2 presents the intrinsic parameters for the CNTs. Both models with filling factor $f = 0.6$ are able to reproduce all details of the measured FIR spectrum.

The main difference between the two models lies in the fitted scattering rate Γ (Table 2) which is considerably smaller, one order of magnitude, for the BM than for the MG model. Moreover, we also notice that $\omega_p(\alpha_{||}) > \omega_p(\alpha_{\perp})$ and that ω_p is slightly larger in BM compared to MG. According to the band structure

calculation performed by Tasaki et al. [5] in the tight binding model, the CNTs should be metallic in $\alpha_{||}$ and insulating in α_{\perp} . They also calculated the plasma frequency for $\alpha_{||}$ and found a value in agreement with the one obtained experimentally in this work. Tasaki et al. believe that the metallic behaviour found experimentally along α_{\perp} could originate from the disorder in the tube alignment [5]. This is possible, especially below the first few surface layers. Effectively, due to the tubes preparation – they were first β aligned, then mechanically α aligned – it is possible that we end up with a large spatial dispersion of the tubes which would account for the metallic behaviour in the α_{\perp} direction (see also below the discussion about the anisotropy).

Table 2. These parameters refer to the Maxwell-Garnett (Eq.(6)) and Bruggeman calculations with a filling factor $f \approx 0.6$. N denotes the geometrical factor. All other values are in eV.

h.o.	Maxwell-Garnett			Bruggeman		Glassy carbon
	$\alpha_{ }$	α_{\perp}	β	$\alpha_{ }$	α_{\perp}	
N	0.333	0.530	0.280	0.333	0.450	
$\hbar\omega_p$	0.140	0.115	0.119	0.162	0.123	
$\hbar\Gamma$	$1.54 \cdot 10^{-3}$	$4.30 \cdot 10^{-3}$	$4.10 \cdot 10^{-3}$	$1.67 \cdot 10^{-4}$	$4.42 \cdot 10^{-4}$	
$\hbar\omega_{p,1}$	0.397	0.486	0.336	0.439	0.423	1.00
$\hbar\Gamma_1$	0.106	0.269	0.138	0.153	0.271	0.770
$\hbar\omega_1$	$2.30 \cdot 10^{-2}$	$2.30 \cdot 10^{-2}$	$2.30 \cdot 10^{-2}$	$2.30 \cdot 10^{-2}$	$2.30 \cdot 10^{-2}$	0.165
$\hbar\omega_{p,2}$	4.81	2.89	0.259	4.81	2.89	4.03
$\hbar\Gamma_2$	7.52	4.77	0.204	7.52	4.77	4.30
$\hbar\omega_2$	1.20	1.20	0.167	1.20	1.20	1.31
$\hbar\omega_{p,3}$	3.14	1.77		3.14	1.77	1.30
$\hbar\Gamma_3$	3.13	1.99		3.13	1.98	1.41
$\hbar\omega_3$	2.50	2.50		2.50	2.50	2.50
$\hbar\omega_{p,4}$	6.69	6.15		6.69	6.15	2.96
$\hbar\Gamma_4$	1.04	1.36		1.04	1.36	1.04
$\hbar\omega_4$	4.96	4.96		4.96	4.96	4.22

The filling factor is in good agreement with estimation from electron microscopy [6]. A filling factor of about 0.6 was obtained in all cases. The filling factor sensitively determines the position of the resonance at ω_{rs} , which indeed shifts in frequency for different specimens. Moreover it is important to observe that f is already quite large and close to the boundary value for a percolation limit (which is ~ 0.7 for spheres and ~ 0.9 for cylinders). The realisation of such a limit would lead to a low frequency metallic Drude-like component in $\sigma_1(\omega)$ for the composite. At present, this possibility seems to be

ruled out in our specimens. Contrary to f , the geometrical factor N gives contrasting results. For α_{\perp} , the expected value of 0.5 (see Table 1) is experimentally satisfied. But for α_{\parallel} , the value of 0.3 (which corresponds to the value of a sphere) is unexpected for cylinders. According to Eq.(7) and Table 1, N should be smaller. However, the resonance at $\omega_{rs} = 7$ meV, is actually a convolution of several resonances corresponding to tubes with different geometrical shapes (i.e., the tubes might be bundled together or have different diameters or orientations). Such a convolution might lead to a distribution of geometrical factor N .

What is striking in our model calculations is the rather good agreement of the ω_p and Γ parameters for α_{\parallel} between our optical (in the MG model) and the ESR results [7]. In fact, the ESR scattering time $\tau^{\text{ESR}} = 10^{-13}$ s along the quasi one-dimensional CNTs implies a σ_{dc} of 10^3 S/cm for α_{\parallel} [7], which is in agreement with $\sigma_{dc} = \epsilon_0 \omega_p^2 / \Gamma = 1700$ S / cm evaluated from the optical parameters (Table 2). This suggests an intrinsic metallic behaviour of the single CNTs. In this respect, Fig. 12 presents the intrinsic reflectivity (a) and optical conductivity spectra (b) of a hypothetical "bulk" (i.e., $f = 1$) CNTs specimen, using the parameters of Table 2. The low frequency metallic behaviour is easily recognised. (The reflectivity tends to 100 % when the frequency goes to zero and

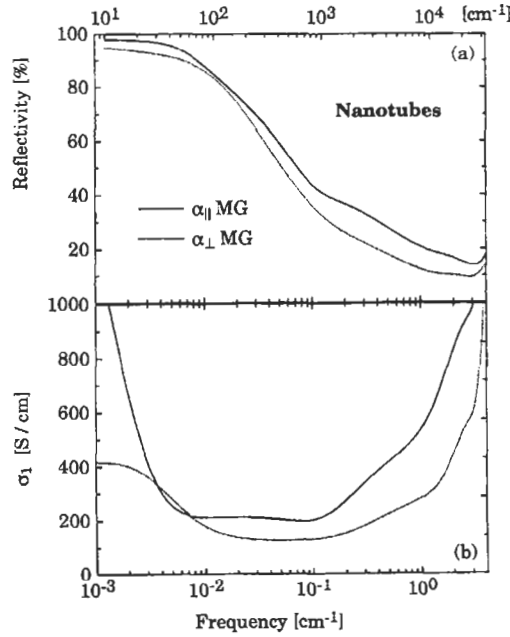


Fig. 12. (a) The intrinsic reflectivity and (b) optical conductivity calculated for a "bulk" CNTs specimen (i.e. $f = 1$). They were calculated within the MG framework with the parameters of Table 2 for both α_{\parallel} and α_{\perp} .

the optical conductivity displays a Drude behaviour. Moreover, the "bulk" calculations of Fig. 12 clearly point out the anisotropic behaviour between $\alpha_{||}$ and α_{\perp} . The dc value is about four times larger for $\alpha_{||}$ than for α_{\perp} . The anisotropy is mainly incorporated in the Γ values, while the plasma frequency does not change significantly in the different polarisation directions. The parameters for the β direction support a similar intrinsic behaviour of $\sigma_1(\omega)$ as for α_{\perp} (Fig. 4).

Our optical work clearly indicates a microscopic metallic behaviour of the CNTs. Dai et al. [22] performed microscopic electrical measurements. They established the resistivity of individual multi-walled CNTs (MWCNTs). Conventional lithography was used to contact electrically single ends of CNTs. A force microscope equipped with a conducting probe tip, allowed to map simultaneously the structure and the resistance of the material. They found a linear resistance vs. distance dependence for the tubes, leading to a resistivity of 78 m Ω cm at room temperature which corresponds to a dc conductivity of 13 S/cm i.e., two orders of magnitude lower than the one obtained by optical investigations. But the authors of ref. 22 consider their value as an upper limit to the intrinsic resistivity of a perfect MWCNT. As a matter of fact, impurities and structural defects in the CNTs increase the resistivity through electron scattering relative to an ideal structure. Therefore, Dai et al. believe that studies of single-walled CNT (SWCNT) (see below) will ultimately provide an intrinsic conductivity measurement of CNTs [22]. This would also make possible a more realistic comparison with theory [1,5], since SWCNTs instead of MWCNTs have been theoretically investigated in detail.

6 Conclusion

The possible metallic nature of CNTs was an open question and a matter of debate which we addressed from the optical point of view. We have interpreted our optical results of oriented CNT films within the effective medium Maxwell-Garnett and Bruggeman models. This analysis allowed us to establish the intrinsic metallic nature of the CNTs, with intrinsic parameters (see Table 2) in agreement with those inferred by other contactless techniques, as ESR, and theoretical calculations. On the other hand, resistivity measurements on single CNTs give evidence for a conductivity up to two orders of magnitude smaller than the one obtained by optical means. In addition, the optical results indicate a remarkable anisotropic conductivity between $\alpha_{||}$, α_{\perp} and β . Our findings further enforce the interpretation of dc resistivity measurements being strongly affected by contact effects and intertube hopping.

As future outlook, it would be of great relevance to be able to eventually enhance the intrinsic conductivity of CNTs. In this respect, the latest development in alkali metal intercalated CNTs looks rather promising. In fact, Chauvet et al. recently succeeded to dope aligned CNT by potassium and found that the Pauli susceptibility increases a factor of 3 upon doping, indicating that K-doped tubes are still good conductors [23].

To conclude this work, we would like to digress on some possible applications of the materials investigated here. The exceptionally good electron field emitting characteristics of the CNTs make them potentially very attractive for applications in devices such as displays or electron microscopes as shown by W. A. de Heer and co-worker [24]. One can also imagine to use them for nanoscale devices or take a single CNT as an electric wire. This would probably be the ultimate level of miniaturisation in microchip technology. Indeed and just to quote one single example, Collins et al. recently succeeded in measuring the conductivity of SWCNTs by scanning tunnelling microscope [25]. The conductivity changes as the active length of the CNT is increased, suggesting that different segments of the CNT exhibit different electronic properties. Carbon with its wide range of sp bond hybridisation appears as the key element of a future nanotechnology. However, so far there is almost no control over the formation processes, and the structures of interest cannot be built at will. Tubes, for example, are produced under the very virulent conditions of a plasma discharge and one would like to have more elegant tools to manipulate the carbon structures, a task which remains a challenge for the future.

Acknowledgements

The authors are very grateful to P. Wachter for the generous support in providing the access to the technical facilities, and to K. Sattler and D. Ugarte for fruitful discussions, and to J. Müller for technical assistance. One of us (L.D.) wishes to acknowledge the financial support of the Swiss National Foundation for the Scientific Research and of the ETH Research Council.

References

1. Iijima, S., *Nature*, 1991, **354**, 56.
2. Mintmire, J. W., Dunlap, B. I. and White, C. T., *Phys. Rev. Lett.*, 1992, **68**, 631.
3. Hamada, N., Sawada, S. and Oshiyama, A., *Phys. Rev. Lett.*, 1992, **68**, 1579.
4. Blase, X., Benedict, L. X., Shirley, E. L. and Louie, S. G., *Phys. Rev. Lett.*, 1994, **72**, 1878.
5. Tasaki, S., Maekawa, K. and Yamabe, T., *Phys. Rev. B*, 1998, **57**, 9301.
6. de Heer, W. A., Bacsá, W. S., Châtelain, A., Gerfin, T., Humphrey-Baker, R., Forro, L. and Ugarte, D., *Science*, 1995, **268**, 845.
7. Chauvet, O., Forro, L., Bacsá, W. S., Ugarte, D., Doudin, B. and de Heer, W. A., *Phys. Rev. B*, 1995, **52**, R6963.
8. van der Pauw, L. J. *Philips Res. Rept.*, 1958, **13**, 1.
9. Ramirez, A. P., Haddon, R. C., Zhou, O., Fleming, R. M., Zhang, J., McClure, S. M. and Smalley, R. E., *Science*, 1994, **265**, 84.
10. Bacsá, W. S., de Heer, W. A. and Forro, L., private communication.
11. Ebbesen, T. W. and Ajayan, P. M., *Nature*, 1992, **358**, 220.
12. Bommeli, F., Degiorgi, L., Wachter, P., Bacsá, W. S., de Heer, W. A. and Forro, L., *Solid State Commun.*, 1996, **99**, 513.
13. Bommeli, F., Ph. D. thesis, ETH-Zurich, 1997.

14. Taft, E. A. and Philipp, H. R., *Phys. Rev.*, 1965, **138**, A 197.
15. Simon, Ch., Batallan, F., Rosenman, I., Lauter, H. and Furdin, G., *Phys. Rev. B*, 1983, **27**, 5088.
16. Lamb, W., Wood, D. M. and Ashcroft, N. W., Electrical transport and optical properties of inhomogeneous media, AIP conference, J. C. Garland and D. B. Tanner, Ohio State University, 1977.
17. Cohen, R. W., Cody, G. D., Coutts, M. D. and Abeles, B., *Phys. Rev. B*, 1973, **8**, 3689.
18. Bruggeman, D. A. G., *Ann. Phys.*, 1935, **24**, 636.
19. van de Hulst, H. C., *Light Scattering by Small Particles*, Dover Publication, New York, 1981.
20. Wooten, F., *Optical Properties of Solids*, Academic Press, San Diego, 1972.
21. Noh, T. W., Kaplan, S. G. and Sievers, A. J., *Phys. Rev. B*, 1990, **41**, 307 and references therein.
22. Dai, H., Wong, E. W. and Lieber, C. M., *Science*, 1996, **272**, 523.
23. Chauvet, O., Baumgartner, G., Carrard, M., Bacsá, W. S., Ugarte, D., de Heer, W. A. and Forro, L., *Phys. Rev. B*, 1996, **53**, 13996.
24. de Heer, W. A., Châtelain, A. and Ugarte, D., *Science*, 1995, **270**, 1179.
25. Collins, P.G., Zettl, A., Brando, H., Thess, A. and Smalley, R. E., *Science*, 1997, **278**, 100.

CHAPTER 10

Electrical Transport Properties in Carbon Nanotubes

JEAN-PAUL ISSI and JEAN-CHRISTOPHE CHARLIER

*Unité de Physico-Chimie et de Physique des Matériaux
Université Catholique de Louvain
1, Place Croix du Sud, B-1348 Louvain-la-Neuve, Belgium*

1 Introduction

In a prophetic vision of our physical world, Richard Feynman issued in 1959 his famous statement "There is plenty of room at the bottom". He was essentially suggesting experiments and technologies which could be performed at extremely small scales. We know nowadays that Feynman's expectations were beyond what has been achieved since he made his prediction.

Carbon nanotubes (CNTs) should be included among these fascinating developments of the nanoworld which took place at the end of this millennium. These tiny entities, which may be considered as elongated fullerenes in a bottom up approach, or as ultimate carbon fibres viewed from our macroworld, consist in one (single-walled) or more (multi-walled) seamless cylindrical shells of graphitic sheets. Each cylinder can be visualised as the conformal mapping of a 2D honeycomb lattice onto its surface. These systems combine reduced dimensionality and small size which allows to probe physics in 2, 1 or 0 dimension and, when the temperature is lowered, to observe quantum effects at the nanoscopic scale. Dimensionality as well as mesoscopic regime are relative concepts. On one hand, all real systems are 3D, but some properties may, under certain conditions, be approximated by means 2, 1 or 0D models. On the other hand, the same sample may be considered as macroscopic under certain conditions (temperature, magnetic field, ...) and mesoscopic if these conditions are modified. These considerations are well illustrated for the case of carbons and graphites, as will be shown below.

In order to discuss electron transport properties we need to know about the electronic distribution. This means that, for the case of metals and semimetals, we must have a model for the Fermi surface and for the phonon spectrum. The electronic structure is discussed in Chap. 5. We also need to estimate or determine some characteristic lengths.

For multi-walled CNT (MWCNT), as for the case of graphites, some specific aspects need to be considered:

- the *semimetallic behaviour* which has a drastic effect on the band structure and on the scattering mechanisms
- the effects of *reduced dimensionality*
- the impact of weak disorder, mainly in relation to *quantum aspects of conduction*
- the possibility of *intercalation* and its effects.

The results of electrical resistivity measurements on CNTs have revealed so far interesting pieces of information. MWCNT behaves as an ultimate carbon fibre. At high temperature its electrical conductivity may be described by means of the semiclassical models which were successful in describing graphite. At low temperature, they reveal 2D quantum transport features, one of them having previously been observed in bulk carbons and graphites (weak localisation), while the other can only be observed in a mesoscopic form (universal conductance fluctuations). Single-walled CNTs (SWCNTs) should behave instead as pure quantum wires, which, if limited in length, reduce to quantum dots. Oddly enough, in the first case we are facing an exceptional physical system, a 1D conductor with vanishingly small Peierls distortion. So, each type of CNT has its own features which are strongly dependent on the dimensionality of the system. Whether single- or multi-walled, we will show below how interesting the physics of these systems is.

After briefly introducing the main electronic features of CNTs (Sec. 2) and some general aspects of electronic conduction and transmission (Sec. 3), we will show how complex electrical measurements to perform on such tiny entities are (Sec. 4). Then we will present the main experimental results obtained on the electrical resistivity of MWCNT and SWCNT and the very recent data relative to the thermopower of SWCNT bundles (Sec. 5). We will also discuss the effect of intercalation on the electrical resistivity of SWCNT bundles (Sec. 6). Finally, we will present some potential applications (Sec. 7).

2 Main Electronic Features

Using the notion of helicity introduced by Iijima [1], three types of CNTs are defined: *armchair*, *zigzag* and *chiral* CNTs, depending on how the two-dimensional (2D) graphene sheet is rolled up. Such classification is easily explained in terms of the unit cell (Fig. 1(a)) and the so-called chiral vector of the CNT, C_h , which is defined by $C_h = n \mathbf{a}_1 + m \mathbf{a}_2$, where \mathbf{a}_1 and \mathbf{a}_2 are unit vectors in the bidimensional hexagonal lattice, and n and m are integers. When the graphene sheet is rolled up to form the cylindrical part of the CNT, the ends of the chiral vector meet each other. The chiral vector thus forms the circumference of the CNTs circular cross-section, and different values of n and m lead to different CNT structures. Armchair CNTs are formed when $n=m$ (the carbon-carbon bond being perpendicular to the tube axis); and zigzag ones when n or m are zero (the carbon-carbon bond being parallel to the tube axis). All other (n, m) CNTs are known as chiral ones.

The unique electronic properties of CNTs are due to the quantum confinement of electrons normal to the CNT axis. In the radial direction, electrons are

confined by the monolayer thickness of the graphene sheet. Around the circumference of the CNT, periodic boundary conditions come into play. Because

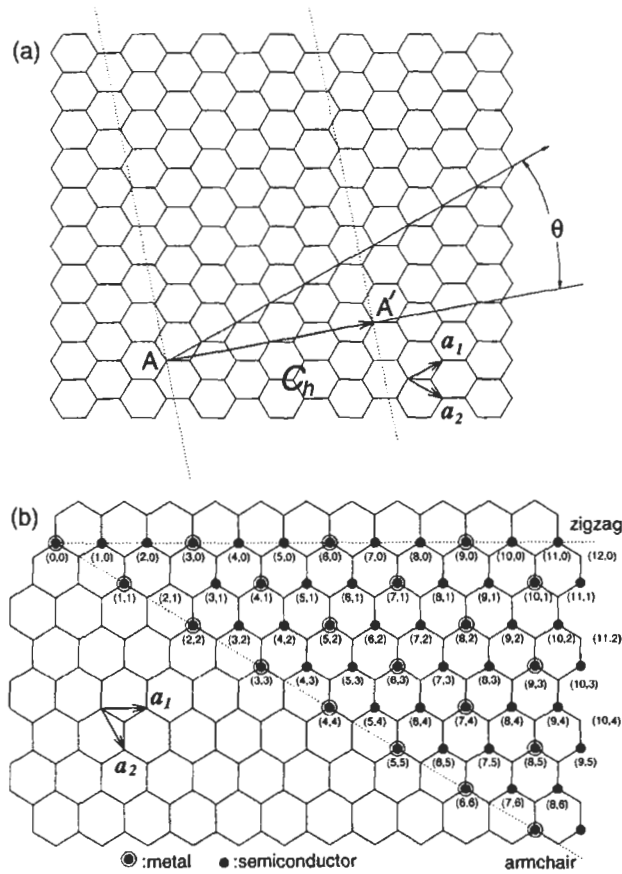


Fig. 1. (a) The vectors AA' or $C_h = n a_1 + m a_2$ on the honeycomb lattice defined by unit vectors a_1 and a_2 , and the chiral angle θ with respect to the zigzag axis: (b) A graphite sheet that, when rolled up in such a way as to superimpose the origin (0, 0) on a given hexagon in the sheet, a CNT will result with the properties indicated in the edge of each hexagon: large dots and small bullets, denoting metallic (or narrow band gap semiconductor) and moderate band gap semiconducting behaviour, respectively [3].

of this quantum confinement, electrons can only propagate along the CNT axis, and so their wavevectors point in this direction. The resulting number of 1D conduction and valence bands effectively depends on the standing waves that are set up around the circumference of the CNT. Early theoretical works [2-4] have reported on the calculation of dispersion relations of these 1D bands for different

types of CNTs. All these calculations lead to one important conclusion: the electronic properties of the CNT should vary in a periodic way from metallic to semiconductor as a function of both diameter and helicity. These studies show that about one-third of SWCNTs are metallic, while the others are semiconducting with a band gap inversely proportional to the tube diameter. In general, an (n, m) CNT is metallic when $|n-m| = 3q$, where q is an integer (Fig. 1(b)). All armchair CNTs are metallic, as are one third of all possible zigzag CNTs. Although conventional metals have a smooth density of states (DOS), the CNT DOS are characterised by a number of singularities, where each peak corresponds to a single quantum subband. These singularities are important when interpreting experimental results, such as scanning tunnelling spectroscopy (STS) and resonant Raman spectra.

Experiments to test these remarkable theoretical predictions have been extremely difficult to carry out, largely because the electronic properties are expected to depend strongly on the diameter and the chirality of the CNT. Apart from the problems associated with making electronic measurements on structures just a nanometer across, it is also crucial to gain information on the symmetry of the CNT. Recently, the Delft [5] and Harvard [6] groups used scanning tunnelling microscope (STM) probes at low temperature to observe the atomic geometry (the CNT diameter and helicity), and to measure the associated electronic structure (DOS). The singularities in the DOS are very clearly seen in STS studies at 4 K [5]. Furthermore, a non-zero DOS at the Fermi level is reported [6] in the metallic CNTs, as expected; and a vanishingly small DOS is measured in the semiconducting CNTs. Both groups also confirm an inverse linear dependence of the band gap on the CNT diameter. These experiments [5,6] have provided the clearest confirmation to date that the electronic DOS have singularities typical of a 1D system.

3 Electrical Conduction and Transmission

The expression for the Boltzmann electrical conductivity for a given group of charge carriers is given by:

$$\sigma = eN\mu = \frac{e^2 N \tau}{m^*} \quad (1)$$

where e is the electronic charge, N the charge carrier density, μ the mobility, τ the relaxation time and m^* the carrier effective mass. The mean free path, $l = v_F \tau$, is the distance travelled between two collisions.

If there is more than one type of carrier, i.e. electrons and positive holes, as in MWCNT, the contribution of each type of carrier should be taken into account. In that case, the total electrical conductivity is given by the sum of the partial conductivities.

The main contributions to the electrical resistivity of metals, ρ , consists of an intrinsic temperature-sensitive ideal term, ρ_i , which is mainly due to electron-

phonon interactions and an extrinsic temperature independent residual term, ρ_r , due to static lattice defects:

$$\rho = \rho_r + \rho_i \quad (2)$$

So, the resistivities due to various scattering mechanisms add, as well as the contributions to the conductivity from different carrier groups.

Static defects scatter elastically the charge carriers. Electrons do not loose memory of the phase contained in their wave function and thus propagate through the sample in a coherent way. By contrast, electron-phonon or electron-electron collisions are inelastic and generally destroy the phase coherence. The resulting *inelastic mean free path*, L_{in} , which is the distance that an electron travels between two inelastic collisions, is generally equal to the phase coherence length, the distance that an electron travels before its initial phase is destroyed:

$$L_\phi = \sqrt{D\tau_\phi} \quad (3)$$

where D is the diffusion constant. This expression shows that the motion between two phase-randomising collisions is diffusive.

In the presence of weak disorder, one should consider an additional contribution to the resistivity due to *weak localisation* resulting from quantum interference effects and/or that due to *Coulomb interaction* effects. A single-carrier weak localisation effect is produced by constructive quantum interference between elastically back-scattered partial-carrier-waves, while disorder attenuates the screening between charge carriers, thus increasing their Coulomb interaction. So, both effects are enhanced in the presence of weak disorder, or, in other words, by defect scattering. This was previously discussed for the case of carbons and graphites [7].

These quantum effects, though they do not generally affect significantly the magnitude of the resistivity, introduce new features in the low temperature transport effects [8]. So, in addition to the semiclassical ideal and residual resistivities discussed above, we must take into account the contributions due to quantum localisation and interaction effects. These localisation effects were found to confirm the 2D character of conduction in MWCNT. In the same way, experiments performed at the mesoscopic scale revealed quantum oscillations of the electrical conductance as a function of magnetic field, the so-called universal conductance fluctuations (Sec. 5.2).

At low temperatures, in a sample of very small dimensions, it may happen that the phase-coherence length in Eq.(3) becomes larger than the dimensions of the sample. In a perfect crystal, the electrons will propagate ballistically from one end of the sample and we are in a *ballistic regime* where the laws of conductivity discussed above no more apply. The propagation of an electron is then directly related to the quantum probability of transmission across the global potential of the sample.

4 Experimental Challenges

After the theoretical predictions concerning the electronic properties of CNTs were made, there was a crucial need for experiments which would confirm the validity of these models. This is particularly true for the electronic band structure. It was felt that the theoretical predictions concerning this structure in CNTs would be difficult to verify experimentally because of the strong dependence of the predicted properties on their diameter and chirality. This means that the electronic DOS should be determined on individual SWCNTs, that have been assigned the right diameter and chiral angle. It was only very recently that this has been finally verified experimentally [5,6]. Furthermore, since CNTs are often produced in bundles, obtaining data on single, well-characterised CNTs is a challenging performance.

Concerning the electrical conductivity, it is generally a rather easy task to determine whether a macroscopic sample is electrically conductive or not, since, except for extreme cases of very low or very high values, electrical resistivity is one of the easiest measurement to perform. However, the measurement of very tiny samples such as CNTs, metal microtubules, single crystals of fullerenes and of charge transfer salts, fibrils of conducting polymers,... requires a drastic miniaturisation of the experimental techniques, which leads to very delicate handling and requires a high degree of sophistication. This is particularly the case for CNTs, where one has to deal with samples with diameters of the order of a nanometer, i.e. the equivalent of a few interatomic distances! One has first to detect a sample among others, then apply to it electrical contacts, which means four metallic conductors, two for the injected current and two for measuring the resulting voltage. Indeed, in order to test the theoretical predictions concerning the electronic properties of CNTs by means of electrical resistivity measurements, one has to solve at least two delicate experimental problems:

- to realise a four-probe measurement on a single CNT. This means that one has to attach four electrical connexions on a sample of a few nm diameter and about a μm length. This requires the use of nanolithographic techniques [9,10].
- to characterise this sample with its contacts in order to determine its diameter and helicity.

For CNT bundles (ropes), it is somewhat easier to attach electrical contacts. This is probably why thermoelectric power measurements were first performed on CNT bundles [11]. For these measurements an additional problem is that one has to establish a temperature gradient along the sample, and, in addition to the voltage difference resulting from this gradient, one has to measure the corresponding temperature difference. Thermal conductivity measurements are even more delicate to realise, since one has to avoid heat losses to the surroundings when one end of the sample is heated. This is a formidable problem to solve when we consider the small conductance of the sample due to its very small diameter. However, one can take advantage of the low dimensionality of the samples in that sense that heat will be conducted preferentially along the sample axis, thus reducing to some extent radial heat losses.

Fortunately, in parallel to the CNT story, the field of nanotechnology, including nanolithography, have made tremendous strides. By using an STM,

experimentalists were soon able to realise metallic structures of several nm dimensions and, eventually, to manipulate individual atoms and molecules. By applying these newborn technical achievements to CNTs, Langer *et al.* [9] succeeded in depositing electrical contacts on a *single microbundle* of 50 nm diameter. They used nanolithographic patterning of gold films with an STM to attach electrical contacts to the microbundle and have measured its electrical resistivity down to 0.3 K (Fig. 2). However, these first results did not allow a direct quantitative comparison with the existing theoretical predictions for mainly two reasons. First, all the conducting CNTs in the bundle are not necessarily contacted electrically. Second, when they are not single-walled, the unknown cross sections of the CNTs where conduction takes place is affected by their inner structure.

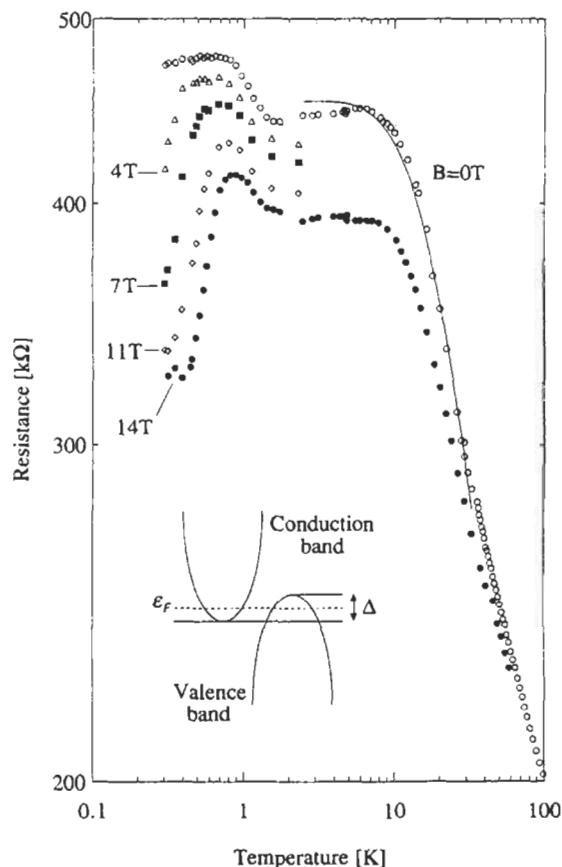


Fig. 2. Electrical resistance as a function of the temperature at the indicated magnetic fields for a bundle of CNTs. The dashed lines separate three temperature ranges, while the continuous curve is a fit using the two-band model for graphite (see inset) with an overlap of 3.7 meV and a Fermi level right in the middle of the overlap [9].

Later on, Langer *et al.* [10] succeeded in 1996 in depositing three electrical contacts on an individual multi-walled nested CNT about 20 nm in diameter. These results suggested that it was possible to attach electrodes to tiny SWCNT devices that are less than 1.5 nm in diameter, the only way to compare theory and a measurement on a CNT. An important breakthrough in that direction was first made by Smalley's group at Rice University, who obtained large quantities of long SWCNTs produced by laser-vapourisation of carbon with a Ni/Co admixture [12]. 30 to 40 % of these CNTs were found to be armchair (10, 10) tubes, which are expected to be 1D conductors. Having at hand these SWCNTs with high yields and structural uniformity combined with modern nanolithographic techniques, two groups presented new interesting results. Electrical measurements on these materials were performed by researchers at the Lawrence Berkeley Institute and the University of California. They observed transport through ropes of CNTs between two contacts separated by 200 to 500 nm [13]. Finally, experiments on individual SWCNT were performed by the Delft group [14].

We will discuss below the recent experimental observations relative to the electrical resistivity and magnetoresistance of individual and bundles of MWCNTs. It is interesting to note however that the ideal transport experiment, i.e., a measurement on a well characterised SWCNT at the atomic scale, though this is nowadays within reach. Nonetheless, with time the measurements performed tended gradually closer to these ideal conditions. Indeed, in order to interpret quantitatively the electronic properties of CNTs, one must combine theoretical studies with the synthesis of well defined samples, which structural parameters have been precisely determined, and direct electrical measurements on the same sample.

5 Experimental Results

5.1 General

The fractal-like organisation of CNTs produced by classical carbon arc discharge suggested by Ebbesen *et al.* [15] lead to conductivity measurements which were performed at various scales.

Ebbesen and Ajayan [16] measured a conductivity of the order of $10^{-2} \Omega\text{cm}$ in the black core bulk material, inferring that the carbon arc deposit contains electrically conducting entities. A subsequent analysis of the temperature dependence of the electrical resistivity of similar bulk materials [17,18] revealed that the resistivities were strongly sample dependent.

Later on, Song *et al.* [19] performed a four-point resistivity measurement on a large bundle of CNTs of 60 μm diameter and 350 μm distance between the two voltage probes. They interpreted their resistivity, magnetoresistance and Hall effect results in terms of semimetallic conduction and 2D weak localisation as for the case of disordered turbostratic graphite.

Several months later, Langer and co-workers measured a microbundle of total diameter around 50 nm of MWCNTs [9]. At high temperature a typical

semimetallic behaviour was observed which was ascribed to rolled up graphene sheets. Then, Langer *et al.* [10] measured the electrical resistivity of an individual MWCNTs, with three electrical contacts, down to 20 mK in the presence of a transverse magnetic field. A room temperature electrical resistivity of $\approx 10^{-4} \Omega\text{cm}$ was estimated for the single CNT [10] and of $\approx 10^{-3} \Omega\text{cm}$ for the microbundle [9].

Moreover, as shown by two further publications [20,21], the electrical properties of MWCNTs were found to vary significantly from one tube to another.

Whitesides and Weisbecker [22] developed a technique to estimate the conductivity of single CNTs by dispersing CNTs onto lithographically defined gold contacts to realise a 'nano-wire' circuit. From this 2-point resistance measurement and, after measuring the diameter of the single CNTs by non-contact atomic force microscopy (AFM), they estimated the room-temperature electrical resistivity along the CNT axis to be around $10^{-2} \Omega\text{cm}$.

The electrical measurements performed by Bockrath *et al.* [13] revealed a gap in the current-voltage curves at low temperatures and peaks in the conductance as a function of the gate voltage. Although the interpretation in terms of single-electron charging and resonant tunnelling through the quantised energy levels accounted for the major features in the data, many interesting aspects still remained to be explored. In fact, it was not clear whether electrical transport was indeed occurring predominantly along a single tube. Experiments on individual SWCNTs were then performed by the Delft group [14]. The SWCNT appeared to behave as a genuine coherent quantum wire or dot. However, since the group in Delft did not determine the structural parameters of the measured samples, a direct link to a theoretical simulation was not possible.

We have seen that to a given dimensionality is associated a specific quantum transport behaviour at low temperature: while some MWCNTs seem to be 2D systems, SWCNTs behave as 1D or 0D systems.

5.2. Electrical resistivity and magnetoresistance of MWCNT

Above 2 K, the temperature dependence of the zero-field resistivity of the microbundle measured by Langer *et al.* [9] was found to be governed by the temperature dependence of the carrier densities and well described by the simple two-band (STB) model derived by Klein [23] for electrons, n , and hole, p , densities in semimetallic graphite:

$$n = C_n k_B T \ln \left[1 + \exp\left(\frac{\epsilon_F}{k_B T}\right) \right] \quad (4)$$

and

$$p = C_p k_B T \ln \left[1 + \exp\left(\frac{\Delta - \epsilon_F}{k_B T}\right) \right] \quad (5)$$

where ϵ_F is the Fermi energy and Δ is the band overlap. C_n and C_p are the fitting parameters.

From Eqs.(4) and (5) a value of nearly 4 meV was obtained for the band overlap, with the Fermi energy right in the middle of the overlap. This value of the overlap is small compared to that of 40 meV for highly oriented pyrolytic graphite (HOPG). This large difference was ascribed to the turbostratic stacking of the adjacent layers which should reduce drastically the interlayer interactions, like in disordered graphite. Within the frame of the STB model, the smaller overlap implies that the carrier density is also one order of magnitude smaller than in HOPG.

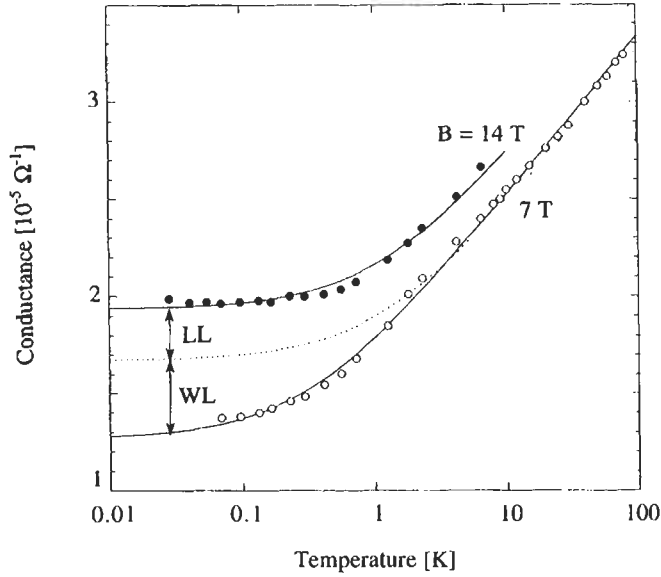


Fig. 3. Electrical conductance of an MWCNT as a function of temperature at the indicated magnetic fields. The solid line is a fit to the data (see ref. 10). The dashed line separates the contributions to the magnetoconductance of the Landau levels and the weak localisation [10].

By applying a magnetic field normal to the tube axis of the microbundle, Langer *et al.* [9] observed a magnetoresistance which, in contrast to the case of graphite, remained negative at all fields. The negative magnetoresistance was found consistent with the formation of a Landau level predicted by Ajiki and Ando [24]. This Landau level, which should lie at the crossing of the valence and conduction bands, increases the DOS at the Fermi level and hence lowers the resistance. Moreover, the theory predicts a magnetoresistance which is temperature independent at low temperature and decreasing in amplitude when $k_B T$ becomes larger than the Landau level. This is also what was experimentally observed.

Langer *et al.* [10] measured also electrical resistance of *individual MWCNTs* at very low temperatures and in the presence of a transverse magnetic field. As for the case of the microbundle, the CNTs were synthesised using the standard carbon arc-discharge technique. Electrical gold contacts have been attached to the CNTs via local electron beam lithography with an STM. The measured individual MWCNT had a diameter of about 20 nm and a total length of the order of 1 μm .

In Fig. 3 we present the temperature dependence of the conductance for one of the CNTs, measured by means of a three-probe technique, in respectively zero magnetic field, 7 T and 14 T. The zero-field results showed a logarithmic decrease of the conductance at higher temperature, followed by a saturation of the conductance at very low temperature. At zero magnetic field the saturation occurs at a critical temperature, $T_c = 0.3$ K, which shifts to higher temperatures in the presence of a magnetic field.

As was the case for the microbundle, a significant increase in conductance, i.e. a *positive magnetoconductance* (negative magnetoresistance), appears in the presence of a magnetic field normal to the tube axis. Both the temperature and field dependences of the CNT conductance were interpreted consistently in the frame of the theory for 2D weak localisation [10] that we discussed above. However, for the particular case of CNTs one must take into account that, owing to the very small dimensions of the sample, we are close to the mesoscopic regime in the lowest temperature range [10]. This situation is responsible for the conductance fluctuations that we will discuss in the following paragraphs.

For the case studied, 2D weak localisation predicts that the resistance should be independent of magnetic field in the temperature range where it varies as a logarithmic function of T . One may see that this is not what is observed. The data in Fig. 3 show that there is an additional contribution to the magnetoconductance of the CNT which is temperature dependent up to the highest temperature investigated, including in the $\log T$ variation range. This magnetoconductance was ascribed to the formation of Landau states which we discussed above for the case of the CNT microbundle. Both 2D weak localisation and "Landau level" contributions to the magnetoconductance can be separated as illustrated in Fig. 3.

Typical magnetoconductance data for the individual MWCNT are shown in Fig. 4. At low temperature, reproducible aperiodic fluctuations appear in the magnetoconductance. The positions of the peaks and the valleys with respect to magnetic field are temperature independent. In Fig. 5, we present the temperature dependence of the peak-to-peak amplitude of the conductance fluctuations for three selected peaks (see Fig. 4) as well as the rms amplitude of the fluctuations, $\text{rms}[\Delta G]$. It may be seen that the fluctuations have constant amplitudes at low temperature, which decrease slowly with increasing temperature following a weak power law at higher temperature. The turnover in the temperature dependence of the conductance fluctuations occurs at a critical temperature $T_c^* \approx 0.3$ K which, in contrast to the T_c values discussed above, is independent of the magnetic field. This behaviour was found to be consistent with a quantum transport effect of universal character, the *universal conductance fluctuations* (UCF) [25,26]. UCFs were previously observed in mesoscopic weakly disordered

metals [27,28] and semiconductors [29,30] of various dimensionalities. In such systems, where the size of the sample, L , is smaller or comparable to both L_ϕ , the phase coherence length, and the thermal diffusion length:

$$L_T = \left(\frac{\hbar D}{k_B T} \right)^{1/2} \quad (6)$$

elastic scattering of electron wave functions generates an interference pattern which gives rise to a sample-specific, time-independent correction to the classical conductance [31]. The interference pattern, and hence the correction to the conductance, can be modified by either applying a magnetic field or by changing the electron energy in order to tune the phase or the wavelength of the electrons, respectively [27-30]. The resulting phenomenon is called universal conductance fluctuations, because the amplitude of the fluctuations ΔG has a universal value: $\text{rms}[\Delta G] \approx q^2/h$ as long as the sample size, L , is smaller than L_ϕ and L_T . When the relevant length scale, L_ϕ or L_T , becomes smaller than L , the amplitude of the observed fluctuations decreases due to self-averaging of the UCF in phase-coherent subunits. When the relevant length scale decreases with temperature, the amplitude of the fluctuations decreases as a weak power law: $T^{-\alpha}$ where α depends on dimensionality and limiting diffusion length, L_ϕ or L_T [31]. $\alpha = 1/2$ for a 2D system with $L_\phi \ll L, L_T$.

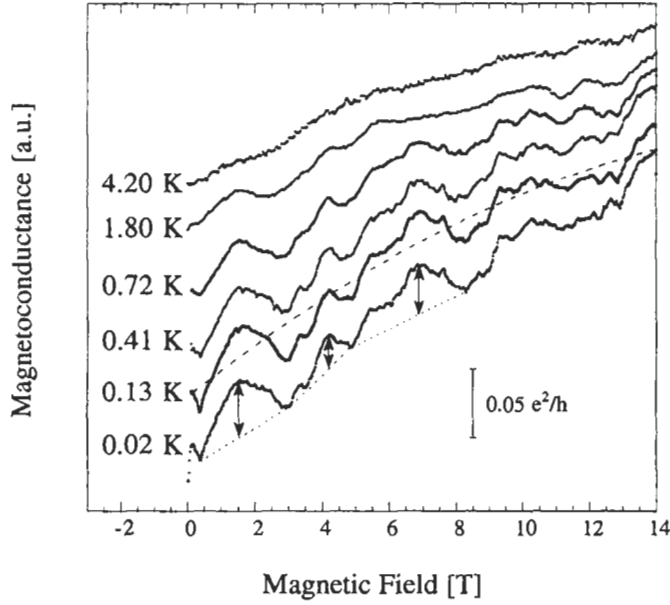


Fig. 4. Magnetic-field dependence of the magnetoconductance of an MWCNT at different temperatures [10].

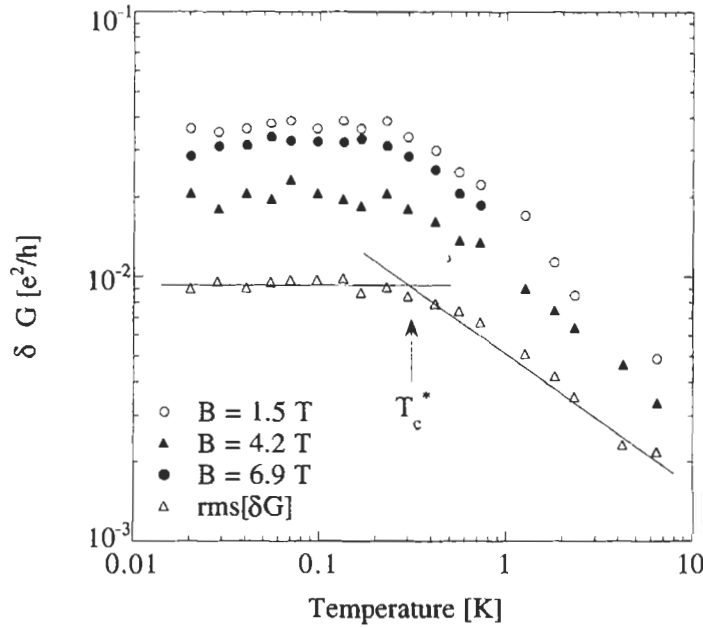


Fig. 5. Temperature dependence of the amplitude of δG for three selected peaks [10].

So, despite the very small diameter of the MWCNT with respect to the de Broglie wavelengths of the charge carriers, the cylindrical structure of the honeycomb lattice gives rise to a 2D electron gas for both weak localisation and UCF effects. Indeed, both the amplitude and the temperature dependence of the conductance fluctuations were found to be consistent with the universal conductance fluctuations models for mesoscopic 2D systems applied to the particular cylindrical structure of MWCNTs [10].

5.3 Transport in individual SWCNT and bundles

5.3.1 Electrical resistivity

Electrical resistivity measurements have also been performed on individual SWCNT and on bundles of SWCNT. In the latter case thermoelectric power measurements have been carried out very recently (cf. Sec. 5.3.2).

As shown above, experiments on individual MWCNTs allowed to illustrate a variety of new electrical properties on these materials, including 2D quantum interference effects due to weak localisation and UCFs. However, owing to the relatively large diameters of the concentric shells, no 1D quantum effects have been observed. In addition, experimental results obtained on MWCNTs were found difficult to interpret in a quantitative way due to simultaneous contributions of concentric CNTs with different diameters and chiralities.

The experiments recently performed by the Delft group on individual SWCNTs [14] have inferred their 1D nature. They suggest that SWCNTs behave as quantum wires, or quantum dots in the case of small lengths, which was the case for the tubes investigated so far. Indeed, though their length to diameter ratio may be very large, the finite length of the tubes (a few micrometers) limits the number of allowed wavevectors along the CNT axis. This gives rise to discrete energy states, which can be detected by measuring the conductance as a function of the voltage. For a CNT with 3- μm length, the Delft group [14] found that discrete states near the Fermi level are separated in energy by about 0.4 meV. This value is consistent with a "particle-in-a-box" energy separation between levels of a 3- μm -long 1D tube:

$$\Delta E = \frac{\hbar v_F}{2L} \cong 0.6 \text{ meV} \quad (7)$$

where L is the length of the CNT and the Fermi velocity, v_F , is estimated to be around $8 \times 10^5 \text{ ms}^{-1}$.

Coulomb charging effects have also been observed in SWCNT. The energy needed to add an electron to an SWCNT is 2.6 meV. This is the energy needed to overcome the Coulomb repulsion between electrons. Coulomb charging occurs when the contact resistance is larger than the quantum resistance ($R_K = \hbar/e \cong 26 \text{ k}\Omega$) and when the total capacitance C of the system is so small that adding a single electron costs a significant charging energy:

$$E_c = \frac{e^2}{C} \cong 2.5 \text{ meV} \quad (8)$$

where $C \cong 3 \times 10^{-17} \text{ F}$ is estimated as the geometrical self-capacitance of a 3- μm -long tube. At low temperature, that is when $k_B T \ll E_c$, the current is thus blocked (Coulomb blockade) and will flow only when a threshold bias voltage will be applied ($V_{bias} > e/2C$).

Peaks were also observed in the electrical conductance of individual bundles (ropes) of SWCNTs as a function of the gate voltage that modulated the number of electrons in the rope [13]. The results were interpreted in terms of single-electron charging and resonant tunnelling through the quantised energy levels of the 1D SWCNTs that constitute the rope. Recent calculations [32] have shown that the interaction between tubes in a rope could induce a pseudogap of about 0.1 eV at the Fermi level. This pseudogap should strongly modify the electronic properties, thus predicting a semimetal-like temperature dependence of the electrical conductivity. The existence of both electron and hole charge carriers would also lead to different thermopower and Hall-effect behaviours from those expected from a typical metal with one type of carriers.

An SWCNT a few microns long with electrical contacts deposited via nanolithography techniques is an ideal system to study single-molecule transistor effects, in which an electrode (V_{gate}) close to the conducting CNT is used to modulate the conductance [33].

A determination of the structural (n, m) parameters of the samples investigated is still needed in order to establish a direct link to theoretical simulations.

5.3.2 Thermoelectric power

The thermoelectric power (TEP) or Seebeck coefficient, S , is defined as the potential difference, ΔV , resulting from an applied unit temperature difference, ΔT , across an electrical conductor. On one hand, the *diffusion thermoelectric power*, is due to the diffusion of charge carriers from hot to cold caused by the redistribution of their energies due to the difference in temperature. Charge carriers tend to accumulate at the cold end of the sample giving rise to an electric field. This field acts to counterbalance the stream of diffusing carriers until a steady state is reached. On the other hand, the *phonon drag thermoelectric power* consists in an anisotropic transfer of momentum from the phonon system to the electron system when the coupling between the two systems is strong. This results in a drag on the charge carriers causing an extra electronic drift with an additional electric field to counterbalance it.

The general expression for the diffusion thermoelectric power for a given group of charge carriers is given by the Mott formula:

$$S_d = \frac{\pi^2 k_B^2}{3e} T \left[\frac{\partial \ln \sigma}{\partial \epsilon} \right]_{\epsilon_F} \quad (9)$$

where σ is the electrical conductivity and the derivative is taken at the Fermi level. It may be seen from Eq.(9) that, for a given scattering mechanism, the diffusion thermoelectric power for a degenerate electron gas depends mainly on the Fermi energy. The smaller the Fermi energy, the higher the diffusion thermoelectric power.

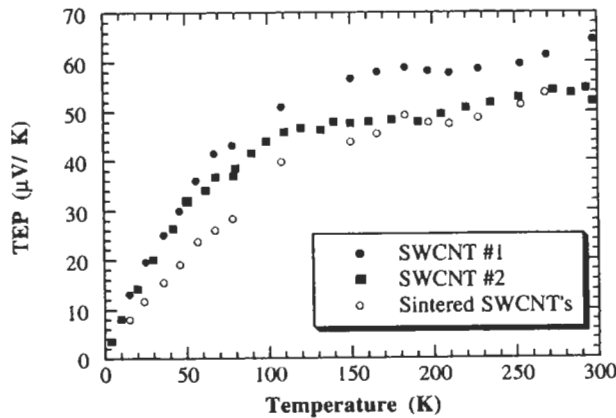


Fig. 6. Temperature dependence of the thermoelectric power of three SWCNT samples [11].

Hone *et al.* [11] have measured the temperature variation of the thermoelectric power from 4.2 to 300 K on bundles of SWCNTs. They have also reported on the temperature dependence of the electrical resistivity of their samples in the same temperature range. The three samples, two pristine and one sintered, on which the thermoelectric power was measured, exhibited the same qualitative behaviour and almost the same values (Fig. 6). The thermoelectric power was found to be positive in all the temperature range investigated. As may be seen from Fig. 6, it increases first linearly at low temperature and then tends to reach an almost constant value around 100 K to increase slowly again with temperature around roughly 200 K. The room temperature values, around 50 $\mu\text{V/K}$, are considerably higher than that of metallic samples (a few $\mu\text{V/K}$), but comparable to those observed in semimetals. Oddly enough, the temperature variation resembles more that observed in graphite intercalation compounds (GICs) [34] than in the pristine material, though the room temperature value measured in SWCNTs is about twice that reported for GICs.

The interpretation of thermoelectric power data in most materials is a delicate job and this is particularly true for the case of carbons and graphites. In the case of SWCNTs the data are not consistent with those calculated from the known band structure which leads to much smaller values than observed. Hone *et al.* [11] suggest from their data that they may indicate that the predicted electron-hole symmetry of metallic CNTs is broken when they are assembled into bundles (ropes).

6 Intercalation

Intercalation in MWCNT should be similar to intercalation in HOPG or fibres. This means that one would expect in helical samples that the intercalate would be introduced between the layers with a dramatic increase of its diameter. For concentric CNTs, it would require a large amount of defects for intercalation to occur between the planes and an important distortion of the host structure.

In Fig. 7 we present the effect of Br_2 intercalation on the temperature dependence of the electrical resistivity of pristine SWCNT bundles before and after heat treatment in vacuum at 450 K for several hours [35]. In Fig. 8 the effect of potassium intercalation is presented for different treatments.

For SWCNT bundles [35], 1D intercalation would occur between the CNTs columns as it is the case for polyacetylene. Intercalation either by acceptors (Fig. 6) or donors (Fig. 7) increases the electrical conductivity as expected, however the effect is less pronounced than in bulk graphite [34].

It would be interesting to extend these measurements to lower temperatures to observe the quantum effects in these quasi-1D metallic systems.

7 Potential applications

SWCNTs exhibit exceptional properties which are directly related to their defect-free graphitic structure. The current list of possible applications includes:

superstrong cables, wires for nanosized electronic devices, charge-storage devices for battery, tiny electron guns for flat-screen televisions, ...

From what we know from graphite and carbon fibres, we may expect that CNTs should exhibit exceptionally high Young's moduli [36]) and mechanical strength. Molecular dynamics simulations [37] indicate that a CNT could be elongated by several percent before fracture. Moreover, it can be twisted, flattened and bent even around sharp bends without breaking and in many cases, recover its original shape when the constraints distorting it are removed (complete elasticity). The extreme stiffness of CNTs could make them great for building strong, lightweight composite materials.

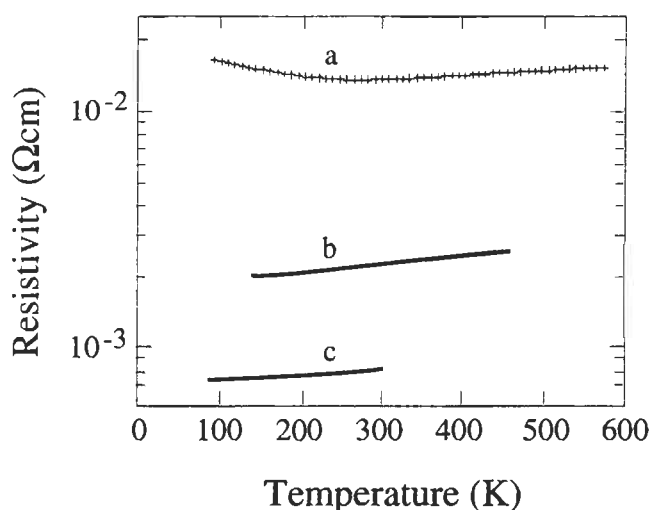


Fig. 7. The effect of Br_2 intercalation on the temperature dependence of the resistivity of a bulk SWCNT sample. Curve a, pristine material; curve b, saturation-doped with Br_2 ; curve c, after heating in the cryostat vacuum to 450 K for several hours [35].

Probing the electronic properties of CNTs is currently an active field of research. Recently, a room-temperature CNT-based transistor has been built by researchers at Delft [38]. The device consists in a semiconducting CNT bridging two platinum electrodes atop a silicon surface coated with SiO_2 . A third gate electrode is used to apply an electric field to the silicon, thus switching on and off the flow of current along the CNT. Using 5/7 pair defects, it is also possible to connect two CNT junctions which exhibit different electronic behaviours (i.e. metal-semiconductor). Such devices can act as a molecular diode, which allows electrical current to flow in one direction, from a semiconductor to a metal, but not in the opposite direction [39]. CNTs could also be used in displays or for the tips of electron probes. The field emission properties [40] of these systems are directly related to the cap termination (atomic topology containing pentagons)

which induces localised states close to the Fermi energy [41]. A CNT-based display has already been built by a research group in Japan [42].

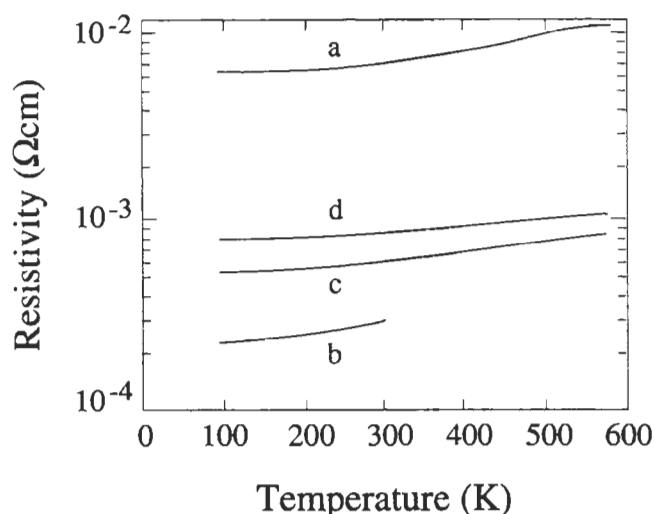


Fig. 8. The effect of potassium intercalation on the temperature dependence of the resistivity of a bulk SWCNT sample. Curve a, pristine material from a different batch than in Fig. 6; curve b, after doping with potassium; curve c, after heating in the cryostat vacuum to 580 K overnight; curve d, after 3 days at 580 K [35].

The chemical robustness of the CNT walls and the straightforward covalent chemistry available at the tube ends (open or closed) are also very fascinating properties, which were recently used to obtain better images of biological molecules [43]. By attaching different chemical groups to the end of a MWCNT, researchers at Harvard were able to create a CNT-based probe which could recognise specific chemical groups on a surface, thus recording not just the surface contour but also identifying the molecules [43].

Other applications could result from the fact that CNT can retain relatively high gas pressures within their hollow cores [44]. This new property would make CNTs interesting as storage media for both hydrogen gas power fuel cells and liquid electrolytes for batteries. Unfortunately, before all these potential applications for CNTs could be transferred from the research laboratory to industry, it is crucial to increase the yield in the synthesis technique. Although a recent work [45] reveals a new effective method to produce very long MWCNTs (2 mm in length), a large effort in the understanding of growth mechanisms has to be made in order to be able to produce CNT by tons as required for most industrial processes.

8 Conclusions

In conclusion, we have shown the interesting information which one can get from electrical resistivity measurements on SWCNT and MWCNT and the exciting applications which can be derived. MWCNTs behave as an ultimate carbon fibre revealing specific 2D quantum transport features at low temperatures; weak localisation and universal conductance fluctuations. SWCNTs behave as pure quantum wires which, if limited in length, reduce to quantum dots. Thus, each type of CNT has its own features which are strongly dependent on the dimensionality of the electronic gas. We have also briefly discussed the very recent experimental results obtained on the thermopower of SWCNT bundles and the effect of intercalation on the electrical resistivity of these systems.

References

1. Iijima, S., *Nature*, 1991, **354**, 56.
2. Hamada, N., Sawada, S. and Oshiyama, A., *Phys. Rev. Lett.*, 1992, **68**, 1579.
3. Saito, R., Fujita, M., Dresselhaus, G. and Dresselhaus, M. S., *Appl. Phys. Lett.*, 1992, **60**, 2204; *Phys. Rev. B*, 1992, **46**, 1804.
4. Mintmire, J. W., Dunlap, B. I. and White, C. T., *Phys. Rev. Lett.*, 1992, **68**, 631.
5. Wildöer, J. W. G., Venema, L. C., Rinzler, A. G., Smalley, R. E. and Dekker, C., *Nature*, 1998, **391**, 59.
6. Odom, T. W., Huang, J. -L., Kim, P. and Lieber, C. M., *Nature*, 1998, **391**, 62.
7. Issi, J. -P. Electronic conduction In *World of Carbon*, ed. P. Delhaes, Gordon and Breach, UK, 1998; Charlier, J. -C. and Issi, J. -P., *Appl. Phys. A*, 1998, **67**, 79.
8. Abrahams, E., Anderson, P. W., Licciardello, D. C. and Ramakrishnan, T. V., *Phys. Rev. Lett.*, 1979, **42**, 613; Bergmann, G., *Phys. Rev. B*, 1983, **28**, 2914; Hikami, S., Larkin, A. I. and Nagaoka, Y., *Prog. Theor. Phys.*, 1980, **63**, 707; Altshuler, B. L., Aronov, A. G. and Lee, P. A., *Phys. Rev. Lett.*, 1980, **44**, 1288; Fukuyama, H., *J. Phys. Soc. Jpn.*, 1980, **48**, 2169; Piraux, L., *J. Mater. Res.*, 1990, **5**, 1285.
9. Langer, L., Stockman, L., Heremans, J. P., Bayot, V., Olk, C. H., van Haesendonck, C., Bruynseraede, Y. and Issi, J. -P., *J. Mater. Res.*, 1994., **9**, 927.
10. Langer, L., Bayot, V., Grivei, E., Issi, J. -P., Heremans, J. P., Olk, C. H., Stockman, L., van Haesendonck, C. and Bruynseraede, Y., *Phys. Rev. Lett.*, 1996, **76**, 479.
11. Hone, J., Ellwood, I., Muno, M., Mizel, A., Cohen, M. L., Zettl, A., Rinzler, A. G., and Smalley, R. E., *Phys. Rev. Lett.*, 1998, **80**, 1042.
12. Thess, A., Lee, R., Nikolaev, P., Dai, H., Petit, P., Robert, J., Xu, C., Lee, Y. H., Kim, S. G., Colbert, D. T., Scuseria, G., Tománek, D., Fischer, J. E. and Smalley, R. E., *Science*, 1996, **273**, 483.
13. Bockrath, M., Cobden, D. H., McEuen, P. L., Chopra, N. G., Zettl, A., Thess, A. and Smalley, R. E., *Science*, 1997, **275**, 1922.
14. Tans, S. J., Devoret, M. H., Dai, H., Thess, A., Smalley, R. E., Geerligs, L. J. and Dekker, C., *Nature*, 1997, **386**, 474.
15. Ebbesen, T. W., Hiura, H., Fujita, J., Ochiai, Y., Matsui, S. and Tanigaki.

- K., *Chem. Phys. Lett.*, 1993, **209**, 83.
16. Ebbesen, T. W. and Ajayan, P. M., *Nature*, 1992, **358**, 220.
17. Heyd, R., Charlier, A., Maréché, J. F., McRae, E. and Zharikov, O. V., *Solid State Commun.*, 1994, **89**, 989.
18. Seshardi, R., Aiyer, H. N., Govindaraj, A. and Rao, C. N., *Solid State Commun.*, 1994, **91**, 195.
19. Song, S. N., Wang, X. K., Chang, R. P. H. and Ketterson, J. B., *Phys. Rev. Lett.*, 1994, **72**, 697.
20. Dai, H., Wong, E. W. and Lieber, C. M., *Science*, 1996, **272**, 523.
21. Ebbesen, T. W., Lezec, H. J., Hiura, H., Bennett, J. W., Ghaemi, H. F. and Thio, T., *Nature*, 1996, **382**, 54.
22. Whitesides, G. M. and Weisbecker, C. S., private communication.
23. Klein, C. A., *J. Appl. Phys.*, 1964, **35**, 2947.
24. Ajiki, H. and Ando, T., *J. Phys. Soc. Jpn.*, 1993, **62**, 1255.
25. Al'tshuler, B. L., *JETP Lett.*, 1985, **41**, 648.
26. Lee, P. A. and Stone, A. D., *Phys. Rev. Lett.*, 1985, **55**, 1622.
27. Umbach, C. P., Washburn, S., Laibowitz, R. B. and Webb, R. A., *Phys. Rev. B*, 1984, **30**, 4048.
28. Washburn, S., Umbach, C. P., Laibowitz, R. B. and Webb, R. A., *Phys. Rev. B*, 1985, **32**, 4789.
29. Licini, J. C., Bishop, D. J., Kastner, M. A. and Melngailis, J., *Phys. Rev. Lett.*, 1985, **55**, 2987.
30. Skocpol, W. J., Mankiewich, P. M., Howard, R. E., Jackel, L. D., Tennant, D. M. and Stone, A. D., *Phys. Rev. Lett.*, 1986, **56**, 2865.
31. Lee, P. A., Stone, A. D. and Fukuyama, H., *Phys. Rev. B*, 1987, **35**, 1039.
32. Delaney, P., Choi, H. J., Ihm, J., Louie, S. G. and Cohen, M. L., *Nature*, 1998, **391**, 466.
33. Tans, S. J., Verschueren, A. R. M. and Dekker, C., *Nature*, 1998, **393**, 49.
34. Issi, J. -P., Transport properties of metal chloride acceptor graphite intercalation compounds. In *Graphite Intercalation Compounds*, Springer Series in Materials Science, Vol. 2, ed. H. Zabel and S. A. Solin, Springer-Verlag, Berlin, 1992.
35. Lee, R. S., Kim, H. J., Fischer, J. E., Thess, A. and Smalley, R. E., *Nature*, 1997, **388**, 255.
36. Treacy, M. M. J., Ebbesen, T. W. and Gibson, J. M., *Nature*, 1996, **381**, 678.
37. Yakobson, B. J., Brabec, C. J. and Bernholc, J., *Phys. Rev. Lett.*, 1996, **76**, 2511.
38. Tans, S. J., Verschueren, A. R. M. and Dekker, C., *Nature*, 1998, **393**, 49.
39. Collins, P. G., Zettl, A., Bando, H., Thess, A. and Smalley, R. E., *Science*, 1997, **278**, 100.
40. de Heer, W. A., Chatelain, A. and Ugarte, D., *Science*, 1995, **270**, 1179.
41. Carroll, D. L., Redlich, P., Ajayan, P. M., Charlier, J. -C., Blase, X., de Vita, A. and Car, R., *Phys. Rev. Lett.*, 1997, **78**, 2811.
42. Saito, Y., Uemura, S. and Hamaguchi, K., *Jpn. J. Appl. Phys.*, 1998, **37**, L346; also see Normile, D., *Science*, 1998, **281**, 632.
43. Wong, S. S., Joselevich, E., Woolley, A. T., Cheung, C. L. and Lieber, C. M., *Nature*, 1998, **394**, 52.
44. Dillon, A. C., Jones, K. M., Bekkedahl, T. A., Kiang, C. H., Bethune, D.

- S. and Heben, M. J., *Nature*, 1997, **386**, 377.
45. Pan, Z. W., Xie, S. S., Chang, B. H., Wang, C. Y., Lu, L., Liu, W., Zhou, W. Y., Li, W. Z. and Qian, L. X., *Nature*, 1998, **394**, 632.

CHAPTER 11

Capillarity in Carbon Nanotubes

DANIEL UGARTE,¹ THOMAS STÖCKLI,²
JEAN-MARC BONARD,² ANDRÉ CHÂTELAIN²
and WALTER A. DE HEER³

¹*Laboratório Nacional de Luz Síncrotron (CNPq / MCT),
Caixa Postal 6192, 13083-970 Campinas SP, Brazil.*

²*Institut de Physique Expérimentale, Dept. Physique
Ecole Polytechnique Fédérale de Lausanne, 1015 Lausanne, Switzerland.*

³*School of Physics, Georgia Institute of Technology,
Atlanta, GA 30332, USA*

Hollow carbon nanotubes (CNTs) can be used to generate nearly one-dimensional nanostructures by filling the inner cavity with selected materials. Capillarity forces can be used to introduce liquids into the nanometric systems. Here, we describe experimental studies of capillarity filling in CNTs using metal salts and oxides. The filling process involves, first a CNT-opening steps by oxidation; secondly the tubes are immersed into different molten substance. The capillarity-introduced materials are subsequently transformed into metals or oxides by a thermal treatment. In particular, we have observed a size dependence of capillarity forces in CNTs. The described experiments show the present capacities and potentialities of filled CNTs for fabrication of novel nanostructured materials.

1 Introduction

The engineering of novel devices requires, in many cases, materials with finely selected and preestablished properties. In particular, one of the most promising lines of synthetic materials research consists in the development of nanostructured systems (nanocomposites). This term describes materials with structures on typical length scale of 1-100 nm. Nanometric pieces of materials are in an intermediate position between the atom and the solid, displaying electronic, chemical and structural properties that are distinct from the bulk. The use of nanoparticles as a material component widens enormously the available attributes that can be realised in practice, which otherwise would be limited to bulk solid properties.

Both from the experimental or theoretical point of view, clusters studies present many difficulties due to their typical size (1-10 nm), usually larger than current systems studied in chemistry, but also too small for many physical standard techniques of characterisation and manipulation.

Since the discovery of fullerenes [1], carbon nanostructures have attracted a great deal of interest [2]. Numerous novel and exceptional properties have been observed or predicted for these pure carbon systems. From the large variety of members in the fullerene family, lately carbon nanotubes (CNT) have focused the attention [3] of the scientific and technological community. The basic structural unit of a CNT is a graphitic sheet rolled into a cylinder, while the tube tips are closed by hemispherical or polyhedral graphitic domes. These tubes present impressive aspect ratios from 100 to 1000, with diameters as small as a 1 nm and lengths ranging from microns to millimeters. Experimentally, CNTs may be classified into two different types: single-walled CNT (SWCNT) [4-6] and multi-walled CNT (MWCNT) [3]. The first class includes cylinders, 1-2 nm in diameter, formed by a single graphitic layer. The second class describes a system formed by several graphitic cylinders arranged coaxially. The main scientific and technological justification for the enormous interest in CNTs is the expected electronic properties which would be directly related to the geometrical parameters of CNTs (diameter and helicity) [2].

In addition to chemical or physical properties, a fascinating aspect of fullerene related materials is their central empty space, where atoms, molecules or particles can be enclosed. The enclosed particles are then protected by the robust graphitic layers from chemical or mechanical effects. The very long cavities of CNTs have a special potential due to their high aspect ratio and they can be used as templates to fabricate elongated nanostructures.

First attempts to fill CNTs were based on the rather uncontrolled process based on the electric arc. Some successful results have been reported on the formation of long nanometric filaments electrodes impregnated with the desired filling material [7]. Although the arc discharge have led to the observation of a large variety of interesting filled graphitic structures, the control of this process is very low, hindering further development.

As the production methods of MWCNTs is very efficient [8] (see Chaps. 2 and 12), it is an advantage to implement a filling procedure after the synthesis. A promising approach to fill CNT cavities, could exploit the capillary properties that have been revealed by Ajayan and Iijima [9]. Subsequent studies by Dujardin et al. [10] allowed the estimations of a surface tension threshold in order to select materials that are good candidates to wet and fill CNTs.

Here, we will describe experimental studies on capillary filling of CNTs. Because of the focus of this chapter, we have taken examples from the work in our own laboratory; certainly we may have inadvertently ignored other exciting work from other laboratories in the world. Still the preparation of a sample of purified and filled CNTs have yet to be developed, so that the study of filled tubes have been and can only be performed by electron microscopy and associated techniques. We have tried to describe in detail all the steps involved in the procedure of capillary filling, such as CNT production, opening, filling and final thermal processing.

2 CNT Synthesis

The standard method to synthesize MWCNTs is based on the electric-arc experiment proposed by Ebbesen and Ajayan [8]. Basically, the production system is similar to the one used by Krätschmer et al. [11] to produce macroscopic quantities of C₆₀ and the main difference between the two experiments is the inert gas pressure, that must be rather low (20-100 mbar) for an efficient fullerene production [11], but must be increased to 350-700 mbar to generate nanotubes efficiently [8].

Our experimental set-up uses 6 mm graphite electrodes, and the DC applied voltage is generated by an AC power supply, and rectifying diodes. We have generally used a voltage of 18-20 Volts, and a stable discharge is obtained for currents of 60-80 A. In our set-up, the inert-gas atmosphere is static, which means that the helium is introduced at the beginning (350 mbar) and then the evaporation chamber is closed; during the experiment the pressure increases and it usually attains 450 mbar after 10-15 min.

During the discharge one electrode is moved in such a way that the discharge remains stable (this can be monitored by the current value). After this period, a deposit (10-15 mm long) forms on the cathode, which is composed of a hard grey shell formed, and a black inner core. An eye observation of the black core easily reveals a columnar texture in the direction of the deposit growth. The columns are actually formed by bundles of CNTs.

Some details of the arc-discharge process must be considered when analysing the quality of the generated samples. The electric arc is basically dynamic and the regions where the discharge originates moves constantly over the electrode surface. As a consequence, important temperatures variations are produced and this fact is probably at the origin of the large CNT size distributions.

Figure 1 shows some of the typical structural parameters of CNT generated in our laboratory. On the average, we can think that an MWCNT is a 1 micron long structure formed by about 10-15 concentric graphitic cylinders, the external one with a diameter of 12 nm, and the innermost tube has a diameter of about 2 nm. Hence, these tubes can be used as templates, the generated enclosed wires would have dimensions of a few nm in diameter when filled, or a few tens of nm when CNTs are covered with materials.

A major disadvantage of the arc-synthesized CNT sample is that it also contains an important percentage (30-50 %) of small polyhedral graphitic (onion-like) particles (3-50 nm) [12,13]. Several purification methods have been tried to extract pure CNT samples with a variable degree of success, former methods were based on the oxidation of the whole sample [14], the basic idea of the procedure is that as CNT is very long, spheroidal particles should be oxidised completely before the tubes; both thermal oxidation [14], liquid-oxidation [15] or combination on chemical treatment followed by thermal oxidation [16,17] were used, but the final efficiency of the process is rather low. Recently an approach based on the use of surfactants and filtering was reported [18]. Although chemical methods require the sample to be washed many times in order to eliminate the residues, after the washing undesired residues frequently

remain [17]. In our experiments, we always use the unprocessed raw sample including tubes and nanoparticles.

It must be emphasised that electric-arc synthesis must be optimised for each particular apparatus and that different laboratories may actually produce quite diverse samples. Hence, it is important to carefully characterise the CNT samples used in any experiment.

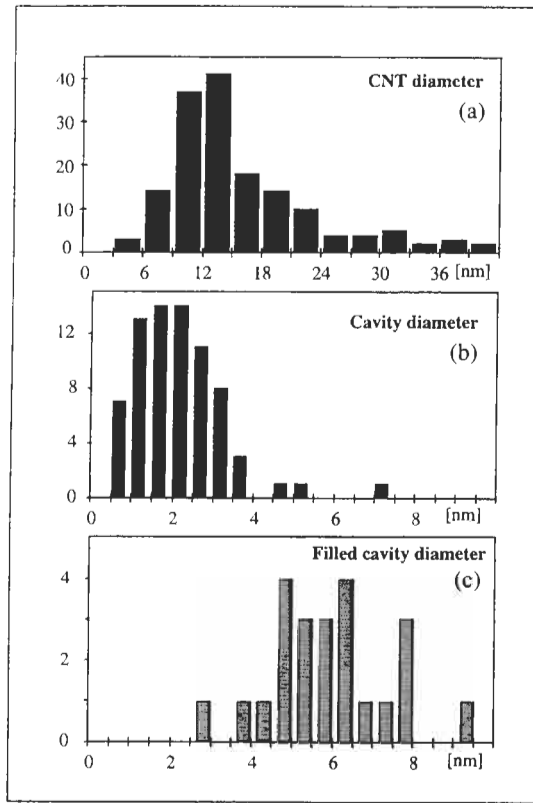


Fig. 1. Typical size distribution of electric-arc generated MWCNTs (see text for details): (a)external diameter, (b)internal diameter and (c)silver nitrate-filled cavities.

3 CNT-Filling Methods

Wetting and capillarity occurs when the liquid-solid contact angle Θ_c is less than 90° (see Fig. 2) and Θ_c is related to liquid surface tension γ by

$$\cos \Theta_c = (\gamma_{SV} - \gamma_{SL}) \gamma^{-1} \quad (1)$$

where γ_{SV} and γ_{SL} indicate the surface tensions at solid-vapour and solid-liquid interfaces, respectively.

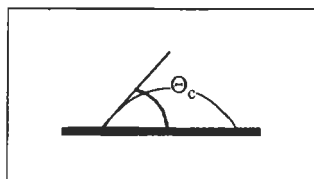


Fig. 2. Definition of contact angle Θ_c of a liquid droplet on a solid surface.

In their study on CNT capillarity, Dujardin et al. [10] observed the spontaneous immersion/floatation of CNTs in different substances. This experiments allowed the authors to derive a threshold surface tension value over which no wetting and in consequence no capillary effect was expected. They showed that compounds displaying a surface tension $< 100\text{--}200 \text{ mNm}^{-1}$ are potential candidates for CNT-filling materials. The list includes many solvents such as water, ethanol, acids, some low surface tension oxides (PbO , V_2O_5 , etc.) and some low melting point substances as S, Cs, Rb and Se [19]. However, these experiments revealed that most of the scientific and technological interesting materials to form nanometric needles such as low melting point metals (Pb, Ga, Hg, etc.) would not enter the tubes spontaneously [19].

A different filling approach was proposed by Tsang et al. [20] who developed a simple wet chemical to fill the CNTs. This process is based on the chemical attack of tube tips by concentrated nitric acid containing a dissolved metal salt. The tube tips are opened and the salt solution enters the CNT. Subsequently a calcinating step is performed and the precipitation of elongated metal or metal/oxide particles is obtained (3-6 nm in diameter and 10-30 nm in length). Briefly, the approaches to fill CNTs may be classified in two methods [21]: a) physical, where a molten material enters the CNT due to capillarity forces [9,10]; and b) chemical, based on wet chemistry [20]. In both cases, the enclosed material obtained can be modified by a subsequent treatment (thermal annealing [20] or electron irradiation [22]). The wet chemical approach has a big advantage in the flexibility of materials introduced into the CNTs [20-26]. Nevertheless, it has a major drawback such that rather low effective quantity of enclosed matter is achieved and that usually it is formed by isolated particles, not always filling completely the CNT cavity. As for material choice, the physical filling method is much more restrictive, but the amount of enclosed matter can be significantly larger; furthermore, it may yield long continuous filaments (nanorods) [9,21,22,26,27].

The CNT cavity is not directly accessible for experiments for CNTs obtained from the cathode deposit because, their tips are almost always closed by multishell hemispherical or polyhedral domes. The first step of any capillary-filling procedure consists of an opening process, that will be discussed in detail in the following section.

4 Opening CNTs

The curvature and closing of an hexagonal carbon network requires the inclusion of pentagons (or other defects) in the graphene layer. As this non-six-member rings concentrate the curvature, they are subjected to the largest strain; in consequence, these bonds display higher chemical reactivities than six-member ring bonds [28]. In CNTs, the pentagons are localised at the tips so that any chemical attack, such as oxidation, will erode firstly these regions, and generate opened tubes [29,30].

Tsang et al [20] have used nitric acid to open CNTs, but the simplest opening technique is thermal oxidation [29,30] where CNTs are heated in air or oxygen atmosphere to temperatures of the order of 600-700°C. As mentioned above, tips are eroded first.

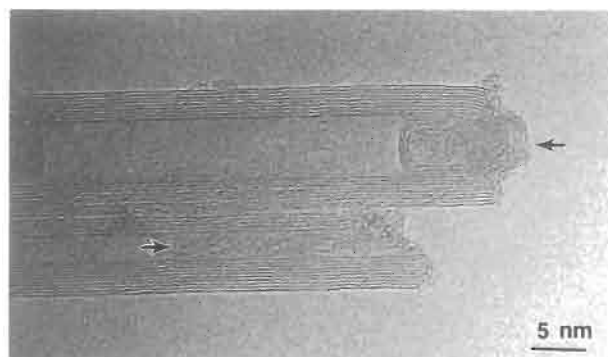


Fig. 3. High-resolution electron micrograph (HREM) of oxidised CNT tips. Note the amorphous carbon residue inside the lower nanotube (marked with an arrow).

Although thermal oxidation can be performed in any conventional furnace attaining 700°C, an efficient processing is only obtained for highly dispersed CNT bundles. If the bundles are not disassembled (by crushing, ultrasound, etc.), the operation yields a highly heterogeneous sample (shortened tubes mixed with unprocessed tubes), and with an unpredictable low percentage of opened tubes.

The thermal oxidation procedure has also been suggested as a purification method: since particles are shorter than CNTs they are completely oxidised before the long tubes [14]. Although the apparent simplicity, the obtained results have been variable and the efficiency has been extremely low (1 %). This basic difficulty has hindered the practical use for CNT purification [14,31].

After the thermal oxidation opening, an amorphous carbon (a-C) residue is frequently left on/over the tip or even inside the cavity close to the tube extrema [29,32] (see Fig. 3); this a-C actually plugs the CNT. To eliminate this plug, we have performed an additional high temperature annealing (2000-2100°C, 10^{-5} Torr) [22]. The furnace used for this steps was very simple: the CNTs were

compacted in a tantalum tube, which was resistively heated within the same vacuum chamber where the tube are synthesized [33]. After this treatment, the a-C plug is graphitised and the dangling bonds at the tube tip are eliminated [22, 32] so that the ragged oxidised edges are transformed into a toroidal graphitic structure on the tube extremity (see Fig. 4).

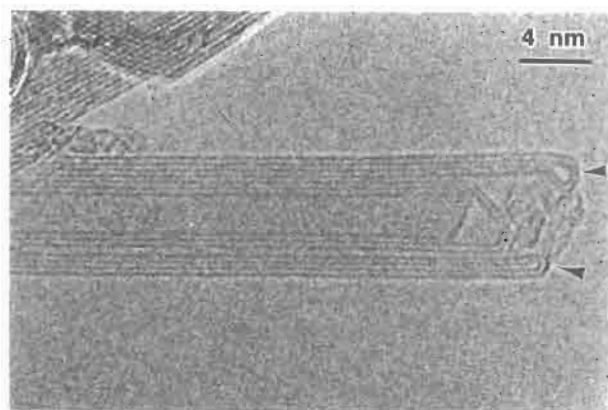


Fig. 4. Typical tip morphology obtained after high-temperature treatment (2000 °C) of oxidation opened CNTs. Note the elimination of dangling bonds by a bending of graphitic layer (marked with arrows).

5 Physical Filling of CNTs

This approach is based on the immersion of opened tubes in a molten material. With a view to generate metal nanorods we analysed various metal compounds that represent potential candidates for filling. In addition to an appropriate surface tension, the filling substance must fulfill a few requirements as low melting temperature (T_m) and that it could be easily transformed into a metal by a subsequent processing. It would also be desirable that the whole filling processing would not damage the CNTs. For example, the capillarity filling could be easily performed in air if the melting temperature of the substance would be lower than 600°C.

Silver nitrate (AgNO_3) is a compound that fulfills the precedent requirements ($T_m = 212^\circ\text{C}$), and also it can be easily decomposed into pure silver by thermal treatment at 400 °C. As mentioned before, the basic characterisation technique for this studies is transmission electron microscopy (TEM); the atoms with rather high atomic number would facilitate the detection of the nanorods.

In order to facilitate the mixing of CNTs and the nitrate, they were crushed ensemble in a mortar. The mixture was then heated within a Pyrex crucible in furnace up to 230°C for a period of 1 h. Subsequently, the sample was crushed to a fine powder in the mortar and disposed on a holey carbon grid. TEM

observations confirmed that the nitrate had indeed entered the opened tubes and that about $\approx 2\text{--}3\%$ of the CNTs were filled along their entire length. Due to the preparation method, the tubes were often partially embedded in large salt particles. We have tried to dissolve away the salt particles outside the tubes by washing the sample with water, but this attempts were unsuccessful because it also caused the nitrate inside the tubes to be removed as well [22].

Much care had to be taken during the TEM observations of silver nitrate filled tubes, because this salt is very sensitive to electron irradiation and the continuous filaments transformed quickly into a chain of silver particles (see Fig. 5) [22].

Enclosed nitrate filaments can be thermally decomposed to silver by a simple heat treatment. In opposition to electron irradiation that fragments the filaments, the simple heating yields continuous metal nanorods (see Fig. 6 for a silver filament generated by a 60 min. treatment at 400°C , pressure 10^{-2} Torr).

The successful introduction of silver nitrate leads us to test other nitrates. In particular some transition metal nitrates have even lower melting temperatures ($\approx 55^\circ\text{C}$ for cobalt nitrate).

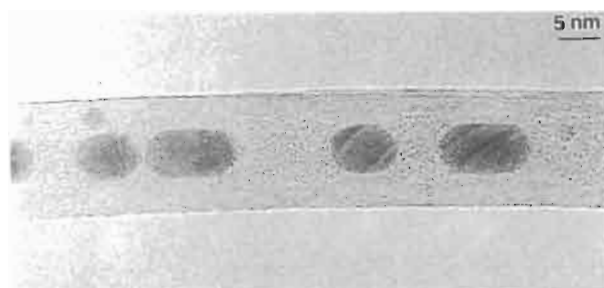


Fig. 5. HREM of enclosed silver particles in CNTs. The metallic particles were obtained by electron irradiation-induced decomposition of introduced silver nitrate. Note that the gases produced by the nitrate decomposition have eroded the innermost layer of the tube.

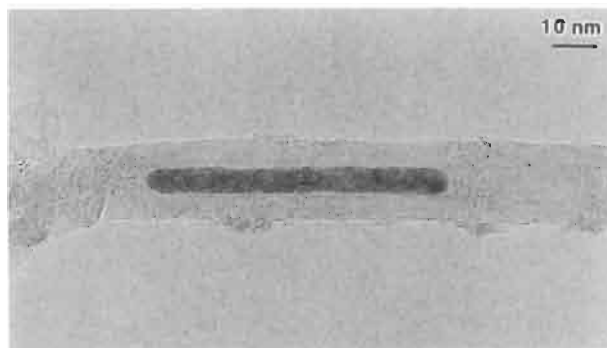


Fig. 6. HREM picture of a CNT enclosing a silver nanorod generated by thermal treatment of silver nitrate filled CNTs.

Filling experiment using Co nitrate showed similar results, but the observation of Co nitrate filaments was more difficult because usually this compound was in an amorphous structure when enclosed in CNTs. As for the decomposition of Co nitrate, it would be extremely interesting to be able to generate pure metal nanorods, but actually we obtained cobalt monoxide (CoO) filaments, as could be measured by electron diffraction and high-resolution electron micrograph (HREM) imaging. Figure 7 shows a micrograph of a CNTs enclosing two CoO nanorods whose diameter is of the order of 2 nm. It is important to emphasise that our TEM observations showed that smaller CNTs are filled with Co nitrate compared to the silver analog.

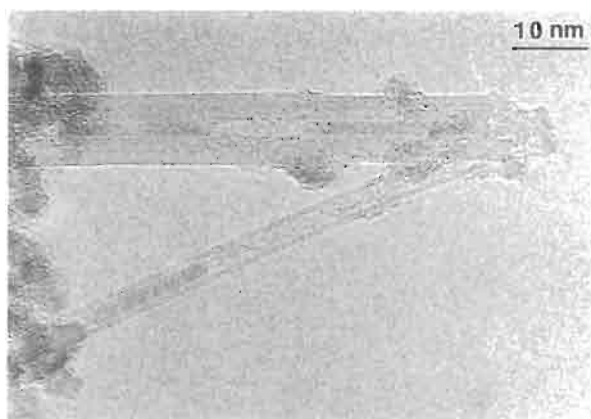


Fig. 7. Silver nanorod enclosed in a CNT generated by thermal treatment of silver nitrate and close CNTs. See text for explanations.

The decomposition of the nitrates produces oxygen molecules, and we have verified that if a mixture of silver nitrates and closed tubes is submitted to a thermal treatment (400°C) decomposing the salt, it is possible to observe filled CNTs (Ag, Co, Cu [34]). It appears that oxygen liberated during the thermal decomposition of the metal salt erodes the CNT tip and the yet un-decomposed salt then enters by capillarity (see Fig. 8). We have also observed during the electron-irradiation decomposition of enclosed nitrate that the liberated gases erodes the CNT cavity [22] (see the innermost tubes in Fig. 5).

Although we have made several efforts to optimise the filling process, our efforts were unsuccessful and the percentage of filled tubes remained low (2-3 %); this filling efficiency was in contradiction with our estimation of the opening process efficiency being of the order of 60 % [22]. After a detailed analysis, we concluded that there would be additional factors involving the simple size-independent macroscopic wetting models considered previously. An important evidence can be obtained from the filled-cavities size distribution; TEM measurements indicated that the filling diameters were in the range of 4-10 nm (Fig. 1(c)). These values were typical of our experiments, and also similar sizes could be inferred from most electron microscopy images reported in the literature [21,22,26,27,35]. As

can be seen in Fig. 1(b), the distribution of the inner CNT diameter is centred on much smaller values (maximum at ≈ 2 nm). Hence, there appears to be a tendency to fill wider cavities. Our results indicate that the low quantity of filled tubes, in first approximation, represents basically the low quantity of CNT with large inner cavity, and it suggests that narrower tubes are not filled due to a reduced capillarity effect. A simple minded explanation of this effect is given in Sec. 7.

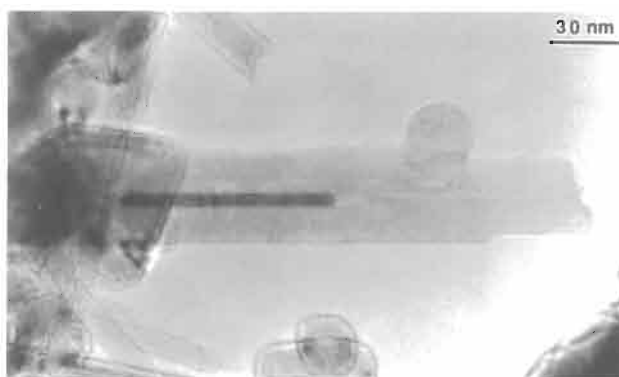


Fig. 8. CNTs filled with CoO filaments produced by thermal treatment of enclosed cobalt nitrate. Note the small diameter of the CoO filaments (≈ 2 nm).

We have described above the main observed phenomena for capillary effects by silver nitrates, however other chemical compounds display a different behaviours as it is described in the next section for lead oxides.

6 Lead Oxide Filling

CNT capillarity was firstly discovered by heating a sample composed of tubes and lead nanoparticles in air, and TEM studies revealed that a few tubes presented some material inside their cavities [9]. Although fillings could present impressive length (100 nm) and diameters as small as 2 nm. The phase that had entered the tubes could not be clearly identified by the authors and they also speculated on the possible formation of new phases.

When CNTs are filled with lead [9,32] or bismuth [29] compounds, the tube tip displays an erosion pattern and it is covered by a filling material droplet. This phenomenon can be observed in Fig. 9 (indicated with arrows), where we show typical results obtained for a mixture of opened MWCNTs and lead oxide (PbO_2) heated in air at 450°C . The lead-compound filling can be clearly seen as a darker band at the centre of the tubes; these continuous filaments are about 400 nm in length and 4 nm in diameter. The existence of these plugs indicates that the tip must somewhat play an active role in the filling process. Maybe it acts as catalysis or reducing agent.

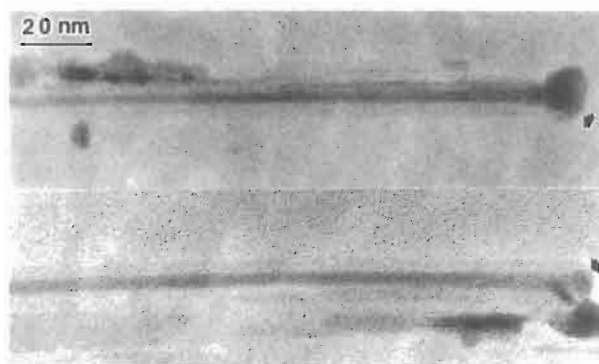


Fig. 9. Lead-compound filled CNTs. Note the very long continuous filament inside the tubes, and also the plugs formed at the tube tips (marked with arrows).

Our results indicate that the number of filled tubes is rather low, but the filled ones display astonishing narrow and very long filaments (2-3 nm in diameter and several hundreds of nm in length) [32]. If capillary filling is extremely efficient for these cases, it seems rather contradictory that filled tubes are so rare. We have not yet been able to identify the factors governing the exceptional capillary behaviour of only a few tubes.

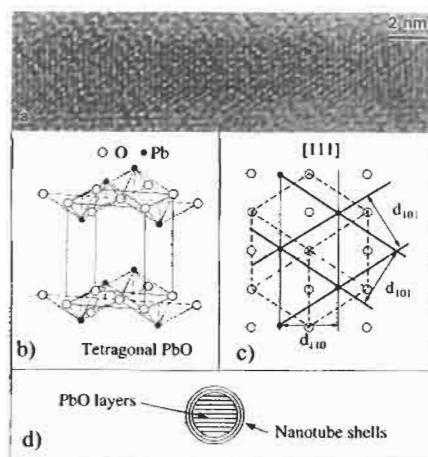


Fig. 10. Analysis of the atomic lattice images of the lead compound entering CNTs by capillary forces; (a) detailed view of the high resolution image of the filling material, (b) tetragonal PbO atomic arrangement, note the layered structure and (c) tetragonal PbO observed in the [111] direction, note that the distribution of lead atoms follows the contrast pattern observable in (a). (d) bidimensional projection of the deduced PbO filling orientation inside CNTs as viewed in the tube axis direction, note that PbO layers are parallel to the cylindrical CNT cavity.

The energy dispersive X-ray spectroscopy (EDX) analysis of the lead compound filled tubes revealed the presence of lead, oxygen and carbon. By this kind of chemical analysis it is not possible to determine if the carbon signal is only associated to the CNT layers or if the filling materials also contain carbon (lead carbonate).

The filling lattice fringes provides very good information to determine the enclosed material. A detailed view of an HREM image of enclosed filament is shown in Fig. 10; here we can detect three family of atomic planes. The first one is composed by lattice fringes with a period of 0.28 nm that are observed perpendicular to the axis; the other two have a periodicity of 0.31 nm and form an angle of ≈ 33 degrees with the tube axis.

The observed lattice spacing displays a good agreement with lead monoxide (PbO) values. This compound has two possible structures; the main one is tetragonal and the other orthorhombic (actually a slight distortion of the tetragonal arrangement). As our data do not allow to discriminate between the two possible structures, we will consider only the tetragonal phase in which the (110) and (101) spacings correspond to 2.809 and 0.3115 nm, respectively.

The basic structure of tetragonal PbO is composed of a stacking (in the [001] direction) of layers of Pb-O connected by weak interlayer bond (see Fig. 10(b)). If these crystals are observed following the [111] direction with the [110] vector parallel to the tube axis, the spatial distribution of Pb atoms is in very good accordance with the HREM observed contrast pattern (see Fig. 10(c)); the expected angle between the (101) and the tube axis is 33.5 degrees, being in very good agreement with the measured value of 33 degrees. A more conclusive evidence of this assignment has been verified by image simulation [36]. As the tube axis coincides with the [110] direction of PbO, we can also deduce that the stacking direction [001] of PbO layers is orthogonal to the CNT axis. This orientation means that the layers are continuous and parallel to the cavity axis (see schematic representation in Fig. 10(d)); this is expected spatial arrangement of a layered material in a cylindrical cavity in order to minimise the surface energy.

We must emphasise that PbO has already been suggested as a good candidate to fill tubes due to its low surface tension [19]. Our experimental observations are very well explained by the PbO fillings, but several questions remain opened in order to understand completely the capillary process. The main controversial point is that PbO is the high-temperature stable phase of lead oxides requiring heat treatment in air at 550°C, and it would not be formed during our experiment at 450°C. For the range of temperatures used in our experiments, the presence of Pb_3O_4 or PbO_x ($x > 1$) should be expected. Other question concerns the melting temperature of PbO (886°C) that is much higher than the parameters used during thermal treatments (450°C). Other compounds such as stoichiometric lead oxides or lead carbonate have lower melting temperatures (PbO_2 290°C, Pb_3O_4 500°C, Pb_2O_3 370°C, PbCO_3 315°C), so that, if these are present in the experiments they would be liquid and could be the candidates for capillary filling.

In spite of a detailed analysis, many crucial aspects are yet to be understood, such as the role of the tube tips in possible chemical activity (formation of lead carbonate or reduction of lead oxides), or a possible lowering of melting

temperature for the nanometric volumes of material concerned in these experiments [37].

7 Size Effects in CNT Capillary

The capillary filling of CNTs is basically and usually described using macroscopic thermodynamic approximations. For example, Dujardin et al. [10] concluded that the surface-tension threshold value for filling a CNT was $100\text{--}200\text{ Ncm}^{-2}$.

Wetting and capillarity can be expressed in terms of dielectric polarisabilities when van der Waals forces dominate the interface interaction (no chemical bond or charge transfer) [37]. For an arbitrary material, polarisabilities can be derived from the dielectric constants (ϵ) using the Clausius-Mossotti expression [38]. Within this approximation, the contact angle can be expressed as:

$$\cos \Theta_c = 2 (\alpha_S / \alpha_L) - 1 \quad (2)$$

where α_L and α_S are the polarisabilities of the liquid and solid, respectively.

As it can be seen in Fig. 1(c), there is a minimum size for the silver nitrate filling. If we assume that the polarisability of the enclosed material is identical to the bulk value, we can estimate the CNT cavity polarisability by using the measured minimal filled CNT. Then, if the cavity polarisability is size dependent, this approach can be used to measure the tube cavity properties, and we could also predict the wetting properties (or minimal filled tubes) for different materials.

Using the data obtained from the silver nitrate experiments, we have derived a simple approximation to calculate the cavity polarisability as a function of diameter [22]. If we apply this model to cobalt nitrate, the derived threshold for filling is 0.8 nm [32]; this result qualitatively agrees with our observations that cobalt nitrate-filled cavities are much narrower ($\approx 2\text{ nm}$) than obtained with silver nitrate ($\approx 4\text{ nm}$).

8 Summary

Filling CNTs represents a remarkable example of manipulation of matter at the nanometric level. The experiments described here clearly show example of the capacities and potentialities for nanofabrication of novel materials.

Most of our results have been obtained by TEM studies of individual tubes that can be considered nanolaboratories; the ability to control and observe such small objects is very impressive. However, it also strains a limitation concerning the lack of an efficient method to generate macroscopic quantities of filled tubes, where we could be able to apply conventional macroscopic characterisation techniques.

There are many aspects to be considered before a comprehensive understanding of nanocapillary could be developed such as the effect of the electronic properties of

CNTs, or changes of structure or melting point of liquid in nanometric cavities, etc. Many interesting experimental and theoretical studies are in progress on the CNT filling, and the obtained new knowledge will not only be useful for fullerene-related materials field, but also it will illuminate the development of the whole field of nanotechnologies.

Acknowledgements

Electron microscopy studies were performed at the Centre Interdépartemental de Microscopie Electronique (CIME), Ecole Polytechnique Fédérale de Lausanne. We are grateful to the Brazilian Council for Scientific and Technologic Research (CNPq) and the Swiss National Science Foundation for financial support.

References

1. Kroto, H. W., Heath, J. R., O'Brien, S. C., Curl, R. F. and Smalley, R. E., *Nature*, 1985, **318**, 162.
2. Dresselhaus, M. S., Dresselhaus, G. and Eklund, P. C., *Science of Fullerenes and Carbon Nanotubes*, Academic Press, San Diego, 1996.
3. Iijima, S., *Nature*, 1991, **354**, 56.
4. Iijima, S. and Ichihashi, T., *Nature*, 1993, **363**, 603.
5. Bethune, D. S., Kiang, C. H., de Vries, M. S., Gorman, G., Savoy, R., Vasquez, J. and Beyers, R., *Nature*, 1993, **363**, 605.
6. Thess, A., Lee, R., Nikolaev, P., Dai, H., Petit, P., Robert, J., Xu, C., Lee, Y. H., Kim, S. G., Rinzler, A. G., Colbert, D. T., Scuseria, G., Tománek, D., Fischer, J. E. and Smalley, R. E., *Science*, 1996, **273**, 483.
7. Guerret-Piécourt, C., Le Bouar, Y., Loiseau, A. and Pascard, H., *Nature*, 1994, **372**, 761.
8. Ebbesen, T. W. and Ajayan, P. M., *Nature*, 1992, **358**, 220.
9. Ajayan, P. M. and Iijima, S., *Nature*, 1993, **361**, 333.
10. Dujardin, E., Ebbesen, T. W., Hiura, H. and Tanigaki, K., *Science*, 1994, **265**, 1850.
11. Krätschmer, W., Lamb, L. D., Foristopoulos, K. and Huffman, D. R., *Nature*, 1990, **347**, 354.
12. Iijima, S., *J. Cryst. Growth*, 1980, **50**, 675.
13. Ugarte, D., *Chem. Phys. Lett.*, 1992, **198**, 596.
14. Ebbesen, T. W., Ajayan, P. M., Hiura, H. and Tanigaki, K., *Nature*, 1994, **367**, 519.
15. Hiura, H., Ebbesen, T. W. and Tanigaki, K., *Adv. Mater.*, 1995, **7**, 275.
16. Ikazaki, F., Oshima, S., Uchida, K., Kuriki, Y., Hayakawa, H., Yumura, M., Takahashi, K. and Toshima, K., *Carbon*, 1994, **32**, 1539.
17. Chen, Y. K., Green, M. L. H., Griffin, J. L., Hammer, J., Lago, R. M. and Tsang, S. C., *Adv. Mater.*, 1996, **8**, 1012.
18. Bonard, J. M., Stora, T., Salvetat, J. P., Maier, F., Stöckli, T., Duschl, C., Forro, L., de Heer, W. A. and Châtelain, A., *Adv. Mater.*, 1997, **9**, 827.
19. Ebbesen, T. W., *J. Phys. Chem. Solids*, 1996, **57**, 951.

20. Tsang, S. C., Chen, Y. K., Harris, P. J. F. and Green, M. L. H., *Nature*, 1994, **372**, 159.
21. Sloan, J., Cook, J., Green, M. L. H., Hutchison, J. L. and Tenne, R., *J. Mater. Chem.*, 1997, **7**, 1089.
22. Ugarte, D., Châtelain, A. and de Heer, W. A., *Science*, 1996, **274**, 1897.
23. Chu, A., Cook, J., Heesom, R., Hutchison, J. L. and Green, M. L. H., *J. Sloan Chem. Mater.*, 1996, **8**, 2751.
24. Satishkumar, B. C., Govindaraj, A., Mofokeng, J., Subbanna, G. N. and Rao, C. N. R., *J. Phys. B*, 1996, **29**, 4925.
25. Sloan, J., Cook, J., Heesom, R., Green, M. L. H. and Hutchison, J. L., *J. Cryst. Growth*, 1997, **173**, 81.
26. Chen, Y. K., Chu, A., Cook, J., Green, M. L. H., Harris, P. J. F. Heesom, R., Humpries, M., Sloan, J., Tsang, S. C. and Turner, J. F. C., *J. Mater. Chem.*, 1997, **7**, 545.
27. Chen, Y. K., Green, M. L. H. and Tsang, S. C., *J. Chem. Soc., Chem. Commun.*, 1996, 2489.
28. Haddon, R. C., *Science*, 1993, **261**, 1545.
29. Ajayan, P. M., Ebbesen, T. W., Ichihashi, T., Iijima, S., Tanigaki, K. and Hiura, H., *Nature*, 1993, **362**, 522.
30. Tsang, S. C., Harris, P. J. F. and Green, M. L. H., *Nature*, 1993, **362**, 520.
31. Bacsá, W. S., Ugarte, D., Châtelain, A. and de Heer, W. A., *Phys. Rev. B*, 1994, **50**, 15473.
32. Ugarte, D., Stöckli, T., Bonard, J. M., Châtelain, A. and de Heer, W. A., *Appl. Phys. A*, 1998, **67**, 101.
33. de Heer, W. A. and Ugarte, D., *Chem. Phys. Lett.*, 1993, **207**, 480.
34. Zarbin, A. G. and Ugarte, D., unpublished.
35. Ajayan, P. M., Stephan, O., Redlich, P. and Colliex, C., *Nature*, 1995, **375**, 564.
36. Ugarte, D., Stöckli, T., Bonard, J. M., Châtelain, A. and de Heer, W. A., in preparation.
37. Buffat, Ph. and Borel, J. -P., *Phys. Rev. A*, 1976, **13**, 2287.
38. de Gennes, P. G., *Rev. Mod. Phys.*, 1985, **57**, 827.
39. Jackson, J. D., *Classical Electrodynamics*, John Wiley & Sons, Inc., New York, 1967.

CHAPTER 12

Large-Scale Synthesis of Carbon Nanotubes by Pyrolysis

KAZUYOSHI TANAKA,¹
MORINOBU ENDO,² KENJI TAKEUCHI,²
WEN-KUANG HSU,³ HAROLD W. KROTO,³ MAURICIO
TERRONES³ and DAVID R. M. WALTON³

¹*Department of Molecular Engineering, Graduate School of Engineering, Kyoto University, Kyoto 606-8501, Japan*

²*Department of Electrical and Electronic Engineering, Faculty of Engineering, Shinshu University, Nagano 380-8553, Japan*

³*School of Chemistry, Physics and Environmental Science, University of Sussex, Brighton BN1 9QJ, UK*

1 Introduction

Most carbon nanotubes (CNTs) employed in current research have been produced by the arc-discharge or laser ablation methods. This emphasis is easily understood because multi-walled CNTs (MWCNTs) were first found in the carbon cathode associated with the arc-discharge technique used to prepare fullerenes [1] and because single-walled CNTs (SWCNTs) were formed when arc-discharging [2,3] and laser ablation [4,5] were conducted in the presence of metal catalysts. Unfortunately, both methods suffer from serious drawbacks arising from difficulties encountered in eliminating by-products, namely carbon nanoparticles and amorphous carbon fragments, which lead to inefficient commercial production. Purification difficulties are considerable because CNTs are insoluble and, hence, liquid chromatography cannot, as is the case for fullerenes, be used to purify them. As a result the arc-discharge and laser ablation methods appear to provide unpromising approaches to CNTs.

Most researchers were not apparently aware of earlier CNT preparations in the context of ultra-thin vapour-grown carbon fibres (VGCF). This type of CNT is termed pyrolytic (PCNT) and its preparation shows promise of large-scale synthesis. Needless to say, it is of practical importance to provide sufficient CNTs at reasonable cost. This chapter highlights the preparation methods, structural characteristics and current commercial status of PCNTs and includes a description of the devices used hitherto to obtain aligned PCNTs. By way of

comparison, researches into large-scale CNT synthesis by the arc-discharge or laser ablation methods are also summarised.

2 Optimisation of Conventional CNT Production

2.1 MWCNTs

MWCNTs were first found as a deposit in the inner core of the carbon cathode used in the arc-discharge process for generating fullerenes [1]. Optimal production of MWCNTs has been achieved by varying several parameters [6]. The optimised arc-discharge process uses He (500 Torr) as the background gas in conjunction with a 10-18 V supply and 100 A dc current. These conditions convert 75% of the consumed graphite anode into a cathode deposit containing MWCNTs. The purified MWCNTs are 2-20 nm in diameter and several micrometers in length. The tubes are multi-walled with an inter-wall separation of *ca.* 0.34 nm.

2.2 SWCNTs

It has been reported that SWCNTs form in the soot generated in the arc-discharge chamber when metal catalysts are present. This preparation technique was published almost concurrently by two groups [2,3]. Thus Iijima and Ichihashi [2], employing an Fe catalyst and a mixture of CH₄ (10 Torr) and Ar (40 Torr), obtained *ca.* 1 nm diameter SWCNTs, whereas Bethune *et al.* [3] produced *ca.* 1.2 nm diameter SWCNTs using He (100-500 Torr) and Co as the catalyst. It has been reported, that laser vapourisation of a graphite rod doped with 1.2 at. % of a 1:1 mixture of Co and Ni powder in an oven at 1200°C generates close-packed SWCNT bundles in greater than 70% yield [4,5].

Optimisation of SWCNT production has been attempted within the framework of the arc-discharge method in which anode and cathode were made of graphite rods, a hole in the anode being filled with metal catalysts such as Y (1 at.%) and Ni (4.2 at.%) [7]. A dense "collar" deposit (*ca.* 20% of the total mass of graphite rod) formed around the cathode under He (*ca.* 500 Torr), with 30 V and 100 A dc current. It was confirmed that this optimal "collar" contained large amounts of SWCNT bundles consisting of (10, 10) SWCNTs (diameter 1.4 nm). Such morphology resembles that produced by the laser ablation technique [4,5].

3 VGCFs (PCNT background)

It is generally recognised that most organic compounds, including resins and polymers, yield charcoal, coal and amorphous carbon when decomposed under non-oxidising conditions. The reactions often involve dehydration and dehydrogenation. The morphology and solid-state properties of the carbon materials thus prepared depend strongly on the starting materials and parameters

associated with the carbonisation process, such as pyrolysis temperature, retention time and so on. It is noteworthy that these parameters can be readily controlled.

On the other hand, organic materials of relatively low molecular weight such as acetylene, benzene, ethylene and methane, can produce vapour-grown carbon materials by imperfect combustion or by exposing their vapour to a heated substrate in an electric furnace in the presence of a metal catalyst. The latter process generates VGCFs. Other precursors to VGCF include polyacrylonitrile (PAN), isotropic or mesophase pitch, rayon or nylon [8].

VGCFs have typical diameters of 100 nm - 100 μ m with hollow cores [9]. Thus VGCFs are 10^2 - 10^5 times thicker than CNTs. A preparation method for VGCFs was first developed by Endo [10,11] who decomposed benzene at 1150-1300°C in an electric furnace in the presence of H₂ (99.9% pure) as the carrier gas (see Fig. 1). Ultra-fine particles of Fe (*ca.* 10 nm diameter) or its compounds, such as Fe(NO₃)₃ or ferrocene, were introduced into the chamber as a catalyst.

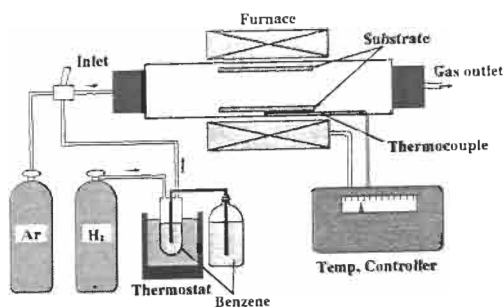


Fig. 1. Apparatus for the VGCF production; suitable for PCNTs [18].

It is known that the temperature of the chamber and partial pressure of the benzene vapour needs to be carefully controlled for effective VGCF growth. Further heat treatment of such a VGCF at *ca.* 3000°C yields highly crystalline CFs, comparable with graphite whiskers prepared by dc discharge of graphite electrodes under Ar at 3900 K, as described by Bacon [12]. The structural and electrical properties of VGCFs thus prepared have been well documented [10, 11, 13-16]. The VGCF growth mechanism has been explained on the basis of three processes [8] listed in Table 1.

Table 1. VGCF growth process from benzene vapour.

Process	Temperature range	Fibre length	Fibre outer diameter
Nucleation	1000-1010 °C	-	-
Elongation	1010-1040 °C	10-60 mm	< 5 μ m
Thickening	1040-1100 °C	60 mm	5-25 μ m

4 Pyrolytic Carbon Nanotubes (PCNTs)

4.1 *Endo PCNTs*

The preparation of PCNTs from benzene has been reported by Endo *et al.* [17-20]. The process is essentially similar to that used for VGCFs described above, but without secondary wall-thickening phase (see Fig. 2). Thus PCNTs can be regarded as the precursor for VGCFs, but having a much smaller nanometer-scale

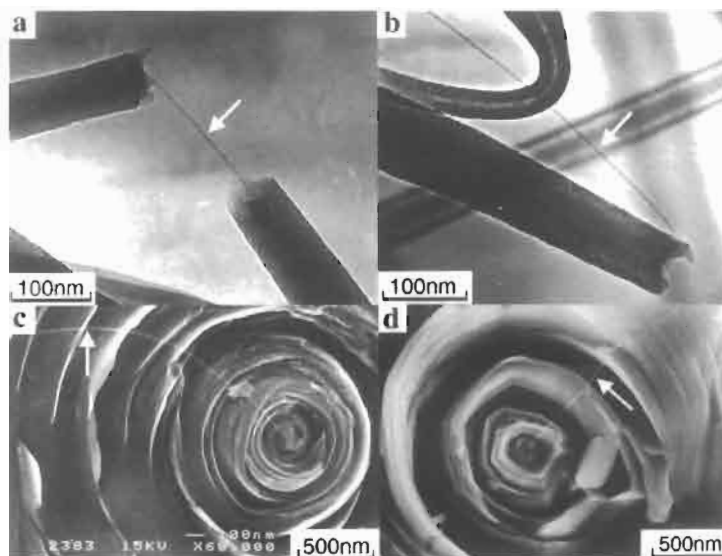


Fig. 2. (a) (b) Transmission electron microscopy (TEM) images of as-grown VGCFs (broken portion) with the PCNT core exposed; field emission-type scanning electron microscopy (FE-SEM) image of (c) as-grown and (d) heat-treated VGCFs (broken portion) at 2800°C with PCNT (white line) exposed [20].

diameters. An apparatus, basically similar to that shown in Fig. 1, can be employed for PCNT preparation, where it is most important to exercise fine control over parameters such as temperature, retention time, benzene partial pressure, hydrogen gas flow and so on. It has been reported that pyrolysis of hydrocarbon vapour in the presence of a Fe catalyst at *ca.* 1040°C yields PCNTs possessing 2-3 nm diameters [8]. Thermal decomposition of a gaseous mixture of benzene and H₂, as used in the VGCF preparation, yields multi-walled PCNTs (Fig. 3) in which at least two coaxial tubes are present. PCNTs are MWCNTs in general.

The uniform growth of PCNTs generally requires the partial pressure of benzene to be as low as possible. Following a 1 h retention time, the chamber is cooled to room temperature and the H₂ atmosphere is replaced by Ar. The product, deposited on the substrate is collected and then annealed at 2000-3000°C under Ar

in order to achieve graphitisation and to enhance crystallinity. It is of interest that thin coiled PCNTs (15–20 nm outer diameter, 30 μm length) have been prepared from acetylene in the presence of a Co catalyst on silica at 600°C [21]. It must be emphasised that under the optimised preparation conditions, *no by-products*, such as carbon nanoparticles or amorphous carbon fragments are formed. Thus this preparation method for PCNTs is promising for large-scale synthesis of MWCNTs, since apart from removal of the metal catalyst tedious purification processes are avoided.

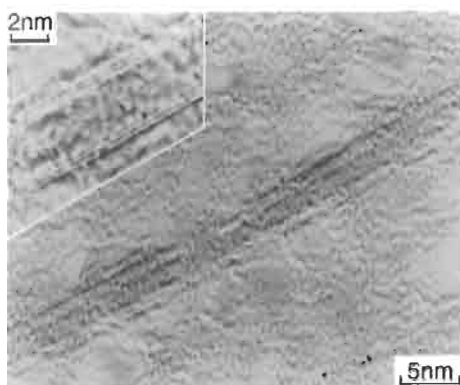


Fig. 3. Heat-treated PCNT; two concentric layers and a hollow core (2.4 nm diameter) [18].

4.2 Hyperion PCNTs

PCNTs are marketed commercially by Hyperion Catalyst International Inc. (Cambridge, Mass. USA), based on a patent [22]: Graphite FibrilsTM. The method of production appears to be essentially the same as that used for *Endo* PCNTs. The material consists of MWCNTs, 10–20 nm in diameter and 10–12 μm long, with *ca.* 10 coaxial layers within each tube. The tubes have hollow cores of *ca.* 3 nm diameter. The Brunauer-Emmett-Teller (BET) analysis characteristically shows a surface area of 250 m^2/g , true density 2.0 g/cm^3 and bulk density of less than 0.1 g/cm^3 (95% void vol).

The Hyperion PCNTs are typically prepared as follows [22]: a metallic catalyst [$\text{Fe}(\text{NO}_3)_3$ supported on Al_2O_3] is dispersed in a ceramic boat which is then placed in an electric furnace. After pre-treatment (flushing with Ar at 500°C) the temperature is raised to 900°C under an H_2 flow, and a vapour consisting of H_2 and benzene (9:1 vol %) is introduced into the furnace for 2 h. MWCNTs collect in the ceramic boat and, after cooling to room temperature under an Ar flow, the product is harvested.

The MWCNTs are *per se* virtually by-product-free and the potential for large-scale synthesis is considerable. However, the Hyperion MWCNTs appear to be rather entangled [23]. Nevertheless the patent [22] covers a wide area of MWCNTs and requires attention in the context of commercialisation.

5 Preparation of Aligned PCNTs

It is important to construct aligned CNT arrays in order to measure properties of individual tubes and to advance the development of electrical and/or electronic devices. From this viewpoint recent developments concerning CNT preparations involve the creation of aligned CNT bundles.

In earlier research the alignment operation was applied to CNTs in the form of a CNT-polymer resin [24] or CNT suspended in a solvent [25]. In the method developed by Ajayan *et al.* [24], purified MWCNTs were dispersed in an epoxy resin which was cut with a diamond knife and a microtome in order to obtain aligned CNTs. De Heer *et al.* [25] used a 0.2 μm pore ceramic filter in order to create an MWCNT suspension in ethanol, and to obtain a black deposit which was transferred to a plastic surface (Delrin or Teflon) by pressing the filter onto the polymer. However, only a moderate degree of orientation and uniformity in length of the CNTs was achieved by this method.

More sophisticated CNT alignments have been employed by direct deposition of PCNTs onto an aligned template using a patterned catalyst or its equivalent [26-29]. Aligned PCNTs have been generated perpendicular to the surface of mesoporous silica by growth from pores containing embedded iron nanoparticles as catalysts. A flow of acetylene (9%) in N_2 over the porous silica, maintained at 700°C was used and aligned MWCNTs consisting of *ca.* 40 concentric layers and *ca.* 30 nm diameter were obtained, with 100 nm spacing between each tube. After 2-5 h the length of the MWCNT attained 50-100 μm ; neither filled tubes nor carbon nanoparticles were observed in the product.

Terrones *et al.* [27] have investigated the possibility of preparing aligned MWCNTs by pyrolysis of 2-amino-4,6-dichloro-*s*-triazine over a catalyst prepared by laser etching linear tracks in Co deposited on a silica substrate. Aligned MWCNTs with interlayer spacings of 0.34 nm and 30-50 nm external diameter were obtained. The tube length almost reached 50 μm and by-products, such as nanoparticles, were absent. The authors noted that the configuration of the furnace is important because the PCNT generation process is influenced by gravity.

It has been reported that thermal decomposition of silicon carbide (α -SiC) generates aligned CNTs by surface diffusion as shown in Fig. 4 [28]. In this method an α -(0001) SiC wafer ($3 \times 5 \times 0.34 \text{ mm}^3$) with a carbon-termination plane is placed in a vacuum furnace (1×10^{-4} Torr) and heated to 1300-2000°C. The longest (0.15 μm) MWCNTs, 2-5 nm diameter, were obtained by heating at 1700°C for 30 min, and the capped tubes grew from the SiC surface. The density of MWCNTs grown in this way amounted to 30,000 tubes/ μm^2 and, hence a large area CNT film could in principle be prepared by extending this method. Electron diffraction (ED) analysis confirmed the high degree of CNT alignment and good graphitisation. The tube interlayer distance was found to be 0.344 nm compared with 0.335 nm for pure graphite.

Employment of higher temperatures (*e.g.* 2000°C) yielded only graphite, aligned parallel to the SiC surface. At low temperatures (1000-1300°C) almost no MWCNTs grew on the SiC surface. By evoking the presence of traces of O_2 in the furnace the following thermal decomposition was proposed.



The formation mechanism is illustrated in Fig. 5. CNT film has also been found to grow epitaxially on the surface of a β -SiC crystal particle [29]. The present method should prove to be applicable to flat panel displays or to electronic devices utilising MWCNTs.

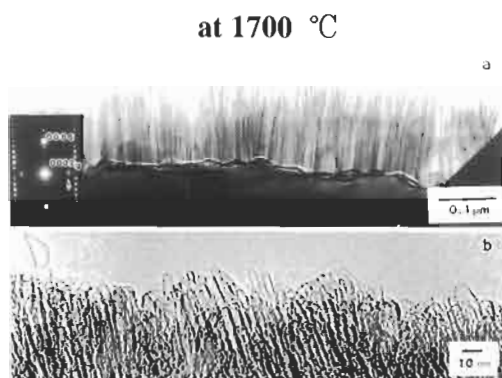


Fig. 4. (a) TEM image and ED pattern (left) of the surface of a decomposed α -SiC (0001) wafer; (b) top portion of the tubes in (a). Caps (2-5 nm diameter) on well-aligned CNTs [28].

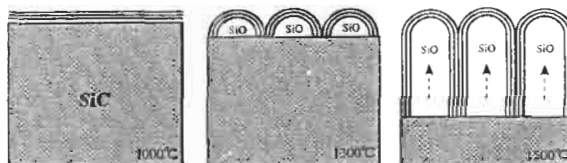


Fig. 5. Formation mechanism for CNT film on α -SiC (Courtesy of Dr. M. Kusunoki).

6 Recent Preparation Methods

CNTs have been prepared recently by electrolysis and by electron irradiation of tube precursors. For example, Hsu *et al.* [30,31] have described the condensed-phase preparation of MWCNTs by an electrolytic method using a graphite rod (cathode) and carbon crucible (anode) (Fig. 6) in conjunction with molten LiCl as the electrolyte, maintained at 600°C under an Ar atmosphere. Application of a dc current (3-20 A, <20 V) for 2 min yielded MWCNTs (2-10 nm in diameter, >0.5 μm in length) consisting of 5-20 concentric layers with an interlayer

spacing of 0.34 nm. By-products, such as amorphous carbon and encapsulated CNTs, were also formed.

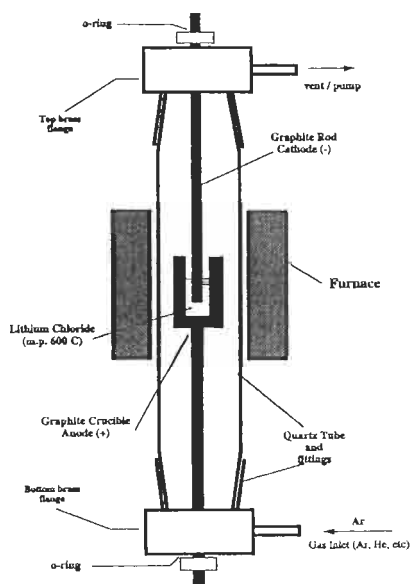
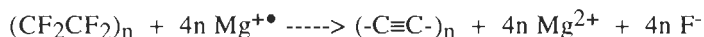


Fig. 6. Electrolysis apparatus [31].

It has recently been reported that a molecule, claimed to contain a high concentration of conjugated alkyne units, can be prepared by electrochemical reduction of polytetrafluoroethylene (PTFE) [32,33]. The reduction is carried out using magnesium and stainless steel as anode and cathode respectively. The electrolyte solution contains THF (30 cm³), LiCl (0.8 g) and FeCl₂ (0.48 g). A 10 × 10 nm² PTFE film, covered with solvent, is reduced to "carbyne" (10 V for 10 h)



The PTFE film turns black and the product exhibits a 2100-2200 cm⁻¹ band, characteristic of the C≡C bond in the i.r. and Raman spectra. It might be worth noting that, in the experience of some, pure condensed molecules of these types are known to explode violently.

Electron irradiation (100 keV) of the sample, heated to 800°C, yields MWCNTs (20-100 nm in length) attached to the surface. Such nanotube growth does not take place if natural graphite, carbon nanoparticles or PTFE are subjected to electron irradiation. The result implies that the material may be a unique precursor for CNTs and may constitute a new preparation method.

7 Concluding Remarks

Preparation methods for PCNTs have been reviewed in the context of parameters which may lead to large-scale MWCNT synthesis free of by-products. It is noteworthy that the formation of aligned CNTs is currently an active area of research in conjunction with PCNT preparation. The use of SWCNTs and/or MWCNTs in electronic devices are being developed. As yet it has not proved possible to produce CNTs with diameters and helicities to order. The formation of SWCNTs by the PCNT process has not yet been reported and it is of interest to examine whether this process can be used to prepare them.

Acknowledgements

KT is grateful to financial support from the project of Institute for Fundamental Chemistry, supported by the Japanese Society for the Promotion of Science - Research for the Future Program (JSPS-RFTF98P00206). ME thanks the support from Grant-in-Aid for Scientific Research on Priority Area (Carbon Alloys, No. 09243105, 1997). W-KH and MT thank The Royal Society for financial assistance.

References

1. Iijima, S., *Nature*, 1991, **354**, 56.
2. Iijima, S. and Ichihashi, T., *Nature*, 1993, **363**, 603.
3. Bethune, D. S., Kiang, C. -H., de Vries, M. S., Gorman, G., Savoy, D., Vazquez, J. and Beyers, R., *Nature*, 1993, **363**, 605.
4. Guo, T., Nikolaev, P., Thess, A., Colbert, D. T. and Smalley, R.E., *Chem. Phys. Lett.*, 1995, **243**, 49.
5. Thess, A., Lee, R., Nikolaev, P., Dai, H., Petit, P., Robert, J., Xu, C., Lee, Y. H., Kim, S. G., Rinzler, A. G., Colbert, D. T., Scuseria, G. E., Tománek, D., Fischer, J. E. and Smalley, R. E., *Science*, 1996, **273**, 483.
6. Ebbesen, T. W. and Ajayan, P. M., *Nature*, 1992, **358**, 220.
7. Journet, C., Maser, W. K., Bernier, P., Loiseau, A., Lamy de la Chapelle, M., Lefrant, S., Deniard, P., Lee, R. and Fischer, J. E., *Nature*, 1997, **388**, 756.
8. See, e.g., Endo, M., Saito, R., Dresselhaus, M. S. and Dresselhaus, G., From carbon fibers to nanotubes. In *Carbon Nanotubes: Preparation and Properties*, ed. T. W. Ebbesen, CRC Press, Boca Raton, FL, 1997, Chap. 2.
9. Tibbetts, G. G., *J. Crystal Growth*, 1984, **66**, 632.
10. Endo, M., Ph. D. Thesis, Nagoya University, Nagoya, Japan, 1978.
11. Endo, M., *Chemtech*, 1988, **18**, 568.
12. Bacon, R., *J. Appl. Phys.*, 1960, **31**, 283.
13. Oberlin, A., Endo, M. and Koyama, T., *J. Crystal Growth*, 1976, **32**, 335.
14. Endo, M., Koyama, T. and Hishiyama, Y., *Jpn. J. Appl. Phys.*, 1976, **15**, 2073.
15. Endo, M., Oberlin, A. and Koyama, T., *Carbon*, 1976, **14**, 133.

16. Endo, M., Hishiyama, Y. and Koyama, T., *J. Phys. D: Appl. Phys.*, 1982, **15**, 353.
17. Endo, M., Fujiwara, H. and Fukunaga, E., In 18th Meeting Japanese Carbon Society, 1991, pp. 34.
18. Endo, M., Takeuchi, K., Igarashi, S., Kobori, K., Shiraishi, M. and Kroto, H. W., *J. Phys. Chem. Solids*, 1993, **54**, 1841.
19. Endo, M., Takeuchi, K., Kobori, K., Takahashi, K., Kroto, H. W. and Sarkar, A., *Carbon*, 1995, **33**, 873.
20. Endo, M., Takeuchi, K., Hiraoka, T., Furuta, T., Kasai, T., Sun, X., Kiang, C.-H. and Dresselhaus, M. S., *J. Phys. Chem. Solids*, 1997, **58**, 1707.
21. Ivanov, V., Nagy, J. B., Lambin, Ph., Lucas, A., Zhang, X. B., Zhang, X. F., Bernaerts, D., van Tendeloo, G., Amelinkcx, S. and van Landuyt, J., *Chem. Phys. Lett.*, 1994, **223**, 329.
22. Tennent, H. G. (Hyperion Catalysis International) US Patent No. 4663230, 1987.
23. Niu, C., Sichel, E. K., Hoch, R., Moy, D. and Tennent, H., *Appl. Phys. Lett.*, 1997, **70**, 1480.
24. Ajayan, P. M., Stephan, O., Colliex, C. and Trauth, D., *Science*, 1994, **265**, 1212.
25. de Heer, W. A., Bacsá, W. S., Châtelain, A., Gerfin, T., Humphrey-Baker, R., Forro, L. and Ugarte, D., *Science*, 1995, **268**, 845.
26. Li, W. Z., Xie, S. S., Qian, L. X., Chang, B. H., Zou, B. S., Zhou, W. Y., Zhao, R. A. and Wang, G., *Science*, 1996, **274**, 1701.
27. Terrones, M., Grobert, N., Olivares, J., Zhang, J. P., Terrones, H., Kordatos, K., Hsu, W. K., Hare, J. P., Townsend, P. D., Prassides, K., Cheertham, A. K., Kroto, H. W. and Walton, D. R. M., *Nature*, 1997, **388**, 52.
28. Kusunoki, M., Shibata, J., Rokkaku, M. and Hirayama, T., *Jpn. J. Appl. Phys.*, 1998, **37**, L605.
29. Kusunoki, M., Rokkaku, M. and Suzuki, T., *Appl. Phys. Lett.*, 1997, **71**, 2620.
30. Hsu, W. K., Hare, J. P., Terrones, M., Kroto, H. W., Walton, D. R. M. and Harris, P. J. F., *Nature*, 1995, **377**, 687.
31. Hsu, W. K., Terrones, M., Hare, J. P., Terrones, H., Kroto, H. W. and Walton, D. R. M., *Chem. Phys. Lett.*, 1996, **262**, 161.
32. Yasuda, H., Kawase, N., Matsui, T., Shimidzu, T., Yamaguchi, C. and Matsui, H., Paper presented at 8th International Conference on Polymer Based Technology (POC'98), Ma'ale Hachamisha, Israel, June 28-July 3, 1998.
33. Yasuda, H., Kawase, N., Matsui, T., Yamaguchi, C. and Matsui, H., Paper presented at Science and Technology of Carbon, Strasbourg, France, July 5-9, 1998.

CHAPTER 13

Carbon Nanotubes as a Novel π -Electron Material and Their Promise for Technological Applications

SUSUMU YOSHIMURA

Advanced Materials Research Laboratory, Matsushita Research Institute Tokyo, Inc., 3-10-1 Higashimita, Tama-ku, Kawasaki 214-8501, Japan

π -Electron materials, which are defined as those having extended π -electron clouds in the solid state, have various peculiar properties such as high electron mobility and chemical/biological activities. We have developed a set of techniques for synthesizing carbonaceous π -electron materials, especially crystalline graphite and carbon nanotubes, at temperatures below 1000°C. We have also revealed new types of physical or chemical interactions between π -electron materials and various other materials. The unique interactions found in various π -electron materials, especially carbon nanotubes, will lay the foundation for developing novel functional, electronic devices in the next generation.

1 Introduction to π -Electron Materials

Carbon is a flexible atom in the way of bonding and hence presents various and unique physical, chemical and biological behaviours in the solid state. Of the two types of bonding of carbon, the sp^3 and sp^2 bondings as in diamond and graphite, respectively, the existence of the latter " π -electron bonding" provides grounds for believing in carbon's versatile talents. Those materials that have extended π -electron clouds are called ' π -electron materials', which include graphite, carbon nanotubes (CNTs), fullerenes and various carbonaceous materials.

Among these carbonaceous materials, pyropolymers have long been known as one of electrically conducting polymers which are conductive without doping and are appreciated as a conductive polymer of high stability, for they are obtained by heating organic molecules or polymers at higher temperatures, usually between 400 and 1200°C [1]. The synthetic procedure for the pyropolymers has been out of favour with most of chemists as "dirty chemistry." One of the major reasons for this may be that the structure and property of the products cannot fully be

identified because of their complex reaction procedures in the non-equilibrium state. However, the synthetic procedure has a possibility of yielding various new ordered materials from the non-equilibrium chaos. For example, poly-perinaphthalene, which is a ladder-type polymer and a typical one-dimensional graphite, has been synthesized via thermal decomposition and condensation of perylene derivatives at about 520°C [1, 2]. Furthermore, heat treatment of condensation polymers, like polyimide and polyamide, has yielded a film composed of highly oriented and nearly ideal graphite crystallites at temperatures above 2700°C [1, 3]. It did not take long before this procedure was proved to be a treasure island, when fullerenes, C₆₀, C₇₀ and so on, were discovered in the carbon mist evaporated from graphite via laser ablation [4]. After the discovery, the pursuit of the "dirty chemistry" became more and more hot and, another new material, CNT, was found in the carbon deposit from graphite in an arc-discharge vessel [5]. The CNT may have been regarded as a fullerene extended to one direction, or as "bucky tube," but its physical properties are totally different from the latter. The CNT is thought to be an allotrope of graphite and, thanks to its highly stable nature, it has much promise for technological applications, which seems to be one of the major reasons for the very extensive research in these days.

Graphite is the most typical example among the π -electron materials defined above and it has created a "wonderful world," because of its superior physical properties. The specific properties of graphite mark many "world records" among all of the existing materials, such as the electrical conductivity ($\sigma = 10^6 \text{ Scm}^{-1}$) of graphite intercalation compounds (GICs), the sound velocity ($v = 23,000 \text{ ms}^{-1}$) and thermal stability (over 3000°C) of graphite. The electron mobility of graphite at lower temperatures ($\mu > 10^6 \text{ cm}^2\text{V}^{-1}\text{s}^{-1}$ at 4 K) [6] is comparable with that of superlattice structures of compound semiconductors. The technological application of high-quality or highly-crystalline graphite has been limited to the fields of so-called high-end use, owing to its very expensive nature. For example, graphite has only been employed in such areas as optical elements for x-ray or neutron radiation [7,8], atomically-flat substrates for scanning force microscopes, high-frequency loud speakers for Hi-Fi audio appliances [9] and heat radiation aids for electronic devices [10]. In particular, the last two applications make use of high sound velocity ($v = 18,000 \text{ ms}^{-1}$) and thermal conductivity ($\kappa = 800 \text{ WK}^{-1}\text{m}^{-1}$) of graphite to the reproduction of clear and natural sound and the liberation of excess heat from high-capacity and high-speed microprocessors, respectively. However, there have been little or no attempts to develop high electron mobility devices, optical devices or quantum devices taking advantage of such superior physical properties of graphite. The major problems hampering the wide range of electronic applications of graphite come from the fact that graphite has to be synthesized at extremely high temperatures (at 2800°C at the lowest) and that the electronic properties of semi-metallic graphite has not fully been controlled intentionally.

This chapter describes some of the recent results on the low-temperature synthesis of crystalline graphite and CNTs, referring to various characteristics relating to the π -electron materials, which have been found in "the Yoshimura π -Electron Materials Project" [11] of the ERATO program in Japanese

governmental projects. Another objective of this chapter is to review the possibility of applying the π -electrons materials, especially CNTs, to new electronic devices based on their unique characteristics.

2 Low-Temperature Graphitisation and CNT Formation

2.1 Metal-catalyzed low-temperature graphitisation

Traditionally, graphite has been synthesized at temperatures as high as 3000°C and, in order to utilise graphite in ordinary semiconductor processes or to construct superlattices with metals or semiconductors, the temperature should be lowered to below 1000°C at the least. For this purpose, attempts were made to select starting materials and catalysts for carbonisation and graphitisation based on the chemical vapour deposition (CVD) process. Using 2-methyl-1,2'-naphthylketone (Fig. 1 (1)) as a starting material, it was found that crystalline graphite was synthesized at 600°C on a nickel or platinum substrate [12]. Furthermore, highly-oriented graphite with a mosaic spread less than 0.20 Å was obtained on a platinum film deposited on a sapphire single crystal, which mosaic spread implies the highest orientation among all the artificial graphite [13]. The role of the metallic catalysts was considered to promote a quite unique reaction in which the starting monomers coupled directly to form graphite via dehydrogenation of the former. Various other interesting reactions with the metallic catalysts were found to proceed; crystallisation of amorphous carbon to graphite at temperature above 800°C [14] and transformation of diamond-like carbon to crystalline graphite above 500°C [15].

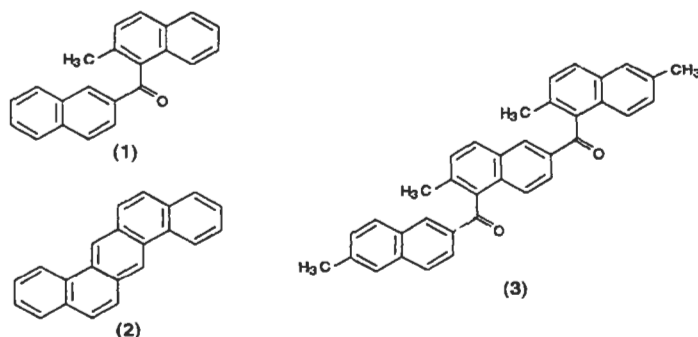


Fig. 1. Chemical structure of the starting materials for low-temperature graphitisation: (1) is 2-methyl-1,2'-naphthylketone mainly considered in this chapter.

2.2 Low-temperature synthesis of CNTs

The metal-catalyzed low-temperature graphitisation process was further developed to the synthesis of CNTs at temperatures below 1000°C. Namely, when 2-methyl-1,2'-naphthylketone was vacuum-deposited via CVD on a thin nickel film (5 nm in thickness), CNTs including nickel cylinders within the hollow space of the tube were obtained at 700°C [16]. Transmission electron microscopy (TEM) observation, Raman spectroscopy and x-ray diffraction patterns altogether showed that the nanotube was almost completely graphitic in spite of the very low deposition temperature. Contrary to the case of graphite formation described in the above section, the evaporated nickel film was annealed and transformed to particles of 20-30 nm in diameter during the deposition. The particles were first covered with graphite sheaths following the same reaction scheme as described above and then the sheaths were considered to split open to form a tubular structure developing longitudinally with the nickel particles transformed to a cylindrical form in the tube (Fig. 2) [17].

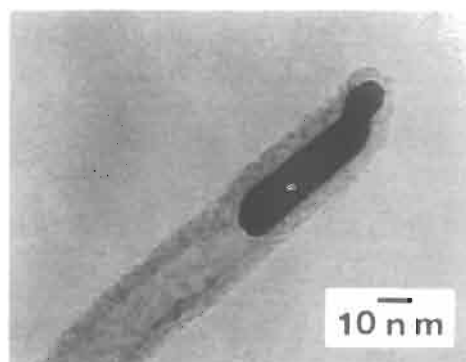


Fig. 2. TEM image of a CNT obtained by CVD of 2-methyl-1,2'-naphthylketone on a vacuum-evaporated nickel film (5 nm in thickness) at 700°C.

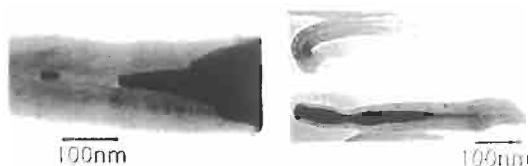


Fig. 3. TEM images of CNTs obtained by CVD of nickel phthalocyanine on a quartz substrate at 800°C: the bottom of the tube (right) and tip of the tube (left).

CNTs were also synthesized at lower temperatures starting from some metal phthalocyanines [18]. Nickel-, cobalt- and iron-phthalocyanines were deposited in vacuum and CNTs were grown perpendicularly on a quartz substrate at 700 and 800°C at relatively high yield. At the base of the nanotubes, a cluster of metal

was encapsulated as a conical shape (Fig. 3), which indicates that the decomposed metal served as a nucleation centre for the graphite formation. Toward the tip of the tubes, the diameter gradually decreases and the tube becomes curled or even coiled at the end. A possible explanation for this is that the CNTs synthesized from phthalocyanines are composed of nitrogen-containing heterographite [19].

3 Interactions between π -Electron Materials and Various Other Materials

Since the carbonaceous materials can be very active in interacting with other materials, the materials science of the π -electron materials is the investigation and control of various interactions between π -electron materials and other materials, some of which are related to the synthesis of new materials and some are going to be a key technology in the development of new functional devices. Various specific interactions including those of π -electron materials with metals, semiconductors and silica glasses have been found in the Yoshimura π -Electron Materials Project [11]. Some other interesting interactions were observed with organic polymers and biological substances, namely epitaxial polymerisation of functional polymers on the basal plane of graphite [20] and promotion of proliferation of biological cells contacting with graphitic materials [21]. These should be regarded as typical and/or specific examples of versatile interactions which the π -electron materials can exhibit and some of the typical interactions will be discussed in more detail.

Metals play very important roles in the synthesis of new π -electron materials and the realisation of new physical or chemical properties. A nickel catalyst was found to contribute to a fanciful "scooter mechanism" [22] of the formation of single-walled CNTs (SWCNTs), keeping the tube open and facilitating the longitudinal growth of the tube very efficiently, when it was incorporated in a carbon target of laser beam evaporation at 1200°C. Nickel, cobalt and iron have catalyzed the formation of multi-walled and highly-graphitised CNTs at temperatures below 1000°C when some low-molecular organic molecules were decomposed on them [12, 23]. One of the effects of the metallic catalysts is to exert a remarkable lowering of the graphitisation temperature (to about 500°C) [15]. That carbon or graphite is a very stable material may be a superstition when it comes to the interaction with metals; as an example, chemical-vapour deposited carbon was found to corrode platinum metal and to transform itself to highly-crystallised graphite embedded in the latter [13].

The formation of fullerenes and CNTs has also been affected by their environmental atmosphere [22] and, in particular, a hydrogen atmosphere plays an important role in forming graphitic structures of multi-walled CNTs (MWCNTs) in the form of "buckybundles" [24]. Intercalation into MWCNTs has been difficult or impossible, because there is no space for intercalants to enter into a Russian-doll-type structure of the nanotubes. However, the buckybundles formed in the hydrogen arc discharge were found to be successfully intercalated with potassium and ferric chloride (FeCl_3) without breaking the

tubular structure. The CNT GICs thus synthesized were found to have a characteristic bead-string structure (Fig. 4) and could be de-intercalated reversibly [25], providing evidence that the hydrogen-arc MWCNTs are very unique in that they have a scroll type structure spatially distributed in an ordinary Russian-doll structure. For the MWCNTs with the latter type structure, only the intercalation into the interstitial channels of nanotube bundles may be allowed as has been experienced with some SWCNTs [26, 27].

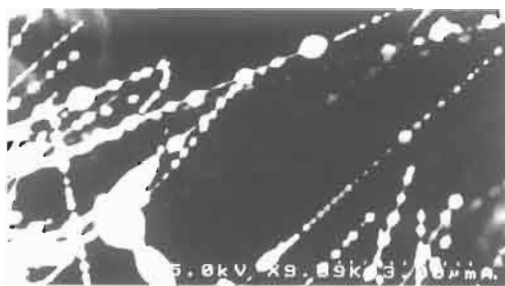


Fig. 4. Scanning electron microscope (SEM) image of FeCl₃-intercalated CNTs assuming a bead-string structure with partially intercalated and swelled portions.

The structure of MWCNTs is a matter of some critical debate and one of underlying tender problems is that it strongly depends on the method of preparation with various factors affecting the development of graphene sheets being rolled up into tubes. Amerinckx and Bernaerts [28] have presented a complete set of geometry for MWCNTs, the configuration of the graphene layers and chirality of the tubules, for example, based on their electron diffraction patterns (see Chap. 3). Various researchers have encountered MWCNTs filled with metals or other materials which are thought to be formed during the nanotube formation as the result of interaction between the materials to be filled and decomposed carbon sources. The materials incorporated in the tubes include nickel, cobalt [16, 23], copper, germanium [29], chromium [30] and silicon nitride [31] which form themselves into a nanowire or nanorod settled in the cylindrical holes of the MWCNTs.

Being stimulated by the chemistry and physics of fullerenes and CNTs, the materials science of traditional carbon has come to its active phase again and various procedures for synthesizing new π -electron materials have been found. A new quasi-one-dimensional carbon, 'carbolite' [32], has been discovered, indicating that carbon still has a possibility of exhibiting a widest variety of allotropes. A variety of new starting materials, catalysts and synthetic methods has been used for obtaining carbon and graphite crystals [33], which gives, in turn, a renewed opportunity of the CNTs synthesized from various starting materials [34, 35] with various procedures [36].

4 Properties and Technological Applications of CNTs and Some New π -Electron Materials

The electronic band structure and electrical properties of graphite have almost fully been understood in this century [6]. CNTs, which are made of the graphene sheets rolled up into tubes, are believed to exhibit various new electronic properties depending upon their diameter and helicity. The SWCNTs can be either a one-dimensional metal or a semiconductor, in contrast to graphite which is a semimetal, and can also exhibit quantum effects under certain circumstances. Both metallic and semiconductive SWCNTs were observed using scanning tunnelling spectroscopy [37, 38]. Direct measurements of electrical conductivity have shown that metallic nanotubes exhibit discrete electron states due to quantum effects and also that coherent electron transport can be maintained through the nanowires [39], which have served as an incentive to theoretical study on their transport properties [40]. And very recently, a field-effect transistor operating at room temperature has been provided using semiconductive tubes [41], which is a first step in developing nano-scale electronic devices and is likely to be followed by various other advances.

One of the characteristic properties of a mesoscopic conductor has been well evidenced by the measurement of 'universal conductance fluctuation (UCF)' in magnetoresistance of a single MWCNT [42]. The UCF of CNT GICs was first found [43] with the hydrogen-arc MWCNTs intercalated with potassium [25]. Strikingly, the electrical conductivity of the GICs was lower by about 2 orders of magnitude than that of the pristine sample and a fluctuation of the magnetoresistance was manifested at temperatures below 10 K. The decrease in their electrical conductivity upon intercalation and the appearance of the UCF are thought to be caused as a result of the confinement of the electron motion into a mesoscopic region (≈ 20 nm) formed by the beads as shown in Fig. 4.

Field emission of electrons has been observed from the tips of CNTs (MWCNTs) [44,45] where, in addition to a very low field emission, an excellent coherent, monochromatic electron beams were obtained coming from one-dimensional atomic wires extending out from the inner layer of MWCNTs. The coherence of the emitted electrons was considerably higher than that with a standard tungsten point source emitter and will open up a wide range of applications as hologram generation [46] or a cold cathode for flat panel display devices. Some of the properties found with CNTs are very new as compared with those of graphite single crystals but some can be reproduced with a single graphene sheet (or two-dimensional graphite), which has not been synthesized till now. One of the great advantages of the graphene sheet is that the electrical properties can be modified by substituting the carbon atoms with other atoms, boron or nitrogen, or with some defects, thus creating a p-n junction within the sheet. This idea has been proposed for forming a heterojunctions in a CNT by introducing pentagon-heptagon defects into the hexagonal network [47] and the formation of boron-nitride nanotubes [48] may further be pursued in this line of modifying the electronic properties of CNTs. In the case of graphite crystals, however, the incorporation of heteroatoms or pentagon-heptagon defects (non-benzenoid graphite) into the graphene sheets has not been successful so far and

every effort should be devoted in order that graphite and/or CNTs are to be utilised as electronic devices.

Physics and chemistry of GICs, or the intercalation of carbonaceous π -electron materials in general, have entered upon a new stage of development, partly because new intercalants like alkali metal oxides and various gasses are introduced [49] and partly because they have come to have a very significant technological importance in that the capacity of lithium-ion secondary batteries strongly depends on the nature of carbon electrodes. Various new carbon materials including amorphous carbons starting from polymeric materials [50] and CNTs [51] have been examined as a high-capacity cathode and some of them will be put into commercial use in the near future. The CNTs, especially SWCNTs, has found their utility in the area of energy storage technology as in hydrogen storage reservoirs [52] and electrochemical capacitors [53], both displaying higher performances than those with conventional materials aiming at the application to zero-emission electric vehicles. Further fundamental study is still required to design and synthesize carbonaceous materials with enhanced energy density.

5 Conclusions

"Carbon" has been a good friend of human beings since the dawn of history and recent research in this field is certainly breathing new wind to this old and new material. And there will be various new fields of potential interest in electronic, chemical and biological areas which will encourage further study of the π -electron materials; for example, from high electron mobility transistors to proliferation/mutation of biological cells. They will require a wide range of scientific investigation and it would take long to realise these dreams. However, new horizons will be given through comprehensive and interdisciplinary research on re-valuing the unique and excellent, physical and chemical properties of carbonaceous materials.

References

1. Yoshimura, S., Murakami, M. and Yasujima, H., From pyropolymers to low-dimensional graphites. In *Polymers for High Technology*, ed. J. Bowden and S. P. Turner. American Chemical Society (Symposium Series 346), 1987, pp. 584-599.
2. Murakami, M., Iijima, S. and Yoshimura, S., *J. Appl. Phys.*, 1986, **60**, 3856.
3. Murakami, M., Watanabe, K., and Yoshimura, S., *Appl. Phys. Lett.*, 1986, **48**, 1594.
4. Kroto, H. W., Heath, J. R., O'Brien, S. C., Curl, R. F. and Smalley, R. F., *Nature*, 1985, **318**, 162.
5. Iijima, S., *Nature*, 1991, **354**, 56.
6. Spain, I. L., Electronic transport properties of graphite, carbons, and related materials. In *Chemistry and Physics of Carbon*, Vol. 16, ed. P. L. Walker, Jr. and P. A. Thrower. Dekker, New York, 1981, pp. 119-304.

7. Murakami, M., Nishiki, N., Nakamura, K., Ehara, J., Okada, H., Kouzaki, T., Watanabe, K., Hoshi, T. and Yoshimura, S., *Carbon*, 1992, **30**, 255.
8. Ohno, K., Murakami, M., Hoshi, T., Kobayashi, Y., Shoji, T. and Arai, T., Characteristics of new pyrolytic graphite crystal for X-ray diffraction and fluorescence analysis. In *Advances in X-Ray Analysis*, ed. J. V. Gilfrich et al., Plenum Press, New York, 1994, pp. 545 552.
9. Murakami, M., Nakamura, K., Nishiki, N., Tajima, I., Okazaki, M. and Yoshimura, S., High-quality graphite for speaker diaphragms. In *Proceedings of International Symposium on Carbon*, Tsukuba, Japan, November 4-8, 1990, pp. 978 981.
10. Ohki, Y., Taomoto, A., Tsuchiya, S., Kawashima, T. and Nishiki, N., Thermal properties of newly developed flexible graphite sheet. In *Extended Abstracts and Programme of Science and Technology of Carbon (Eurocarbon '98)*, Vol. II, Strasbourg, France, July 6-7, 1998, pp. 679 680.
11. Yoshimura, S. and Chang, R. P. H., *Supercarbon, Synthesis, Properties and Applications*, Springer Series in Material Science, Vol. 33. Springer-Verlag, Heidelberg, 1998.
12. Yudasaka, M., Kikuchi, R., Matsui, T., Kamo, H., Ohki, Y., Yoshimura, S. and Ota, E., *Appl. Phys. Lett.*, 1994, **64**, 842.
13. Yudasaka, M., Kikuchi, R., Matsui, T., Ohki, Y., Ota, E. and Yoshimura, S., *phys. stat. sol. (a)*, 1996, **156**, 107.
14. Yudasaka, M., Kikuchi, R., Matsui, T., Ohki, Y., Ota, E. and Yoshimura, S., *J. Vac. Sci. Tech. A*, 1995, **13**, 2142.
15. Yudasaka, M., Kikuchi, R., Tasaka, K., Ohki, Y., Ota, E. and Yoshimura, S., *Appl. Phys. Lett.*, 1997, **81**, 7623.
16. Yudasaka, M., Kikuchi, R., Matsui, T., Ohki, Y., Ota, E. and Yoshimura, S., *Appl. Phys. Lett.*, 1995, **67**, 2477.
17. Yudasaka, M., Kikuchi, R., Ohki, Y., Ota, E. and Yoshimura, S., *Appl. Phys. Lett.*, 1997, **70**, 1817.
18. Yudasaka, M., Kikuchi, R., Ohki, Y. and Yoshimura, S., *Carbon*, 1977, **35**, 195.
19. Matsui, T., Yudasaka, M., Kikuchi, R., Ohki, Y. and Yoshimura, S., *Appl. Phys. Lett.*, 1994, **65**, 2145.
20. Sano, M., *Adv. Mater.*, 1996, **8**, 521.
21. Matsuhashi, M., Pankrushina, A. N., Endoh, K., Watanabe, H., Ohshima, H., Tobi, M., Endo, S., Mano, Y., Hyodo, M., Kaneko, T., Otani, S. and Yoshimura, S., *J. Gen. Appl. Microbiol.*, 1996, **42**, 315.
22. Thess, A., Roland, L., Nikolaev, P., Dai, H., Petit, P., Robert, J., Xu, C., Lee, Y. H., Kim, S. G., Rinzler, A. G., Colbert, D. T., Scuseria, G., Tománek, D., Fisher, J. E., and Smalley, R. E., *Science*, 1996, **273**, 483.
23. Hernadi, H., Fonseca, A., Nagy, J. B. and Bernaerts, D., Catalytic synthesis of carbon nanotubes. In *Supercarbon, Synthesis, Properties and Applications*, ed. S. Yoshimura and R. P. H. Chang. Springer-Verlag, Heidelberg, 1998, pp. 75 91.
24. Wang, X. K., Lin, X. W., Dravid, V. P., Ketterson, J. B. and Chang, R. P. H., *Appl. Phys. Lett.*, 1995, **66**, 2430.
25. Mordkovich, V. Z., Baxendale, M., Yoshimura, S. and Chang, R. P. H., *Carbon*, 1996, **34**, 1301.
26. Lee, R. S., Kim, H. J., Fischer, J. E., Thess, A. and Smalley, R. E., *Nature*, 1997, **388**, 255.

27. Grigorian, L., Williams, K. A., Fang, S., Sumanasekera, G. U., Loper, A. L., Dickey, E. C., Pennycook, S. J., and Eklund, P. C., *Phys. Rev. Lett.*, 1998, **80**, 5560.
28. Amelinckx, S. and Bernaerts, D., The geometry of multishell nanotubes. In *Supercarbon, Synthesis, Properties and Applications*, ed. S. Yoshimura and R. P. H. Chang. Springer-Verlag, Heidelberg, 1998, pp. 45-74.
29. Setlur, A. A., Lauerhaas, J. M., Dai, J. Y., and Chang, R. P. H., *Appl. Phys. Lett.*, 1996, **69**, 345.
30. Okuyama, F. and Ogasawara, I., *Appl. Phys. Lett.*, 1997, **71**, 623.
31. Han, W., Fan, S., Li, Q. and Gu, B., *Appl. Phys. Lett.*, 1997, **71**, 2271.
32. Tanuma, S., Synthesis and structure of quasi-one-dimensional carbon crystal "carbolite" and intercalation with alkali metals and halogens. In *Supercarbon, Synthesis, Properties and Applications*, ed. S. Yoshimura and R. P. H. Chang, Springer-Verlag, Heidelberg, 1998, pp. 120-127.
33. Ohki, Y., New π -electron materials: preparation and properties. In *Supercarbon, Synthesis, Properties and Applications*, ed. S. Yoshimura and R. P. H. Chang. Springer-Verlag, Heidelberg, 1998, pp. 149-166.
34. Seok, W. -S., Hamada, E., Kondo, Y. and Takayanagi, K., *Appl. Phys. Lett.*, 1996, **69**, 278.
35. Kusunoki, M., Rokkaku, M. and Suzuki, T., *Appl. Phys. Lett.*, 1997, **71**, 2620.
36. Yamamoto, K., Koga, Y., Fujikawa, S. and Kubota, M., *Appl. Phys. Lett.*, 1996, **69**, 4174.
37. Wildoer, J. W. G., Venema, L. C., Rinzler, A. G., Smalley, R. E. and Dekker, C., *Nature*, 1998, **391**, 59.
38. Odom, T. W., Huang, J. -L., Kim, P. and Lieber, C. M., *Nature*, 1998, **391**, 62.
39. Tans, S. J., Devoret, M. H., Dai, H., Thess, A., Smalley, R. E., Geerligs, L. J. and Dekker, C., *Nature*, 1997, **386**, 474.
40. White, C. T. and Todorov, T. N., *Nature*, 1998, **393**, 240.
41. Tans, S. J., Verschueren, A. R. M., and Dekker, C., *Nature*, 1998, **393**, 49.
42. Langer, L., Bayot, V., Grivei, E., Issi, J. -P., Hermans, J. P., Olk, C. H., Stockman, L., van Haesendonck, C., and Bruynseraede, Y., *Phys. Rev. Lett.*, 1996, **76**, 479.
43. Baxendale, M., Mordkovich, V. Z., Yoshimura, S. and Chang, R. P. H., *Phys. Rev. B*, 1977, **56**, 210.
44. Rinzler, A. G., Hafner, J. H., Nikolaev, P., Lou, L., Kim, S. G., Tománek, D., Nordlander, P., Colbert, D. T. and Smalley, R. E., *Science*, 1995, **269**, 1550.
45. Wang, Q. H., Corrigan, T. D., Dai, J. Y., Chang, R. P. H. and Krauss, A. R., *Appl. Phys. Lett.*, 1997, **70**, 3308.
46. Schmid, H. and Fink, H. -W., *Appl. Phys. Lett.*, 1997, **70**, 2679.
47. Chico, L., Crespi, V. H., Benedict, L. X., Louie, S. G. and Cohen, M. L., *Phys. Rev. Lett.*, 1996, **76**, 971.
48. Loiseau, A., Willaime, F., Demoncy, N., Hug, G. and Pascard, H., *Phys. Rev. Lett.*, 1996, **76**, 4737.
49. Enoki, T., Novel carbon-based host-guest systems. In *Supercarbon, Synthesis, Properties and Applications*, ed. S. Yoshimura and R. P. H. Chang. Springer-Verlag, Heidelberg, 1998, pp. 129-138.
50. Sato, K., Noguchi, M., Demachi, A., Oki, N. and Endo, M., *Science*,

- 1994, **264**, 556.
51. Che, G., Lakshmi, B. B., Fisher, E. R. and Martin, C. R., *Nature*, 1998, **393**, 346.
52. Dillon, A. C., Jones, K. M., Bekkedahl, T. A., Kiang, C. H., Bethune, D. S. and Heben, M. J., *Nature*, 1997, **386**, 377.
53. Niu, C., Sichel, E. K., Hoch, R., Moy, D. and Tennent, H., *Appl. Phys. Lett.*, 1997, **70**, 1480.

CHAPTER 14

Frontiers of Carbon Nanotubes and Beyond

HIROKI AGO^{1,2} and TOKIO YAMABE^{1,3}

¹*Department of Molecular Engineering, Graduate School of Engineering, Kyoto University, Sakyo-ku, Kyoto, 606-8501, Japan*

²*Cavendish Laboratory, Madingley Road, Cambridge, CB3 0HE, UK*

³*Institute for Fundamental Chemistry, 34-4 Nishihiraki-cho, Takano, Sakyo-ku, Kyoto, 606-8103, Japan*

1 Introduction

Since the discovery of metallic conductivity in chemically doped polyacetylene [1], interest in π -conjugated conducting polymers has grown continuously [2]. A great deal of research has been devoted to their metallic conducting properties, especially the transport mechanisms, the synthesis of more stable polymers and increasing their conductivity, as well as application to macroscale devices. Along with the attempt to realise intrinsic synthetic metals by increasing the dimensionality of conducting polymers, chemical doping experiments have also been performed on these materials. However, both of these methods have suffered from insolubility of materials or sensitivity to air and thus hindered the application to many fields. On the other hand, by taking advantage of semiconducting electronic structure in undoped polymers, the organic polymer-based light-emitting diodes have been fabricated [3] and form a very active field. The discovery of carbon nanotubes (CNTs) [4] and the following prediction of a variation of electronic structure with chiral angle and diameter [5-8] has attracted a great deal of interests [9-11]. The main characteristics of CNTs arise from their peculiar one-dimensionality and their nanoscale diameter. This is especially true for single-walled CNTs (SWCNTs) which are difficult to manipulate accurately by the conventional patterning technology [12]. Furthermore, their stability, mechanical strength and flexibility make CNTs much more useful than conducting polymers in many fields. The variety of electronic structure with the chiral angle and diameter, and inter-wall interaction in multi-walled CNTs (MWCNTs) provides the opportunity to choose particular types of CNTs for particular applications.

In this final chapter, we will review the current frontier of the applications of CNTs. Nanoscale applications such as nanoscale devices and ultra-fine probe, as well as macroscale applications such as field emission, energy storage and

macroscale devices will be discussed. We also consider the possibilities of manipulation, selection and modification of CNTs.

2 Individual CNTs for Nanotechnology

Though MWCNTs are useful because they are stabilised by a large number of layers and available in relatively large quantities, SWCNTs are more ideal for understanding electronic structure and transport phenomenon. They also lend themselves to nanoscopic applications because they have exceptionally high one-dimensional (1D) structure, a nanoscale diameter and they are not affected by inter-layer interactions. Interestingly, as-prepared SWCNTs are almost free from defects in spite of their small diameters, while catalytically grown MWCNTs [13] and even arc-evaporated MWCNTs always contain some defects [14]. Because SWCNTs are so small and not protected by outer layers, their formation seems to be subject to a kind of selection rule: CNTs with defects will be eliminated spontaneously due to their unstability during synthesis. The recent discovery of a new synthetic route to SWCNTs using nickel/cobalt catalysts, by the group in Rice University, has pushed forward research into nanoscopic study remarkably [15]. This is due to the fact that their samples possess an uniform distribution of diameter (1.38 ± 0.02 nm) and a high yield (more than 70 %). Actually, much of the research presented in this section was performed on samples synthesised by this group. We review the nanoscopic studies of CNTs mainly emphasising their electronic structures.

2.1 Experimental verification of existence of metallic and semiconducting CNTs

As described in Chap. 5, CNTs show a variety of electronic structure depending on their chiral angle and diameter: CNTs with the armchair configuration (a, a) and the configuration (a, b) satisfying $2a+b=3n$ (n is integer) are true 1D metallic, and other configurations make CNTs semiconductors with a finite band gap [6,16]. The investigation into the relationship between atomic configurations and electronic structures is very important, not only from scientific interest but also from potential to nanotechnology.

The temperature dependence of conductivity has been studied by many groups for various forms of CNTs, although simultaneous correlation with atomic configurations was not considered [17-21]. Figure 1 [24] shows conductivity or resistivity of individual and films of MWCNTs, ropes and films of SWCNTs and, for the sake of comparison, chemically doped conducting polymers. In MWCNTs, the semiconducting behaviour, i.e. increasing conductivity with increasing temperature, has been observed for all the samples, though the slope is different for each sample. For instance, the individual MWCNTs studied by the group at NEC have shown almost metallic property (Fig. 1(a), Ebbesen). This semiconducting behaviour is accounted for by a two-dimensional (2D) weak localisation effect (modelled by a 2D disordered graphene sheet) and inter-layer and inter-tube hopping barriers [17,18,24].

On the other hand, the rope of SWCNTs gave an increase of resistivity with increasing temperature which suggests the existence of metallic CNTs [21]. This is accounted for by the small effect of inter-chain barrier and the absence of inter-layer hopping processes.

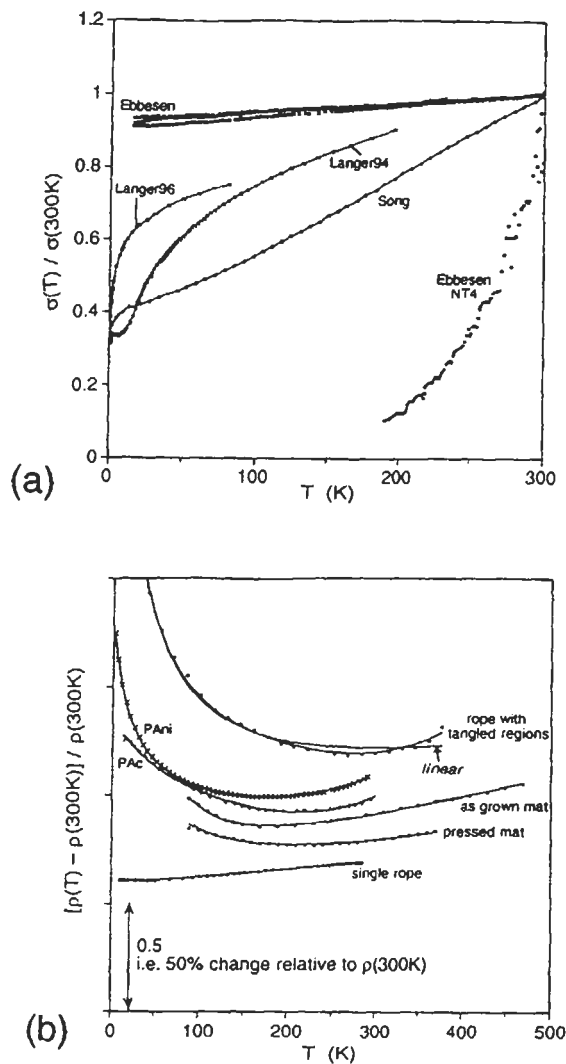


Fig. 1. (a) Comparison of normalised electrical conductivity of individual MWCNTs (Langer 96 [17], Ebbesen [18]) and bundles of MWCNTs (Langer 94 [19], Song [20]). (b) Temperature dependence of resistivity of different forms (ropes and mats) of SWCNTs [21], and chemically doped conducting polymers, PAc (FeCl_3 -doped polyacetylene [22]) and PAni (camphor sulfonic acid-doped polyaniline [23]) [24].

Very recently, the groups in Delft University of Technology [25] and Harvard University [26] have successfully verified the theoretical prediction of a correlation between the atomic configurations and the electronic structures of SWCNTs. This was achieved by the combination of scanning tunnelling microscope/scanning tunnelling spectroscopy (STM/STS). The atomic scale image of the SWCNT which is conjectured to possess semiconducting configuration (14, -3) is shown in Fig. 2.

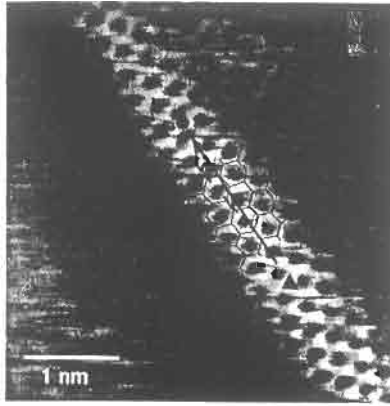


Fig. 2. Atomically resolved STM image of an SWCNT exposed at the surface of a rope. This SWCNT has a diameter of 0.95 nm and the possible configuration of (14, -3) [26].

From the analysis of STS spectra measured at under low temperature (4 K), two clear features were found in the density of states (DOS) near the Fermi energy as indicated in Fig. 3. Comparison with the calculated DOS indicated in Fig. 4 [6] gives strong evidence that the positions of the observed sharp peaks, which represent singularities originating in 1D structure, are due to the semiconducting and metallic natures of SWCNTs. The CNTs with the semiconducting configuration possess no DOS at the Fermi energy and a narrow spacing of about 0.6 eV between the two peaks (see Fig. 3, nos. 1-4 and Fig. 4 (a)), while the CNTs satisfying the metallic condition show a finite DOS at the Fermi energy together with two sharp peaks separated apart by about 1.8 eV (Fig. 3, nos. 5-7 and Fig 4(b)). It is noted that the presence of the singularities with a particular energy separation has also been suggested by the optical conductivity of SWCNTs [27]. Moreover, the theoretical prediction of the relationship between the diameter of semiconducting CNTs and the band gap has been confirmed experimentally (Fig. 5). These data are in good agreement with the theoretical estimation that, $E_g = 2\gamma a_{C-C}/d$ [9], where γ , a_{C-C} and d are the nearest-neighbour transfer integral, the C-C bond length and the diameter, respectively. However, the radii obtained by the group in Harvard [26] are smaller than the expected value of 1.38 ± 0.02 nm [15].

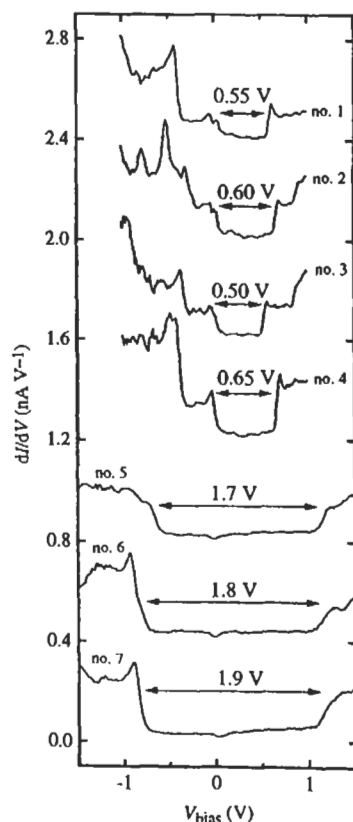


Fig. 3. Derivatives of the tunnelling current of individual SWCNTs obtained by the STS measurement. Different features are clearly seen in the spectra of nos. 1-4 and nos. 5-7 [25].

2.2 Nanodevices

Since the proposal in 1974 that organic molecules may be utilised in nanoscale devices (nanodevices) [28], a number of configurations and circuits comprising molecules have been designed hypothetically. The principle idea is that molecules can make devices much smaller and faster than the current inorganic technologies. It does however, remain just an idea since the problems associated with connecting and contacting molecular scale components have yet to be overcome. The synthesis of CNTs with the length of the order of one micron and high stability of CNTs have enabled us to "see" an individual CNT by atomic force microscope (AFM) and STM, and also to make contacts with metal electrodes. From these respects, CNTs, especially SWCNTs are considered to be

ideal material for nanoscale electronics. In comparison, C_{60} is far too small to manipulate and too sensitive to air and metals.

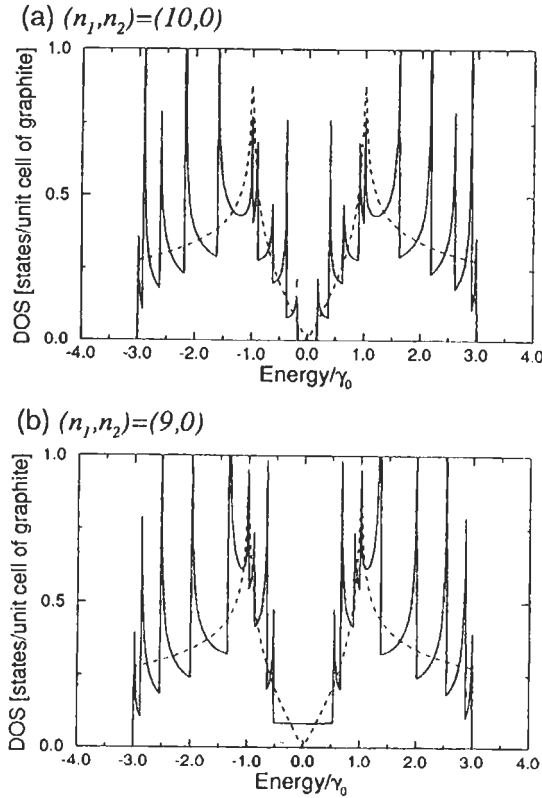


Fig. 4. Calculated density of states for two zigzag individual SWCNTs with (a) semiconducting $(10, 0)$ and (b) metallic $(9, 0)$ configurations. Tight-binding approximation was used for the calculation [6].

The group in Delft University of Technology [29] has fabricated a nanodevice by using an individual SWCNT as shown in Fig. 6. They reported the existence of two types of CNTs with different current-bias voltage (I - V_{bias}) profiles at room temperature [29]: one shows linear I - V_{bias} curves independent on the gate voltage, and the other shows nonlinear curves which are strongly dependent on the gate voltage. According to the group, the former is regarded as metallic and the latter as semiconducting. In the following, we will first examine the device properties of individual metallic CNTs and then move onto semiconducting CNTs. The group in Delft has measured individual SWCNTs in vacuum at very low temperatures (0.1 to 1 K) to avoid thermal fluctuations of the orbital energies of the CNTs [31]. I - V_{bias} curves with different gate voltages are shown

in Fig. 7. The observed step-wise increase of the current can be explained in terms of single electron tunnelling through a CNT.

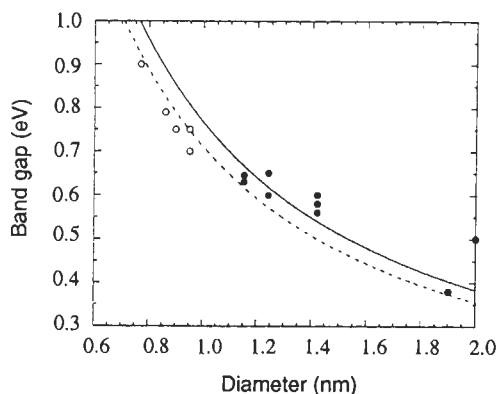


Fig. 5. Relationship between observed band gap and the diameter of individual SWCNTs. Closed and open circles indicate the data from refs. 25 and 26, respectively. The data are fitted with the equation, $E_g = 2\gamma a_{C-C}/d$, where the nearest-neighbour transfer integral γ is 2.7 eV and 2.5 eV for linear and broken lines, respectively.

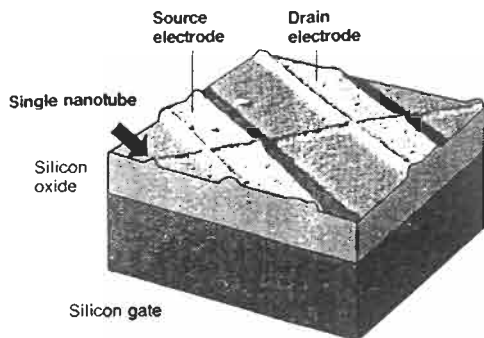


Fig. 6. The image of the nanodevice using an individual SWCNT (modified from ref. 30).

The schematic model is depicted in Fig. 8. As the bias voltage increases, the number of the molecular orbitals available for conduction also increases (Fig. 8) and it results in the step-wise increase in the current. It was also found that the conductance peak plotted vs. the bias voltage decreases and broadens with increasing temperature to ca. 1 K. This fact supports the idea that transport of carriers from one electrode to another can take place through one molecular orbital delocalising over whole length of the CNT, or at least the distance between two electrodes (140 nm). In other words, individual CNTs work as coherent quantum wires.

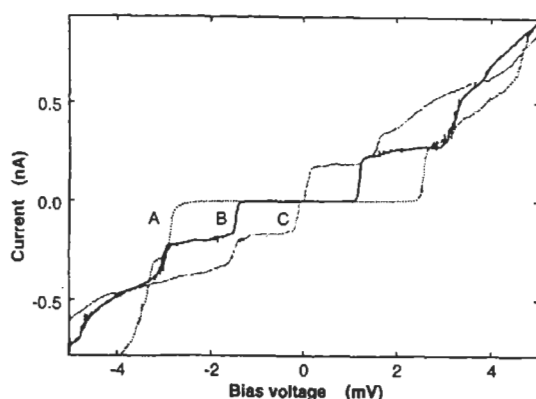


Fig. 7. I - V_{bias} curves of an individual SWCNT device with the gate voltage of (A) 88.2 meV, (B) 104.1 meV and (C) 120 meV [31].

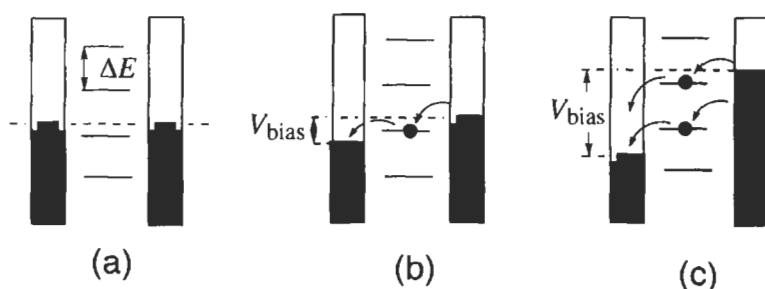


Fig. 8. Schematic illustration of the tunnelling in a CNT-based device: (a) under no bias voltage, there are no orbitals available for conduction, (b) with small bias voltage, only one molecular orbital of a CNT contributes to the carrier transport and (c) when the next molecular orbital enters the bias window, current increases stepwise. Gate voltage can shift all the orbitals upward or downward. ΔE indicates the energy separation of molecular orbitals.

These results are surprising, and such a high stability of molecular orbitals was considered to be a consequence of the stiff and almost defect-free structure of metallic CNTs [31]. From the gate voltage dependence of the current, the energy separation between molecular orbitals (ΔE) has been determined to be 0.4 meV, which is very close to the value predicted by calculations based on the particle-in-a-box model (0.6 meV for 3 μm -long tube). The Coulomb charging energy ($E_C = e^2/2C$, where e and C are electric charge and the capacitance of a CNT, respectively), which represents the energy required to put one electron into an individual CNT by overcoming Coulomb repulsion, has been calculated to be 2.6 meV.

It is worth noting that similar results have been obtained for a rope of SWCNTs consisting of about 60 CNTs [32]. In this case, however, the energy separation

of molecular orbitals and Coulomb charging energy are about 1 meV and 10-20 meV, respectively. These values are slightly higher than those obtained for individual CNTs [31]. This is counter intuitive since the energy separation and charging energy should be reduced due to the delocalisation of molecular orbitals over the whole rope. However, the difference between these two results is not necessarily conclusive since the groups have used different techniques to make contacts and the CNTs would be greatly affected by the doping effect of metal electrodes [31]. In addition the SWCNT can be damaged during the purification and the device processing procedures. Actually it has been suggested that a CNT is regarded as a number of quantum wires connected in series [33].

As described above, metallic CNTs are of great interest because they possess molecular orbitals which are highly delocalised. However, metallic CNTs are very difficult to use in actual devices because they require very low temperatures to control their carrier transfer. On the contrary, even at room temperature, the nonlinear I - V_{bias} curve and the effective gate voltage dependence have been presented by using individual semiconducting SWCNTs [29].

Because the finite band gap of around 0.4-0.6 eV for 1 nm diameter [11,25] is high enough to suppress thermal excitation of electrons from occupied molecular orbitals to unoccupied orbitals, they are available at room temperature. Figure 9 shows the I - V_{bias} curve of this semiconducting CNT-based device. The gate voltage dependence can be explained on the basis of the concept of a p-type metal-oxide-semiconductor field-effect transistor (MOSFET), and this CNT-based FET has shown an on/off ratio, which corresponds to the switching efficiency, as high as 10^6 .

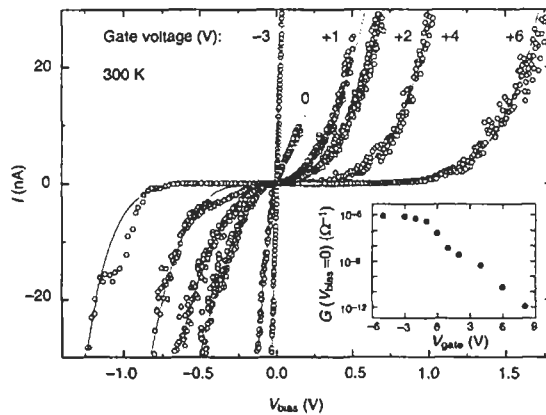


Fig. 9. I - V_{bias} curve of an individual semiconducting SWCNT with different gate voltages measured at room temperature [29].

This novel semiconducting CNT-based FET is expected to work with very high speed and makes the transistor remarkably small [30]. Since the research on nanodevices utilising CNTs only began in 1997, many interesting nanoscopic phenomena from CNTs can be expected in near future.

As for the coherent length in CNTs, a very interesting paper has been published from the group at the Georgia Institute of Technology about the conductance of individual MWCNTs [34]. They have observed the quantisation of conductance by changing the distance between the two electrodes. This result indicates ballistic conduction in a CNT, which suggests the formation of stationary waves of electrons inside CNTs.

2.3 Probes for nanoscale structure

The peculiar features of individual CNTs, high one-dimensionality and nanoscale diameter (usually 1-50 nm), are also ideal for use as nanoscale probes in scanning force microscopy (SFM). Probes employing CNTs are expected to be useful for imaging deep trenches and to be highly durable owing to strength and flexibility. In 1996, the group in Rice University succeeded in fabricating an SFM by attaching MWCNT bundles to silicon cantilever [35]. The bundles consisted of about 5 to 10 CNTs from which one single CNT (diameter of 5 nm) protruded by 250 nm (Fig. 10).

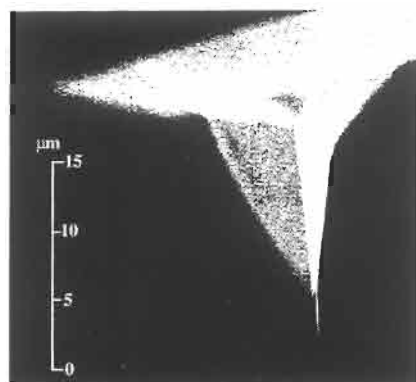


Fig. 10. Scanning electron microscope (SEM) image of the probe with an MWCNT attached to a silicon cantilever [35]. Protruding of one individual MWCNT has been confirmed by transmission electron microscope (TEM) measurement (not shown here).

Tapping-mode SFM observes surface geometry by detecting the minute force between a probe and surface through the resonant frequency between a probe and a cantilever. The Euler buckling force which indicates mechanical strength against vertical force was calculated for the MWCNT (250 nm long and 5 nm diameter) to be 5 nN [35]. Though this value is not as high as the standard silicon tip (> 100 nN), the group at Rice expects that CNTs are still useful because they can flex when they hit the surface or touch it laterally.

The SFM images shown in Fig. 11 have proved that CNTs are promising for nanoscale structural investigation and are better than the normal silicon nitride probes [36].

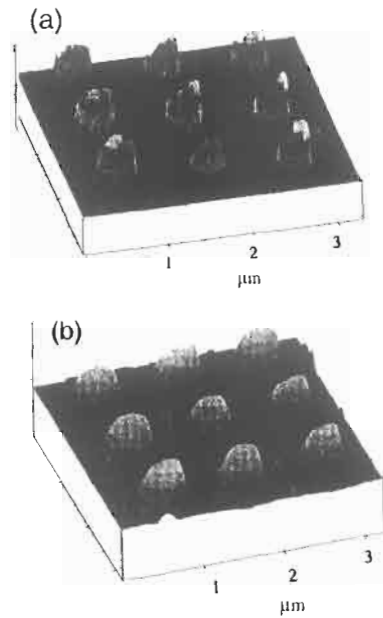


Fig. 11. SFM pictures of etched GaAs surface obtained by using (a) the MWCNT probe and (b) standard silicon nitride probe [36].

It is noted that much higher resolution is expected when an individual SWCNT is used. By taking advantages of the high conductivity of CNTs, STM images have also been obtained using a CNT probe [35].

Since the tips of CNTs can be modified chemically, CNTs can be used as probes for investigating surface chemistry. The group in Harvard University has prepared a CNT probe whose tip is covered with carboxyl groups by oxidation, and also with amide groups by chemical reaction from carboxyl groups [37]. They have succeeded in observing differences in the force between CNT probes terminated with different functional groups and sample surfaces of varying pH. For instance, probes with carboxyl groups give drastic changes of force as a function of pH of the surface, while the probe with amide groups is not affected by pH. Hence, when the attachment of CNT-probes becomes routine, further progress will be expected in these applications.

3 Application of CNTs for Macroscale Purposes

Nanoscale diameter, hollow structure, high conductivity, mechanical strength and inertness of CNTs are also very useful for macroscale applications. MWCNTs have been more widely used for macroscopic applications since they are more readily available in larger quantities and are more stable than SWCNTs.

Also, macroscopic devices tend not to require the highly 1D properties of single-CNTs. Very recently studies using SWCNTs have just emerged. Though well-aligned CNT films are preferable for many purposes, the insolubility of CNTs makes them difficult to align. Instead, bundles, mechanically stressed mats and films stabilised with resin have been examined. In this section, we review some interesting applications of bulk CNTs.

3.1 Field emission

Field emission applicable to flat-panel display is one of the most advanced and energetically studied applications of CNTs. The apparatus is illustrated in Fig. 12 along with pictures of closed-tips of MWCNTs. In spite of their high workfunction (4.3 eV for MWCNTs [39]), CNTs emit electrons from their tips when high voltages (100-1000 V) are applied between the metal grid of the accelerator and the CNT film which are separated by 20 μm [38].

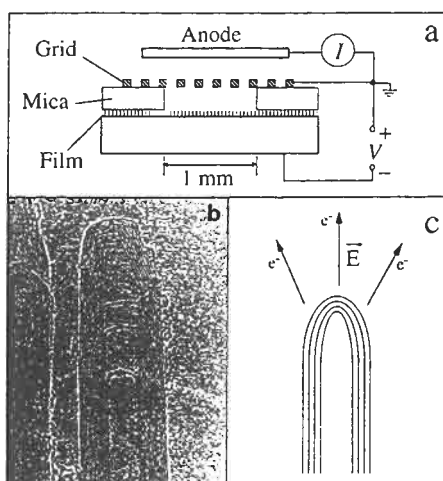


Fig. 12. (a) Schematic illustration of the setup for field emission experiment using a CNT film. (b) TEM picture of a tip of an MWCNT where electrons are emitted. (c) Illustration of the electron emission by applied electric field [38].

This is because of their 1D structure and high electrical conductivity. The electrons emitted from the CNTs pass through the grid and reach the phosphor screen to give high luminescence. This field emission has been observed in individual SWCNTs [40], individual MWCNTs [41], carefully aligned MWCNT films [42] and randomly oriented MWCNT films [43]. SWCNTs were not stable under such severe conditions [40]. The advantages of CNT-based field emitters are a narrow energy range of emitted electrons (0.2 eV) and room temperature operation (conventional tungsten emitters need to be heated) [38].

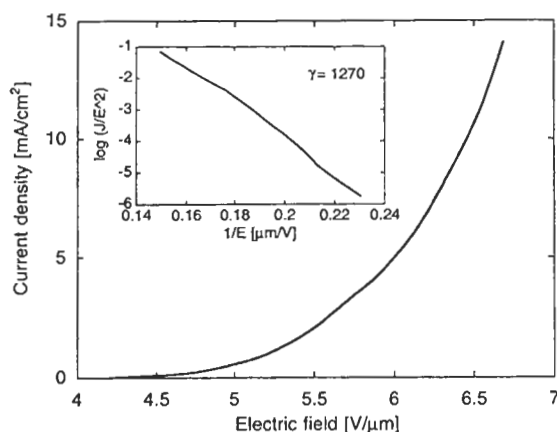


Fig. 13. Electric-field dependence of the emission current obtained for a carefully aligned MWCNT film [38]. Inset: Fowler-Nordheim plot, where γ is the field-enhancement factor.

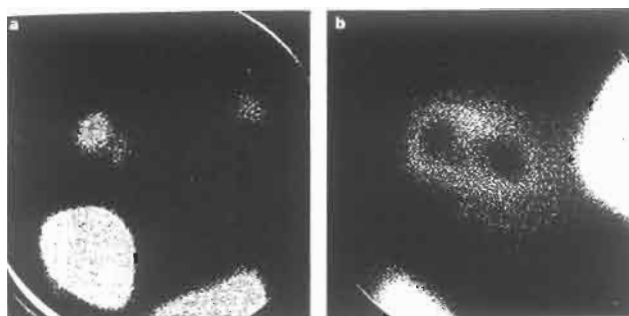


Fig. 14. Field emission patterns from (a) closed-tip and (b) open-tip MWCNTs taken by a CCD camera [46].

This interesting phenomenon has been explained by the tunnelling of electrons from localised states at a tip with energies close to the Fermi energy, stimulated by the enhancement of the electric field from their 1D structure [38]. Based on the Fowler-Nordheim model (Fig. 13 inset), it was calculated that the electric field at the tip is enhanced about 1300 times [38], but there is some discussion on the validity of this model [44]. The model that electrons are emitted from single atomic wires protruding from the tips of CNTs [41] is still hypothetical and has not been confirmed. It is very interesting to note that the opening of tips by oxidation with either oxygen-plasma treatment or by heating in oxygen-gas makes CNTs more highly emissive [41,45]. Considering the hollow image of emission of open-tip MWCNTs shown in Fig. 14 [46], the emission from almost all the carbon atoms around the tip is plausible.

The calculations of the electronic structure of the closed-tip CNTs with finite length suggest that largely localised orbitals exist at the tip (mainly at the five-membered rings) with energies close to the Fermi energy [47]. However, considering the fact that electrons are accelerated by the strong electric field and actually go through the cylinder of a CNT before reaching the tip, it seems that consideration of such localised orbitals is insignificant. Moreover there have been no definite explanations for the high emission from open-tips rather than closed-tips. We think the curvature and existence of localised orbitals at a five-membered ring decelerates the electron through the scattering effect. Very recently more advanced research has been performed. The group in Mie University has fabricated cathode ray tubes (CRT) which show very high luminescence intensity (6×10^4 cd/m²) under very high applied voltage (10 kV) and has obtained very long life time of more than 4000 hours [48]. The group in Northwestern University has fabricated a matrix display (32×32) by employing phosphor-coated indium-tin oxide (ITO) glass as the anode [49]. The establishment of inexpensive synthetic routes and preparation methods of aligned CNT films, as well as a clarification of the mechanism of emission are strongly desired for further development.

3.2 Energy storage

The hollow spaces of CNTs, similar to those of zeolites, offer many intriguing properties: places to store the guest molecules and to perform chemical reactions with selected-size molecules. Though, to our knowledge, the latter has not yet been studied, there have been some interesting studies on the former application. In the following, we will look at this capillary effect of the hollow space. Initially, theoretical study based on the local-density approximation (LDA) suggested that a capillary effect will occur in the hollow spaces of CNTs [50]. The group at NEC has actually observed filling and wetting in the hollow space of an open-tip MWCNT [51].

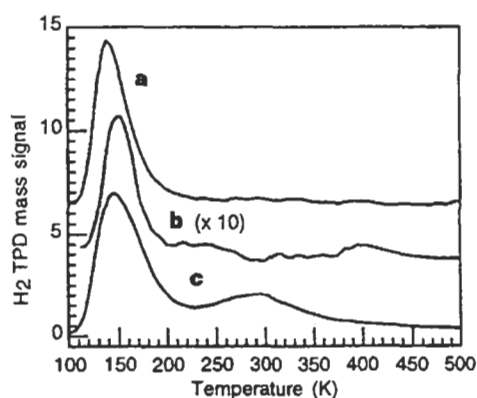


Fig. 15. Temperature-programmed desorption (TPD) spectra of (a) closed-tip SWCNTs, (b) activated carbon and (c) open-tip SWCNTs [52].

The group in the National Renewable Energy Laboratory has recently provided the evidence that the hollow space can store and stabilise a large number of hydrogen molecules [52]. This hydrogen storage is very attractive from the view point of fuel cell technology which requires a very high density of hydrogen molecules for clean combustion (i.e. which exhausts only water). The temperature-programmed desorption (TPD) profiles of closed- and open-tip SWCNTs with diameters of around 1.2 nm are shown in Fig. 15, together with the results of activated carbon which has micropores with diameters of around 3.0 nm.

The peak at 133 K seen in all the samples is known to originate in the hydrogen molecules adsorbed inside the contamination amorphous carbon. This hydrogen is not useful because it cannot be used at room temperature. A new peak at 288 K, found only in the open-tip CNTs, suggests that the hydrogen molecules are incorporated inside the hollow spaces of CNTs. The high temperature desorption (288 K) of a large number of hydrogen molecules is a fascinating property for this application. The heat of adsorption for this site (19.6 kJ/mol) is larger than those for graphite (~ 4 kJ/mol) and activated carbons (12 kJ/mol for low coverage and 4 kJ/mol for high coverage) and provides strong van der Waals force within the CNTs, but the origin of this high stabilisation effect by hollow space is ambiguous at the moment. The well-aligned SWCNTs with the diameter of 2.0 nm was predicted to be a good candidate for the use in vehicles, much better than metal hydrides [52], but it seems uncertain because the van der Waals force could become smaller in the CNTs with larger diameters.

The hollow space is also attractive for the application to lithium-ion batteries in which lithium ions are stored with high stability inside the anode materials made of carbons, such as graphite and amorphous carbons [53]. Carbon nanotubes [54] finished in a membrane consisting of well-ordered tubular pores of graphitised carbon produced by the template method have been studied for lithium storage and showed higher capacity (490 mAh/g) than that of graphite (372 mAh/g). The substitution of open-tip CNTs for this study will surely prove most interesting. Although it is supposed that the hollow space inside CNTs is essential for these high molecule/ion storage, the detailed mechanism is not fully understood and further study is necessary for designing the appropriate structure of CNTs and their film.

3.3 Macroscopic devices

CNT films are also of interest from morphological aspect because their structure provides nanoscale voids within the networks of CNTs. For example, composites with conducting polymers are very interesting both from scientific and technological interests, since we would expect CNTs to give a well-dispersed film.

The group in the Swiss Federal Institute of Technology [55] has fabricated a macroscale device by depositing the conducting polymer (poly(*p*-phenylenevinylene)) on the MWCNT film (Fig. 16). They have observed the characteristic rectifying effect from the *I-V* curve, which suggests the CNTs inject holes efficiently into the polymer layer. However, due to the difficulty in

making a good film of CNTs, very thick films are needed in order to avoid short-circuits between CNTs and top metal contacts. Therefore, the interfacial interaction between CNTs and polymers has not been clearly observed.

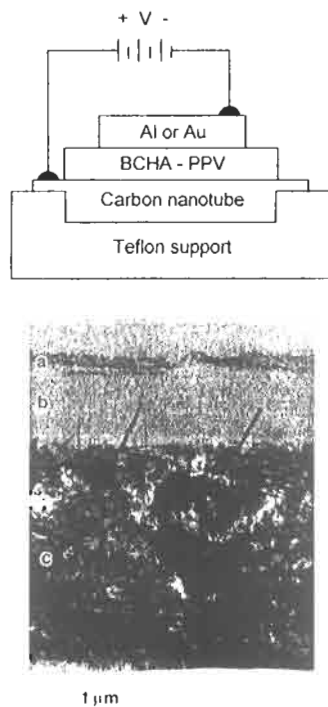


Fig. 16. Top: Illustration of the macroscopic device. BCHA-PPV is poly(2,5-bis(cholestanoxo)-1,4-phenylenevinylene) [55]. Bottom: Cross section of the device (a) Al contact, (b) polymer layer and (c) CNT film.

C₆₀ is a good electron-acceptor and shows highly efficient charge separation when mixed with conducting polymers and excited by illumination with visible light [56-58]. The photovoltaic devices using C₆₀ and conducting polymers, which absorb visible light in the polymer and generates electricity by charge separation at the polymer/C₆₀ interface, have been fabricated and shown very high quantum efficiencies of around 9 % [58]. Therefore, it must be very interesting to study interfacial interaction between CNTs and photo-excited conducting polymers. In addition CNTs would give high mechanical strength to the polymer composite.

4 Manipulation of CNTs and Beyond

As seen in previous sections, applications of CNTs have been flourishing in recent years. However, it seems there remain great difficulties in commercialisation from two reasons, manipulation and selection of CNTs. At present it is still not easy to obtain pure and well-ordered films or to align multiple CNTs properly against electrodes in large scale. It should be more explicitly required to control the chirality, diameter, length and electronic structure of CNTs for pragmatic usage. The modification is the other way to control electronic properties. It should be noted that the establishment of a low-cost synthetic method will be necessary for future commercialisation. In this last section, we review recent attempts to surmount these difficulties and some modification methods.

Regarding macroscale alignment of CNTs in a film, the quest for a new synthetic route which gives highly aligned CNT films by using laser-etched catalysts has been reported [59]. Deposition of aligned films on certain substrates would require soluble CNTs. Very recently, there has been reported an attempt to prepare soluble CNT by terminating the short-cut SWCNT [60] with long-chain amide group [61] or by chemical oxidation of the catalytically-grown MWCNT [62]. As for nanoscale alignment, it has been shown that the shape and position of individual CNTs can be controlled by an AFM probe [63,64]. However, problems still remain for the manipulation because the AFM method takes time and manipulation of more advanced architecture calls for sophisticated technology. Concerning the selection of specific CNTs, chirality and diameter are more difficult to control than length because length can be changed by oxidation [65,66] and cutting by AFM probes [64,67], and selected by column separation [68]. On the other hand, choosing the chirality and diameter seems to be achievable only by improvement to or finding of new synthetic routes, like etching of catalysts and using polymers as a starting materials, as was used by the group in Rice University to prepare CNTs with uniform diameter [15].

Next, let us look at modification of CNTs. There are many approaches to modifying the electronic structure of CNTs: oxidation [39], doping (intercalation) [69], filling [70] and substitution by hetero elements like boron and nitrogen atoms [71,72]. There have been few studies on the application of these CNTs but it will be interesting to study applications as well as electronic properties.

Today, a large number of researchers from a variety of fields are enthusiastically working on CNTs. Field emission has a relatively long history and has proceeded considerably, while the investigation into nanodevices has just begun. Some of research only involves the replacement the well-established material by CNTs. It is, however, more exciting to find out the new physical concepts through research of this novel material, CNTs.

Acknowledgements

We are grateful to financial support from the project of Institute for Fundamental Chemistry, supported by the Japanese Society for the Promotion of Science - Research for the Future Program (JSPS-RFTF98P00206). HA acknowledges the

JSPS Research Fellowships for Young Scientists, and K. Tsukagoshi of Hitachi Cambridge Laboratory and R. H. Friend and S. Thomas of Cavendish Laboratory for valuable discussions.

References

1. Shirakawa, H., Louis, E. J., MacDiarmid, A. G., Chiang, C. K. and Heeger, A. J., *J. Chem. Soc., Chem. Commun.*, 1977, 578.
2. Skotheim, T. A. ed., *Handbook of Conducting Polymers*. Marcel Dekker, New York, 1986, Vols. 1 and 2.
3. Burroughes, J. H., Bradley, D. D. C., Brown, A. R., Marks, R. N., Mackay, K., Friend, R. H., Burns, P. L. and Holmes, A. B., *Nature*, 1990, **347**, 539.
4. Iijima, S., *Nature*, 1991, 354, 56.
5. Tanaka, K., Okahara, K., Okada, M. and Yamabe, T., *Chem. Phys. Lett.*, 1992, **191**, 469.
6. Saito, R., Fujita, M., Dresselhaus, G. and Dresselhaus, M. S., *Appl. Phys. Lett.*, 1992, **60**, 2204.
7. Hamada, N., Sawada, S. and Oshiyama, A., *Phys. Rev. Lett.*, 1992, **68**, 1579.
8. Mintmire, J. W., Dunlap, B. I. and White, C. T., *Phys. Rev. Lett.*, 1992, **68**, 631.
9. Dresselhaus, M. S., Dresselhaus, G. and Eklund, P. C., *Science of Fullerenes and Carbon Nanotubes*, Academic Press, San Diego, 1996.
10. Ajayan, P. M. and Ebbesen, T. W., *Rep. Prog. Phys.*, 1997, **60**, 1025.
11. Dresselhaus, M. S., Dresselhaus, G., Eklund, P. C. and Saito, R., *Physics World*, 1998, 33.
12. Rai-Choudhury, P. ed., *Handbook of Microlithography, Micromachining and Microfabrication*. Vol. 1: microlithography, SPIE Optical Engineering Press, Washington, 1997.
13. Dai, H., Wong, E. W. and Lieber, C. M., *Science*, 1996, **272**, 523.
14. Zhou, O., Fleming, R. M., Murphy, D. W., Chen, C. H., Haddon, R. C., Ramirez, A. P. and Glarum, S. H., *Science*, 1994, **263**, 1744.
15. Thess, A., Lee, R., Nikolaev, P., Dai, H., Petit, P., Robert, J., Xu, C., Lee, Y. H., Kim, S. G., Rinzler, A. G., Colbert, D. T., Scuseria, G. E., Tománek, D., Fischer, J. E. and Smalley, R. E., *Science*, 1996, **273**, 483.
16. Okahara, K., Tanaka, K., Aoki, H., Sato, T. and Yamabe, T., *Chem. Phys. Lett.*, 1994, **219**, 462.
17. Langer, L., Bayot, V., Grivei, E., Issi, J. -P., Heremans, J. P., Olk, C. H., Stockman, L., Van Haesendonck, C. and Bruynseraede, Y., *Phys. Rev. Lett.*, 1996, **76**, 479.
18. Ebbesen, T. W., Lezec, H. J., Hiura, H., Bennett, J. W., Ghaemi, H. F. and Thio, T., *Nature*, 1996, **382**, 54.
19. Langer, L., Stockman, L., Heremans, J. P., Bayot, V., Olk, C. H., Van Haesendonck, C., Bruynseraede, Y. and Issi, J. -P., *J. Mater. Res.*, 1994, **9**, 927.
20. Song, S. N., Wang, X. K., Chang, R. P. H. and Ketterson, J. B., *Phys. Rev. Lett.*, 1994, **72**, 697.

21. Fischer, J. E., Dai, H., Thess, A., Lce, R., Hanjani, N. M., Dehaas, D. L. and Smalley, R. E., *Phys. Rev. B*, 1997, **55**, R4921.
22. Tsukamoto, J., *Adv. Phys.*, 1992, **41**, 509.
23. Yoon, C. O., Reghu, M., Moses, D., Heeger, A. J. and Cao, Y., *Synth. Met.*, 1994, **63**, 47.
24. Kaiser, A. B., Düsberg, G. and Roth, S., *Phys. Rev. B*, 1998, **57**, 1418.
25. Wildöer, J. W. G., Venema, L. C., Rinzler, A. G., Smalley, R. E. and Dekker, C., *Nature*, 1998, **391**, 59.
26. Odom, T. W., Huang, J. -L., Kim, P., Lieber, C. M., *Nature*, 1998, **391**, 62.
27. Pichler, T., Knupfer, M., Golden, M. S., Fink, J., Rinzler, A. and Smalley, R. E., *Phys. Rev. Lett.*, 1998, **80**, 4729.
28. Aviram, A. and Ratner, M. A., *Chem. Phys. Lett.*, 1974, **29**, 277.
29. Tans, S. J., Verschueren, A. R. M. and Dekker, C., *Nature*, 1998, **393**, 49.
30. McEuen, P. L., *Nature*, 1998, **393**, 15.
31. Tans, S. J., Devoret, M. H., Dai, H., Thess, A., Smalley, R. E., Geerligs, L. J. and Dekker, C., *Nature*, 1997, **386**, 474.
32. Bockrath, M., Cobden, D. H., McEuen, P. L., Chopra, N. G., Zettl, A., Thess, A. and Smalley, R. E., *Science*, 1997, **275**, 1922.
33. Bezryadin, A., Verschueren, A. R. M., Tans, S. J. and Dekker, C., *Phys. Rev. Lett.*, 1998, **80**, 4036.
34. Frank, S., Poncharal, P., Wang, Z. L. and de Heer, W. A., *Science*, 1998, **280**, 1744.
35. Dai, H., Hafner, J. H., Rinzler, A. G., Colbert, D. T. and Smalley, R. E., *Nature*, 1996, **384**, 147.
36. Navy, G., Levy, M., Scarmozzino, R., Osgood, Jr., R. M., Dai, H., Smalley, R. E., Michaels, C. A., Flynn, G. W. and McLane, G. F., *Appl. Phys. Lett.*, 1998, **73**, 529.
37. Wong, S. S., Joselevich, E., Woolley, A. T., Cheung, C. L. and Lieber, C. M., *Nature*, 1998, **394**, 52.
38. de Heer, W. A., Bonard, J. -M., Fauth, K., Châtelain, A., Forró, L. and Ugarte, D., *Adv. Mater.*, 1997, **9**, 87.
39. Ago, H., Kugler, Th., Cacialli, F., Petritsch, K., Friend, R. H., Salaneck, W. R., Ono, Y., Yamabe, T. and Tanaka, K., Paper presented at 14th International Conference on Science and Technology of Synthetic Metals, WEP153, Montpellier, July 12-18, 1998; *Synth. Met.*, in press.
40. Saito, Y., Hamaguchi, K., Nishino, T., Hata, K., Tohji, K., Kasuya, A. and Nishina, Y., *Jpn. J. Appl. Phys.*, 1997, **36**, L1340.
41. Rinzler, A. G., Hafner, J. H., Nikolaev, P., Lou, L., Kim, S. G., Tománek, D., Nordlander, P., Colbert, D. T. and Smalley, R. E., *Science*, 1995, **269**, 1550.
42. de Heer, W. A., Châtelain, A. and Ugarte, D., *Science*, 1995, **270**, 1179.
43. Collins, P. G. and Zettl, A., *Appl. Phys. Lett.*, 1996, **69**, 1969.
44. Collins, P. G. and Zettl, A., *Phys. Rev. B*, 1997, **55**, 9391.
45. Wang, Q. H., Corrigan, T. D., Dai, J. Y., Chang, R. P. H. and Krauss, A. R., *Appl. Phys. Lett.*, 1997, **70**, 3308.
46. Saito, Y., Hamaguchi, K., Hata, K., Uchida, K., Tasaka, Y., Ikazaki, F., Yumura, M., Kasuya, A. and Nishina, Y., *Nature*, 1997, **389**, 554.
47. Caroll, D. L., Redlich, P., Ajayan, P. M., Charlier, J. C., Blase, X., de Vita, A. and Car, R., *Phys. Rev. Lett.*, 1997, **78**, 2811.

48. Saito, Y., Uemura, S. and Hamaguchi, K., *Jpn. J. Appl. Phys.*, 1998, **37**, L346.
49. Wang, Q. H., Setlur, A. A., Lauerhaas, J. M., Dai, J. Y., Seelig, E. W. and Chang, R. P. H., *Appl. Phys. Lett.*, 1998, **72**, 2912.
50. Pederson, M. R. and Broughton, J. Q., *Phys. Rev. Lett.*, 1992, **69**, 2689.
51. Dujardin, E., Ebbesen, T. W., Hiura, H. and Tanigaki, K., *Science*, 1994, **265**, 1850.
52. Dillon, A. C., Jones, K. M., Bekkedahl, T. A., Kiang, C. H., Bethune, D. S. and Heben, M. J., *Nature*, 1997, **386**, 377.
53. Ago, H., Nagata, K., Yoshizawa, K., Tanaka, K. and Yamabe, T., *Bull. Chem. Soc. Jpn.*, 1997, **70**, 1717.
54. Che, G., Lakshmi, B. B., Fisher, E. R. and Martin, C. R., *Nature*, 1998, **393**, 346.
55. Romero, D. B., Carrard, M., de Heer, W. A. and Zuppiroli, L., *Adv. Mater.*, 1996, **8**, 899.
56. Morita, S., Zakhidov, A. A. and Yoshino, K., *Jpn. J. Appl. Phys.*, 1993, **32**, L873.
57. Sariciftci, N. S., Braun, D., Zhang, C., Srdanov, V. I., Heeger, A. J., Stucky, G. and Wudl, F., *Appl. Phys. Lett.*, 1993, **62**, 585.
58. Halls, J. J. M., Pichler, K., Friend, R. H., Moratti, S. C. and Holmes, A. B., *Appl. Phys. Lett.*, 1996, **68**, 3120.
59. Terrones, M., Grobert, N., Zhang, J. P., Terrones, H., Olivares, J., Hsu, W. K., Hare, J. P., Cheetham, A. K., Kroto, H. W. and Walton, D. R. M., *Chem. Phys. Lett.*, 1998, **285**, 299.
60. Liu, J., Rinzler, A. G., Dai, H., Hafner, J. H., Bradley, R. K., Boul, P. J., Lu, A., Iverson, T., Shelimov, K., Huffman, C. B., Rodriguez-Macias, F., Shon, Y.-S., Lee, T. R., Colbert, D. T. and Smalley, R. E., *Science*, 1998, **280**, 1253.
61. Chen, J., Hamon, M. A., Hu, H., Chen, Y., Rao, A. M., Eklund, P. C. and Haddon, R. C., *Science*, 1998, **282**, 95.
62. Shaffer, M. S. P., Fan, X. and Windle, A. H., *Carbon*, 1998, **36**, 1603.
63. Curran, S., Carroll, D. L., Ajayan, P. M., Redlich, P., Roth, S., Rühle, M. and Blau, W., *Adv. Mater.*, 1998, **3**, 311.
64. Hertel, T., Martel, R. and Avouris, P., *J. Phys. Chem. B*, 1998, **102**, 910.
65. Morishita, K. and Takarada, T., *Carbon*, 1997, **35**, 977.
66. Hiura, H., Ebbesen, T. W. and Tanigaki, K., *Adv. Mater.*, 1995, **7**, 275.
67. Venema, L. C., Wildöer, J. W. G., Tuinstra, H. L. J. T., Dekker, C., Rinzler, A. G. and Smalley, R. E., *Appl. Phys. Lett.*, 1997, **71**, 2629.
68. Duesberg, G. S., Burghard, M., Muster, J., Phillip, G. and Roth, S., *J. Chem. Soc., Chem. Commun.*, 1998, 435.
69. Baxendale, M., Mordkovich, V. Z., Yoshimura, S. and Chang, R. P. H., *Phys. Rev. B*, 1997, **56**, 2161.
70. Satishkumar, B. C., Govindaraj, A., Mofokeng, J., Subbanna, G. N. and Rao, C. N. R., *J. Phys. B*, 1996, **29**, 4925.
71. Miyamoto, Y., Rubio, A., Cohen, M. L. and Louie, S. G., *Phys. Rev. B*, 1994, **50**, 4976.
72. Redlich, Ph., Loeffler, J., Ajayan, P. M., Bill, J., Aldinger, F. and Rühle, M., *Chem. Phys. Lett.*, 1996, **260**, 465.

SUBJECT INDEX

- acoustic mode 53
- Aharonov-Bohm (AB) effect 65
- Aharonov-Bohm (AB) magnetic flux 65
- aligned carbon nanotube (CNT) 5, 80, 91, 148
- amorphous carbon (a-C) 9, 133, 160
- annealed carbon nanotube (CNT) 80
- arc discharge 3, 130, 144
- armchair-type carbon nanotube (CNT) 41, 45, 53, 55, 108
- atomic force microscope (AFM) 168, 180
- atomic scattering factor 22

- ballistic regime 111
- band gap (bandgap) 42, 45, 167
- band structure 42
- bead-string structure 158
- Bessel function 24
- bond alternation 43
- boron-nitride nanotubes 159
- Bruggeman model (BM) 95, 100
- Brunauer-Emmett-Teller (BET) analysis 147
- buckybundle 157
- bundle 47, 112, 119, 144

- C₆₀ 77
- ¹³C nuclear magnetic resonance (NMR) 42
- capillarity 131
- capillary effect 177
- capillary filling 129, 138
- carbolite 158
- carbon electrode 160
- carbon nanotube (CNT)
 - cavity 132, 136
 - junction 123
 - tip 136
- carbyne 150
- catalyst metal 5
- catalytic decomposition of hydrocarbon 4
- cathode ray tube (CRT) 177
- chemical vapour deposition (CVD) 155
- chiral angle 19
- chiral vector 41, 108
- chiral (or helical)-type carbon nanotube (CNT) 41, 45, 55, 108

Clausius-Mossotti expression 140
 Clausius-Mossotti model 95
 coaxial cylinder model 16
 cobalt monoxide (CoO) filament 136
 coherent quantum wire 170
 collar 144
 conduction electron spin resonance (CESR) 77
 core-loss region 35
 coronae 19
 Coulomb blockade 120
 Coulomb charging energy 171
 Curie law 77
 current-bias voltage 169
 cyclotron orbit 66

 density of states (DOS) 167
 diamagnetism 78
 dielectric constant 140
 dielectric function 95
 differential susceptibility 72
 diffraction vector 20
 dipole moment 96
 dirty chemistry 154
 disordered stacking model 19
 doped carbon nanotube (CNT) 82
 dynamical matrix 53
 Dysonian 85

 effective medium 95, 100
 elastic constant 54
 electrical conductivity 110
 electrochemical capacitor 160
 electrolysis 149
 electron diffraction (ED) pattern 14
 electron energy loss spectroscopy (EELS) 32
 electron irradiation 150
 electron spectroscopic image (ESI) 33
 electron spin resonance (ESR) 77
 electron spin resonance (ESR) linewidth 78, 90
 Endo pyrolytic carbon nanotube (Endo PCNT) 146
 energy dispersive X-ray spectroscopy (EDX) 139
 energy-loss near-edge structure (ELNES) 32
 Ewald's construction 23
 exciton 69
 extended energy-loss fine-structure (EXELFS) 32

 far infrared (FIR) absorption 93

- Fermi energy 116
- field emission 7, 123, 159, 175
- field-effect transistor (FET) 172
- filling material droplet 137
- force constant 52
- Fowler-Nordheim model 176

- g-value 78
- Gatan imaging filter (GIF) 33
- graphene sheet 159
- graphite
 - electron mobility 154
 - intercalation compound (GIC) 154, 160
 - sound velocity 154
 - thermal conductivity 154

- helical (or chiral)-type carbon nanotube (CNT) 41, 45, 55, 108
- hexagonal lattice 18, 59
- high-resolution electron micrograph (HREM) 133, 136
- high-resolution transmission electron microscopy (HRTEM) 26
- highly oriented pyrolytic graphite (HOPG) 77, 92, 116
- hologram generation 159
- homogeneous shear model 19
- host medium 101
- hydrogen arc 158
- hydrogen storage 160, 178
- Hyperion pyrolytic carbon nanotube (Hyperion PCNT) 147

- inelastic mean free path 111
- inter-chain barrier 166
- inter-layer hopping 166
- intercalated carbon nanotube 158
- intercalated graphite 82
- intercalation 122, 180
- interlayer interaction 47
- intertube interaction 47

- K-shell 31
- Kekulé distortion 69
- Kekulé type 44
- kinematical diffraction theory 20
- Korringa-like relation 42
- Kramers-Kronig transformation 92
- k•p** equation 65

- L-shell 31
- Landau level 66, 116

laser ablation 4, 9, 144
 laser vapourisation 144
 lattice distortion 69
 lattice fringe 16
 lead-compound filling 137
 light-emitting diode 164
 linewidth (see electron spin resonance linewidth)
 liquid surface tension 131
 liquid-solid contact angle 131
 lithium-ion (secondary) battery 160, 178
 local-density approximation (LDA) 177
 localised orbital 177
 longitudinal acoustic (LA) mode 54
 Lorentz-Drude model 97
 low-temperature graphitisation 155
 luminescence intensity 177

magnetic length 78
 magnetic moment 73
 magnetic susceptibility 81
 magnetisation 72
 magnetoconductance 117
 magnetoresistance 74, 115, 159
 matrix display 177
 Maxwell-Garnett (GM) model 94, 95
 mean free path 110
 mesoscopic system 1
 metal catalyst 144, 145
 metal phthalocyanine 156
 metal-insulator transition 43
 metallic (property) 42, 46, 92, 165
 mirror symmetry 69
 moiré pattern 17

nanoparticle 6
 nanorod 132, 136, 158
 nanoscale device (nanodevice) 164, 168
 nanoscale void 178
 nanotechnology 165
 nanowire 158
 narrow-gap semiconductive 46

optical absorption 67
 optical conductivity 92, 103, 167

p-n junction 158
 π plasmon 34

- π -conjugated conducting polymer 164
- π -electron bonding 153
- π -electron material 153, 157
- Pauli spin matrices 64
- Pauli susceptibility 42, 77, 90
- Peierls transition 43, 46, 108
- percolation limit 100
- phonon density of states (DOS) 53
- phonon dispersion 52
- photovoltaic device 179
- plasmon loss 34
- polarisability 140
- polarisation 67, 96
- polyacetylene 43, 164
- polymer/ C_{60} interface 179
- purification 8, 10
- pyrolytic carbon nanotube (PCNT) 146

- quantum transport 115

- Raman intensity 55
- Raman spectra 52, 59
- Raman-active mode 52
- rectifying effect 178
- reflectivity 92, 103
- reflexion 18
- relativistic Dirac equation 70
- resonant tunnelling 115
- rope 16, 23, 47, 112, 171
- rotating-cathode arc-discharge 3
- Russian-doll structure 158

- scanning electron microscope (SEM) 7, 158
- scanning force microscopy (SFM) 173
- scanning tunnelling microscope (STM) 3, 167
- scanning tunnelling spectroscopy (STS) 167
- scattering density 23
- Schrödinger-cat state 1
- scooter mechanism 157
- semiconductor 165
- semimetallic behaviour 84
- silicon carbide 148
- simple two-band (STB) model 115
- single electron tunnelling 170
- single microbundle 113
- single-molecule transistor 120
- soluble carbon nanotube (CNT) 180

spin susceptibility 83
streaked spot 14
superconducting quantum interference device (SQUID) 77
superconductivity 48
surface tension threshold 129
thermal oxidation 130, 133
thermoelectric power (TEP) 121
tight-binding 42, 65
tight-binding molecular dynamics (TBMD) 52
transmission electron diffraction (TED) 30
transmission electron microscope (or -py) (TEM) 8, 30, 32, 134, 156
transverse acoustic (TA) mode 53
transverse optical (TO) phonon mode 93
twisting acoustic (TW) mode 54
two-dimensional (2D) graphite 52, 64, 159

ultra-fine probe 164
universal conductance fluctuation (UCF) 117, 159

van der Waals force 15, 140
vapour-grown carbon fibre (VGCF) 143, 145

weak localisation 111, 165
wetting 131
Weyl's equation 64
wide-gap semiconductive 46

Young's modulus 54

zigzag-type carbon nanotube (CNT) 41, 45, 53, 55, 108

AUTHOR INDEX

- Ago, H. 164
Ajiki, H. 63
Amelinckx, S. 14
Ando, T. 63
- Bommeli, F. 89
Bonard, J. -M. 128
- Charlier, J. -C. 107
Châtelain, A. 128
- de Heer, W. A. 89, 128
Degiorgi, L. 89
Dresselhaus, G. 51
Dresselhaus, M. S. 51
- Endo, M. 143
- Forro, L. 89
Fukui, K. 1
- Hanada, T., 29
Hsu, W. -K. 143
Huang, Y. 40
- Issi, J. -P. 107
- Kosaka, M. 76
Kroto, H. W. 143
- Lambin, P. 14
Lucas, A. 14
- Okada, M. 40
Okada, Y. 29
- Saito, R. 51
Stöckli, T. 128
- Takeuchi, K. 143
Tanaka, K. 40, 143
Tanigaki, K. 76

Terrones, M. 143

Ugarte, D. 128

Walton, D. R. M. 143

Yamabe, T. 164

Yase, K. 29

Yoshimura, S. 153

Yumura, M. 2

ISBN 0 08 042696 4



9 780080 426969